Design, Fabrication, and Electrochemical Surface Plasmon Resonance Analysis of Nanoelectrode Arrays

by

Mahdieh Atighilorestani
B.Sc., Azad University Kerman Unit, 2005
M.Sc., Azad University Yazd Unit, 2008

A Dissertation Submitted in Partial Fulfillment
of the Requirements for the Degree of

DOCTOR OF PHILOSOPHY

in the Department of Chemistry

Supervisory Committee

Design, Fabrication, and Electrochemical Surface Plasmon Resonance Analysis of Nanoelectrode Arrays

by

Mahdieh Atighilorestani
B.Sc., Azad University Kerman Unit, 2005
M.Sc., Azad University Yazd Unit, 2008

Supervisory Committee

Dr. Alexandre G. Brolo (Department of Chemistry)
Supervisor

Dr. David Harrington (Department of Chemistry)
Departmental Member

Dr. Scott Mclndoe (Department of Chemistry)
Departmental Member

Dr. Rustom Bhiladvala (Department of Mechanical Engineering)
Outside Member

Abstract

Supervisory Committee

Dr. Alexandre G. Brolo (Department of Chemistry)
Supervisor
Dr. David Harrington (Department of Chemistry)
Departmental Member
Dr. Scott Mclndoe (Department of Chemistry)
Departmental Member
Dr. Rustom Bhiladvala (Department of Mechanical Engineering)
Outside Member

Recent advances in nanofabrication techniques have opened up new avenues and numerous possible applications in both nanoscale electrochemistry and analytical nanoscience by enabling the fabrication of reproducible nanoelectrodes with different new geometries. Nanoelectrodes exhibit advantages including enhanced mass transport, higher current densities, improved signal-to-noise ratios, and lower ohmic drop. In this dissertation, the use of nanoelectrodes in the electrochemical response properties investigations or in the spectroelectrochemical studies is the unifying factor among all the chapters. First (in Chapter 4), we presented a direct comparison between the electrochemical characteristics of two finite nanoelectrodes arrays with different geometries: 6 × 6 recessed nanodiscs and nanorings microarrays. Using computational methods, it was demonstrated that the electrode geometry's parameters have a drastic influence on the mass transport properties of the nanoelectrodes. The results presented here are the first combination of experimental and numerical studies that elucidate the transport on nanoring electrode arrays. The comparison of the electrochemical behavior between nanostructures using full 3D simulations is also unique.

Second, we have provided a comprehensive numerical study on the redox cycling performance properties of a 6 × 6 recessed nanorings-ring electrode array configuration. The simulation results were in good agreement with the experimental data. After validating the model against experiments, a comprehensive computational investigation revealed avenues to optimize the performance of the structure in terms of geometric parameters and scan rates.

The second half of this dissertation is comprised of the spectroelectrochemical studies. The combination of surface plasmon resonance with electrochemistry presents new paths to investigate

redox reaction events at the electrode surface since it brings an additional dimension to the classical electrochemical approaches.

Third, we have reported a novel active plasmonic device based on a new switching mechanism for the nanohole electrodes array to bridge between photonics and electronics at nanoscales. The inner surfaces of the nanohole electrodes in the array were coated with an electroconductive polymer, polypyrrole, (PPy). Then, it was shown that light transmitted through the PPy- modified nanohole electrodes can be easily tuned and controled by applying an external potential. We were also able to switch on and off the transmitted light intensity through the modified nanohole arrays by potential steps, demonstrating the potential of this platform to be incorporated into optoelectronic devices.

Finally, we have fabricated larger area plasmonic periodic nanopillar 3D electrodes using a rapid, high-throughput, and cost-effective approach: the laser interference lithography. Then, the electrochemical behavior of these electrodes was investigated both experimentally and computationally. The properties were ‘compared with a flat electrode with an equivalent geometric area. Afterward, we have successfully probed the changes in the concentration of a reversible redox pair near the electrode surface induced by various applied potentials, in an *in-situ* EC-SPR experiment.

Table of Content

List of Tables

List of Animations

List of Figures

Acknowledgments

I would like to thank:

My supervisor, Professor Alexandre G. Brolo, for giving me the opportunity to work in his group, for giving me the freedom to think and work independently, as well as his trust and guidance.

Professor David Harrington, for lab access and helpful discussions.

All the past and present Brolo's group members for creating an enjoyable and friendly lab environment, helpful discussions and support! Special mention to Nick, Milton, Regivaldo, Meikun, Karolina, Ruth, Fernando, Sabrina, and Diego.

Dr. Jacson W Menezes for laser interference lithography training, great discussions and friendship.

Dr. Ahmed Al Balushi for all his help with the LIL set up alignments, valuable discussions and friendship.

Adam Schuetze and Dr. Elaine Humphrey for SEM and FIB training, for wonderful discussions about the nanoarrays fabrication and for their assistance with the fabrications and Z-contrast imaging.

Jonathan Rudge for insightful and valuable discussions, his support, encouragement, and friendship.

Joe Kolthammer for helpful discussions.

Chris Secord and Jeffrey Allan Trafton (Machine Shop); Dr. Mario Ivanov, Andrew Macdonald, and Shubha Hosalli (Instrument Shop); Sean Adams (Glass Shop); chemistry department office; and chemical store for their help and assistance.

Dr. Irina Paci and Dr. Rustom Bhiladvala for their encouragement.

My family: my parents, my sisters, and my brother, for their unconditional love, endless support and encouragement.

My friends: Mahbubeh, Zeinab, Sedigheh, Azam, Raziyeh, Mehraveh, Soraya, and Zohrab, for their friendship, support, and encouragement.

My special friend and confidant Marilyn who kept me focused, grounded and secure and helped me continue with my studies through the last two years. I would like to dedicate Chapter 6 (Electrochemical Control of Light Transmission through Nanohole Electrode Arrays) to her. This would not have been written without her support.

"The function of education, therefore, is to teach one to think intensively and to think critically. But education which stops with efficiency may prove the greatest menace to society. The most dangerous criminal may be the man gifted with reason, but with no morals…We must remember that intelligence is not enough. Intelligence plus character — that is the goal of true education. The complete education gives one not only power of concentration, but worthy objectives upon which to concentrate…" – Martin Luther King Jr, The Purpose of Education

Dedication

This dissertation is dedicated to my family and the memory of my uncles Mehdi and Ahmadali Atighi.

Chapter 1 : Overview

1.1 Motivations

Microelectrodes are important in electrochemical measurements because they possess several advantages related to their small dimensions. These include enhanced mass transport rates, low double layer capacities, high signal to noise ratios, small IR drops, steady state responses, and high current densities[1-5]. These beneficial properties are even more important when the electrode dimensions are reduced to the nanometer range (nanoelectrodes) [3, 6-7] . Micro/nanoelectrodes have been widely used in a variety of electroanalysis and electrochemical experiments including biological measurements[8-10]. In spite of all their beneficial qualities, the current measured at a single micro or nanoelectrode is very low (pA-nA) and requires sensitive and specialized equipment. One way to overcome this limitation is to use an array of micro or nanoelectrodes operating in parallel [7, 11] . In this case, depending on the electrode size, geometry, spacing, and time scale of the experiment, the mass transport at the small electrodes could shift from radial to linear, due to diffusion layer overlaps between adjacent electrodes in the array[12]. However, in order to maintain the exceptional properties of the small electrodes, the overlapping between the diffusion layers of the elements of the array should be avoided.

A finite microarray of nanoelectrode elements presents a radial diffusion layer over the whole array when the diffusion layer of the individual electrodes extremely overlap. This is due to the small size (micrometer range) of the entire array[12]. Therefore, a key feature of finite microarrays of nanoelectrodes is that they possess a radial mass transport, and consequently a steady-state response in a wide range of scan rates, regardless of the extension of the diffusion layer overlap between their nanoelements[12].

In addition to the size, the geometry is also essential for small electrodes (where the thickness of the diffusion layer is larger than the electrode's dimensions)[3]. The geometry of the electrode drastically affects the shape of the diffusing layer and consequently, the electrochemical behavior. Although the strong influence of the electrode's geometry on mass transport properties at nanoscales is well-known[3], there has been no systematic study on the direct comparison of electrochemical responses at the nanoscale. Existing studies on finite arrays of nanoelectrode have been focused up to now only on the disc geometry[2, 12-13]. While the inlaid and recessed nano/micro disc electrodes can be considered most common geometries, it is also essential to study other electrode's shapes, since they might offer better electrochemical properties. For instance, increased current sensitivity should help on the development of portable/wearable electrochemical sensing devices. Although the electrochemical device sensitivity increases as the electrode size decreases, the small value of the output current places a severe limitation. Therefore, electrodes with different geometries, which might offer a higher current density on the same footprint, are highly desirable and valuable. However, the application of the electrodes with different geometries are hindered due to the lack of sufficient theoretical and experimental studies of their behavior.

In this dissertation, we have reported, for the first time, a detailed description of the behavior of recessed nanoring electrode elements in a finite microarray. The understanding of the behavior of different electrode geometries at the nanoscale is valuable. However, a proper comparison between geometries is essential to the optimization of miniaturized electrochemical devices. On this matter, we have also provided a direct comparison between the electrochemical characteristics of recessed nanorings and nanodiscs microarrays.

As mentioned above, the advantages of using nanoelectrodes are traded off by difficulties arising from measuring their very small absolute output current. This problem can also be

overcome for reversible and quasi-reversible redox pair by using the concept of redox cycling. This approach requires at least two working electrodes (or two arrays of working electrodes) separated by a small gap which can be biased independently. During the redox cycling process one electrode is set to a potential to drive either the oxidation or the reduction of the analyte under investigation, while the other electrode is held at a potential that drives the reverse process. The redox species generated at one electrode (generator) diffuses to the other electrode (collector), where it can be converted back to its original state. The regenerated species will then diffuse away from the collector electrode to the generator electrode, repeating the cycle. The repeated travel of redox species between the two electrodes allows multiple reactions of a single species at the electrode, leading to a greatly enhanced current signal at both the generator and the collector electrodes. Besides the amplified electrochemical signal, selectivity is also boosted using the redox cycling approach because only the current response from the reversible or quasi-reversible analyte of interest is enhanced in a well-designed measurement[14-17]. Due to these valuable features, redox cycling method has been used in a wide range of applications. They include in vitro analysis of dopamine in the presence of ascorbic acid[18-19], the detection of biomolecules[20], the determination of diffusion coefficients[21], the development of DNA biosensor[22], and in the development of electrochemical sensors[23]. The performance of the redox cycling devices greatly depends on the geometry and design of their generator and collector electrodes. The performance of a redox cycling system can be improved by minimizing the generator and collector electrodes' size and spacing between them. Implementing smaller electrodes with reduced separation distances results in fewer redox species escaping from the redox cycling trap into the bulk solution[16, 24-25]. A wide variety of redox cycling system with different designs and geometries has been proposed and studied over the years. They include dual cylinders[26], dual discs[27-28], dual bands[29-30], triple

bands[31-32], planar interdigitated band electrodes[14, 17, 33-35], and planar interdigitated ring electrodes[36-38]. An important alternative to the planar interdigitated configurations is vertically separated electrodes. In these configurations the conducting (electrodes) and insulating (gap) layers can simply be deposited with thin film fabrication methods[39-42]. Therefore, the remarkable advantage of the vertically separated electrodes over the planar configuration is that the gap between the generator and collector electrodes can be easily varied by the insulator layer thickness through deposition, without a need for reconfiguration of the device. Besides, vertically aligned generator and collector electrodes provide more compact devices compare to the planar structure which makes them suitable for lab-on-a-chip integration[39]. In this dissertation, we have demonstrated that proper pattern of these multi-film systems leads to an array of nanoholes containing two working ring electrodes separated by a gap. This type of structure is very efficient for redox cycling. After validating the model against experiments, a comprehensive computational investigation revealed avenues to optimize the performance of the structure in terms of geometric parameters and scan rates.

The second half of this dissertation focuses on the spectroelectrochemical studies. The combination of surface plasmon resonance with electrochemistry introduces new paths to evaluate redox reaction events at the electrode surface since it adds an additional dimension to the classical electrochemical approaches. SPR is a label-free and real-time technique with high sensitivity for characterizing and studying ultrathin films at solid/liquid interfaces[43-45]. Combined with electrochemical measurements, EC-SPR, it becomes a powerful approach for *in situ* observation and characterization of optical and electrochemical properties at electrode/electrolyte interfaces[46-48]. In EC-SPR measurements, a metal film (usually a gold film on a glass slide) is used as both the SPR sensing medium and the working electrode[46].

The transmission spectra properties of metallic nanograting structures (e.g., nanoslits, nanogrooves, and nanoholes array) depend on their material composition, their geometry, their depth, and periodicity[44-45, 49-51] . However, in principle, the optical properties of a given plasmonic nanostructure is fixed once it has been fabricated. As a result, it becomes very challenging to tune its plasmonic characteristics reversibly. On the other hand, surface plasmon resonance (SPR) is a highly sensitive phenomenon to the changes in the refractive index surrounding the metallic nanostructures. For this reason, integrating the plasmonic nanostructures with a medium whose dielectric properties can be varied reversibly by an external trigger results in active plasmonic devices. In active plasmonic devices, the frequency and/or the intensity of the plasmon resonance modes can be easily tuned reversibly via an external physical trigger. Active plasmonic devices have become the topic of important research attempts over the last several years due to their prospective usage in different technological applications, such as nanophotonic integrated circuits, optical communication, smart windows, and high-performance displays[52-53]. Candidates that can serve as an active surrounding medium for constructing an active plasmonic system include liquid crystals, inorganic materials, photochromic molecules, nonlinear optical materials and electroactive conducting polymers[54-62]. The refractive index properties of these materials surrounding the plasmonic nanostructures can be dynamically and reversibly modulated using a proper external stimulus such as heat, light, or electric potential. This, in turn, induces variations in the plasmonic response of the system which is devoted to building thermo-optical, all-optical, and electro-optical devices[54-62]. In particular, electroconductive polymers are promising materials for active plasmonic devices. Electrochemical switching between oxidized and reduced states of an electroconductive polymer immobilized on the metallic nanostructure surfaces has been demonstrated as a simple way to reversibly modulate the optical properties of plasmonic

nanostructures[57, 59]. However, most of the research on electroconductive polymers as an active surrounding medium have been focused on metallic nanoparticles [57, 63-66]. Recently, there have also been few examples of controlling the SPR transmission properties in nanoslits and nanograting using electrochemically switching electroconductive polymers[67-68]. However, there has been no demonstration of using electroconductive polymers as the electro-optical control for nanoholes array. In this dissertation, we have performed an experimental study of the dynamically modulated SPR optical transmission through polymer modified nanoholes array via an externally applied potential. We have demonstrated a novel active plasmonic device based on a new switching mechanism for the nanoholes array to bridge photonics and electronics at nanoscales.

Finally, the fabrication of uniform periodic nanostructured surfaces usually demands tedious and expensive advanced nanofabrication techniques. We developed a fast, high-throughput, and inexpensive fabrication approach based on laser interference lithography (IL) to fabricate a fully conductive periodic gold three-dimensional nanopillar electrodes (3-D Au-NPEs) array on a large area (2 cm× 2 cm). 3-D electrodes provide a notably larger electroactive surface area compared to that of the conventional flat electrodes resulting in higher currents[69-72]. The electrochemical performance of the 3-D Au-NPEs array was explored experimentally and numerically. The 3-D Au-NPEs array was further used for *in-situ* electrochemical and surface plasmon resonance (EC-SPR) measurements.

1.2 Dissertation Outline

This dissertation follows the article-style dissertation format and is organized as follows:

Chapter 2 presents a brief introduction to the microelectrodes, their arrays, and the basics of modeling electrochemistry in COMSOL Multiphysics®.

Chapter 3 provides a brief introduction to surface plasmon resonance and the method used in the fabrication of the nanoelectrodes.

Chapter 4 is based on the following published work: M. Atighilorestani, and A. G. Brolo, Comparing the Electrochemical Response of Nanostructured Electrode Arrays, Anal. Chem. 2017, 89 (11), 6129-6135.

Chapter 5 is based on the published work: M. Atighilorestani, and A. G. Brolo, Recessed Gold Nanoring-Ring Microarray Electrodes, Anal. Chem., http://pubs.acs.org/doi/abs/10.1021/acs.analchem.7b01943

Chapter 6 is based on the published work: M. Atighilorestani, D. P. dos Santos, R. FVV Jaimes, M. M Rahman, M. LA Temperini, and A. G. Brolo, Electrochemical Control of Light Transmission through Nanohole Electrode Arrays, ACS Photonics 2016, 3, 2375-2382.

Chapter 7 is based on the published work: M. Atighilorestani, J. W. Menezes, and A. G. Brolo, Large Area Plasmonic Gold Nanopillar 3-D Electrodes, Electrochimica Acta 2016, 188, 91-97.

1.3 References

1. Davis, F.; Higson, S. P. J., Arrays of Microelectrodes: Technologies for Environmental Investigations. *Environmental Science-Processes & Impacts* **2013**, *15*, 1477-1489.
2. Fernandez, J. L.; Wijesinghe, M.; Zoski, C. G., Theory and Experiments for Voltammetric and Secm Investigations and Application to Orr Electrocatalysis at Nanoelectrode Ensembles of Ultramicroelectrode Dimensions. *Anal. Chem.* **2015**, *87*, 1066-1074.
3. Murray, R. W., Nanoelectrochemistry: Metal Nanoparticles, Nanoelectrodes, and Nanopores. *Chem. Rev.* **2008**, *108*, 2688-2720.
4. Potter, K. A.; Buck, A. C.; Self, W. K.; Callanan, M. E.; Sunil, S.; Capadona, J. R., The Effect of Resveratrol on Neurodegeneration and Blood Brain Barrier Stability Surrounding Intracortical Microelectrodes. *Biomaterials* **2013**, *34*, 7001-7015.
5. Tsigara, A.; Benkhial, A.; Warren, S.; Akkari, F.; Wright, J.; Frehill, F.; Dempsey, E., Metal Microelectrode Nanostructuring Using Nanosphere Lithography and Photolithography with Optimization of the Fabrication Process. *Thin Solid Films* **2013**, *537*, 269-274.
6. Arrigan, D. W. M., Nanoelectrodes, Nanoelectrode Arrays and Their Applications. *Analyst (Cambridge, U. K.)* **2004**, *129*, 1157-1165.
7. Liu, Y.; Sairi, M.; Neusser, G.; Kranz, C.; Arrigan, D. W. M., Achievement of Diffusional Independence at Nanoscale Liquid Liquid Interfaces within Arrays. *Anal. Chem.* **2015**, *87*, 5486-5490.
8. Amatore, C.; Arbault, S.; Bouret, Y.; Guille, M.; Lemaitre, F., Prediction of Local Ph Variations During Amperometric Monitoring of Vesicular Exocytotic Events at Chromaffin Cells. *Chemphyschem* **2010**, *11*, 2931-2941.
9. Conyers, J. L.; White, H. S., Electrochemical Characterization of Electrodes with Submicrometer Dimensions. *Anal. Chem.* **2000**, *72*, 4441-4446.
10. Wightman, R. M., Microvoltammetric Electrodes. *Anal. Chem.* **1981**, *53*, 1125-&.
11. Lanyon, Y. H.; Arrigan, D. W. M., Recessed Nanoband Electrodes Fabricated by Focused Ion Beam Milling. *Sens. Actuators, B* **2007**, *121*, 341-347.
12. Godino, N.; Borrise, X.; Xavier Munoz, F.; Javier del Campo, F.; Compton, R. G., Mass Transport to Nanoelectrode Arrays and Limitations of the Diffusion Domain Approach: Theory and Experiment. *J. Phys. Chem. C* **2009**, *113*, 11119-11125.
13. Zoski, C. G.; Wijesinghe, M., Electrochemistry at Ultramicroelectrode Arrays and Nanoelectrode Ensembles of Macro- and Ultramicroelectrode Dimensions. *Isr. J. Chem.* **2010**, *50*, 347-359.
14. Bard, A. J.; Crayston, J. A.; Kittlesen, G. P.; Shea, T. V.; Wrighton, M. S., Digital-Simulation of the Measured Electrochemical Response of Reversible Redox Couples at Microelectrode Arrays - Consequences Arising from Closely Spaced Ultramicroelectrodes. *Anal. Chem.* **1986**, *58*, 2321-2331.
15. Barnes, E. O.; Lewis, G. E. M.; Dale, S. E. C.; Marken, F.; Compton, R. G., Generator-Collector Double Electrode Systems: A Review. *Analyst (Cambridge, U. K.)* **2012**, *137*, 1068-1081.
16. Cohen, A. E.; Kunz, R. R., Large-Area Interdigitated Array Microelectrodes for Electrochemical Sensing. *Sens. Actuators, B* **2000**, *62*, 23-29.

17. Niwa, O.; Morita, M.; Tabei, H., Electrochemical-Behavior of Reversible Redox Species at Interdigitated Array Electrodes with Different Geometries - Consideration of Redox Cycling and Collection Efficiency. *Anal. Chem.* **1990**, *62*, 447-452.
18. Niwa, O.; Morita, M.; Tabei, H., Highly Sensitive and Selective Voltammetric Detection of Dopamine with Vertically Separated Interdigitated Array Electrodes. *Electroanalysis* **1991**, *3*, 163-168.
19. Oleinick, A.; Zhu, F.; Yan, J. W.; Mao, B. W.; Svir, I.; Amatore, C., Theoretical Investigation of Generator-Collector Microwell Arrays for Improving Electroanalytical Selectivity: Application to Selective Dopamine Detection in the Presence of Ascorbic Acid. *Chemphyschem* **2013**, *14*, 1887-1898.
20. Van Gerwen, P.; Laureyn, W.; Laureys, W.; Huyberechts, G.; De Beeck, M. O.; Baert, K.; Suls, J.; Sansen, W.; Jacobs, P.; Hermans, L.; Mertens, R., Nanoscaled Interdigitated Electrode Arrays for Biochemical Sensors. *Sens. Actuators, B* **1998**, *49*, 73-80.
21. Feldman, B. J.; Feldberg, S. W.; Murray, R. W., An Electrochemical Time-of-Flight Experiment. *J. Phys. Chem.* **1987**, *91*, 6558-6560.
22. Finot, E.; Bourillot, E.; Meunier-Prest, R.; Lacroute, Y.; Legay, G.; Cherkaoui-Malki, M.; Latruffe, N.; Siri, O.; Braunstein, P.; Dereux, A., Performance of Interdigitated Nanoelectrodes for Electrochemical DNA Biosensor. *Ultramicroscopy* **2003**, *97*, 441-449.
23. Morita, M.; Niwa, O.; Horiuchi, T., Interdigitated Array Microelectrodes as Electrochemical Sensors. *Electrochim. Acta* **1997**, *42*, 3177-3183.
24. Ma, C.; Contento, N. M.; Gibson, L. R., II; Bohn, P. W., Redox Cycling in Nanoscale-Recessed Ring-Disk Electrode Arrays for Enhanced Electrochemical Sensitivity. *Acs Nano* **2013**, *7*, 5483-5490.
25. Paeschke, M.; Wollenberger, U.; Kohler, C.; Lisec, T.; Schnakenberg, U.; Hintsche, R., Properties of Interdigital Electrode Arrays with Different Geometries. *Anal. Chim. Acta* **1995**, *305*, 126-136.
26. Seddon, B. J.; Wang, C. F.; Peng, W. F.; Zhang, X. J., Preparation and Amperometric Response of Carbon and Platinum Dual-Cylinder Microelectrodes. *Electrochim. Acta* **1995**, *40*, 455-465.
27. Baur, J. E.; Motsegood, P. N., Diffusional Interactions at Dual Disk Microelectrodes: Comparison of Experiment with Three-Dimensional Random Walk Simulations. *J. Electroanal. Chem.* **2004**, *572*, 29-40.
28. Cutress, I. J.; Wang, Y.; Limon-Petersen, J. G.; Dale, S. E. C.; Rassaei, L.; Marken, F.; Compton, R. G., Dual-Microdisk Electrodes in and Theory Transient Generator-Collector Mode: Experiment. *J. Electroanal. Chem.* **2011**, *655*, 147-153.
29. Barnes, E. O.; Lewis, G. E. M.; Dale, S. E. C.; Marken, F.; Compton, R. G., Dual Band Electrodes in Generator-Collector Mode: Simultaneous Measurement of Two Species. *J. Electroanal. Chem.* **2013**, *703*, 38-44.
30. Rajantie, H.; Strutwolf, J.; Williams, D. E., Theory and Practice of Electrochemical Titrations with Dual Microband Electrodes. *J. Electroanal. Chem.* **2001**, *500*, 108-120.
31. Bartelt, J. E.; Deakin, M. R.; Amatore, C.; Wightman, R. M., Construction and Use of Paired and Triple Band Microelectrodes in Solutions of Low Ionic-Strength. *Anal. Chem.* **1988**, *60*, 2167-2169.
32. Fosset, B.; Amatore, C.; Bartelt, J.; Wightman, R. M., Theory and Experiment for the Collector-Generator Triple-Band Electrode. *Anal. Chem.* **1991**, *63*, 1403-1408.

33. Belmont, C.; Girault, H. H., Coplanar Interdigitated Band Electrodes for Electrosynthesis .3. Epoxidation of Propylene. *Electrochim. Acta* **1995**, *40*, 2505-2510.
34. Tomcik, P.; Krajcikova, M.; Bustin, D., Determination of Pharmaceutical Dosage Forms Via Diffusion Layer Titration at an Interdigitated Microelectrode Array. *Talanta* **2001**, *55*, 1065-1070.
35. Tomcik, P.; Mesaros, S.; Bustin, D., Titrations with Electrogenerated Hypobromite in the Diffusion Layer of Interdigitated Microelectrode Array. *Anal. Chim. Acta* **1998**, *374*, 283-289.
36. Barnes, E. O.; Fernandez-la-Villa, A.; Pozo-Ayuso, D. F.; Castano-Alvarez, M.; Lewis, G. E. M.; Dale, S. E. C.; Marken, F.; Compton, R. G., Interdigitated Ring Electrodes: Theory and Experiment. *J. Electroanal. Chem.* **2013**, *709*, 57-64.
37. Liu, Z. M.; Niwa, O.; Kurita, R.; Horiuchi, T., Carbon Film-Based Interdigitated Array Microelectrode Used in Capillary Electrophoresis with Electrochemical Detection. *Anal. Chem.* **2000**, *72*, 1315-1321.
38. Niwa, O.; Morita, M., Carbon Film-Based Interdigitated Ring Array Electrodes as Detectors in Radial Flow Cells. *Anal. Chem.* **1996**, *68*, 355-359.
39. Ma, C. X.; Contento, N. M.; Gibson, L. R.; Bohn, P. W., Redox Cycling in Nanoscale-Recessed Ring-Disk Electrode Arrays for Enhanced Electrochemical Sensitivity. *Acs Nano* **2013**, *7*, 5483-5490.
40. Menshykau, D.; del Campo, F. J.; Munoz, F. X.; Compton, R. G., Current Collection Efficiency of Micro- and Nano-Ring-Recessed Disk Electrodes and of Arrays of These Electrodes. *Sens. Actuators, B* **2009**, *138*, 362-367.
41. Menshykau, D.; O'Mahony, A. M.; del Campo, F. J.; Munoz, F. X.; Compton, R. G., Microarrays of Ring-Recessed Disk Electrodes in Transient Generator-Collector Mode: Theory and Experiment. *Anal. Chem.* **2009**, *81*, 9372-9382.
42. Niwa, O.; Morita, M.; Tabei, H., Fabrication and Characteristics of Vertically Separated Interdigitated Array Electrodes. *J. Electroanal. Chem.* **1989**, *267*, 291-297.
43. Baba, A.; Advincula, R. C.; Knoll, W., In Situ Investigations on the Electrochemical Polymerization and Properties of Polyaniline Thin Films by Surface Plasmon Optical Techniques. *J. Phys. Chem. B* **2002**, *106*, 1581-1587.
44. Brolo, A. G., Plasmonics for Future Biosensors. *Nature Photonics* **2012**, *6*, 709-713.
45. Valsecchi, C.; Brolo, A. G., Periodic Metallic Nanostructures as Plasmonic Chemical Sensors. *Langmuir* **2013**, *29*, 5638-5649.
46. Baba, A.; Tian, S. J.; Stefani, F.; Xia, C. J.; Wang, Z. H.; Advincula, R. C.; Johannsmann, D.; Knoll, W., Electropolymerization and Doping/Dedoping Properties of Polyaniline Thin Films as Studied by Electrochemical-Surface Plasmon Spectroscopy and by the Quartz Crystal Microbalance. *J. Electroanal. Chem.* **2004**, *562*, 95-103.
47. Badia, A.; Arnold, S.; Scheumann, V.; Zizlsperger, M.; Mack, J.; Jung, G.; Knoll, W., Probing the Electrochemical Deposition and/or Desorption of Self-Assembled and Electropolymerizable Organic Thin Films by Surface Plasmon Spectroscopy and Atomic Force Microscopy. *Sens. Actuators, B* **1999**, *54*, 145-165.
48. Iwasaki, Y.; Horiuchi, T.; Morita, M.; Niwa, O., Time Differential Surface Plasmon Resonance Measurements Applied for Electrochemical Analysis. *Electroanalysis* **1997**, *9*, 1239-1241.
49. Chang, Y. T.; Chuang, T. H.; Yang, C. H.; Tsai, M. W.; Lee, S. C., Transmission through Randomly Arranged Microcells of Subwavelength Holes on an Aluminum Film. *Appl. Phys. Lett.* **2007**, *90*.

50. Fang, X.; Li, Z. Y.; Long, Y. B.; Wei, H. X.; Liu, R. J.; Ma, J. Y.; Kamran, M.; Zhao, H. Y.; Han, X. F.; Zhao, B. R.; Qiu, X. G., Surface-Plasmon-Polariton Assisted Diffraction in Periodic Subwavelength Holes of Metal Films with Reduced Interplane Coupling. *Phys. Rev. Lett.* **2007**, *99*.
51. Sun, M.; Tian, J.; Han, S. Z.; Li, Z. Y.; Cheng, B. Y.; Zhang, D. Z.; Jin, A. Z.; Yang, H. F., Effect of the Subwavelength Hole Symmetry on the Enhanced Optical Transmission through Metallic Films. *J. Appl. Phys.* **2006**, *100*.
52. Jiang, M.-M.; Chen, H.-Y.; Shan, C.-X.; Shen, D.-Z., Tunability of Hybridized Plasmonic Waveguide Mediated by Surface Plasmon Polaritons. *Phys. Chem. Chem. Phys.* **2014**, *16*, 16233-16240.
53. Lee, H. W.; Papadakis, G.; Burgos, S. P.; Chander, K.; Kriesch, A.; Pala, R.; Peschel, U.; Atwater, H. A., Nanoscale Conducting Oxide Plasmostor. *Nano Lett.* **2014**, *14*, 6463-6468.
54. Gao, W. L.; Shi, G.; Jin, Z. H.; Shu, J.; Zhang, Q.; Vajtai, R.; Ajayan, P. M.; Kono, J.; Xu, Q. F., Excitation and Active Control of Propagating Surface Plasmon Polaritons in Graphene. *Nano Lett.* **2013**, *13*, 3698-3702.
55. Koenig, G. M.; Meli, M. V.; Park, J. S.; de Pablo, J. J.; Abbott, N. L., Coupling of the Plasmon Resonances of Chemically Functionalized Gold Nanoparticles to Local Order in Thermotropic Liquid Crystals. *Chem. Mater.* **2007**, *19*, 1053-1061.
56. Kossyrev, P. A.; Yin, A. J.; Cloutier, S. G.; Cardimona, D. A.; Huang, D. H.; Alsing, P. M.; Xu, J. M., Electric Field Tuning of Plasmonic Response of Nanodot Array in Liquid Crystal Matrix. *Nano Lett.* **2005**, *5*, 1978-1981.
57. Leroux, Y.; Eang, E.; Fave, C.; Trippe, G.; Lacroix, J. C., Conducting Polymer/Gold Nanoparticle Hybrid Materials: A Step toward Electroactive Plasmonic Devices. *Electrochem. Commun.* **2007**, *9*, 1258-1262.
58. Leroux, Y.; Lacroix, J. C.; Fave, C.; Trippe, G.; Felidj, N.; Aubard, J.; Hohenau, A.; Krenn, J. R., Tunable Electrochemical Switch of the Optical Properties of Metallic Nanoparticles. *Acs Nano* **2008**, *2*, 728-732.
59. Leroux, Y. R.; Lacroix, J. C.; Chane-Ching, K. I.; Fave, C.; Felidj, N.; Levi, G.; Aubard, J.; Krenn, J. R.; Hohenau, A., Conducting Polymer Electrochemical Switching as an Easy Means for Designing Active Plasmonic Devices. *J. Am. Chem. Soc.* **2005**, *127*, 16022-16023.
60. Ming, T. A.; Zhao, L.; Xiao, M. D.; Wang, J. F., Resonance-Coupling-Based Plasmonic Switches. *Small* **2010**, *6*, 2514-2519.
61. Suh, J. Y.; Donev, E. U.; Lopez, R.; Feldman, L. C.; Haglund, R. F., Modulated Optical Transmission of Subwavelength Hole Arrays in Metal-Vo2 Films. *Appl. Phys. Lett.* **2006**, *88*.
62. Zheng, Y. B.; Kiraly, B.; Cheunkar, S.; Huang, T. J.; Weiss, P. S., Incident-Angle-Modulated Molecular Plasmonic Switches: A Case of Weak Exciton-Plasmon Coupling. *Nano Lett.* **2011**, *11*, 2061-2065.
63. Jiang, N.; Ruan, Q.; Qin, F.; Wang, J.; Lin, H.-Q., Switching Plasmon Coupling through the Formation of Dimers from Polyaniline-Coated Gold Nanospheres. *Nanoscale* **2015**, *7*, 12516-12526.
64. Leroux, Y.; Lacroix, J. C.; Fave, C.; Stockhausen, V.; Felidj, N.; Grand, J.; Hohenau, A.; Krenn, J. R., Active Plasmonic Devices with Anisotropic Optical Response: A Step toward Active Polarizer. *Nano Lett.* **2009**, *9*, 2144-2148.
65. Schaming, D.; Van-Quynh, N.; Martin, P.; Lacroix, J.-C., Tunable Plasmon Resonance of Gold Nanoparticles Functionalized by Electroactive Bisthienylbenzene Oligomers or Polythiophene. *J. Phys. Chem. C* **2014**, *118*, 25158-25166.

66. Stockhausen, V.; Martin, P.; Ghilane, J.; Leroux, Y.; Randriamahazaka, H.; Grand, J.; Felidj, N.; Lacroix, J. C., Giant Plasmon Resonance Shift Using Poly(3,4-Ethylenedioxythiophene) Electrochemical Switching. *J. Am. Chem. Soc.* **2010**, *132*, 10224-10226.
67. Baba, A.; Tada, K.; Janmanee, R.; Sriwichai, S.; Shinbo, K.; Kato, K.; Kaneko, F.; Phanichphant, S., Controlling Surface Plasmon Optical Transmission with an Electrochemical Switch Using Conducting Polymer Thin Films. *Adv. Funct. Mater.* **2012**, *22*, 4383-4388.
68. Xu, T.; Walter, E. C.; Agrawal, A.; Bohn, C.; Velmurugan, J.; Zhu, W.; Lezec, H. J.; Talin, A. A., High-Contrast and Fast Electrochromic Switching Enabled by Plasmonics. *Nat. Commun.* **2016**, *7*.
69. Cherevko, S.; Chung, C.-H., Gold Nanowire Array Electrode for Non-Enzymatic Voltammetric and Amperometric Glucose Detection. *Sensors and Actuators B: Chemical* **2009**, *142*, 216-223.
70. Fan, Z.; Ruebusch, D. J.; Rathore, A. A.; Kapadia, R.; Ergen, O.; Leu, P. W.; Javey, A., Challenges and Prospects of Nanopillar-Based Solar Cells. *Nano Res.* **2009**, *2*, 829-843.
71. Kandziolka, M.; Charlton, J. J.; Kravchenko, II; Bradshaw, J. A.; Merkulov, I. A.; Sepaniak, M. J.; Lavrik, N. V., Silicon Nanopillars as a Platform for Enhanced Fluorescence Analysis. *Anal. Chem.* **2013**, *85*, 9031-9038.
72. Prehn, R.; Abad, L.; Sánchez-Molas, D.; Duch, M.; Sabaté, N.; del Campo, F. J.; Muñoz, F. X.; Compton, R. G., Microfabrication and Characterization of Cylinder Micropillar Array Electrodes. *J. Electroanal. Chem.* **2011**, *662*, 361-370.

Chapter 2 : Introduction to the Micro/nanoelectrodes and electrochemistry modeling by COMSOL

2.1 Effect of electrode size on the electrochemical signal

Microelectrodes (or ultramicroelectrodes) are defined as electrodes containing at least one dimension, referred to as the critical dimension, smaller than the size of the diffusion layer developed next to the electrode surface over the experimental timescale[1]. (The experimental timescale is controlled by the scan rate $v = \frac{\Delta E}{\Delta t}$). The larger size of the diffusion layer with respect to the critical dimension of the electrode leads to the domination of a radial diffusion (or quasi-radial diffusion at a small band electrode) at the electrode surface, as shown in Figure 2-1b, and consequently, results in a steady-state voltammetric response. In contrast, a planar diffusion dominates at the surface of a macroelectrode, as shown in Figure 2-1a, and results in a transient voltammetric response. A macroelectrode is an electrode with a critical dimension on the scale of millimeters, centimeters or meters. The critical dimension of a microelectrode (typically less than 25μm)[2] is given by the geometry of the electrode, for instance: radius for a disk electrode or width for a band electrode.

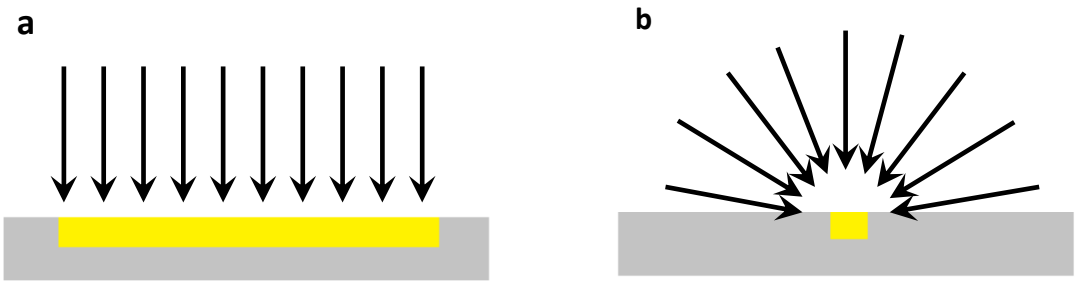

Figure 2-1. Schematic representation of a) planar diffusion to a macroelectrode, b) radial diffusion to a microelectrode.

The size of the diffusion layer (the area close to the electrode where the concentration of the electroactive species is different from its value in the bulk solution) can be estimated based on the Einstein's equation[3] for the root mean square displacement, $\bar{\Delta}$, of diffusing species[4] (in the absence of convection):

$$\bar{\Delta} = \sqrt{2D_{max}t_{tot}} \qquad \text{Eq. 2-1}$$

where D_{max} is the fastest diffusion coefficient of all the species involved in the electrochemical reaction and t_{tot} is the total experimental time. Accordingly, a given electrode with a critical dimension less than 25μm can behave differently in different solutions depending on the diffusion coefficient of the electroactive species and the time scale of the experiment (i.e. a given electrode may behave as a microelectrode in an aqueous solution but displays macroelectrode behavior in an ionic liquid[5]).

The first example of using a microelectrode in the analytical measurement was introduced by Davies and Brink, in 1942[6]. They described the measurement of local oxygen tension in animal tissues using microelectrodes. In the late 1960s, Fleischmann et al. performed major research

studies on microelectrodes[7]. And since the 1980s, the studies on microelectrodes have become an important research topic in electrochemistry[8].

2.2 The advantages of microelectrodes

Miniaturization of electrodes from a macro-scale to a micro- and nanoscale leads to a number of advantages in electrochemical measurements and applications. The small electrode surface area of the microelectrodes results in a very small current and therefore significantly reduces the ohmic drop (IR drop). In addition, the double layer capacitance of the microelectrodes is also greatly decreased due to the small size of the electrode. This is because the double layer capacitance is directly proportional to the electroactive surface area of the electrode[9], while the IR drop is proportional to the current being drawn at the electrode. The greatly reduced IR drop and double layer capacitance allow for the performance of high-speed voltammetric experiments on the microsecond timescale[10-11]. This permits to study fast homogeneous and heterogeneous electron transfer kinetics[9, 12-13] and the exploration of electrochemical reaction mechanisms[14]. The small IR drop also allows the electrochemical experiments to be conducted in solvents of low dielectric constant, in the absence of supporting electrolyte, in non-aqueous solvents (i.e. in organic solvents of high resistance such as benzene, toluene), in gaseous and solid phases[15-18].

As stated before, due to the small size of the microelectrodes, the nature of the diffusion of electroactive species to the electrode surface is radial (three-dimensional or convergent). This convergent diffusion provides a much higher mass transport to and from the surface of the electrode, resulting in a steady-state response and an enhanced current density[19-22]. The smaller the electrode size, the faster is the mass transport and the double layer capacitance also decreases.

Accordingly, the ratio of the faradaic current to the non-faradaic current, signal-to-noise ratio (S/N), is increased and the detection limit is improved[20, 22].

Additionally, due to the small electrode size, a microelectrode can be used for *in vivo* measurements, for example, within single biological cells (i.e. single brain cells)[23]. The small size of a microelectrode also allows for its operation in very low sample volumes[24]. Another advantage of using microelectrodes is that they can simplify the instrumental configuration from the conventional three-electrode to a two-electrode setup[25].

2.3 Effect of microelectrode geometry on the electrochemical signal

In the previous section, we have explained the significant effect of electrode size on the shape of the diffusion layer and consequently on the electrode response. Here, the influence of microelectrode geometry on the voltammetric response is described. In contrast to the macroelectrode (where the critical dimension of the electrode is much larger than the diffusion layer thickness, and, consequently, the effect of electrode geometry is insignificant), the shape of the diffusion layer and its development with time depends on the microelectrode geometry[26-27]. As a result, it is important to consider the electrode geometry of a microelectrode to interpret electrochemical results with good accuracy. The inlaid disc microelectrode is the most common type of electrode geometry used in electrochemical experiments. The other commonly used configurations include spherical, hemispherical, recessed disc, and band-shaped electrodes. Inlaid disc, recessed disc, and hemispherical microelectrodes show a steady-state limiting current, I_{lim}, given by:

Inlaid disc electrode[28]:

$$I_{lim} = 4nFDc_b r \qquad \text{Eq. 2-2}$$

Recessed disc electrode[29]:

$$\mathrm{I_{lim}} = \frac{4\pi \mathrm{nF} c_b \mathrm{Dr}^2}{4\mathrm{L} + \pi \mathrm{r}} \qquad \text{Eq. 2-3}$$

Hemispherical electrode[9]:

$$\mathrm{I_{lim}} = 2\pi \mathrm{nFD} c_b \mathrm{r} \qquad \text{Eq. 2-4}$$

where n is the number of transferred electrons per mole of analyte involved in the reaction, F is the Faraday constant, D is the diffusion coefficient of the electroactive species, c_b is the bulk solution concentration of the electroactive species , r is the radius of the electrode and L is the recessed depth.

Whereas the band microelectrodes do not show a true steady-state current response, they display a quasi-steady-state current, I_{qss}, at long times.

Band electrode[9]:

$$\mathrm{I_{qss}} = \frac{2\pi \mathrm{nFAD} c_b}{w \ln(64\mathrm{Dt}/\mathrm{w}^2)} \qquad \text{Eq. 2-5}$$

where A is area of the electrode, w is width of the band electrode , t is time, and the rest of parameters have been previously defined.

2.4 Microelectrode arrays

Regardless of the advantages emerging from the use of microelectrodes, the current generated at a single microelectrode is very small, and it is difficult to be detected. A solution to this problem is to use arrays of microelectrodes wired in parallel to achieve current amplification [30]. Ideally, the current response of such arrays should be m times higher than that of a single microelectrode, where m is the total number of microelectrodes supported by the array[31]. For example in ideal conditions, the current response of an array of inlaid microdisc electrodes is given by:

$$\mathrm{I_{lim}} = \mathrm{m4nFD}c_b\mathrm{r} \qquad \text{Eq. 2-6}$$

In practice, however, this equation is only correct when there is no overlap between the diffusion regimes of the neighboring electrodes and when an independent radial diffusion is maintained at each individual microelectrode in the array, see Figure 2-2b and Figure 2-3b. The interelectrode distance,d, between neighboring electrodes is a very important factor that helps define if each microelectrode in the array acts as an individual electrode. If the interelectrode distance between the microelectrodes is not sufficiently large, their diffusion layers start to interact/overlap[32].

The calculation of the minimum interelectrode distance required to maintain independent radial diffusion at each microdisc electrode in the array has evolved in the past few years.

The first proposed condition for microdisc electrode independent radial diffusion in an array was introduced based on the work of Saito[28]:

$$d > 12r \qquad \text{Eq. 2-7}$$

Where d is the interelectrode distance and r is the radius of the electrode. However, Girault et al.[33] have shown that this condition is not satisfactory, as it does not show a dependence on the scan rate. Later, Fletcher and Horne[34] suggested another condition derived from the work of Alfred and Odham[35]:

$$d > 20r \qquad \text{Eq. 2-8}$$

Next, Davies and Compton[32] indicated that for determining the minimum interelectrode distance the combination of all factors affecting the mass transport needs to be considered. They include the radius of the electrode, r, the diffusion coefficient of electroactive species, D, and the scan rate, v. The condition derived from their approach was[32]:

$$d > 2\sqrt{2D\frac{\Delta E}{\upsilon}} \qquad \text{Eq. 2-9}$$

where ΔE is the potential range from the initial potential to the switching potential in a voltammetric experiment. Later, Guo and Lindner[36] pointed out that, although Davies and Compton mentioned the importance of the effect of r on the mass transport, they did not considered this factor in their proposed formula (Eq. 2.10). Guo and Lindner[36] suggested that the dimensionless scan rate (V) could be used as a better alternative for deterring the minimum d, instead of using three independent $D, r, v,$ factors.

$$V = \frac{nF}{4RT}\frac{\upsilon r^2}{D} \qquad \text{Eq. 2-10}$$

where R is the universal gas constant, and T is the temperature.

In summary, the mass transport properties of a microelectrode array and consequently the shape and magnitude of its voltammetric response, are controlled by the size and geometry of the electrodes; the diffusion coefficients of electroactive species; the spacing between electrodes; and the time scale of the experiment (e.g. sweep rate in cyclic voltammetry) [27, 32, 36].

The size of the diffusion layers for each individual electrode present in the array changes as a function of the experimental time scale. The current response of the array is then controlled by the extent of the interaction between the diffusion layers of each electrode (i.e. no overlap of diffusion layers, partial overlap, and complete overlap of diffusion layers) which varies as the diffusion layer expands with time [32, 37-38] . Based on these studies, in 2005, Davies and Compton [32] have divided the overall current response of a microelectrode array into four different main categories, illustrated schematically in Figure 2-2 a-d. Two-dimensional simulated concentration profiles of these categories are also shown in Figure 2-3 a-d. These concentrations maps are given to provide a complementary view of the extension of the interaction between the diffusion layers with time. These concentration profiles of the electroactive species are taken at the steady state potentials or at the peak potentials corresponding to the voltammetric wave shapes.

These four categories are as follows[32]:

Category 1. At very short times (very fast scan rates), the diffusion layer thickness is smaller than the critical dimension of the electrodes leading to planar (linear) diffusion dominating mass transport. Thus, a peak-shaped voltammogram is observed. This is represented in Figure 2-2a and Figure 2-3a. The diffusion layers of adjacent electrodes do not interact in this case, and the electrodes are diffusionally isolated. So that the total current collected by such an array is equivalent to a macroelectrode with a geometric area the same as the sum of the individual areas

of each electrode supported by the array and therefore, the current is described by the Randles – Sevcik expression.

Category 2. At intermediate times, when the diffusion layer grows and its thickness becomes larger than the electrode critical dimension, but remains smaller than the interelectrode distances, the radial diffusion becomes the predominant mode of mass transport to each microelectrode in the array. The diffusion layers between the electrodes do not overlap, and the electrodes remain diffusionally isolated, and thus, a steady-state cyclic voltammogram (sigmoidal voltammogram) is achieved. This is represented in Figure 2-2b and Figure 2-3b. The cyclic voltammetric response of such an array can be ascribed to the response of an independent microelectrode multiplied by the number of electrodes making up the array.

Category 3. At longer times (slower scan rates), as the size of diffusion layer becomes greater than the separation distance between the microelectrodes, the diffusion layers of adjacent electrodes begin to overlap. This results in a change in the diffusional mass transport mode from a radial to a mixed diffusion zone, also known as a transition zone, (transition between planar diffusion and radial diffusion). The diffusion layer overlap reduces the flux density at the electrodes and lead to a decrease in the current response of the array. In this case, a quasi-sigmoidal-shape cyclic voltammogram (i.e. intermediate between sigmoidal and peak-shaped) is observed. This is represented in Figure 2-2c and Figure 2-3c.

Category 4. Finally, at long times, when the size of the diffusion layer is much larger than both the electrode size and the electrode spacing, the individual diffusion layers of all the electrodes in the array completely overlap. As a result, the planar diffusion becomes the dominant mode of mass transport over the entire microelectrode array, and a peak-shaped cyclic voltammogram is

obtained. This is represented in Figure 2-2d and Figure 2-3d. The array behaves like a macroelectrode having an equivalent geometric area of the entire array.

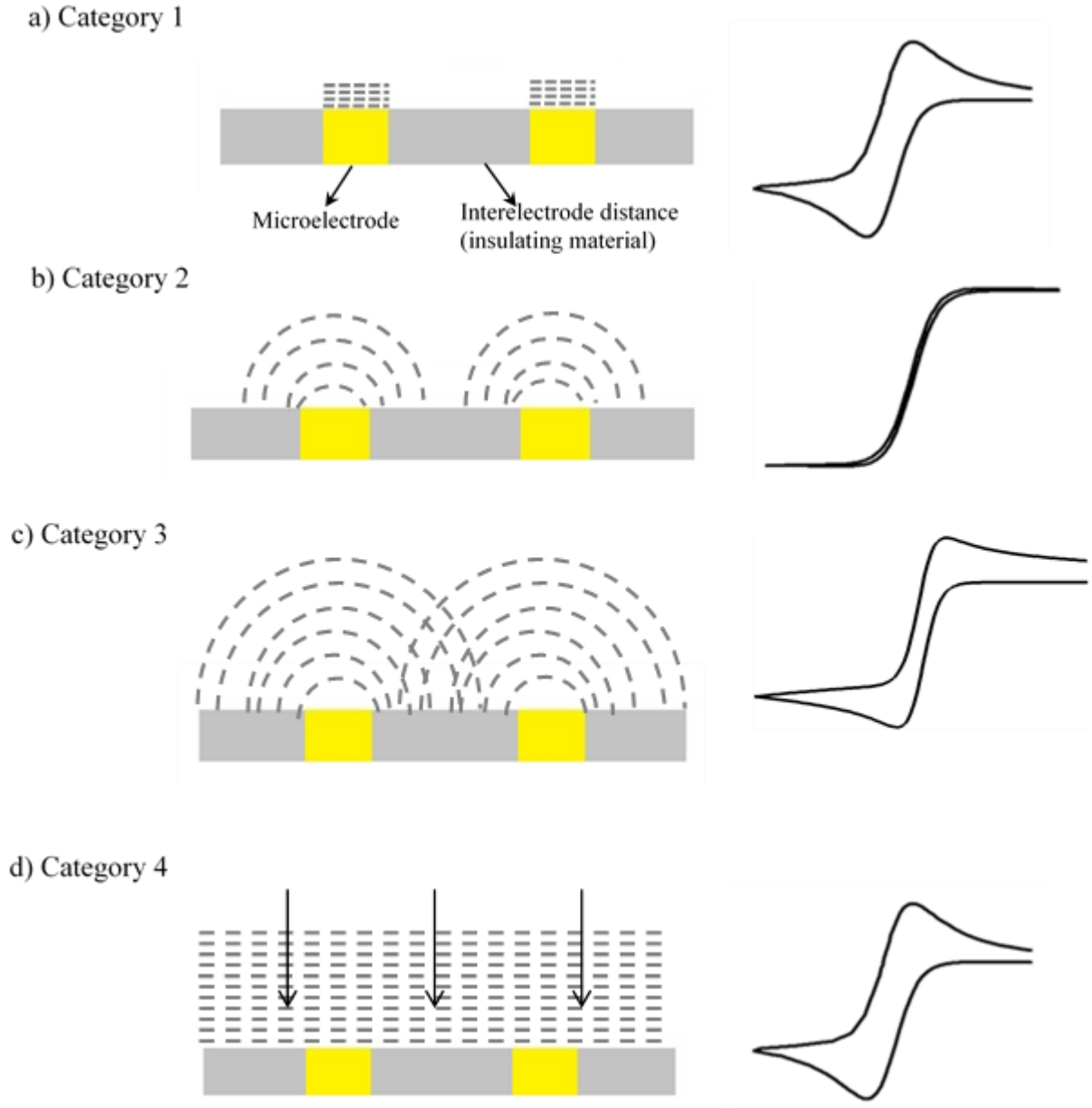

Figure 2-2. Schematic illustrations of the four main diffusion categories and their corresponding voltammograms for an array of microelectrodes.

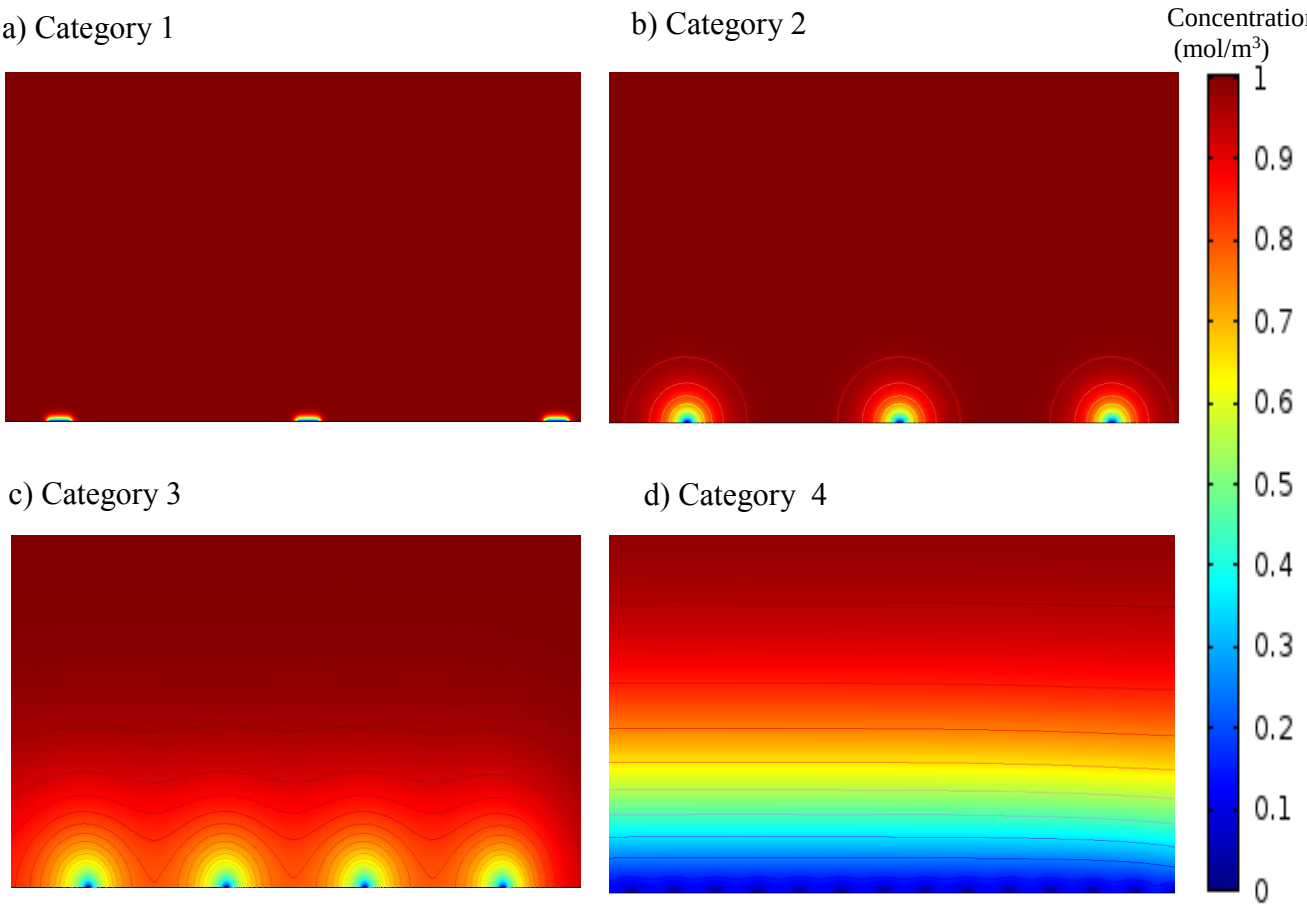

Figure 2-3. Simulated concentration profiles represent the four diffusion categories at an array of microelectrodes. [Resimulated and modified from[36]]

Category 2, in Figs 2-2b and 2-3b, is the optimum condition for the highest faradaic current/background ratio (S/N ratio, sensitivity), which is essential to a single microelectrode device. Mathematical modeling is often necessary for both the design and detailed interpretation/ analysis of the performance of microelectrode arrays. However, the numerical simulation of the behavior of microelectrode arrays is a complex problem, especially the simulation of their linear and cyclic voltammograms. In 2005, Davies and Compton[32] described a two-dimensional simulation method based on the diffusion domain approximation for the cyclic and linear sweep voltammetry of both regular and random arrays of disc microelectrodes arrays. The diffusion

domain approximation simplifies a complicated three-dimensional problem to a two-dimensional simulation with satisfactory results[32, 39]. The diffusion domain approximation was first proposed in 1978 by Matsuda et al. to simulate chronoamperometry and chronopotentiometry[40], and it was also used to simulate cyclic and linear sweep voltammetry[41] at partially covered electrodes. Later, in 1982, Amatore et al. simulated cyclic voltammograms at a disc microelectrodes array using the same concept and reported their famous zone diagram[37].

Figure 2-4a-c is a schematic representation of the diffusion domain approximation concept for a regular array of microdisc electrodes in a cubic arrangement. Each microelectrode can be assigned an independent diffusional compartment in the form of a square of side d, as shown in Figure 2-4a. d is the interelectrode distance between the microelectrodes in the array. In a regular array, the resulting square compartments are identical so that only the response of one square needs to be simulated. The response of the entire array can then be obtained by multiplying the response of this square by the number of microelectrodes in the array. For simplicity, the square compartment is replaced with a circle of the same area with radius $R_0 (\pi R_0^2 = d^2)$, as shown in Figure 2-4b. Therefore, the simulation area is now transformed into a cylindrical unit cell. The symmetrical properties of the cylindrical unit cell allow the problem to be reduced from a three-dimensional problem to a two-dimensional one, as shown in Figure 2-4c. It is worth mentioning that this approximation is most suited for the simulation of large arrays where there is a significantly greater number of microelectrodes inside the array compared to the number of microelectrodes located at the edge of the array. Under these conditions, the contribution of the enhanced diffusion at the external microelectrodes is negligible to the diffusion at the whole array. However, the diffusion domain approximation can fail and shows significant error when employed to the simulation of the behavior of small arrays (i.e. a nanoelectrode array for which the size of the whole array is

similar to the size of one single microelectrode) [33, 38, 42-43] . In other words, the current response from microelectrode /nanoelectrode arrays is extremely dependent on the overall size of the array when diffusion zones among neighboring electrodes overlap. Unlike a peak-shaped voltammetric response achieved with microelectrode/nanoelectrode arrays of millimeter size, a sigmoidal shape response is expected with a nanoelectrode array of micrometric dimension in the above mentioned condition. This behavior is caused by the overall shape of the diffusion layer set in over the entire array. In other words, the linear and radial diffusions of electroactive species towards the whole array surface, as shown in Figure 2-5 a-b, are responsible for obtaining either a transient or a steady-state response, respectively. When the whole array experiences a radial diffusion, the flux density at each nanoelectrode in the array strongly depends on its position in the array. In this case, the two-dimensional simulation base on the diffusion domain approximation is unable to provide satisfactory results, since the diffusion domain approach assumes an identical behavior for all the electrodes in an array. However, for the nanoelectrodes comprising a micrometric array, the contribution of each nanoelectrode element to the overall response of the array differs in terms of its position. Therefore, a three-dimensional simulation needs to be performed in order to accurately study the voltammetric response of the micrometer-sized array[43-44].

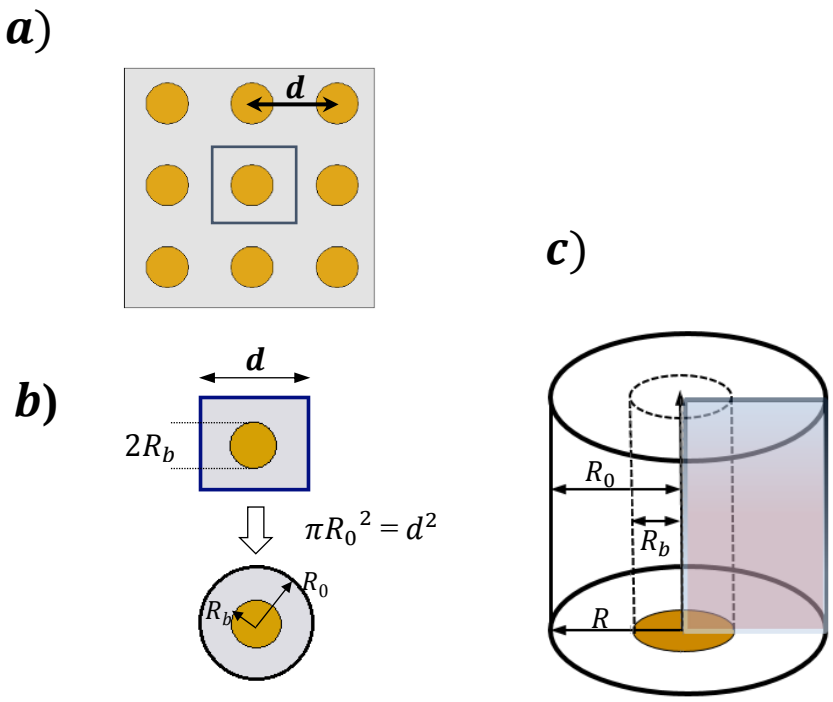

Figure 2-4. Schematic representation of the diffusion domain approximation concept[32] for a regular array of microdisc electrodes in a cubic arrangement. [Reproduced and modified from[32]]

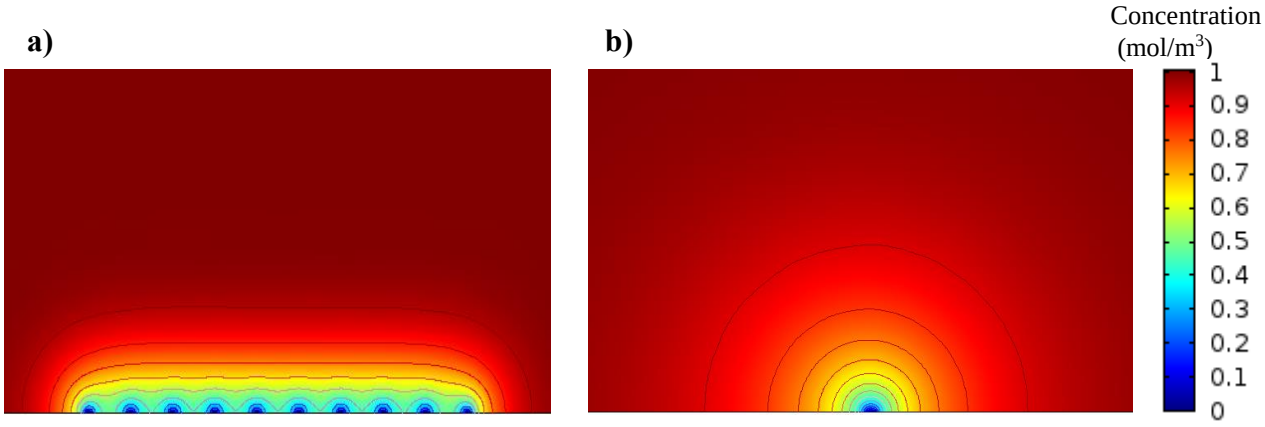

Figure 2-5. Simulated diffusion profile over an array of 10 a) microdisc electrodes, electrodes' radius = 10 μm and interelectrode distance = 150 um b) nanodisc electrodes, nanoelectrodes' radius = 200 nm and interelectrode distance = 450 nm.[43] [Resimulated and modified from[43]]

2.5 Modeling electrochemistry in COMSOL Multiphysics®

In this dissertation, a commercial finite element (FEM) software called COMSOL Multiphysics® has been used to study the electrochemical behavior of recessed nanorings and nanodiscs electrode arrays (in Chapter 4), recessed ring-ring electrodes array (in Chapter 5), and fully conductive nanopillar electrodes array (in Chapter 7).

The two-dimensional simulations based on the diffusion domain approximation have been used to solve the mass transport at fully conductive nanopillar electrodes array and recessed ring-ring nanoelectrodes array, in Chapters 7 and 5, respectively. Figure 2-6 (a-c) shows a two-dimensional representation of the mesh and concentration profiles developed to study the electrochemical response of the recessed ring-ring nanoelectrodes array (in Chapter 5). We have also modeled the mass transport at recessed nanorings and nanodiscs electrode arrays in three-dimensional domains

(in Chapter 4). The three-dimensional simulations were necessary because of the small size of the whole arrays. Note that the diffusion domain approximation falls short in providing accurate results when the size of the whole array is the same as a single microelectrode. Figure 2-7 and Figure 2-8 show the three-dimensional concentration profiles developed to study the mass transport at the recessed nanodiscs and nanorings electrode arrays, respectively (in Chapter 4). We have considered the simulation of a simple reversible redox reaction in all of the studies. Moreover, the diffusion coefficient of both redox species were assumed to be equal. Assuming that the electrochemical process is conducted in a stagnant solution and in the presence of a relatively high concentration of supporting electrolyte, the effects of convection and migration to the mass transport can be neglected. Under these assumptions, the electrochemical methods used in these studies, cyclic voltammetry, and potential step techniques, were both simulated under diffusion-only condition. In addition, we did not consider the IR drops effect between the working and reference electrode in any of the simulation studies in this dissertation. This is because we have used a high concentration of supporting electrolyte in experimental which resulted in high conductivity of the solutions. Note in this dissertation the mass transport at nanoelectrodes have been described by Fick's second law. The Fick's second law appropriately describes the mass transport when the migration is negligible in the system under study (due to the excess use of supporting electrolyte), and for the concentration range used here, and if the length of the device is bigger than 10 nm[45].

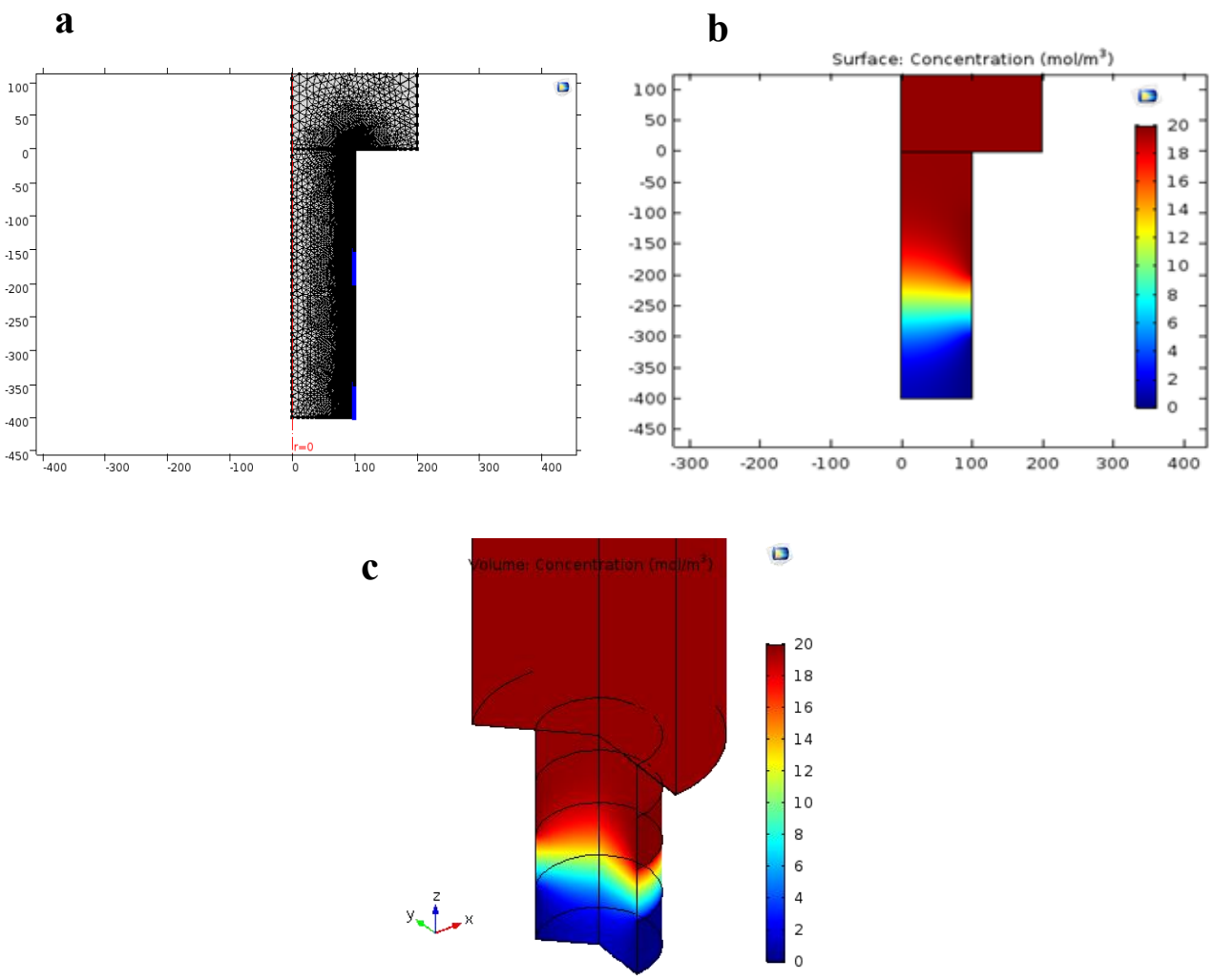

Figure 2-6. a) Mesh in two-dimensional axisymmetric simulation domain near the electrodes b) surface concentration profile c) volume concentration profile for recessed nanoring- ring electrodes.

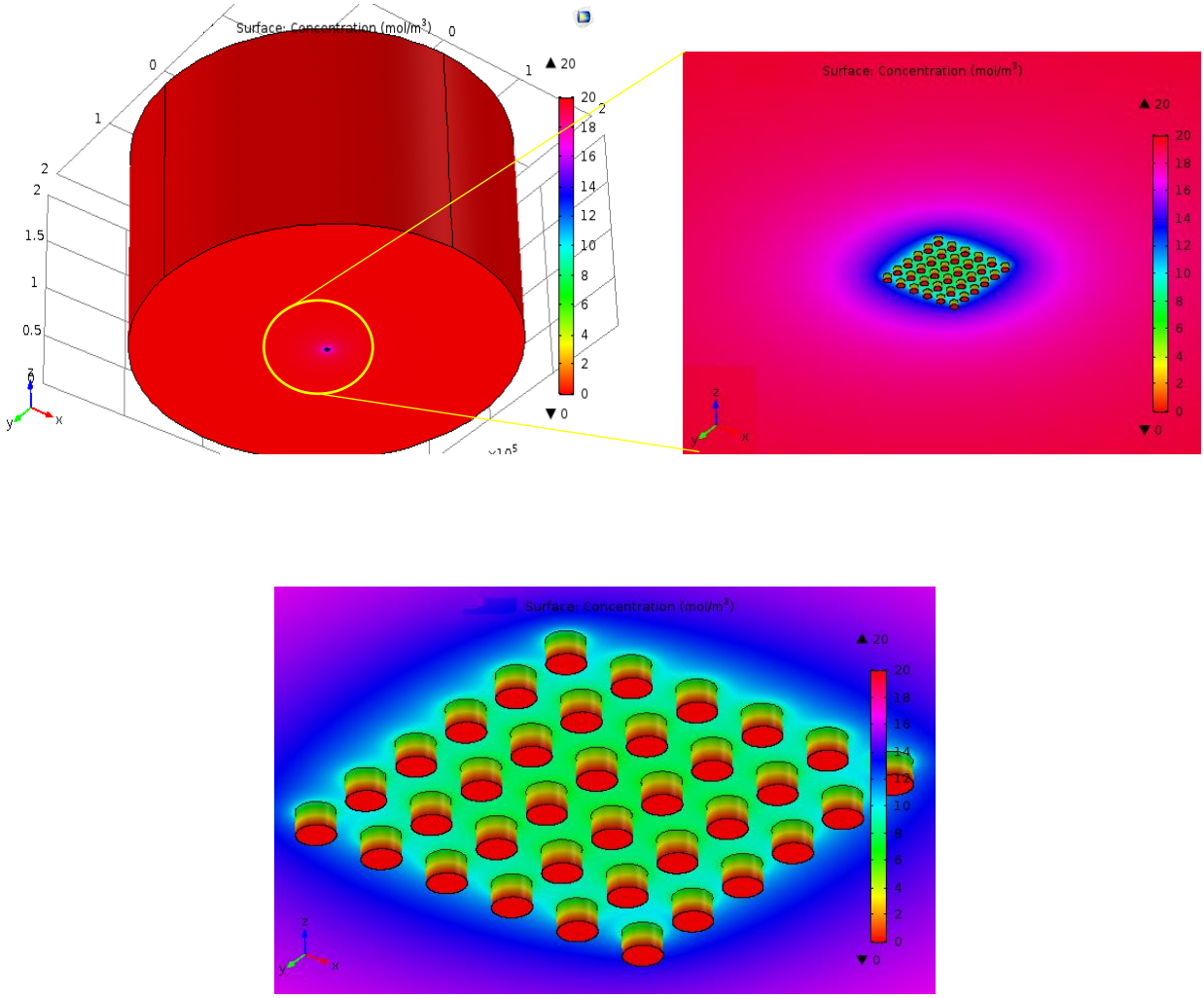

Figure 2-7. Three-dimensional diffusion concentration profiles for a 6×6 recessed nanodisc array. Nanodisc electrode radius (150 nm), recess depth (200 nm), interelectrode distance, 4*r*, (600 nm).

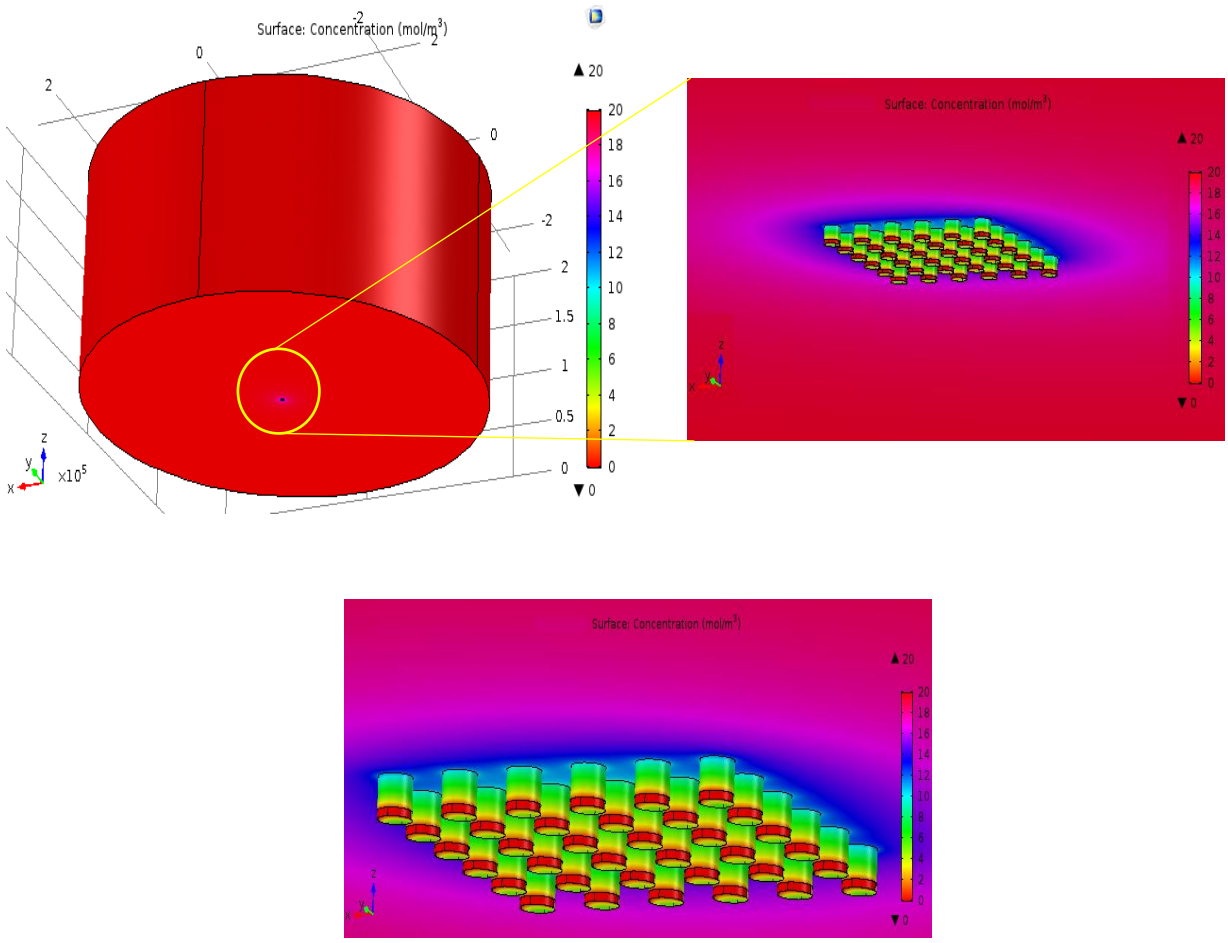

Figure 2-8. Three-dimensional diffusion concentration profiles for a 6×6 recessed nanoring electrode array. Nanohole electrode radius (150 nm), nanoring electrode height (50 nm), recess depth (200 nm), interelectrode distance, 4*r*, (600 nm)

2.5.1 Finite element simulation software package: COMSOL Multiphysics®

COMSOL Multiphysics® (known as FEMLAB before 2005) is a finite element simulation software package for simulating different physics-based problems, particularly for simulating

coupled or multiphysics phenomena[46]. The finite element method used in COMSOL Multiphysics® is a numerical technique that allows solving almost any problem requiring the use of partial differential equations (PDE). COMSOL Multiphysics® has an easy-to-use desktop interface. The first step in solving a problem in COMSOL Multiphysics® is selecting an application mode. COMSOL Multiphysics® is composed of different modules and functions for modeling different applications. For modeling cyclic voltammetry and step potential methods in COMSOL Multiphysics®, either the **Transport of Diluted Species (tds)** interface (which is a sub-module of Chemical Species Transport Module) or **Electroanalysis (elan)** interface (which is a sub-module of Electrochemistry Module) can be used. Both of these physics interfaces (sub-modules) have the predefined equations, boundary conditions, and rate expression terms for modeling mass transport at an electrode[46]. In this dissertation, the tds interface was used for modeling the electrochemical responses of all the nanoelectrodes arrays. The next step in solving a problem in COMSOL Multiphysics® is to set up the simulation geometry (domain). The model geometry can be simply drawn as in any other graphic design program. Once the simulation geometry has been established, the appropriate boundary conditions should be defined for the model. In COMSOL Multiphysics®, the user does not require writing mathematical equations and their boundary conditions. Although, it is possible to manually introduce an expression or equation into the COMSOL whenever it is necessary. For example, you can include your own equations that may describe boundary conditions. Regardless of all the complication associated with the simulation of micro/nanoelectrodes, all the simulation models share some general features related to the electrode kinetics, mass transport, boundary conditions, and meshing. We have considered the simulation of a simple reversible redox reaction with Bulter-Volmer kinetics in all of the studies:

$$O + \bar{e} \underset{k_b}{\overset{k_f}{\rightleftharpoons}} R$$ Eq. 2-11

Where O and R are both soluble species, but only species O is supposed to be present in the solution. Equal diffusion coefficients were assumed for both species. k_f and k_b are the forward and reverse reaction rate constants, defined by:

$$k_f = k^0 exp\left(-\frac{\alpha F}{RT}\left(E - E^{\acute{0}}\right)\right)$$ Eq. 2-12

$$k_b = k^0 exp\left(\frac{(1-\alpha)F}{RT}\left(E - E^{\acute{0}}\right)\right)$$ Eq. 2-13

k^0 is the heterogeneous rate constant for the redox couple, $E^{\acute{0}}$ is the formal electrode potential, E is the potential applied to the electrode, α is the effective transfer coefficient, assumed to be 0.5. The temperature, T, fixed at 298K. R and F are the universal gas constant and Faraday's constant, respectively. Figure 2-9 represents the boundary conditions used for the cyclic voltammetry simulation at an inlaid microdisc electrode in a two-dimensional domain.

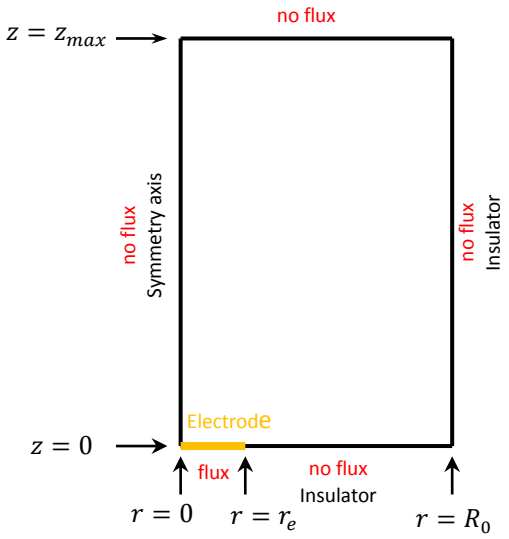

Figure 2-9. Schematic diagram of the whole simulation space for an inlaid microdisc electrode array.

Initial conditions:

$$c_O = c_b, \quad 0 \le r \le R_0, \quad 0 \le z \le z_{\max} \qquad \text{Eq. 2-14}$$

$$c_R = 0, \quad 0 \le r \le R_0, \quad 0 \le z \le z_{\max} \qquad \text{Eq. 2-15}$$

Flux boundary condition at electrode surface:

$$D_O \left[\frac{\partial c_O(r,z,t)}{\partial z} \right]_{z=0} = -D_R \left[\frac{\partial c_R(r,z,t)}{\partial z} \right]_{z=0} = k_f c_O(r,z,t) - k_b c_R(r,z,t) \qquad \text{Eq. 2-16}$$

Symmetry axis boundary condition:

$$D_O \left[\frac{\partial c_O(r,z,t)}{\partial r} \right]_{r=0} = D_R \left[\frac{\partial c_R(r,z,t)}{\partial r} \right]_{r=0} = 0 \qquad 0 < z < z_{\max} \qquad \text{Eq. 2-17}$$

Insulator boundary condition:

$$D_O\left[\frac{\partial c_O(r,z,t)}{\partial r}\right]_{r=R_0} = D_R\left[\frac{\partial c_R(r,z,t)}{\partial r}\right]_{r=R_0} = 0 \qquad 0 < z < z_{\max} \qquad \text{Eq. 2-18}$$

Insulator boundary condition:

$$D_O\left[\frac{\partial c_O(r,z,t)}{\partial z}\right]_{z=0} = D_R\left[\frac{\partial c_R(r,z,t)}{\partial z}\right]_{z=0} = 0 \qquad r_e < r < R_0 \qquad \text{Eq. 2-19}$$

Infinity boundary conditions:

$$c_O = c_b,\ z = z_{\max},\ 0 < r < R_0 \qquad \text{Eq. 2-20}$$

$$c_R = 0,\ z = z_{\max},\ 0 < r < R_0 \qquad \text{Eq. 2-21}$$

After defining the model geometry and appropriate boundary conditions, the model geometry should be discretized into much smaller elements called mesh. Meshing is a crucial step in solving a simulation problem. In the case of simulating the electrochemical behavior, much smaller meshes are required at the micro/nanoelectrode surface and at the edge of the micro/nanoelectrode where there is a discontinuity or singularity (the boundary conditions extremely changes from flux to no flux) [32]. This is because, at these regimes, there is a sharp change in the concentration. In this dissertation, the optimal mesh density has been determined for any of the presented simulations with successive mesh refinement until the results did not appreciably change (less than 1% variation between the results of two following simulations). Once the model is solved, a variety of plot types is available for post-processing simulation results in COMSOL. The numerical data from a plot or table can also be exported to a file to be analyzed with other software, such as Origin® and MATLAB®, as it was the case in this dissertation. The numerical results can be exported as images and animation files as well[46]. Finally, it worth mentioning that because we are using commercial software, COMSOL, to perform the simulations, a stringent validation step was

also performed. In order to validate the accuracy of the simulations, we first performed the simulations for an isolated inlaid and recessed microdisc electrode at steady-state, in both two-dimensional and three-dimensional domains, and compared the simulated result with the known analytical solutions. Results from both the two- dimensional and three-dimensional simulations of the isolated inlaid and recessed microelectrode electrode were in agreement better than 0.1% with those obtained from analytical solutions.

2.6 References

1. Arrigan, D. W. M., Nanoelectrodes, Nanoelectrode Arrays and Their Applications. *Analyst* **2004**, *129*, 1157-1165.
2. Bond, A. M., Past, Present and Future Contributions of Microelectrodes to Analytical Studies Employing Voltammetric Detection - a Review. *Analyst (Cambridge, U. K.)* **1994**, *119*, R1-R21.
3. Einstein, A., *Investigations on the Theory of the Brownian Movement*; Courier Corporation, 1956.
4. Davies, T. J.; Lowe, E. R.; Wilkins, S. J.; Compton, R. G., Voltammetric Sizing of Inert Particles. *Chemphyschem* **2005**, *6*, 1340-1347.
5. Kawano, R.; Watanabe, M., Equilibrium Potentials and Charge Transport of an I-/I-3(-) Redox Couple in an Ionic Liquid. *Chem. Commun.* **2003**, 330-331.
6. Davies, P. W.; Brink, F., Microelectrodes for Measuring Local Oxygen Tension in Animal Tissues. *Rev. Sci. Instrum.* **1942**, *13*, 524-533.
7. Ebbesen, T. W.; Lezec, H. J.; Ghaemi, H. F.; Thio, T.; Wolff, P. A., Extraordinary Optical Transmission through Sub-Wavelength Hole Arrays. *Nature (London, U. K.)* **1998**, *391*, 667-669.
8. Legeai, S.; Chatelut, M.; Vittori, O., Differential Pulse Voltammetry at Microdisk Electrodes. *Electrochim. Acta* **2005**, *50*, 4089-4096.
9. Bard, A. J.; Faulkner, L. R., *Electrochemical Methods : Fundamentals and Applications*, 2nd ed.; Wiley: New York, 2001, p xxi, 833 p.
10. Amatore, C.; Maisonhaute, E.; Simonneau, G., Ohmic Drop Compensation in Cyclic Voltammetry at Scan Rates in the Megavolt Per Second Range: Access to Nanometric Diffusion Layers Via Transient Electrochemistry. *J. Electroanal. Chem.* **2000**, *486*, 141-155.
11. Amatore, C.; Maisonhaute, E.; Simonneau, G., Ultrafast Cyclic Voltammetry: Performing in the Few Megavolts Per Second Range without Ohmic Drop. *Electrochem. Commun.* **2000**, *2*, 81-84.
12. Heinze, J., Ultramicroelectrodes in Electrochemistry. *Angewandte Chemie-International Edition* **1993**, *32*, 1268-1288.
13. Montenegro, M. I.; Pletcher, D., The Determination of the Kinetics of Electron-Transfer Using Fast Sweep Cyclic Voltammetry at Microdisc Electrodes. *J. Electroanal. Chem.* **1986**, *200*, 371-374.
14. Howell, J. O.; Wightman, R. M., Ultrafast Voltammetry of Anthracene and 9, 10-Diphenylanthracene. *The Journal of Physical Chemistry* **1984**, *88*, 3915-3918.
15. Bond, A. M.; Fleischmann, M.; Robinson, J., Electrochemistry in Organic-Solvents without Supporting Electrolyte Using Platinum Microelectrodes. *J. Electroanal. Chem.* **1984**, *168*, 299-312.
16. Daniele, S.; Baldo, M. A.; Ugo, P.; Mazzocchin, G. A., Determination of Heavy-Metals in Real Samples by Anodic-Stripping Voltammetry with Mercury Microelectrodes .1. Application to Wine. *Anal. Chim. Acta* **1989**, *219*, 9-18.
17. Howell, J. O.; Wightman, R. M., Ultrafast Voltammetry and Voltammetry in Highly Resistive Solutions with Microvoltammetric Electrodes. *Anal. Chem.* **1984**, *56*, 524-529.
18. Wang, J., *Analytical Electrochemistry*, 2nd ed.; John Wiley & Sons: New York, 2000, p xvi, 209 pages.
19. Coen, S.; Cope, D. K.; Tallman, D. E., Diffusion Current at a Band Electrode by an Integral-Equation Method. *J. Electroanal. Chem.* **1986**, *215*, 29-48.

20. Streeter, I.; Fietkau, N.; Del Campo, J.; Mas, R.; Munoz, F. X.; Compton, R. G., Voltammetry at Regular Microband Electrode Arrays: Theory and Experiment. *Journal of Physical Chemistry C* **2007**, *111*, 12058-12066.
21. Szabo, A.; Cope, D. K.; Tallman, D. E.; Kovach, P. M.; Wightman, R. M., Chronoamperometric Current at Hemicylinder and Band Microelectrodes - Theory and Experiment. *J. Electroanal. Chem.* **1987**, *217*, 417-423.
22. Wehmeyer, K. R.; Deakin, M. R.; Wightman, R. M., Electroanalytical Properties of Band Electrodes of Submicrometer Width. *Anal. Chem.* **1985**, *57*, 1913-1916.
23. Ching, S.; Dudek, R.; Tabet, E., Cyclic Voltammetry with Ultramicroelectrodes. *J. Chem. Educ.* **1994**, *71*, 602-605.
24. Rahman, A. R.; Justin, G.; Guiseppi-Elie, A., Towards an Implantable Biochip for Glucose and Lactate Monitoring Using Microdisc Electrode Arrays (Mdeas). *Biomed. Microdevices* **2009**, *11*, 75-85.
25. Compton, R. G.; Wildgoose, G. G.; Rees, N. V.; Streeter, I.; Baron, R., Design, Fabrication, Characterisation and Application of Nanoelectrode Arrays. *Chem. Phys. Lett.* **2008**, *459*, 1-17.
26. Amatore, C.; Fosset, B., Equivalence between Microelectrodes of Different Shapes: Between Myth and Reality. *Anal. Chem.* **1996**, *68*, 4377-4388.
27. Dickinson, E. J. F.; Streeter, I.; Compton, R. G., Chronoamperometry and Cyclic Voltammetry at Conical Electrodes, Microelectrodes, and Electrode Arrays: Theory. *J. Phys. C*hem. B 2008, 112, 4059-4066.
28. Saito, Y.; A Theoretical Study on the Diffusion Current at the Stationary Electrodes of Circular and Narrow Band Type: *Review of Polarography* **1968**, *15*, 177-187.
29. Bond, A. M.; Luscombe, D.; Oldham, K. B.; Zoski, C. G., A Comparison of the Chronoamperometric Response at Inlaid and Recessed Disk Microelectrodes. *J. Electroanal. Chem.* **1988**, *249*, 1-14.
30. Ordeig, O.; del Campo, J.; Munoz, F. X.; Banks, C. E.; Compton, R. G., Electroanalysis Utilizing Amperometric Microdisk Electrode Arrays. *Electroanalysis* **2007**, *19*, 1973-1986.
31. Morf, W. E.; de Rooij, N. F., Performance of Amperometric Sensors Based on Multiple Microelectrode Arrays. *Sensors and Actuators B-Chemical* **1997**, *44*, 538-541.
32. Davies, T. J.; Compton, R. G., The Cyclic and Linear Sweep Voltammetry of Regular and Random Arrays of Microdisc Electrodes: Theory. *J. Electroanal. Chem.* **2005**, *585*, 63-82.
33. Lee, H. J.; Beriet, C.; Ferrigno, R.; Girault, H. H., Cyclic Voltammetry at a Regular Microdisc Electrode Array. *J. Electroanal. Chem.* **2001**, *502*, 138-145.
34. Fletcher, S.; Horne, M. D., Random Assemblies of Microelectrodes (Ram (Tm) Electrodes) for Electrochemical Studies. *Electrochem. Commun.* **1999**, *1*, 502-512.
35. Alfred, L. C. R.; Oldham, K. B., The Steady-State at a Pair of Hemispherical Microelectrodes. *J. Electroanal. Chem.* **1995**, *396*, 257-263.
36. Guo, J. D.; Lindner, E., Cyclic Voltammograms at Coplanar and Shallow Recessed Microdisk Electrode Arrays: Guidelines for Design and Experiment. *Anal. Chem.* **2009**, *81*, 130-138.
37. Amatore, C.; Saveant, J. M.; Tessier, D., Charge-Transfer at Partially Blocked Surfaces - a Model for the Case of Microscopic Active and Inactive Sites. *J. Electroanal. Chem.* **1983**, *147*, 39-51.
38. Davies, T. J.; Banks, C. E.; Compton, R. G., Voltammetry at Spatially Heterogeneous Electrodes. *J. Solid State Electrochem.* **2005**, *9*, 797-808.

39. Davies, T. J.; Ward-Jones, S.; Banks, C. E.; del Campo, J.; Mas, R.; Munoz, F. X.; Compton, R. G., The Cyclic and Linear Sweep Voltammetry of Regular Arrays of Microdisc Electrodes: Fitting of Experimental Data. *J. Electroanal. Chem.* **2005**, *585*, 51-62.
40. Gueshi, T.; Tokuda, K.; Matsuda, H., Voltammetry at Partially Covered Electrodes .1. Chronopotentiometry and Chronoamperometry at Model Electrodes. *J. Electroanal. Chem.* **1978**, *89*, 247-260.
41. Gueshi, T.; Tokuda, K.; Matsuda, H., Voltammetry at Partially Covered Electrodes .2. Linear Potential Sweep and Cyclic Voltammetry. *J. Electroanal. Chem.* **1979**, *101*, 29-38.
42. Chevallier, F. G.; Compton, R. G., Regular Arrays of Microdisk Electrodes: Numerical Simulation as an Optimizing Tool to Maximize the Current Response and Minimize the Electrode Area Used. *Electroanalysis* **2006**, *18*, 2369-2374.
43. Godino, N.; Borrise, X.; Munoz, F. X.; del Campo, F. J.; Compton, R. G., Mass Transport to Nanoelectrode Arrays and Limitations of the Diffusion Domain Approach: Theory and Experiment. *Journal of Physical Chemistry C* **2009**, *113*, 11119-11125.
44. Zoski, C. G.; Wijesinghe, M., Electrochemistry at Ultramicroelectrode Arrays and Nanoelectrode Ensembles of Macro- and Ultramicroelectrode Dimensions. *Isr. J. Chem.* **2010**, *50*, 347-359.
45. Xue, J. M.; Zou, X. Q.; Xie, Y. B.; Wang, Y. G., Molecular Dynamics Simulations on the Ionic Current through Charged Nanopores. *Journal of Physics D-Applied Physics* **2009**, *42*.
46. Baba, A.; Advincula, R. C.; Knoll, W., In Situ Investigations on the Electrochemical Polymerization and Properties of Polyaniline Thin Films by Surface Plasmon Optical Techniques. *J. Phys. Chem. B* **2002**, *106*, 1581-1587.

Chapter 3 : Introduction to Electrochemical Surface Plasmon Resonance Spectroscopy

3.1 Spectroelectrochemistry

In electrochemical measurements, the electrochemical processes are usually monitored by electrical variables (current and potential measurements), which are incapable of giving any structural information about the electroactive molecules in the system[1]. Therefore, it is advantageous to combine electrochemical techniques with an optical method. This approach, known as spectroelectrochemistry, provides complementary information about the system under investigation since two types of measurements are acquired simultaneously. Spectroelectro-chemistry is a powerful method to study reaction mechanisms, kinetic parameters, and organic, inorganic and biological redox species and intermediates[1-4,]. In recent years, different spectroscopic methods have been combined with electrochemistry. Examples are UV-visible[5-6], Fourier transform infrared (FTIR)[7-8], electron spin resonance (ESR)-UV/vis-near-infrared(NIR)[9-10], Electron paramagnetic resonance (EPR)[11], quartz crystal microbalance (QCM)[12], scanning probe microscopy (SPM)[13], and surface plasmon resonance (SPR)[14-19].

SPR is a label-free and real-time technique with high sensitivity for characterizing ultrathin films at solid/liquid interfaces[14, 20-21]. Combined with electrochemical measurements, EC-SPR becomes a powerful approach for *in situ* observation and characterization of optical and electrochemical properties at electrode/electrolyte interfaces[22-24]. In EC-SPR, a metal film (usually a gold film on a glass slide) is used as both the SPR sensing medium and the working electrode[22]. However, a smooth, thin metal film cannot support the SPR by direct light illumination due to the momentum

mismatch. Therefore, special momentum matching techniques are required to overcome this problem and to excite the SPs. These techniques include attenuated total internal reflection method using a prism coupler (Kretschmann configuration[25] and Otto configuration[26]) and grating coupling.

EC-SPR has been widely used for *in situ* monitoring of the electrochromic properties of an electroconductive polymer during the electropolymerization or during the anion doping-dedoping process of the deposited polymers[17, 27]. The majority of EC-SPR systems that have been used are based on the Kretschmann configuration for the SPR excitations and measurements[16, 18-19, 22]. However, the Kretschmann configuration needs a prism and complicated optical alignment which provide less opportunity for miniaturization and simplification of the measurement setup. In this dissertation, we have utilized nanohole arrays (Chapter 4) and nanopillars arrays (Chapter 5) in EC-SPR studies that offer the advantages of simple optical collinear arrangement.

3.2 Surface Plasmons Polaritons

Surface plasmons polaritons (SPPs) are electromagnetic waves that propagate along the interface between a metal (with a negative dielectric constant) and a dielectric (with a positive dielectric constant). In other words, SPPs are the collective oscillations of the free electrons on a metal surface excited by an electromagnetic wave (photon) and are highly confined to the metal/dielectric interface[28-30]. Figure 3-1a depicts the SPPs at the metal/dielectric interface. The electromagnetic field intensity is maximum at the interface but decays exponentially in the perpendicular direction on either side of the interface (metal/dielectric), as shown in Figure 3-1b. The decay length of the SPPs electric field in the metal, δ_m, is dependent on the skin depth [28-29, 31-32].

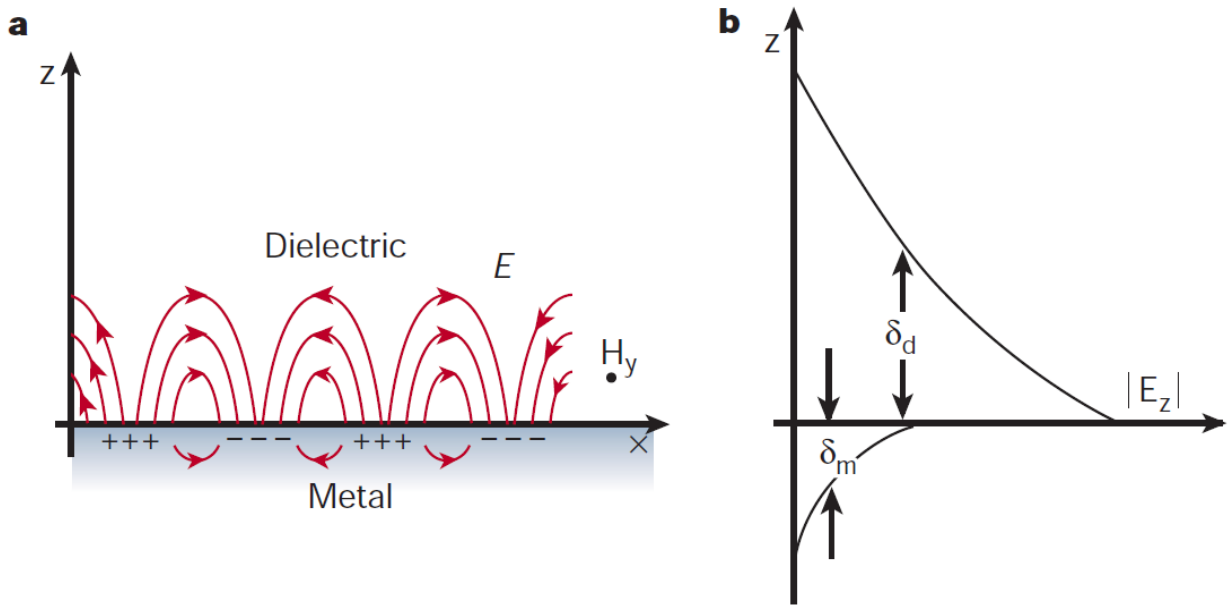

Figure 3-1 a) Schematic representation of surface plasmons polaritons at the metal/dielectric interface. The surface plasmons polaritons waves propagate in the x-direction, parallel along the metal/dielectric interface[28]. b) Illustration of the SPP electric field intensity decaying exponentially on either side of the metal/dielectric interface[28]. [Reprint with permission from[28]]

By solving Maxwell's equations and applying the appropriate boundary conditions, we can obtain the dispersion relation for the SPPs at the metal/dielectric interface. The dispersion relation basically describes the relationship between the angular frequency, ω, (energy) and the wave vector in the propagation direction, k_x, (momentum). The SPPs dispersion relation is given by[33-34]

$$k_{SPP} = \frac{\omega}{c}\sqrt{\frac{\varepsilon_m \varepsilon_d}{\varepsilon_m + \varepsilon_d}} \qquad \text{Eq. 3-1}$$

Where c is the speed of light in vacuum and $\frac{\omega}{c}$ is the wave vector of light in free space. ε_m and ε_d are the dielectric constants of metal and dielectric respectively. The dispersion relation of Eq.

3-1 is depicted in Figure 3-2 for a metal/dielectric interface. The dashed straight line represents the light dispersion, and the black solid curve corresponds to the SPP dispersion on a metal surface.

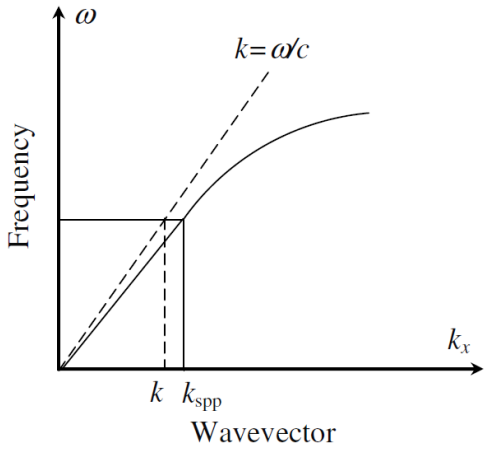

Figure 3-2. SPPs dispersion curve (solid line) and light dispersion (straight dashed line) for a metal/dielectric interface[28]. (Light dispersion is given by $k = \frac{\omega}{c}\sqrt{\varepsilon_d}$, for vacuum $\varepsilon_d \cong 1$). [Reprint with permission from[28]]

As can be seen in Figure 3-2 the momentum (wave vector) of the SPP is always greater than the momentum (wave vector) of the light in free space. In other words, the two curves never coincide, and the SPP dispersion curve is located to the right of the light dispersion line at all frequencies.

$$k < k_{SPP} \qquad \text{Eq. 3-2}$$

$$\frac{\omega}{c}\sqrt{\varepsilon_d} < \frac{\omega}{c}\sqrt{\frac{\varepsilon_m \varepsilon_d}{\varepsilon_m + \varepsilon_d}} \qquad \text{Eq. 3-3}$$

This means that the SPP cannot be excited by direct irradiance of light to the metal surface[35-36]. Therefore, special momentum matching approaches are needed to circumvent this problem and to

excite the SPP. These techniques include attenuated total internal reflection method via a prism coupler (Kretschmann configuration[25] and Otto configuration[26]) and grating coupling.

3.2.1 Attenuated total internal reflection coupling

Kretschmann configuration is a prism coupling method for the excitation of the SPP which was introduced by Kretschmann and Raether in 1968[37]. In this configuration, the surface plasmon is excited via an evanescent wave. Figure 3-3 shows a schematic drawing of this configuration. In this configuration, a thin metal film (usually about 50 nm) is deposited on top of the glass prism. Basically, this metal film is located between the two dielectric media. One medium is the high refractive index glass prism, n_p, and the other one is the dielectric sensing medium with a lower refractive index, n_d, (lower than that of the prism) that can be air or the solutions of interest, as shown in Figure 3-3. The surface plasmon is excited at the interface between the metal layer and the dielectric layer with the lower refractive index (the sensing medium).

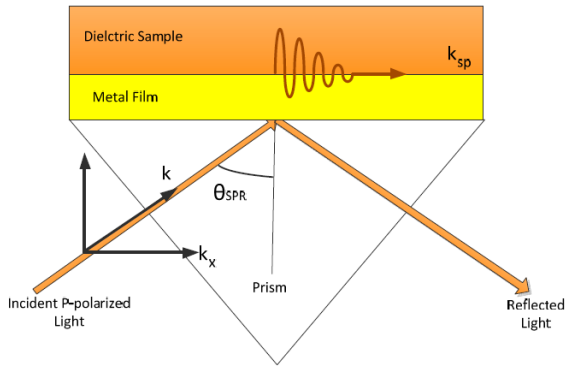

Figure 3-3. A schematic representation of the Kretschmann configuration[38]. [Reprinted with permission from[38] (http://creativecommons.org/licenses/by/3.0/)]

In this configuration, light is illuminated from the glass prism side and undergoes total internal reflection at the prism/metal interface. The evanescent wave is created at the prism/metal interface under the total internal reflection condition when the p-polarized light is incident at an angle equal to or greater than the critical angle, θ_c.

The critical angle, θ_c is given by[39]:

$$\sin\theta_c = \frac{n_d}{n_p} \qquad \text{Eq. 3-4}$$

And propagation constant of the evanescent wave, k_{ev}, at the prism/metal interface is given by[34]:

$$k_{ev} = \frac{\omega}{c}\sqrt{\varepsilon_p}\sin\theta \qquad \text{Eq. 3-5}$$

Where ε_p presents the dielectric constant of the prism material and θ is the incidence angle of the p-polarized light beam.

This evanescent wave penetrates through the metal film and couples with the surface plasmons at the other side and excites the SPP at metal/dielectric interface. The excitation of the surface plasmons at the interface between the metal and the dielectric with the lower reflective index occurs when the wave vector of the evanescent wave is equal to the SPP wave vector of similar frequency and state of polarization [34](in other words the two dispersion curves should coincide as shown in Figure 3-4):

$$k_{ev} = k_{SPP} \qquad \text{Eq. 3-6}$$

$$\frac{\omega}{c}\sqrt{\varepsilon_p}\sin\theta = \frac{\omega}{c}\sqrt{\frac{\varepsilon_m\varepsilon_d}{\varepsilon_m+\varepsilon_d}} \qquad \text{Eq. 3-7}$$

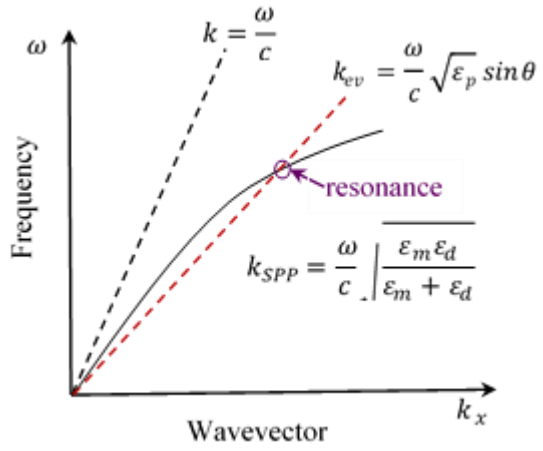

Figure 3-4. Dispersion relation of SPP (solid black curve), light in free space (straight dashed black line) and light traveling through the glass prism (straight dashed red line).

3.2.2 Grating Coupling

The momentum mismatch between the SPP wavevector and the incident light wave vector can also be overcome by using the light diffraction effects of metallic gratings. Metallic gratings, periodically patterned metal surfaces, can include a variety of subwavelength geometries such as arrays of slits, dots, holes, and others[40-42]. A schematic representation of this approach is illustrated in Figure 3-5.

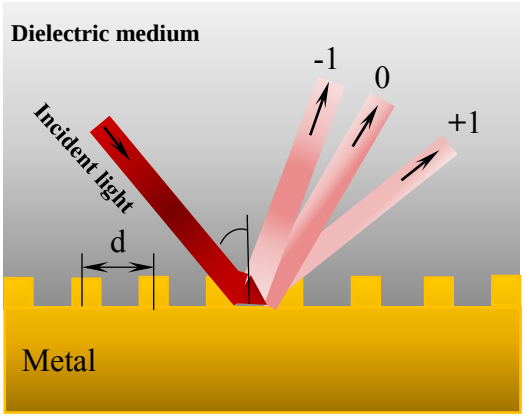

Figure 3-5. Excitation of the SPP using grating coupling approach[43]. [Adapted and reproduced from[43]]

In one-dimensional grating case, the wavevector of the diffracted light is given by[34]:

$$k_{diffracted} = \frac{\omega}{c}\sqrt{\varepsilon_d}\sin\theta \pm n\frac{2\pi}{a_0} \qquad \text{Eq. 3-8}$$

Where $\frac{\omega}{c}\sqrt{\varepsilon_d}\sin\theta$, is the in-plane wavevector of the incident light, a_0 is the grating period, $\frac{2\pi}{a_0}$ is the grating vector, and $n = 1, 2, 3, \ldots$

The excitation of the SPP on the metal grating structure can be achieved whenever the following condition is fulfilled:

$$k_{diffracted} = k_{SPP} \qquad \text{Eq. 3-9}$$

$$\frac{\omega}{c}\sqrt{\varepsilon_d}\sin\theta \pm n\frac{2\pi}{a_0} = \frac{\omega}{c}\sqrt{\frac{\varepsilon_m\varepsilon_d}{\varepsilon_m + \varepsilon_d}} \qquad \text{Eq. 3-10}$$

3.2.3 Extraordinary Optical Transmission

Another fascinating effect of surface plasmons is the extraordinary optical transmission (EOT) through a periodic array of subwavelength apertures perforated in an optically thick metallic film.

In 1944, Bethe described the diffraction properties of a single subwavelength hole. In his prediction, Bethe assumed an ideal condition, a single subwavelength circular hole drilled in an infinitely thin and perfectly conducting plate. According to his aperture theory, the efficiency of light transmission through a single subwavelength circular hole scales as $(r / \lambda)^{4,}$ where r is the radius of the hole. Therefore, based on the Bethe aperture theory, the optical transmission through subwavelength apertures would be very weak. However, in 1998, Ebbesen et al[44]. reported surprisingly very high optical transmission, several orders of magnitude greater than that anticipated by Bethe's aperture theory, through a periodic array of subwavelength circular holes milled in an opaque silver film, Figure 3-6[44]. This phenomenon of enhanced light transmission has been attributed to the excitation of surface plasmon resonance [42, 44-45] by grating coupling, as described in the previous section. Note that such strongly enhanced light transmission through the periodic subwavelength holes is called "extraordinary" because the light transmission efficiency exceeds unity when it is normalized to the area of the holes. The EOT depends on the film material and thickness, the hole geometry, the array periodicity, the light wavelength, and the angle of the incident light [46-47]. The position of the resonance peaks is altered by the periodicity and shape of the hole arrays[48-49].

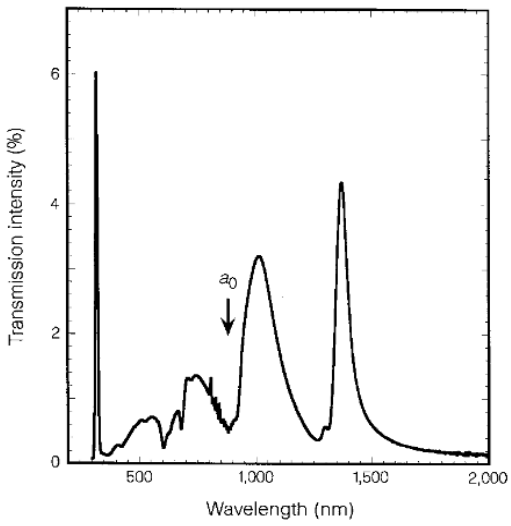

Figure 3-6. Enhanced optical transmission spectrum from a square array of Ag nanoholes with a periodicity of 900 nm. The Ag film thickness was 200 nm, and the nanoholes diameter was 150 nm[44]. [Reprint with permission from[44]]

At normal incident ($\theta = 0$), the peak positions for a square array of nanoholes can be estimated from Eq. 3-11 .(note $\frac{\omega}{c} = \frac{2\pi}{\lambda}$)

$$\lambda_{max}(i,j) = \frac{a_0}{\sqrt{i^2 + j^2}} \sqrt{\frac{\varepsilon_m \varepsilon_d}{\varepsilon_m + \varepsilon_d}} \qquad \text{Eq. 3-11}$$

where i and j correspond to the different scattering orders of the square array. Figure 3-7 show a schematic drawing of enhanced optical transmission through a square array of nanoholes.

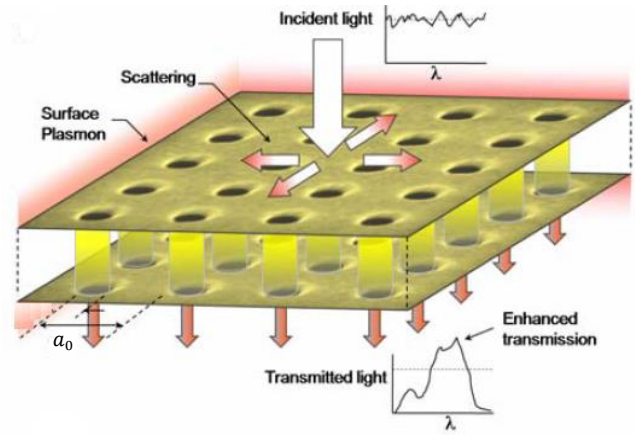

Figure 3-7. A schematic representation of extraordinary optical transmission through a square array of nanoholes[50]. [Reprint with permission from[50]]

3.3 Fabrication of nanoelectrode arrays

There are two primary families of techniques for the fabrication of nanostructured metal surfaces, bottom-up approach, and top-down approach. The bottom-up approach includes electrochemical deposition and nanoparticle formation methods, which are relatively inexpensive. However, the limitation of using bottom-up approach for the fabrication of nanoelectrodes is that there is no control on the separation distances between fabricated electrodes and this approach produces assemblies of nanostructures which are sometimes not reproducible. The top-down approach includes electron beam lithography (EBL), focused ion beam (FIB) milling and laser interference lithography (LIL). The top-down approach enables fabrication of arrays of nanoelectrodes with good control of the production of nanoelectrode arrays; this is due to its reproducibility and its capacity for producing desired geometries and spacing between nanoelectrodes. The LIL approach is a common approach in the mass production of large areas of nanostructure arrays[51-52]. The nanoelectrodes arrays in this dissertation were fabricated using FIB and LIL techniques. Figure 3-10 is a photo of the actual LIL setup used for the fabrication, developed by Dr. Jacson Menezes,

a postdoctoral fellow at the Brolo group. I fabricated all the LIL samples studied in this dissertation.

3.3.1 Fabrication of the nanoelectrodes array by Focused Ion Beam (FIB) Milling

In this dissertation, we investigated different nanoelectrode arrays designs, 30 × 30 nanoholes electrode arrays in Chapter 6, 6 × 6 recessed nanodiscs and nanorings electrode arrays (in Chapter 4), and a 6 × 6 recessed nanoring-ring electrode array (in Chapter 5). The nanohole electrode arrays studied in chapters 4, 5 and 6 were milled by FIB (Hitachi FB-2100 FIB), and then the fabricated nanostructures arrays were imaged via a field emission scanning electron microscope (Hitachi S4800, Hitachi, Japan). FIB is a technique in which a focused beam of ions (usually gallium), driven by high voltages is used to mill through the material and cut the desired pattern on the substrate, Figure 3-8.

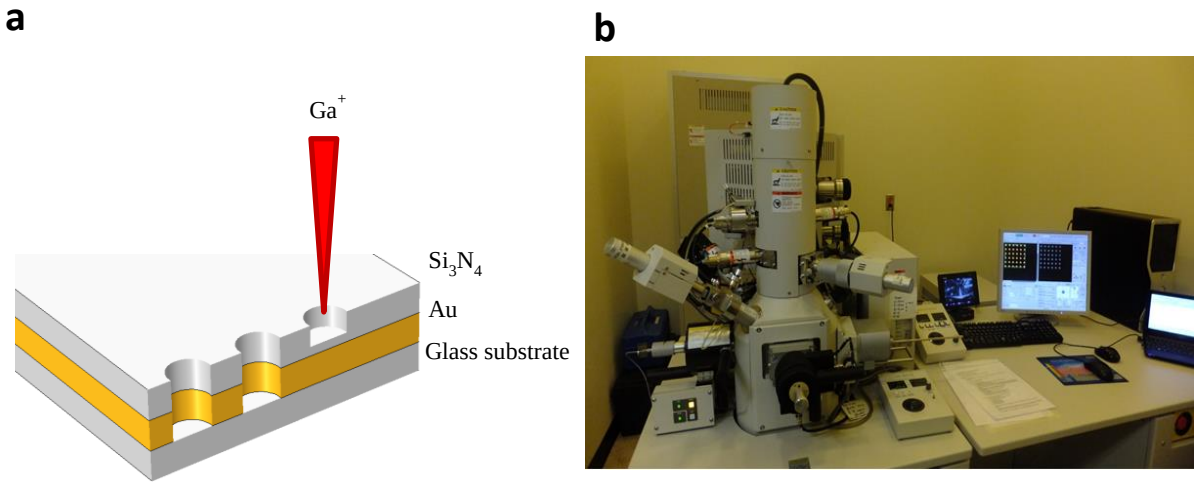

Figure 3-8. Focused ion beam (FIB) milling a) schematic diagram of the FIB process b) photo of the FIB workstation

3.3.2 Laser interference lithography (LIL)

The LIL setup was a Llyod's mirror configuration. Laser light with a wavelength of 458 nm from an Innova 90C Argon ion laser was used. The LIL setup is schematically depicted in Figure 3-9[45]. Figure 3-10 is a photo of the actual Llyod's mirror setup used for the fabrications of the samples in this dissertation. LIL is a maskless lithographic method where a periodic pattern is generated by interference of a laser beam with a second beam created by a mirror very close to the substrate. The period of the structure, Λ, is defined by the laser wavelength and angle between interfering beams given by:

$$\Lambda = \frac{\lambda}{2 \sin \theta} \qquad \text{Eq. 3-12}$$

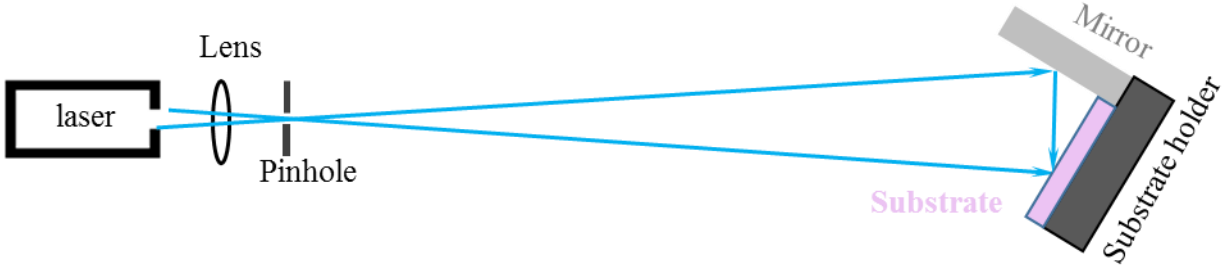

Figure 3-9. A schematic representation of Lloyd's mirror configuration of a laser interference lithography setup. [Reproduced and modified from[45]]

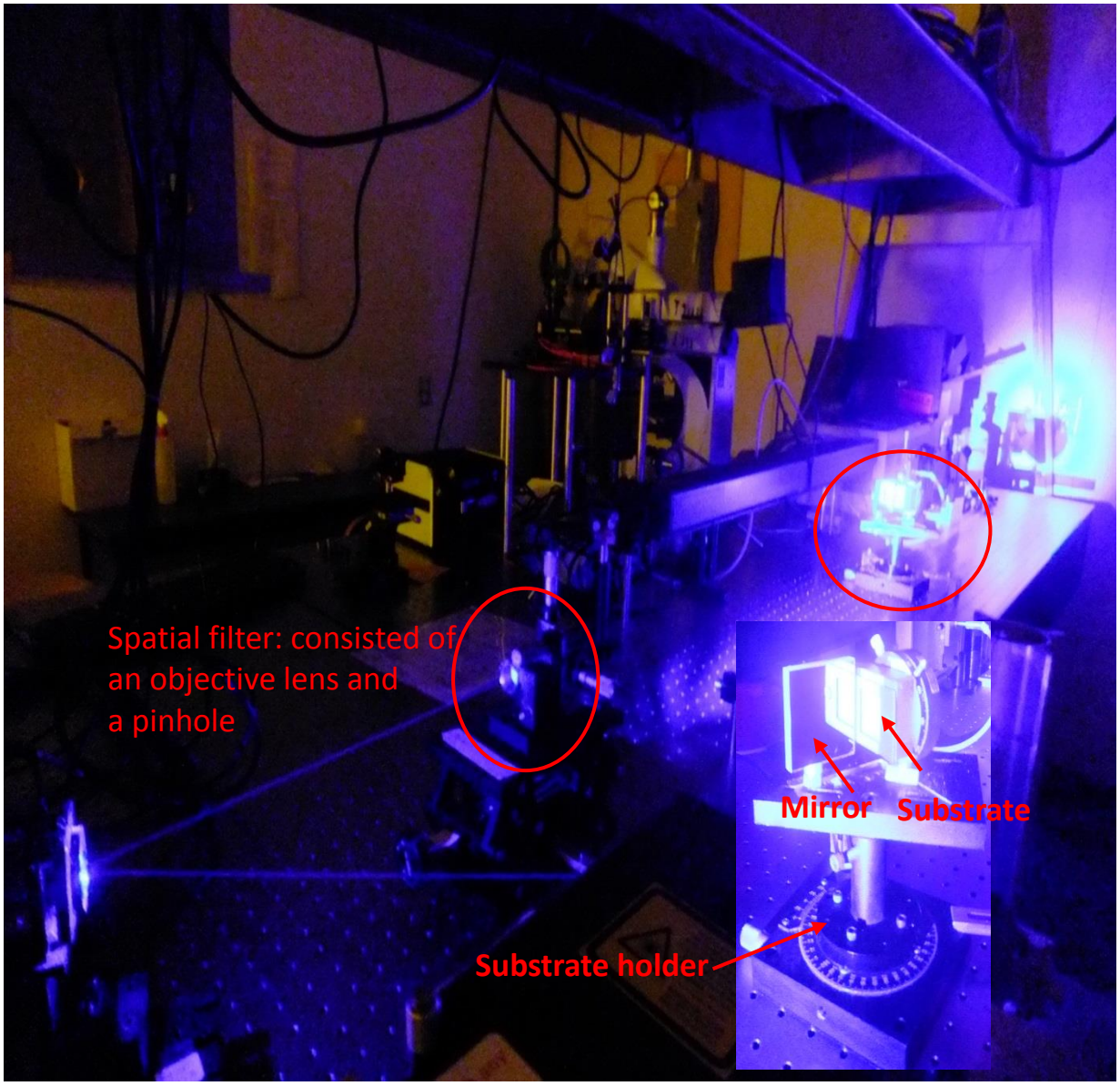

Figure 3-10. Photograph of the developed setup for laser interference lithography.

3.4 References

1. Scholz, F.; Bond, A. M., Electroanalytical Methods Guide to Experiments and Applications. 2nd, rev. and extended ed.; p. 1 online resource. http://ezproxy.rice.edu/login?url=http://dx.doi.org/10.1007/978-3-642-02915-8.
2. Kato, Y.; Sugiura, M.; Oda, A.; Watanabe, T., Spectroelectrochemical Determination of the Redox Potential of Pheophytin a, the Primary Electron Acceptor in Photosystem Ii. *Proc. Natl. Acad. Sci. U. S. A.* **2009**, *106*, 17365-17370.
3. Klod, S.; Dunsch, L., A Combination of in Situ Esr and in Situ Nmr Spectroelectrochemistry for Mechanistic Studies of Electrode Reactions: The Case of P-Benzoquinone. *Magn. Reson. Chem.* **2011**, *49*, 725-729.
4. Murgida, D. H.; Hildebrandt, P., Disentangling Interfacial Redox Processes of Proteins by Serr Spectroscopy. *Chem. Soc. Rev.* **2008**, *37*, 937-945.
5. Cakir, V.; Kantekin, H.; Biyiklioglu, Z.; Koca, A., Synthesis, Electrochemistry, Spectroelectrochemistry and Electropolymerization of Metal-Free and Metallophthalocyanines. *Polyhedron* **2014**, *81*, 525-533.
6. Konev, D. V.; Istakova, O. I.; Sereda, O. A.; Shamraeva, M. A.; Devillers, C. H.; Vorotyntsev, M. A., In Situ Uv-Visible Spectroelectrochemistry in the Course of Oxidative Monomer Electrolysis. *Electrochim. Acta* **2015**, *179*, 315-325.
7. Kellenberger, A.; Dmitrieva, E.; Dunsch, L., Structure Dependence of Charged States in "Linear" Polyaniline as Studied by in Situ Atr-Ftir Spectroelectrochemistry. *J. Phys. Chem. B* **2012**, *116*, 4377-4385.
8. Luo, J. A.; Liu, M. L.; Zhao, Q. Q.; Zhao, J.; Zhang, Y. Y.; Tan, L. A.; Tang, H.; Xie, Q. J.; Li, H. T.; Yao, S. Z., A Study on the Electro-Oxidation and Electropolymerization of a New Ope Linear Molecule by Eqcm and in Situ Ftir Spectroelectrochemistry. *Electrochim. Acta* **2010**, *56*, 454-462.
9. Dmitrieva, E.; Harima, Y.; Dunsch, L., Influence of Phenazine Structure on Polaron Formation in Polyaniline: In Situ Electron Spin Resonance-Ultraviolet/Visible-near-Infrared Spectroelectrochemical Study. *J. Phys. Chem. B* **2009**, *113*, 16131-16141.
10. Gadgil, B.; Dmitrieva, E.; Damlin, P.; Aaritalo, T.; Kvarnstrom, C., Redox Reactions in a Linear Polyviologen Derivative Studied by in Situ Esr/Uv-Vis-Nir Spectroelectrochemistry. *J. Solid State Electrochem.* **2015**, *19*, 77-83.
11. Berdyczko, P.; Domagala, W.; Czardybon, A.; Lapkowski, M., Long Alkyl Chain Bearing Derivatives of Poly(3,4-Ethylenedioxythiophene) Studied by in Situ Epr Spectroelectrochemistry. *Synth. Met.* **2009**, *159*, 2240-2244.
12. Zhao, C. J.; Jiang, Z. Y., Polymerization and Redox Behavior of Polypyrrole (Ppy) Films by in Situ Eqcm and Pt Techniques. *Appl. Surf. Sci.* **2004**, *229*, 372-376.
13. Nichols, R. J.; Schroers, D.; Meyer, H., An in-Situ Scanning Probe Microscopy Study of Copper Electrodeposition on Conductive Polypyrrole. *Electrochim. Acta* **1995**, *40*, 1479-1485.

14. Baba, A.; Advincula, R. C.; Knoll, W., In Situ Investigations on the Electrochemical Polymerization and Properties of Polyaniline Thin Films by Surface Plasmon Optical Techniques. *J. Phys. Chem. B* **2002**, *106*, 1581-1587.
15. Baba, A.; Knoll, W.; Advincula, R., Simultaneous in Situ Electrochemical, Surface Plasmon Optical, and Atomic Force Microscopy Measurements: Investigation of Conjugated Polymer Electropolymerization. *Rev. Sci. Instrum.* **2006**, *77*.
16. Baba, A.; Park, M. K.; Advincula, R. C.; Knoll, W., Simultaneous Surface Plasmon Optical and Electrochemical Investigation of Layer-by-Layer Self-Assembled Conducting Ultrathin Polymer Films. *Langmuir* **2002**, *18*, 4648-4652.
17. Dong, H.; Cao, X. D.; Li, C. M.; Hu, W. H., An in Situ Electrochemical Surface Plasmon Resonance Immunosensor with Polypyrrole Propylic Acid Film: Comparison between Spr and Electrochemical Responses from Polymer Formation to Protein Immunosensing. *Biosensors & Bioelectronics* **2008**, *23*, 1055-1062.
18. Georgiadis, R.; Peterlinz, K. A.; Rahn, J. R.; Peterson, A. W.; Grassi, J. H., Surface Plasmon Resonance Spectroscopy as a Probe of in-Plane Polymerization in Monolayer Organic Conducting Films. *Langmuir* **2000**, *16*, 6759-6762.
19. Gupta, G.; Bhaskar, A. S. B.; Tripathi, B. K.; Pandey, P.; Boopathi, M.; Rao, P. V. L.; Singh, B.; Vijayaraghavan, R., Supersensitive Detection of T-2 Toxin by the in Situ Synthesized Pi-Conjugated Molecularly Imprinted Nanopatterns. An in Situ Investigation by Surface Plasmon Resonance Combined with Electrochemistry. *Biosensors & Bioelectronics* **2011**, *26*, 2534-2540.
20. Brolo, A. G., Plasmonics for Future Biosensors. *Nature Photonics* **2012**, *6*, 709-713.
21. Valsecchi, C.; Brolo, A. G., Periodic Metallic Nanostructures as Plasmonic Chemical Sensors. *Langmuir* **2013**, *29*, 5638-5649.
22. Baba, A.; Tian, S. J.; Stefani, F.; Xia, C. J.; Wang, Z. H.; Advincula, R. C.; Johannsmann, D.; Knoll, W., Electropolymerization and Doping/Dedoping Properties of Polyaniline Thin Films as Studied by Electrochemical-Surface Plasmon Spectroscopy and by the Quartz Crystal Microbalance. *J. Electroanal. Chem.* **2004**, *562*, 95-103.
23. Badia, A.; Arnold, S.; Scheumann, V.; Zizlsperger, M.; Mack, J.; Jung, G.; Knoll, W., Probing the Electrochemical Deposition and/or Desorption of Self-Assembled and Electropolymerizable Organic Thin Films by Surface Plasmon Spectroscopy and Atomic Force Microscopy. *Sens. Actuators, B* **1999**, *54*, 145-165.
24. Iwasaki, Y.; Horiuchi, T.; Morita, M.; Niwa, O., Time Differential Surface Plasmon Resonance Measurements Applied for Electrochemical Analysis. *Electroanalysis* **1997**, *9*, 1239-1241.
25. Kretschmann, E., Decay of Non Radiative Surface Plasmons into Light on Rough Silver Films. Comparison of Experimental and Theoretical Results. *Opt. Commun.* **1972**, *6*, 185-187.
26. Otto, A., Excitation of Nonradiative Surface Plasma Waves in Silver by the Method of Frustrated Total Reflection. *Z. Phys.* **1968**, *216*, 398-410.

27. Baba, A.; Knoll, W., Properties of Poly(3,4-Ethylenedioxythiophene) Ultrathin Films Detected by in Situ Electrochemical-Surface Plasmon Field-Enhanced Photoluminescence Spectroscopy. *J. Phys. Chem. B* **2003**, *107*, 7733-7738.
28. Barnes, W. L.; Dereux, A.; Ebbesen, T. W., Surface Plasmon Subwavelength Optics. *Nature (London, U. K.)* **2003**, *424*, 824-830.
29. Maier, S. A.; SpringerLink (Online service), Plasmonics : Fundamentals and Applications. Springer,: New York, 2007; pp. xxiv, 223 pages. http://proxy.lib.sfu.ca/login?url=http://dx.doi.org/10.1007/0-387-37825-1 view full text.
30. Ritchie, R. H., Plasma Losses by Fast Electrons in Thin Films. *Phys. Rev.* **1957**, *106*, 874-881.
31. Barnes, W. L., Surface Plasmon-Polariton Length Scales: A Route to Sub-Wavelength Optics. *Journal of Optics a-Pure and Applied Optics* **2006**, *8*, S87-S93.
32. Zhang, J. X.; Zhang, L. D.; Xu, W., Surface Plasmon Polaritons: Physics and Applications. *Journal of Physics D-Applied Physics* **2012**, *45*.
33. Homola, J.; Yee, S. S.; Gauglitz, G., Surface Plasmon Resonance Sensors: Review. *Sens. Actuators, B* **1999**, *54*, 3-15.
34. Raether, H., *Surface Plasmons on Smooth and Rough Surfaces and on Gratings*; Springer-Verlag: Berlin ; New York, 1988, p 136 pages.
35. Ritchie, R. H.; Arakawa, E. T.; Cowan, J. J.; Hamm, R. N., Surface-Plasmon Resonance Effect in Grating Diffraction. *Phys. Rev. Lett.* **1968**, *21*, 1530-&.
36. Schasfoort, R. B. M.; Tudos, A. J., Handbook of Surface Plasmon Resonance. Royal Society of Chemistry,: Cambridge, 2008; pp. 1 online resource (xxi, 403 p.). http://dx.doi.org/10.1039/9781847558220.
37. Kretschmann, E.; Raether, H., Notizen: Radiative Decay of Non Radiative Surface Plasmons Excited by Light. *Zeitschrift für Naturforschung A* **1968**, *23*, 2135-2136.
38. Kashif, M.; Bakar, A. A. A.; Arsad, N.; Shaari, S., Development of Phase Detection Schemes Based on Surface Plasmon Resonance Using Interferometry. *Sensors* **2014**, *14*, 15914-15938.
39. Tang, Y. J.; Zeng, X. Q.; Liang, J., Surface Plasmon Resonance: An Introduction to a Surface Spectroscopy Technique. *J. Chem. Educ.* **2010**, *87*, 742-746.
40. Coe, J. V.; Heer, J. M.; Teeters-Kennedy, S.; Tian, H.; Rodriguez, K. R., Extraordinary Transmission of Metal Films with Arrays of Subwavelength Holes. In *Annu. Rev. Phys. Chem.*, 2008; Vol. 59, pp 179-202.
41. Eftekhari, F.; Escobedo, C.; Ferreira, J.; Duan, X. B.; Girotto, E. M.; Brolo, A. G.; Gordon, R.; Sinton, D., Nanoholes as Nanochannels: Flow-through Plasmonic Sensing. *Anal. Chem.* **2009**, *81*, 4308-4311.
42. Porto, J. A.; Garcia-Vidal, F. J.; Pendry, J. B., Transmission Resonances on Metallic Gratings with Very Narrow Slits. *Phys. Rev. Lett.* **1999**, *83*, 2845-2848.
43. http://www.thermalfluidscentral.org/encyclopedia/index.php/File:Surfacepolaritoncouplers.jpg.

44. Ebbesen, T. W.; Lezec, H. J.; Ghaemi, H. F.; Thio, T.; Wolff, P. A., Extraordinary Optical Transmission through Sub-Wavelength Hole Arrays. *Nature (London, U. K.)* **1998**, *391*, 667-669.
45. Kuiper, S.; van Wolferen, H.; van Rijn, C.; Nijdam, W.; Krijnen, G.; Elwenspoek, M., Fabrication of Microsieves with Sub-Micron Pore Size by Laser Interference Lithography. *Journal of Micromechanics and Microengineering* **2001**, *11*, 33-37.
46. Gordon, R.; Brolo, A. G.; Sinton, D.; Kavanagh, K. L., Resonant Optical Transmission through Hole-Arrays in Metal Films: Physics and Applications. *Laser Photonics Rev.* **2010**, *4*, 311-335.
47. Rodrigo, S. G.; Garcia-Vidal, F. J.; Martin-Moreno, L., Influence of Material Properties on Extraordinary Optical Transmission through Hole Arrays. *Phys. Rev. B* **2008**, *77*.
48. Gordon, R.; Sinton, D.; Kavanagh, K. L.; Brolo, A. G., A New Generation of Sensors Based on Extraordinary Optical Transmission. *Acc. Chem. Res.* **2008**, *41*, 1049-1057.
49. Koerkamp, K. J. K.; Enoch, S.; Segerink, F. B.; van Hulst, N. F.; Kuipers, L., Strong Influence of Hole Shape on Extraordinary Transmission through Periodic Arrays of Subwavelength Holes. *Phys. Rev. Lett.* **2004**, *92*.
50. Sinton, D.; Gordon, R.; Brolo, A. G., Nanohole Arrays in Metal Films as Optofluidic Elements: Progress and Potential. *Microfluidics and Nanofluidics* **2008**, *4*, 107-116.
51. Lanyon, Y. H.; Arrigan, D. W., Top-Down Approaches to the Fabrication of Nanopatterned Electrodes. *Nanostructured Materials in Electrochemistry* **2008**, 187-210.
52. Menezes, J. W.; Ferreira, J.; Santos, M. J. L.; Cescato, L.; Brolo, A. G., Large-Area Fabrication of Periodic Arrays of Nanoholes in Metal Films and Their Application in Biosensing and Plasmonic-Enhanced Photovoltaics. *Adv. Funct. Mater.* **2010**, *20*, 3918-3924.

Chapter 4 : Comparing the Electrochemical Response of Nanostructured Electrode Arrays

The following chapter is adapted from: M. Atighilorestani, and A. G. Brolo, Comparing the Electrochemical Response of Nanostructured Electrode Arrays, Anal. Chem. 2017, 89 (11), 6129-6135. *Copyright: Reproduced with permission. The supporting information has been embedded within the text.*

The electrochemical responses from periodic 6×6 arrays of recessed gold nanorings were compared to the 6×6 recessed gold nanodiscs arrays. The nanostructured arrays were fabricated by focussed ion beam milling, and their electrochemical response from a reversible redox pair was obtained. Three-dimensional cyclic voltammetry simulations using COMSOL were performed on 6×6 periodic arrays of both recessed nanodiscs and nanorings to elucidate the differences in mass transport between these geometries. Specific mass transport properties near the electroactive surface of the electrodes were elucidated by analyzing the calculated concentration profiles of the redox species. Relative contributions from radial diffusion regimes inside the nanoholes play an important role on the electrochemical response of the recessed nanorings. Arrays of nanodiscs are common in different types of applications, particularly in biosensors. The results presented here suggest that the performance and sensitivity of electrochemical nanosensors can be simply improved by implementing electrodes with a geometry which offer greater current density while keeping the overall footprint of the sensor element constant.

4.1 Introduction

The size and geometry of an electrode strongly affect its electrochemical behavior. Decreasing the critical dimension of an electrode to less than 25 μm (microelectrode)[1] greatly improves its performance relative to that of a regular-sized (e.g. millimeter-sized) conventional macroelectrode. The benefits gained from electrode miniaturization include enhanced mass transport rates, due to the predominance of the three-dimensional diffusion; reduced ohmic resistance; increased current densities; and enhanced signal-to-noise ratios[2-5]. The combination of these characteristics greatly improves response time and sensitivity in analytical and biosensing applications[6-7]. In addition, microelectrodes can be easily integrated into miniaturized devices that require low sample volumes for (bio)chemical analysis[8].

The benefits gained from microelectrodes can be further amplified by entering the realm of nanoelectrodes (electrode critical dimension below 1 μm)[1, 4-5]. The field of nanoelectrochemistry has flourished in the last few years, due to advances in fabrication methods for the mass-production of nanoelectrodes[9-11]. Electroanalytical methods involving nanoelectrodes are faster and suitable for matrixes with low conductivity. Nanoelectrodes can potentially be essential components of portable devices for extreme biosensing applications, such as single-molecule detection[12-13]. However, a severe drawback to the widespread application of nanoelectrodes is their low output current. The current levels in nanoelectrochemistry are often in the pA-range, requiring specialized, low noise, electronic circuits for detection. This limitation can be overcome by utilizing an array of nanoelectrodes operating in parallel[4, 14] . The overall behavior of a nanoelectrode array depends on several factors, including the diffusion coefficient of the electroactive species, the electrode radius, the inter-electrode spacing, the time scale of the

experiment, the size of the whole array and the electrode geometry[15]. Research activity in the development of nanoelectrode arrays has been intense in the last few years[1-4, 8, 14-16]. Most of the work focused on arrays of (either inlaid or recessed) nanodiscs [2, 8, 15, 17]. This is a relatively simple geometry and very common in the electrochemistry of micro/nanoelectrodes. However, other possible configurations for nanoelectrodes might provide advantages over a simple array of "recessed nanodisc electrodes" (r-NDE) in terms of electrochemical performance at the nanoscale.

Our research group has a vast experience on the application of arrays of nanoholes in gold films as surface plasmon resonance biosensors[18-24]. The nanohole structures support the phenomenon of extraordinary optical transmission, which is an enhancement in the amount of light transmitted through the nanostructures at certain resonant wavelengths[25-26]. Recently, we have transformed a regular array of nanoholes into arrays of "recessed nanoring electrodes" (r-NRE) by coating the top gold surface of the nanoholes array with a thin layer of an insulating material. As a result, the electroactive area remained confined as gold rings within the nanoholes. The nanorings were then coated with a thin layer of an electroconductive material[27], generating an array of polymer-modified nanoring electrodes. The optoelectronic properties of the polymer-modified nanorings array were then explored by electrochemically switching the optical transmission through the nanostructures[27]. Those preliminary experiments suggested that arrays of r-NRE performed well as electrode elements, and since those structures can be fabricated in either large area or microarray format [20, 24, 27-28], they have the potential to be applied in several types of bioanalytical devices. However, before embarking towards the development of applications, one might wonder how the electrochemical performance of a r-NRE array differs from that of one of the most common geometries, such as an array of r-NDE. In this work, a combination of experimental and numerical

simulations was performed to compare the electrochemical characteristics of r-NRE and r-NDE. The results provide guidance to the electrochemical performance characteristics for both geometries.

4.2 EXPERIMENTAL SECTION

4.2.1 Chemicals and Instrumentation

Potassium ferricyanide and potassium chloride were obtained from Caledon Laboratories. All solutions were prepared using ultrapure water (18.2 MΩ·cm) obtained from NANO pure Diamond TM deionization system (Barnstead). Prior to measurements, the solution was deoxygenated by purging with argon gas for 30 min. Voltammetric experiments at r-NRE and r-NDE arrays were performed using a computer-controlled Autolab potentiostat-galvanostat (PGSTAT 30).

4.2.2 Electrochemical Measurements

Silicon rubber squares (approximately 6 mm × 6mm) cut with a laser cutting machine were used as the electrochemical cells. The silicon rubber square was fixed with a dielectric epoxy on the glass/Ti/Au/Ti/Si_3N_4 substrate containing one 6 × 6 nanohole array of either r-NDE or r-NRE fabricated by FIB at the center. The nanohole array was exposed to the solution with a small opening laser cut square which was located at the center of the 6 mm × 6 mm silicon rubber square. The central opening square was approximately 2 mm × 2 mm in size, and its volume was about 10 µL. Cyclic voltammetry was performed on each nanohole electrodes array in a solution of 20 mM potassium ferricyanide with 0.5 M KCl as supporting electrolyte at 50 mV s^{-1}. A background current was also recorded in 0.5 M KCl solution. Background-corrected voltammograms were

obtained by subtracting the electroactive analyte voltammogram from the background voltammograms[29]. Measurements were carried out with a three-electrode cell in which the working electrode was the nanohole array. The counter electrode was a Pt wire, and another Pt wire served as a pseudo-reference electrode. To minimize electrical disturbance, the electrochemical cell was placed inside a Faraday cage. Automatic positive feedback compensation was not used during the voltammetric experiments.

4.2.3 Nanodiscs and Nanorings Electrode Arrays Fabrication

The 6 × 6 r-NDE and r-NRE arrays were fabricated by focused-ion-beam (FIB) milling into 50 nm gold films on glass slides coated with Si_3N_4 (200 nm) insulating layer. The radius of the holes (r) were 100, 150, and 200 nm. The interelectrode distance between the nanoholes was kept as 4r as indicated in Figure 4-2 and Figure 4-5. The sizes of the arrays were 2.2 μm × 2.2 μm, 3.3 μm × 3.3 μm, and 4.4 μm × 4.4 μm for 100 nm, 150 nm, and 200 nm hole radius, respectively.

4.2.4 Fabrication details

We defined the FIB cut with the following parameters: dwell time in microseconds (i.e. the amount of time the beam stays at a particular pixel point as it raster across the pattern) and N (the number of raster passes). We only changed N from array to array while keeping dwell time constant. Next, we used Z-contrast imaging (also called backscattering imaging) to find out which FIB conditions were the proper ones for the fabrication of both nanodiscs and nanorings electrode arrays. The Z-contrast images of arrays cut with different N-values (used in the optimization of the fabrication parameters) are presented in Figure 4-1.

Some notes on Z-contrast imaging

- It uses the SEM's upper backscatter detector to take an image that only contains information on backscattered electrons

- By filtering out secondary electrons, the image does not show topographical information. Instead, the image shows elemental information.

- The shades of gray in the image are Z-contrast.

- With this method, the image shows the presence of gold. With this method**,** one can determine which fabrication conditions are needed to cut through the various layers in the specimen.

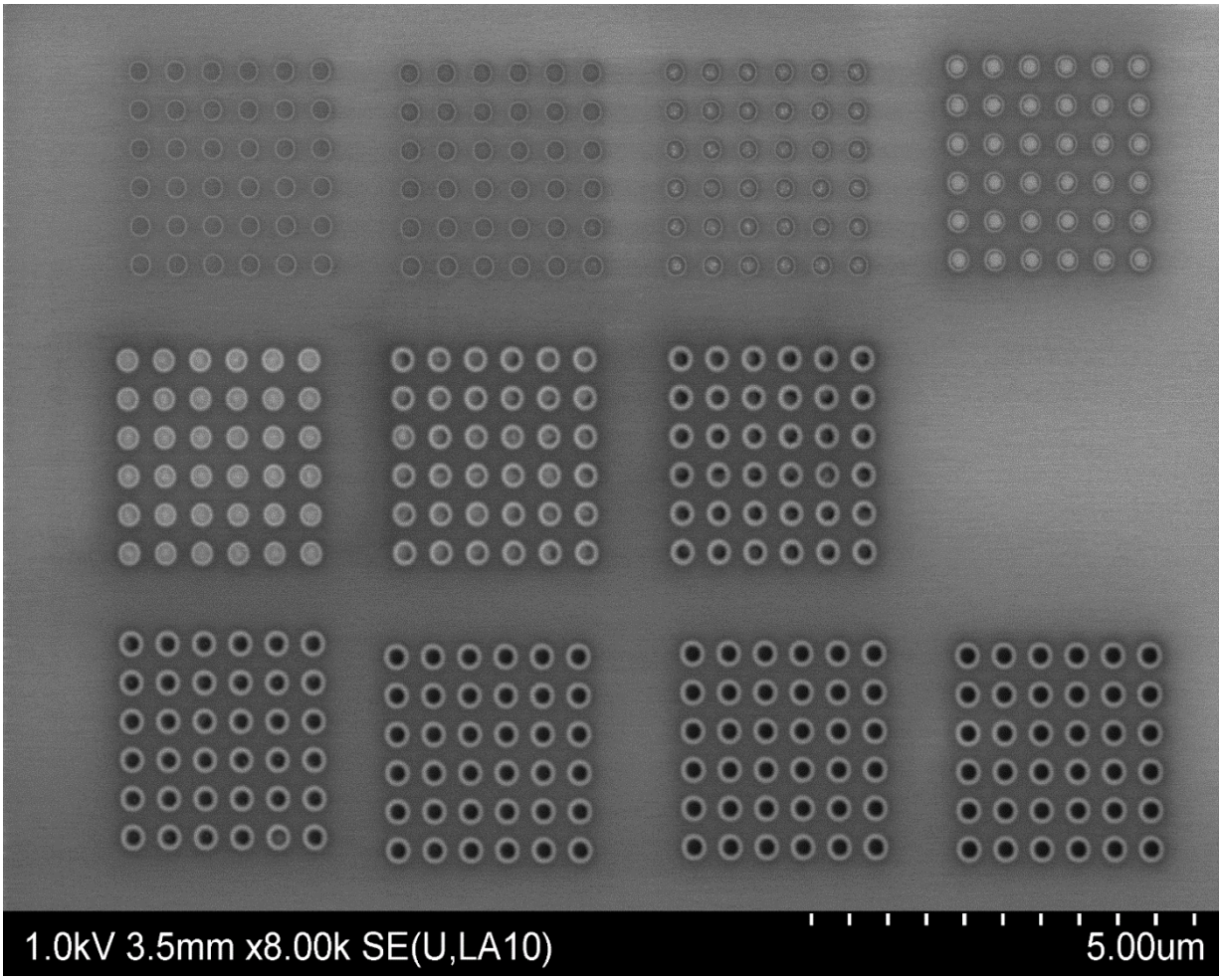

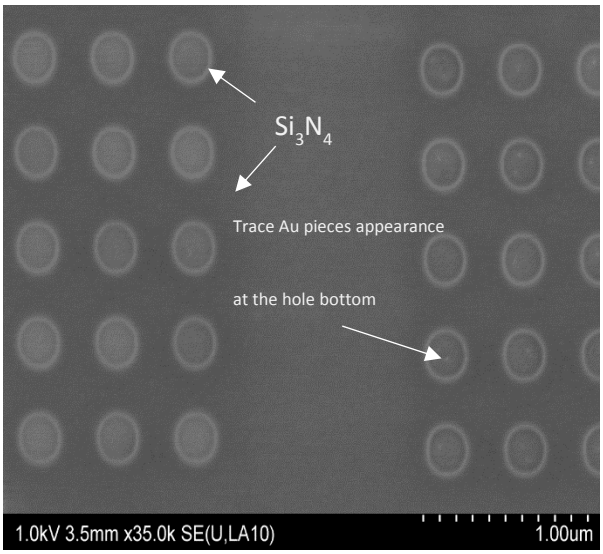
Si_3N_4
Trace Au pieces appearance
at the hole bottom
1.0kV 3.5mm x35.0k SE(U,LA10)
1.00um

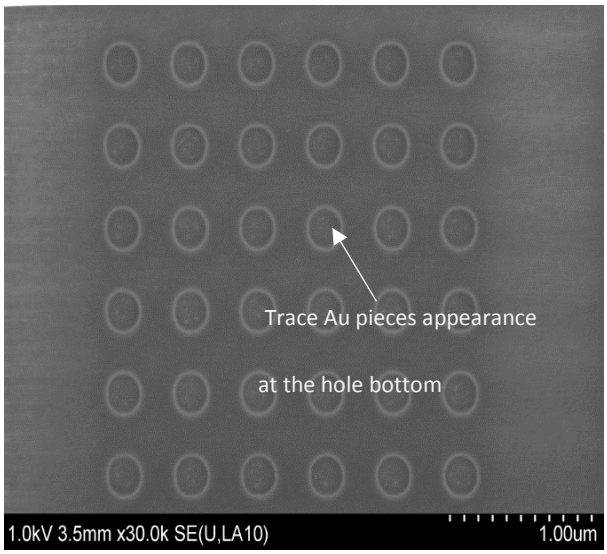
Trace Au pieces appearance
at the hole bottom
1.0kV 3.5mm x30.0k SE(U,LA10)
1.00um

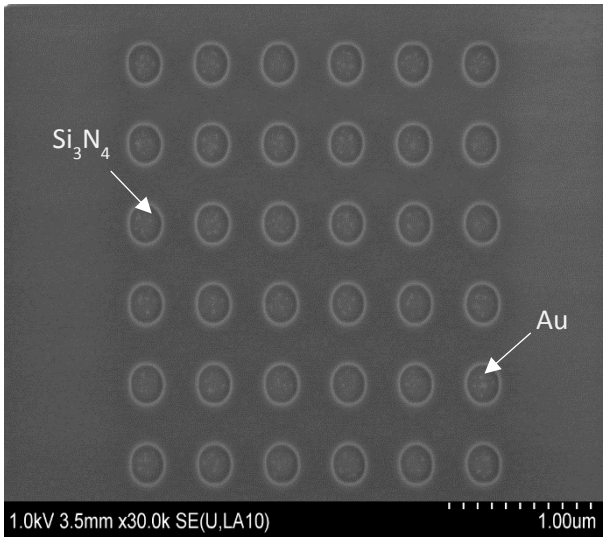
Si_3N_4
Au
1.0kV 3.5mm x30.0k SE(U,LA10)
1.00um

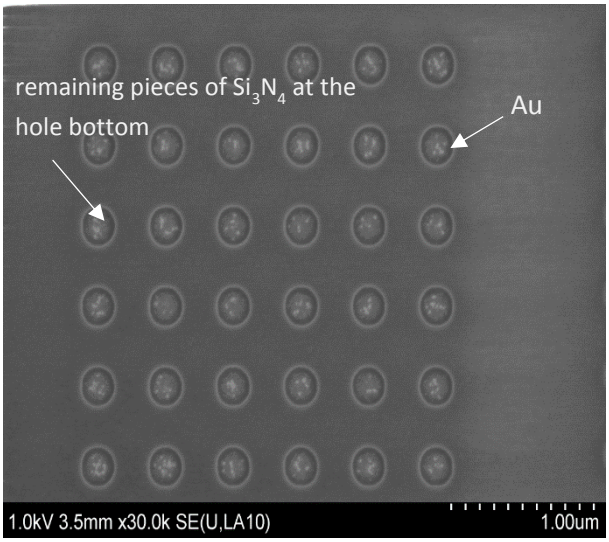
remaining pieces of Si_3N_4 at the hole bottom
Au
1.0kV 3.5mm x30.0k SE(U,LA10)
1.00um

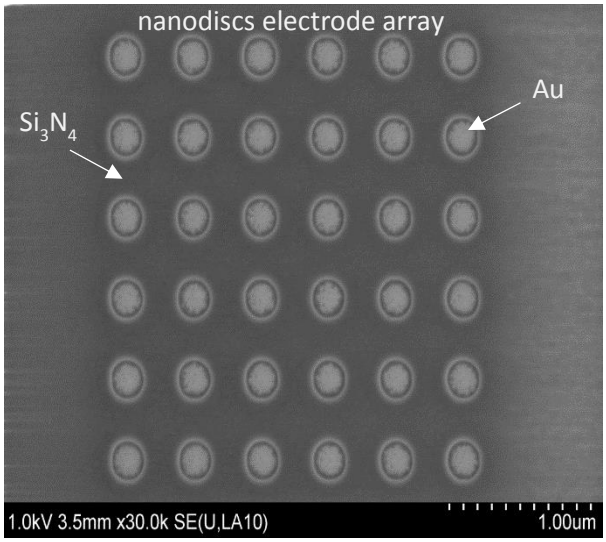
nanodiscs electrode array
Au
Si_3N_4
1.0kV 3.5mm x30.0k SE(U,LA10)
1.00um

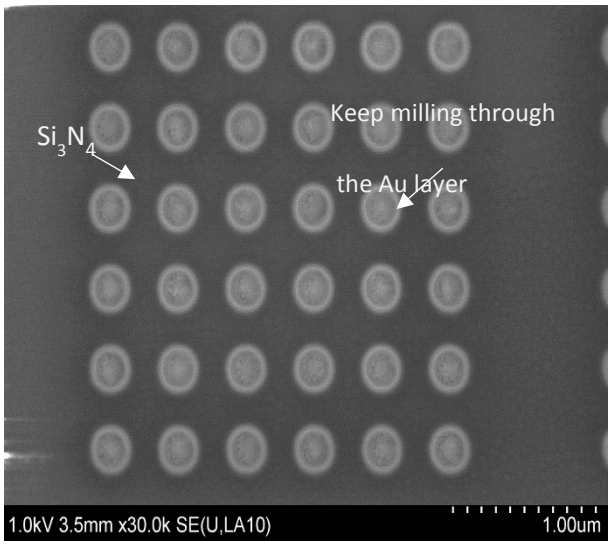
Si_3N_4
Keep milling through
the Au layer
1.0kV 3.5mm x30.0k SE(U,LA10)
1.00um

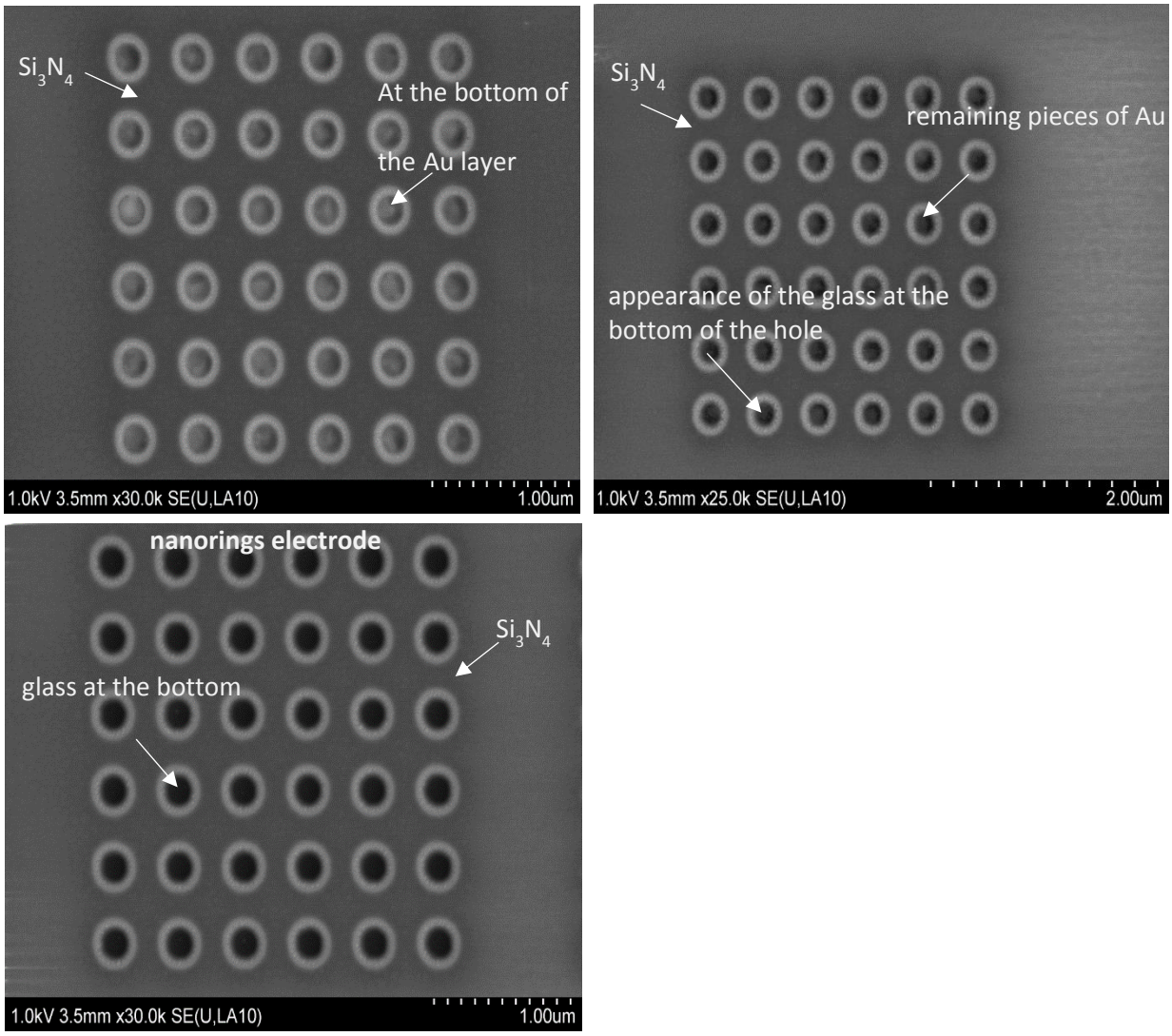

Figure 4-1**.** Z-contrast images of nanohole arrays cut using FIB. (Optimization of the fabrication parameters)

4.2.5 Nanodiscs and Nanorings Electrode Arrays Simulations

All the cyclic voltammogram simulations of the 6 × 6 r- NRE and r-NDE microarrays were performed in three-dimensional domains, using finite element (FEM) software COMSOL Multiphysics version 5.2. The simulation of a simple reversible redox reaction with Butler−Volmer kinetics was considered.

4.2.6 Simulation Details

The cyclic voltammogram simulations of the 6 × 6 r-NRE (Figure 4-2a) and r-NDE (Figure 4-2b) microarrays were performed in three-dimensional domains, using finite element (FEM) software COMSOL Multiphysics® version 5.2. COMSOL Multiphysics® (known as FEMLAB before 2005) is a finite element simulation software package for simulating different physics-based problems, particularly for simulating coupled or multiphysics phenomena[30]. The finite element method used in COMSOL Multiphysics® is a numerical technique which allows solving almost any problems requiring the use of partial differential equations (PDE). COMSOL Multiphysics® has an easy-to-use desktop interface. The first step in solving a problem in COMSOL Multiphysics® is selecting an application mode. COMSOL Multiphysics® is composed of different modules and functions for modeling different applications. For modeling cyclic voltammetry and step potential methods in COMSOL Multiphysics®, either of **Transport of Diluted Species (tds)** interface (which is a sub-module of Chemical Species Transport Module) or **Electroanalysis (elan)** interface (which is a sub-module of Electrochemistry Module) can be used. Both of these physic interfaces (sub-modules) have the predefined equations, boundary conditions, and rate expression terms for modeling mass transport at an electrode[30]. In this work, the Transport of Diluted Species (tds) interface has been used for modeling the electrochemical responses of the r-NDE and r-NRE arrays.

Next step in solving a problem in COMSOL Multiphysics® is to set up the simulation geometry (domain). The model geometry can be simply drawn as in any other graphic design program. Figure 4-3a and Figure 4-4a show the geometry models used to simulate the r-NDE and r-NRE arrays, respectively. Note that in the 3D simulation, the size of the simulation domain cannot be assigned based on the $6\sqrt{t_{tot}D}$ distance from the electrode surface where, $t_{tot,}$ is the total simulation time. In fact**,** a much bigger domain size is needed to accurately simulate the 3D geometry, without any perturbation from the electron transfer processes occurring at the electrodes in the simulation results. Therefore, the size of the simulation area in each of the simulation was verified by probing the concentration close to the domain's walls. Accordingly, the size of the simulation space was made large enough to assure bulk-like concentrations of the redox couple at the boundaries. Figure 4-3a and Figure 4-4a illustrate schematic representationS of the 3D simulation space for the 6 × 6 r-NDE and r-NRE, respectively. Once the simulation geometry has been established, the appropriate boundary conditions should be defined for the model.

Here, the simulation of a simple reversible redox reaction with Butler-Volmer kinetics was considered:

$$O + e^- \rightleftharpoons R \qquad \text{Eq. 4-1}$$

where O and R are both soluble species. Only species O was initially presented in the solution with a bulk concentration of 20 mM. The forward and reverse reaction rate constants, k_f and k_b were given by:

$$k_f = k^0 \exp\left(-\frac{\alpha F}{RT}\left(E - E^{\acute{0}}\right)\right)$$ Eq. 4-2

$$k_b = k^0 \exp\left(\frac{(1-\alpha) F}{RT}\left(E - E^{\acute{0}}\right)\right)$$ Eq. 4-3

k^0 is the heterogeneous rate constant for the redox couple, taken as 10^{-2} ms^{-1} , and $E^{\acute{0}}$ is the formal electrode potential, set at 0.25 V.[31] E is the potential applied to the electrode. α is the effective transfer coefficient, assumed to be 0.5. The temperature, T, was fixed at 298K. R and F are the universal gas constant and the Faraday's constant, respectively.

The mass transport to the electrode was modeled by solving Fick's second law of diffusion in Cartesian coordinates:

$$\frac{\partial c}{\partial t} = D\left(\frac{\partial^2 c}{\partial x^2} + \frac{\partial^2 c}{\partial y^2} + \frac{\partial^2 c}{\partial z^2}\right)$$ Eq. 4-4

where D is the diffusion coefficient (assumed equal for both species (O and R)), taken as 6.5×10^{-10} $m^2 s^{-1}$.[31]

In simulations of the r-NRE arrays, due to the symmetry of the ring electrodes, the flux boundary condition was applied only to half of the ring surface. And the other half of the ring surface was set to the symmetrical boundary condition.

Meshing is a critical factor in correctly solving the simulation problems. Examples of the mesh distributions used in the simulations of 6 × 6 r-NDE array with r = 200 nm and r-NRE array with

r = 150 nm and *h* = 100 nm are shown in Figure 4-3b and Figure 4-4b, respectively. A high mesh density was used at the electrodes' surface and at the singularities (the boundaries between the electrode's surfaces and the insulator's surfaces). The appropriate mesh size was concluded with successive mesh refinements until the difference between the results of the two following simulations was less than 1%.

The simulations of the 6 × 6 r-NDE arrays with *r* = 100 nm and the 6 × 6 r-NRE arrays with *h* = 25 nm and different radiuses were carried out on a PC workstation with 32.0 GB RAM (Lenovo Thinkstation). And the rest of the simulations were run on the WestGrid and Compute Canada clusters due to our computer's memory limitation.

A brief note on the validation of the simulation set ups for r-NDE and r-NRE arrays. To simulate the r-NDR array, we've started by simulating one single recessed nanodisc electrode in the 3D domain and compared the result with the available analytical solution[31] for the recessed disc electrode.

$$I = \frac{4nFcDr_o}{\left(\frac{4L}{\pi r_o} + 1\right)} \qquad \text{Eq. 4-5}$$

Where *n* the number of the electrodes, r_o is the disc radius and *L* is the recess depth value. We refined the mesh until the difference between the simulation result and the analytical solution was less than 0.1%. This gave us a sense of the validity of the simulation set up itself and a sense of the required meshing parameters for simulating the array of the recessed disc electrodes. Then, we began to simulate the arrays of the recessed disc electrodes. To simulate the recessed ring electrodes, there are not any analytical solutions that one can use to check the simulation results. However, we started to simulate the geometries which are in some sense similar to the ring electrode, like that of the cylinder electrode, that have been reported in the literature. We replicated

the results of these papers[32-33], by simulating the cylindrical geometry in both 2D and 3D domains. Then we simulated one single recessed ring electrode in both 2D and 3D domains, with repeated mesh refinements until the difference between the results of the two following simulations was less than 0.1% and also the results of both simulations in 2D and 3D for a single recessed ring were within 0.1%. After that, we simulated the arrays of recessed ring electrodes. Later, the simulation results for both r-NDE and r-NRE arrays were validated by experimental results, Figure 4-5 and Figure 4-13.

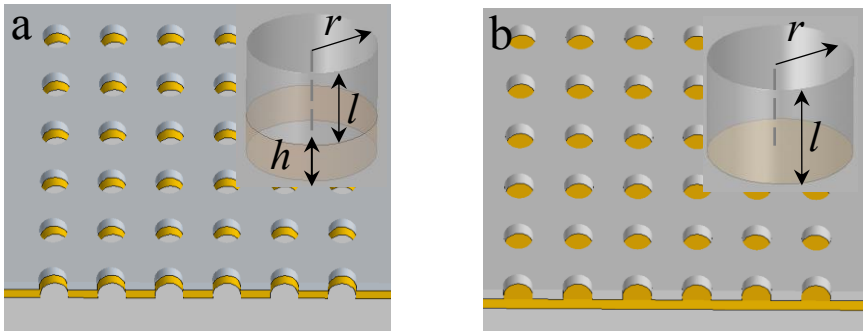

Figure 4-2**.** Schematic representations of the (a) 6×6 r-NRE and (b) 6×6 r-NDE microarrays geometries. Hole radius, *r*, recessed depth, *l*, and ring's height, *h* are indicated on the insets.

a

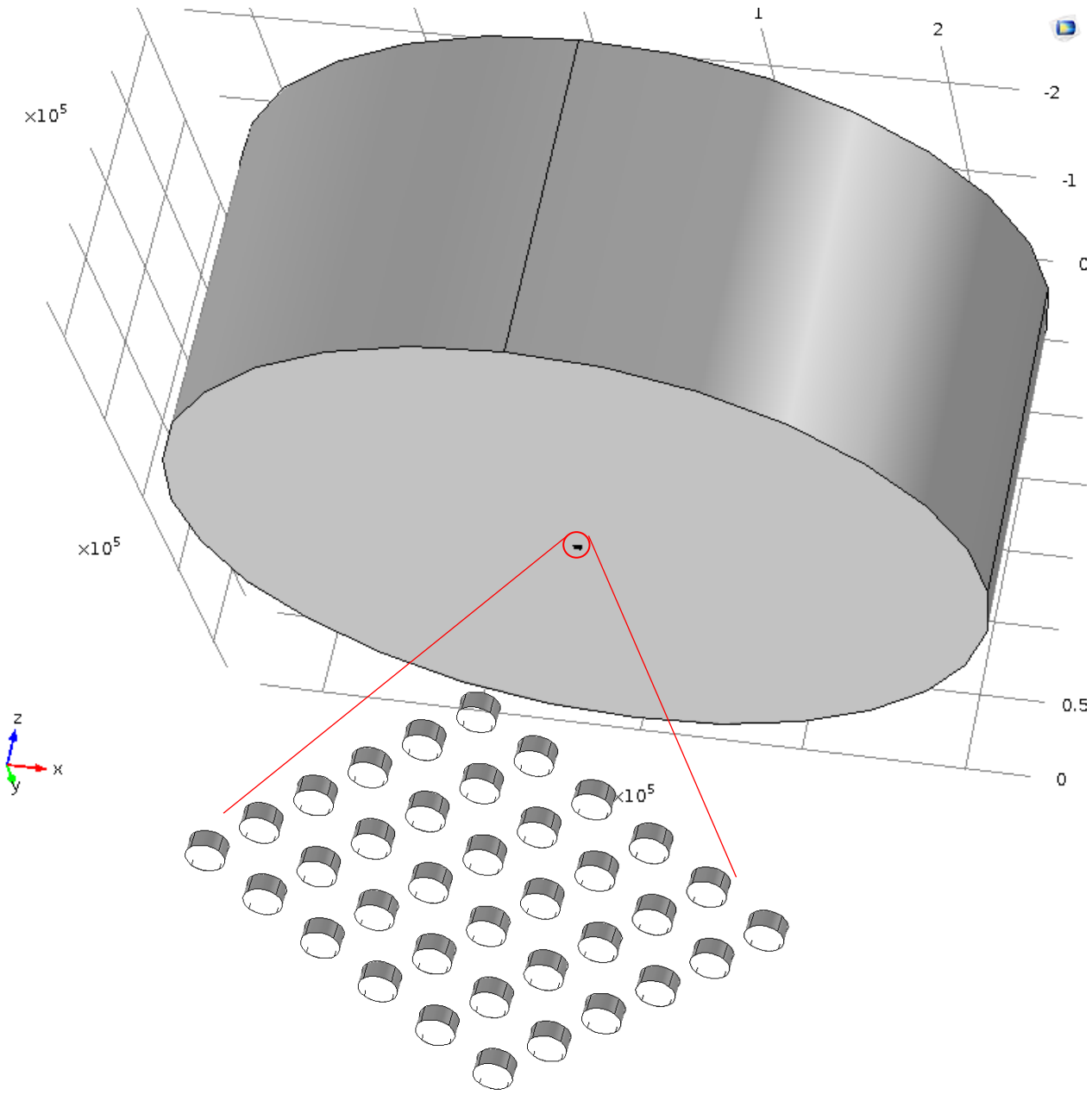

b

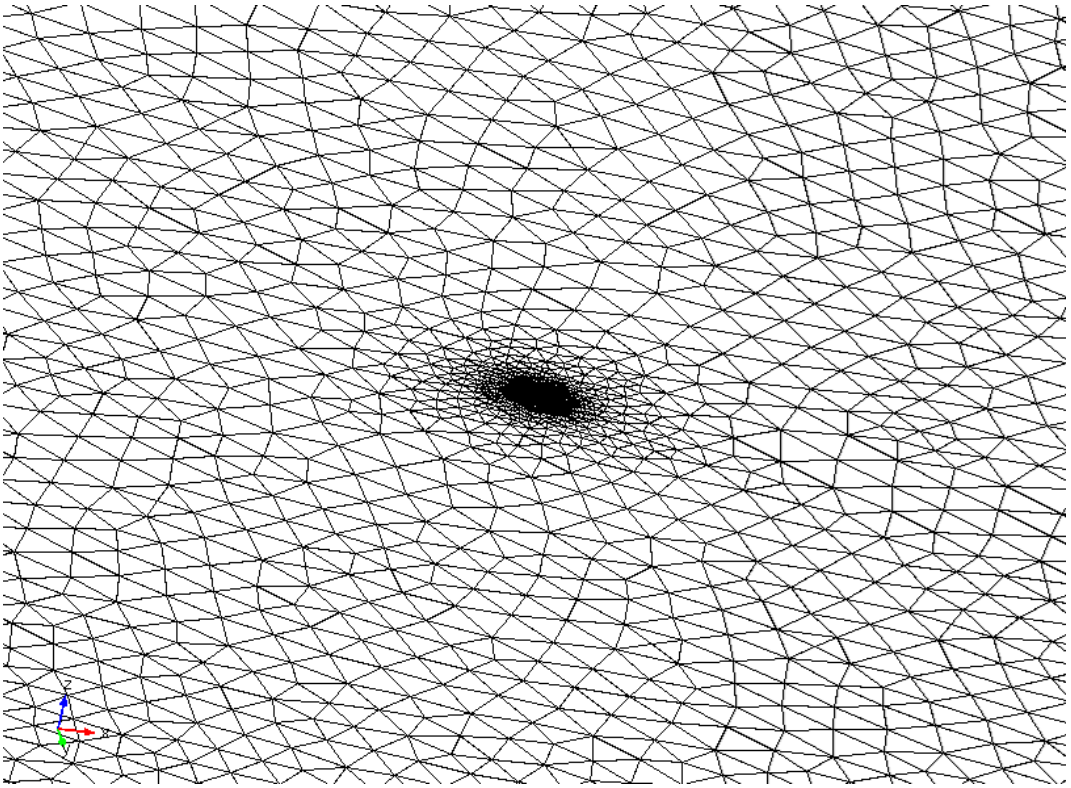

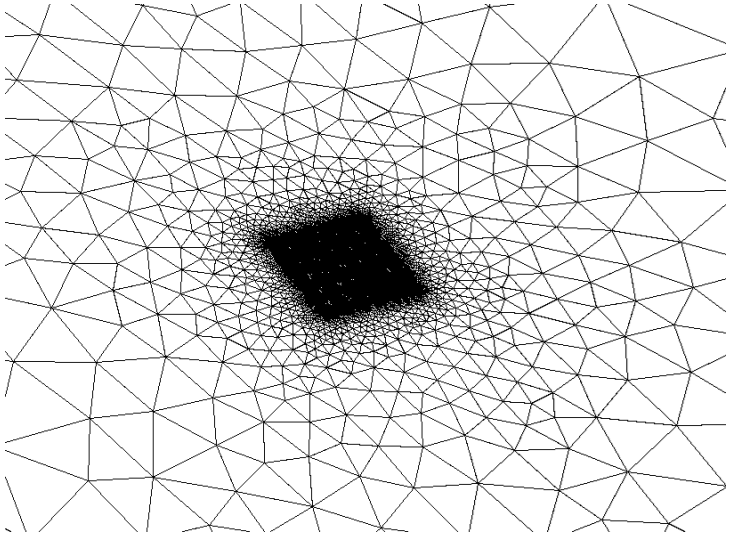

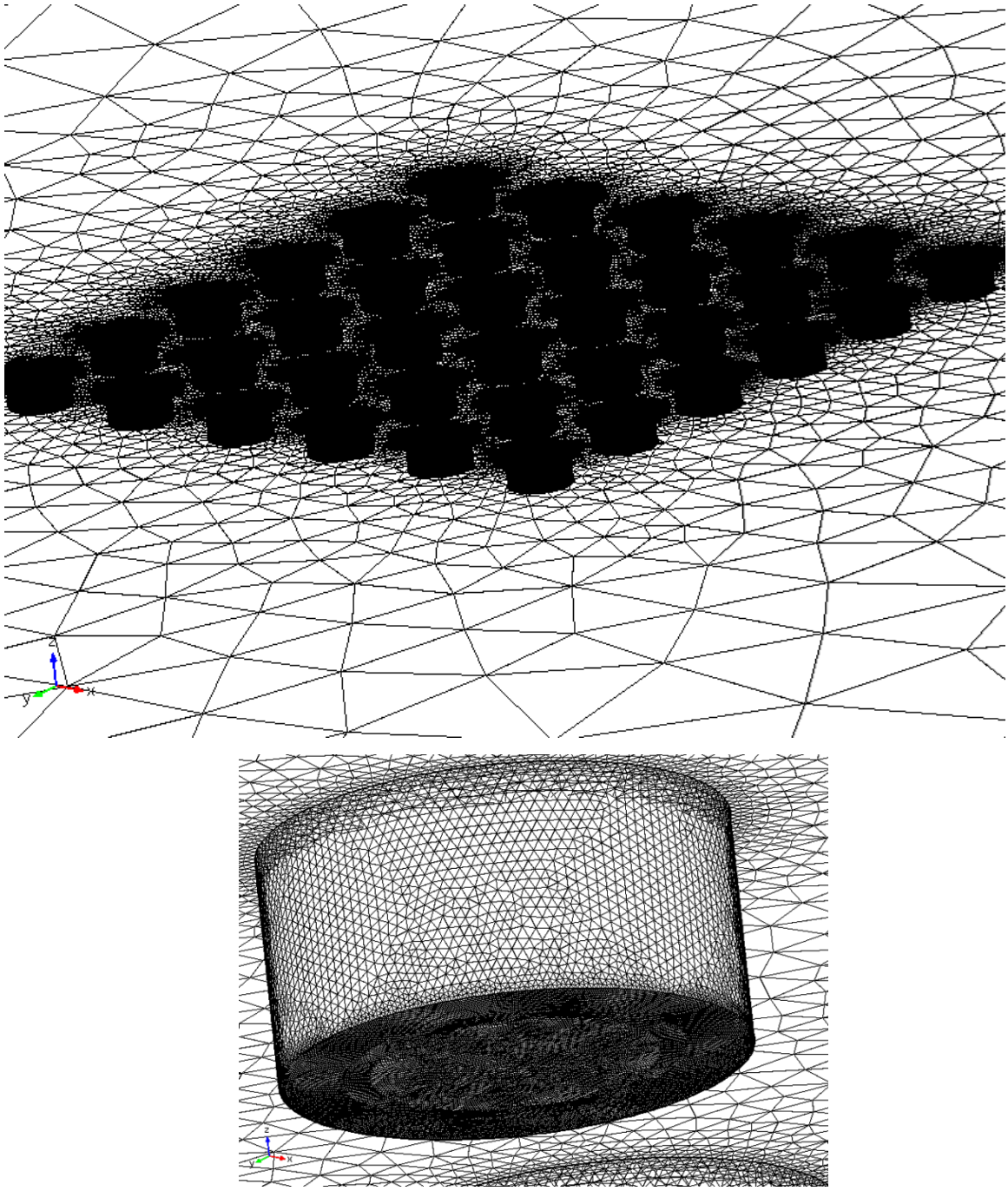

Figure 4-3**.** a) 3D model of the whole simulation space and b) and the appropriate meshing, for the simulation of a 6 × 6 r-NDE array with r = 200 nm.

a

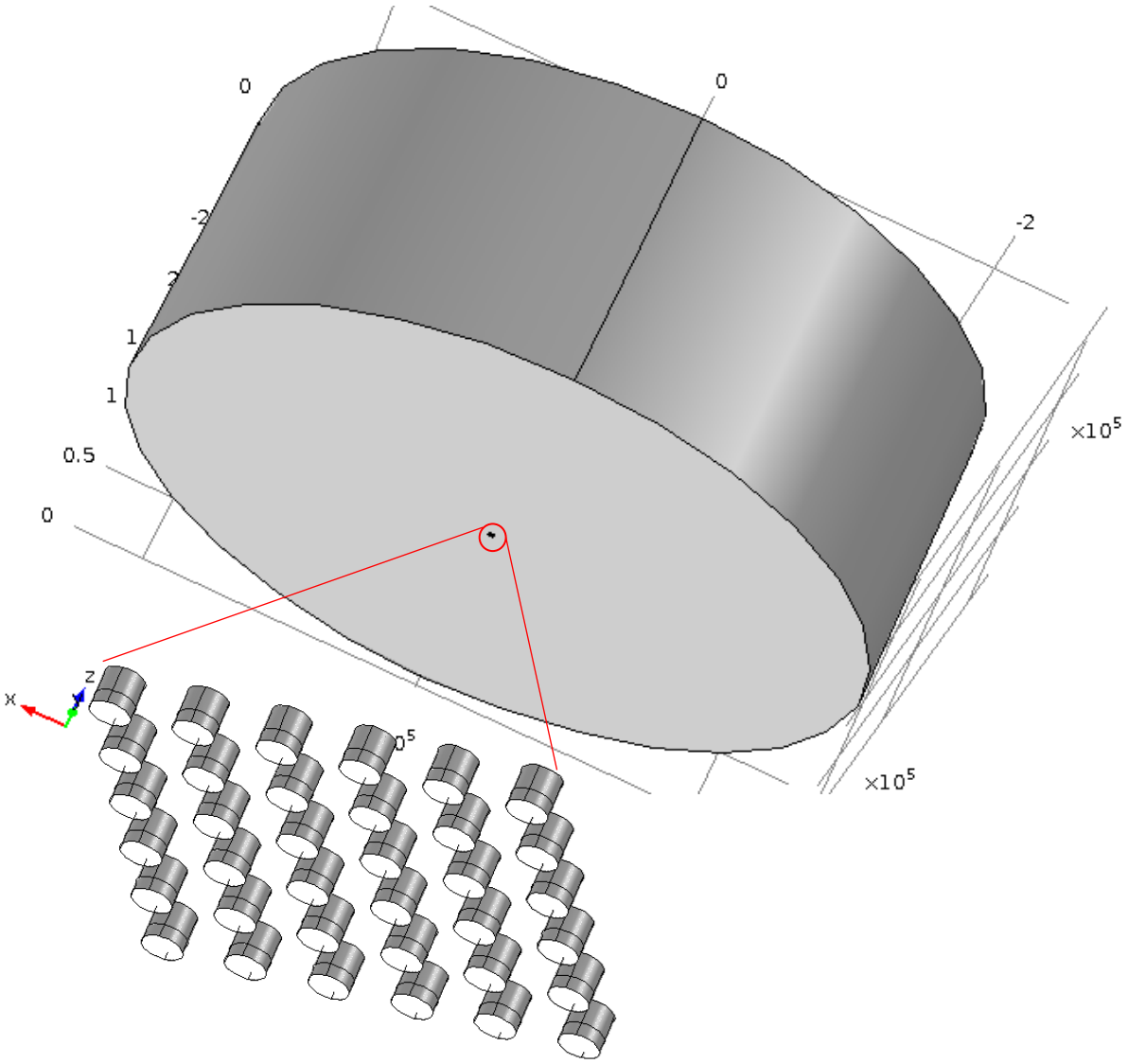

b

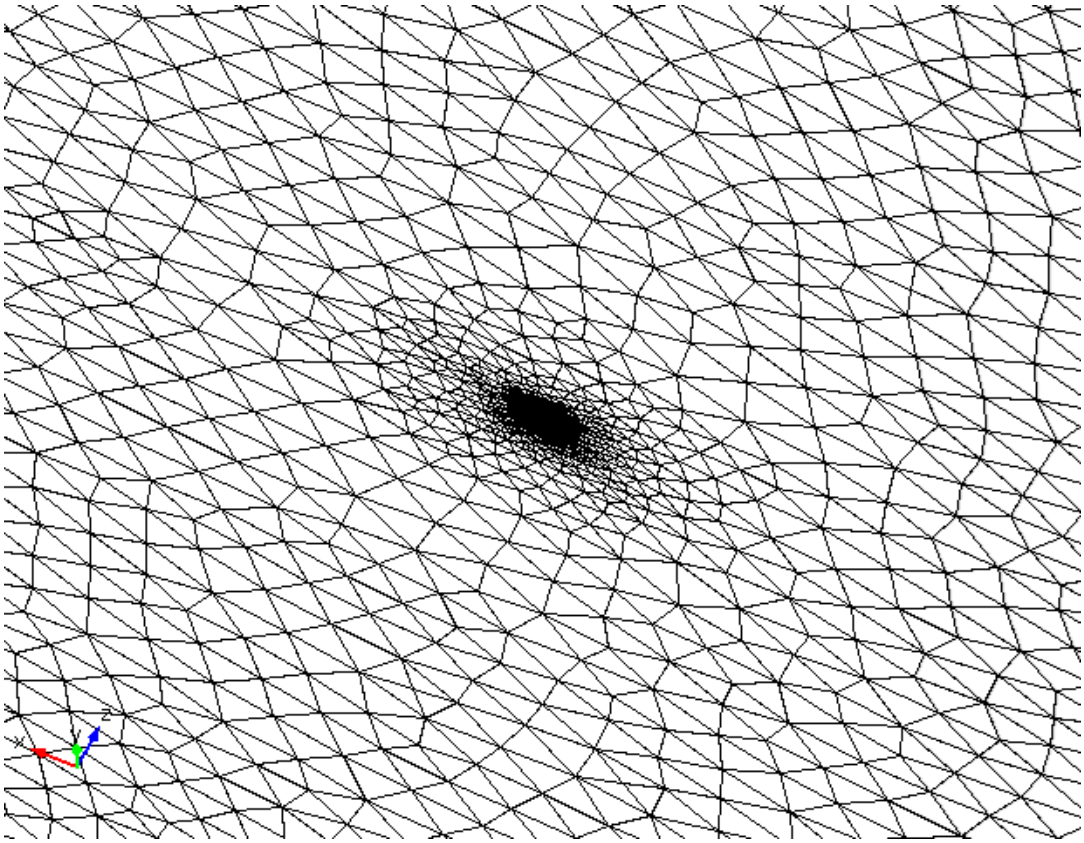

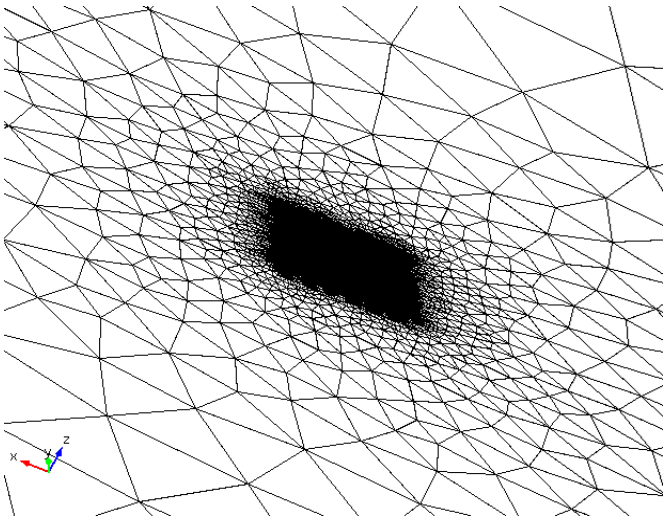

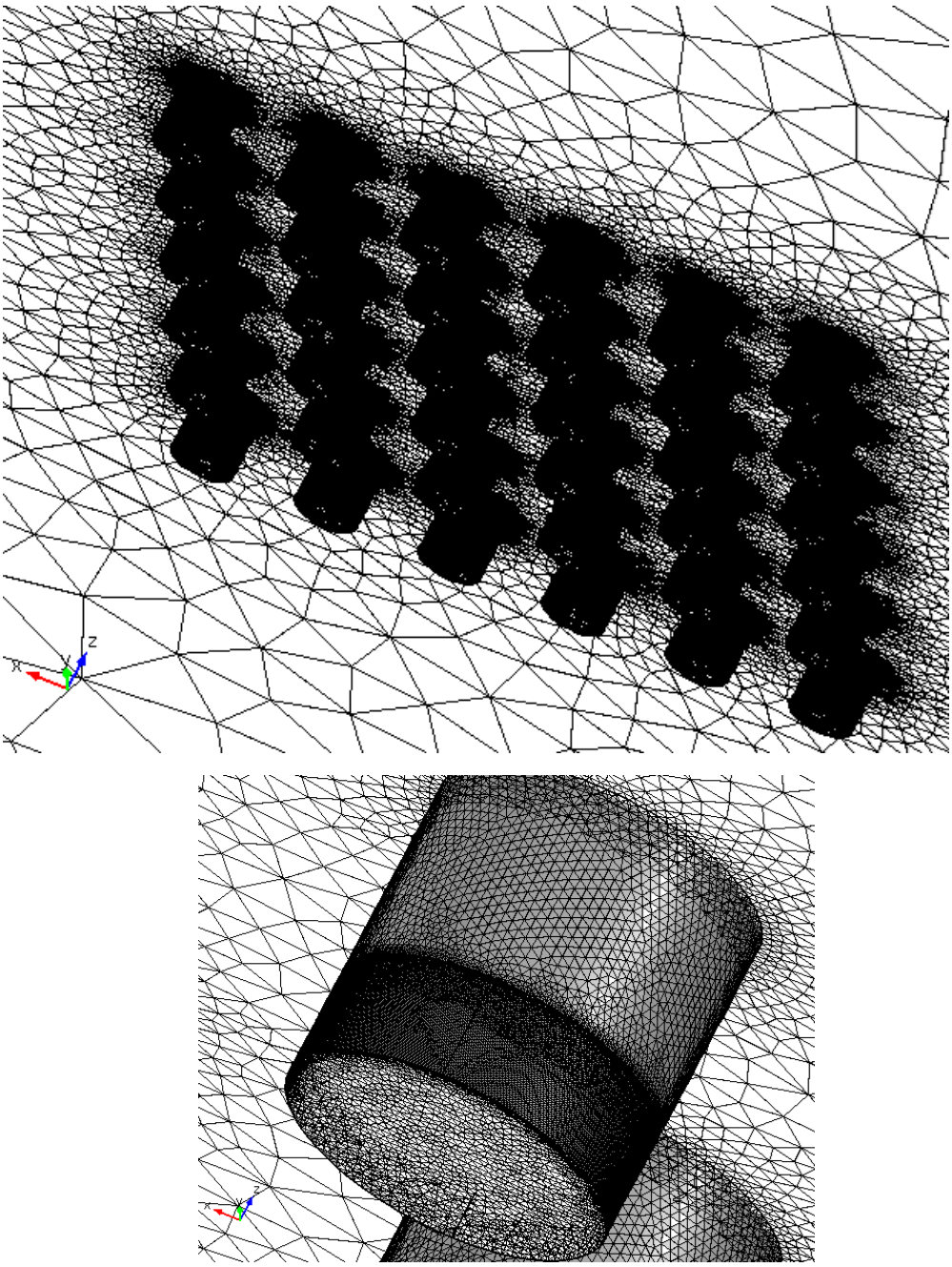

Figure 4-4. a) 3D model of the whole simulation space and b) and the appropriate meshing, for the simulation of a 6 × 6 r-NRE array with r = 150 nm and h = 100 nm.

4.3 RESULTS AND DISCUSSION

4.3.1 Influence of the Electrode Geometry on Voltammetric Response

Figure 4-5 shows a comparison of the electrochemical response from a reversible process (ferricyanide reduction) between an array of r-NRE and an array of r-NDE. Both arrays had 6 × 6 elements, and they were fabricated by focused ion beam (FIB) milling. Scanning electron micrographs of the arrays are shown as insets in Figure 4-5, together with three-dimensional cross-section schemes that represent the geometry of the arrays. The radius, *r*, of both ring and disc were 150 nm (nanohole's radius), and both structures were supported in glass and coated with 200 nm insulating layer of Si_3N_4 (recess depth, *l*). The separation between the nanoelectrodes elements for both arrays in Figure 4-5 was also identical and set to 600 nm, 4r. The ring electrode's height, *h*, was 50 nm. Figure 4-5 shows that the steady-state reduction current density for the array of r-NRE (~ −2.6 nA / μm^2) was about ~22% higher than that of observed for the array of r-NDE (~−2.1 nA / μm^2). Although the absolute area of the r-NRE was 33% smaller than the r-NDE for the fabrication parameters used in Figure 4-5, both arrays occupied the same footprint. This indicates a potential advantage of the r-NRE since its area can be controlled by adjusting the parameter *h* while keeping the radius of the hole and the distance between electrode elements constant.

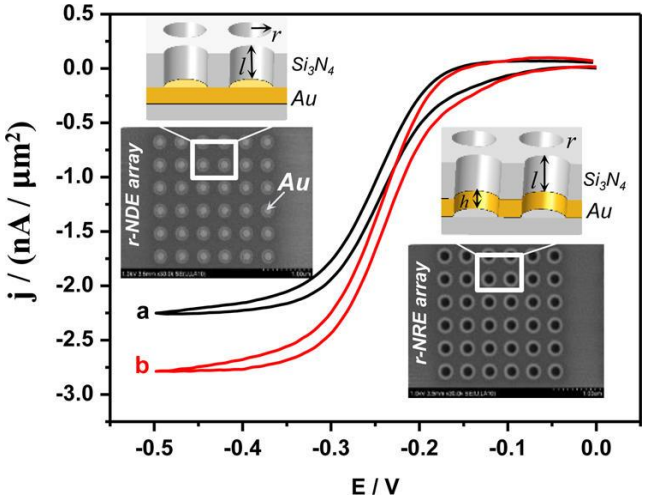

Figure 4-5. Background-subtracted experimental voltammograms for 6 × 6 arrays of (a) r-NDE and (b) r-NRE at a scan rate of 0.05 V s^{-1}. Experiments realized in a 20 mM potassium ferricyanide aqueous solution. 0.5 M KCl was used as supporting electrolyte. The nanohole radius (r = 150 nm), recess depth (l = 200 nm), and interelectrode distance (4r = 600 nm) were the same for both arrays. The height of the gold ring on the r-NRE, h, was 50 nm.

In the experimental conditions of Figure 4-5 (scan rate 0.05 V s^{-1}), the diffusion layer that evolved from each nanohole electrode element is expected to overlap with the diffusion layer from neighboring elements. In the case of extreme overlap between the diffusion layers (which is expected in the case of Figure 4-5, due to the relatively slow scan rate and the small interelectrode distance), the whole array should behave as a single microelectrode with an area that corresponds to the entire size of the array.[15] Since both arrays (nanodiscs and nanorings) were fabricated on the same geometrical area, 3.3 μm × 3.3 μm (the number of the electrode elements present in each array and the radius of the nanoholes were the same for both systems), the difference in the current density magnitude shown in Figure 4-5 should underlie different characteristics of mass-transport for each of the nanometric geometries.

Finite element (FEM) calculations using COMSOL Multiphysics® version 5.2 were performed in order to elucidate the mechanistic aspects of the mass transport towards the nanofeature elements in the arrays. There are intense simulation studies that address the electrochemical behavior of infinite arrays of microelectrodes with different geometries including inlaid and recessed microdiscs[34-36], microbands[37], porous [33], conical [38], and cylindrical microelectrodes[32]. However, there are very few simulation studies on the electrochemical behavior of finite arrays of microdiscs[39-40], as well as regular [15] and random [2] nanodiscs arrays of microsized dimensions. There is no numerical study on the voltammetric response at the microsized array of nanoring electrodes. Moreover, reports on the comparison of the electrochemical responses of electrode arrays with different geometries in the nanoscale are also lacking, despite the fact that the effect of electrode geometry at the nanoscale is amplified [5]. Although there are some comparative studies between (individual) microelectrodes of different geometries that demonstrate differences in their electrochemical behaviors[41-42]. Here we performed simulations of cyclic voltammograms for 6 × 6 r-NDE and r-NRE arrays in three-dimensional domains. A simple reversible redox reaction with Butler-Volmer kinetics was considered.

It is important to emphasize that all simulations in this work were performed in the 3D domain. The diffusion domain approximation[34] has been successfully used for the simulation of the behaviors of nano and microelectrodes on large area[32-33, 35-36, 43- 44] where a significantly greater number of electrodes are available in the inner positions than in the perimetric positions of the microarray, (as a result the convergent effect of the perimetric electrodes could be ignored). This approximation essentially assumes an identical behavior for all the electrodes in an array[31] and allows complicated 3D problems to be treated in 2D domains. However, the current response from nano/microelectrode arrays is extremely dependent on the overall size of the array when the

diffusion zones among neighboring electrodes overlap. Unlike a peak-shaped voltammetric response achieved with nano/microelectrode arrays of millimeter size, when the diffusion layer among the electrodes on the array extremely overlap, a sigmoidal shape response is expected with a nanoelectrode array of micrometric dimension in the above-mentioned condition. This behavior is caused by the overall shape of the diffusion layer set over the entire array[31]. In other words, the linear and radial diffusions of electroactive species towards the whole array surface are responsible for obtaining transient and steady-state responses in large and small arrays, respectively. As for a micro-sized array, a radial diffusion operated in the whole array, the flux density at each nanofeature presented on the array should depend strongly on its position in the array[31]. Therefore, the assumption that every element will behave the same (diffusion domain approximation)[34] is not valid in those conditions. Therefore, three-dimensional simulations are essential to characterize the voltammetric response of these nanostructured micrometer-sized arrays[31] accurately.

Figure 4-6 shows simulated voltammograms obtained for 6 × 6 arrays of r-NDE and r-NRE. The nanohole radius (*r*), recess depth (*l*), interelectrode distance, were all set identical for both arrays and matched the experimental parameters in Figure 4-5. The height of the ring electrode (*h*) was taken as 50 nm to comply with the experimental value (see the definition of the geometric parameters in Figure 4-5).

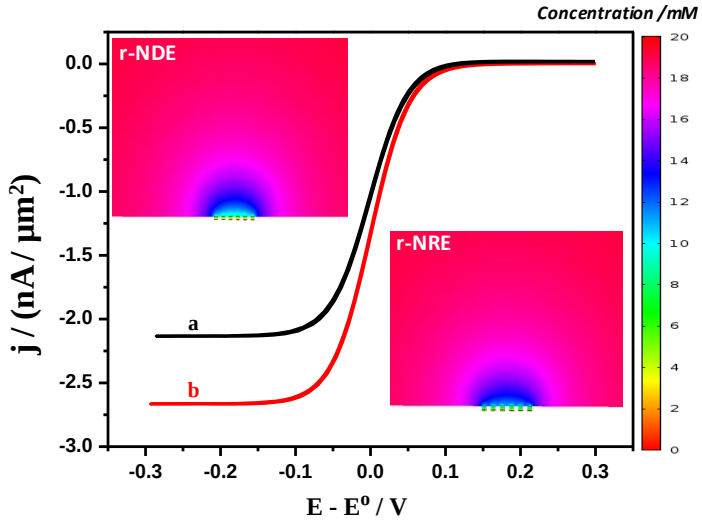

Figure 4-6**.** Comparison of simulated cyclic voltammograms for two 6 × 6 arrays (a) r-NDE and (b) r-NRE at scan rate of $0.05\,Vs^{-1}$. $E^{\acute{0}} = 0.25\,V$, D = 6.5×10^{-10} m^2s^{-1}.[15] The geometric parameters used in the simulations are provided in the text. Insets: 2D slice concentration profiles of species O corresponding to the potential at which the steady-state current was established, on the forward scan.

As it can be seen in Figure 4-6, the r-NRE array presents a larger steady-state current density than that of the r-NDE array for this particular set of geometrical parameters. The simulated current density magnitudes for both arrays in Figure 4-6 matches very well with the experimental values represented in Figure 4-5. Since all the simulation parameters and experimental conditions were similar, the observations from Figure 4-5 and Figure 4-6 indicate that geometric effects contribute to the differences in output current density observed between the arrays.

Qualitatively, the diffusion layer should evolve quickly within each nanohole, reaches the hole opening, and then spreads over the nanohole with a 3D shape[17, 45]. As the diffusion profile of each adjacent nanohole overlaps, the overall shape of the concentration gradient profile, and, consequently, the voltammetric response of the array, will depend on the size of the whole array.

For a micrometer-sized array, the concentration profile over the entire array remains three-dimensional, regardless of the extent of the overlapping diffusion zones of the nanoelectrodes[15].

The radial diffusion pattern over the whole microsized array is responsible for the steady state voltammogram obtained for both r-NDE and r-NRE arrays in Figure 4-5 and Figure 4-6. The calculated radial shape of the diffusion layers over the entire arrays are shown in 2D (y–z plane) slice concentration profiles as insets in Figure 4-6. The 2D slice concentration profiles at the center of the nanoholes were taken from the first row in the arrays (see scheme in Figure 4-7).

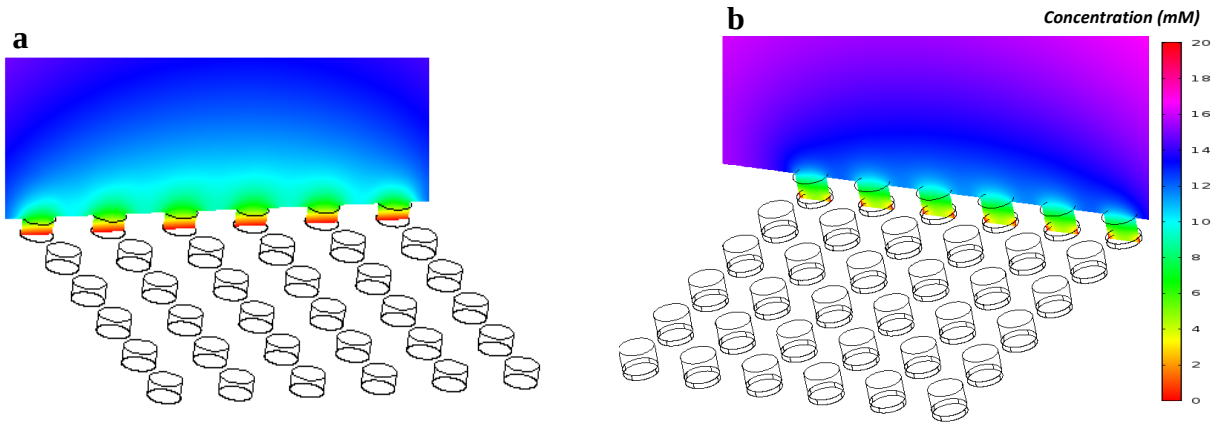

Figure 4-7**.** Schematic representation of the 2D (y-z plane) slice concentration profile on the first row of 6×6 (a) r-NDE and (b) r-NRE arrays.

The 2D slice concentration profiles of ferricyanide were taken at the potential, - 0.2 V, at which the steady-state current was established. 3D concentration profiles for both arrays are also shown in Figure 4-8.

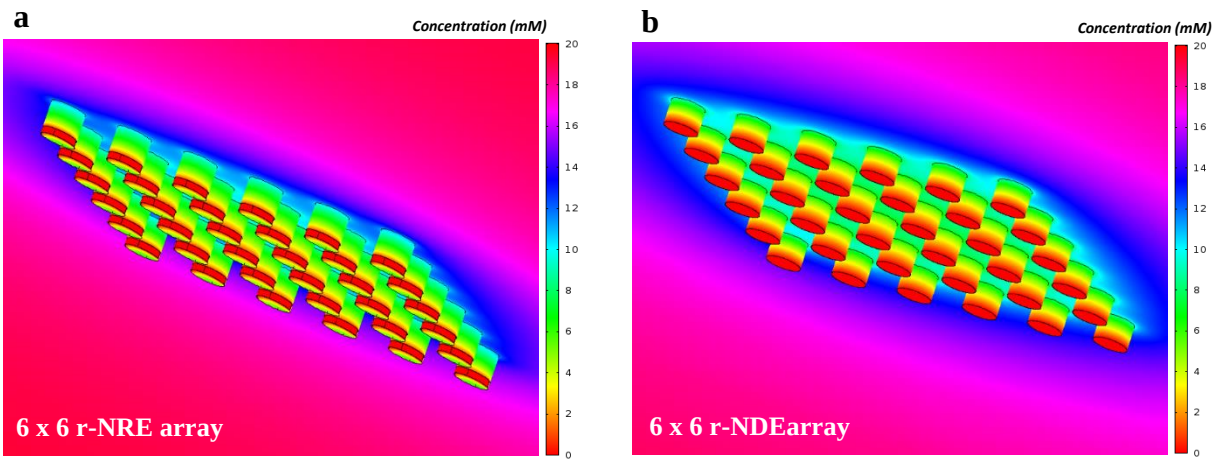

Figure 4-8**.** 3D concentration profiles for 6 × 6 (a) r-NRE and (b) r-NDE arrays. Radius, r = 150 nm; inter-electrode distance = 600 nm; and scan rate, v = 50 mVs^{-1}. All parameters were the same for both arrays. The nanorings height (h) were 50 nm. $E^{0} = 0.25\ V$, D = $6.5 \times 10^{-10}\ m^2s^{-1}$.[31]

The calculated radial diffusion pattern over the whole array is analogous for both r-NDE and r-NRE arrays (Figure 4-6). Animation files further demonstrate the dynamics of the concentration profiles evolution over both arrays for better visualization (Animation 4-1 shows 2D slices, and Animation 4-2 shows 3D concentration gradient evolutions with time). The similar diffusion profile observed from the concentration gradient evolution of both arrays cannot account for differences in transport characteristics at each nanoelectrode element. Therefore, the transport properties at nanometric scale (inside the nanoholes) were further considered in order to find observable differences between the geometries. The geometry of the electrode must influence the supply of fresh redox species from the bulk to the electroactive area. The redox species obviously enters from the hole top and flows down toward the electroactive surface. In the case of the r-NDE, the flux to the electroactive surface (located at the base of the nanohole, see Figure 4-5 and Figure 4-8) is parallel to the hole length (z-direction). However, the mass flux to the r-NRE differs from

r-NDE, as the electroactive surface is confined to the inner walls of the holes. Thus, the normal flux, in this case, is toward the inner walls of the hole, which is perpendicular to the hole length. This is verified by analyzing Figure 4-9, where the calculated concentration profiles across the diffusion layers inside the nanoholes of each array are shown. 2D (y−z plane) slice concentration profiles at the center of the nanoholes are presented in Figure 4-9a, d. The calculated concentration profiles were obtained at the steady-state current at the same potential (E = −0.2 V). Figure 4-9b and e show the close-up images of the concentration maps for a r-NDE and a r-NRE, respectively. The concentration contour maps are shown in Figure 4-9c, f. These contours have been determined using exported data from COMSOL to Matlab, Version 8.3 (R2014a).

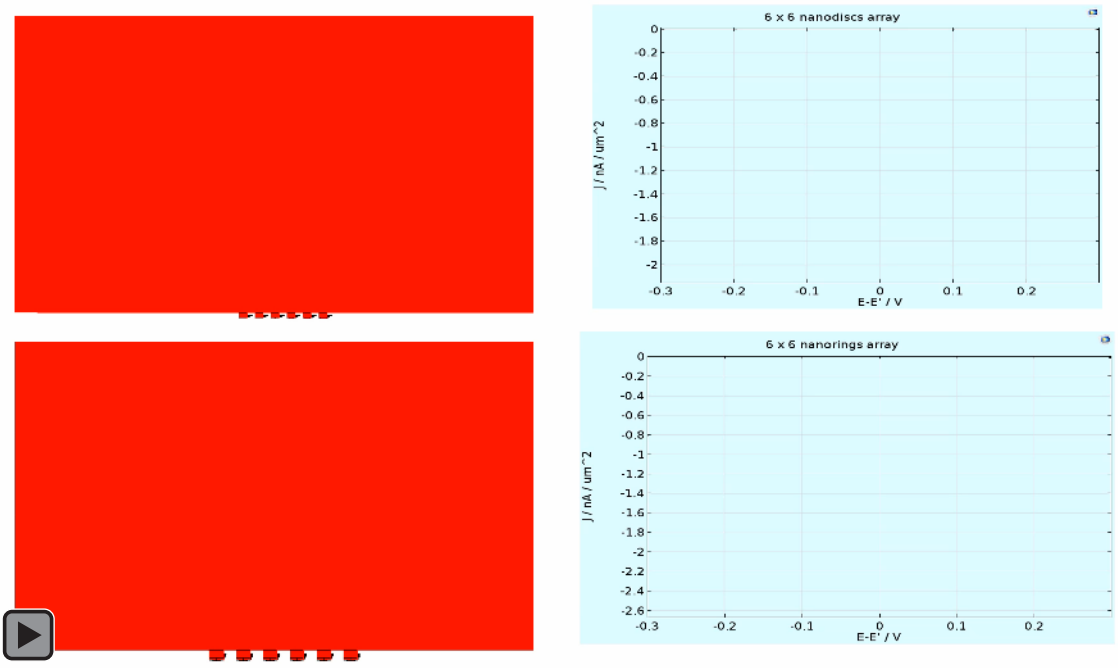

Animation 4-1. 2D slices concentration profiles evolution over the whole arrays of nanorings and nanodiscs with time.

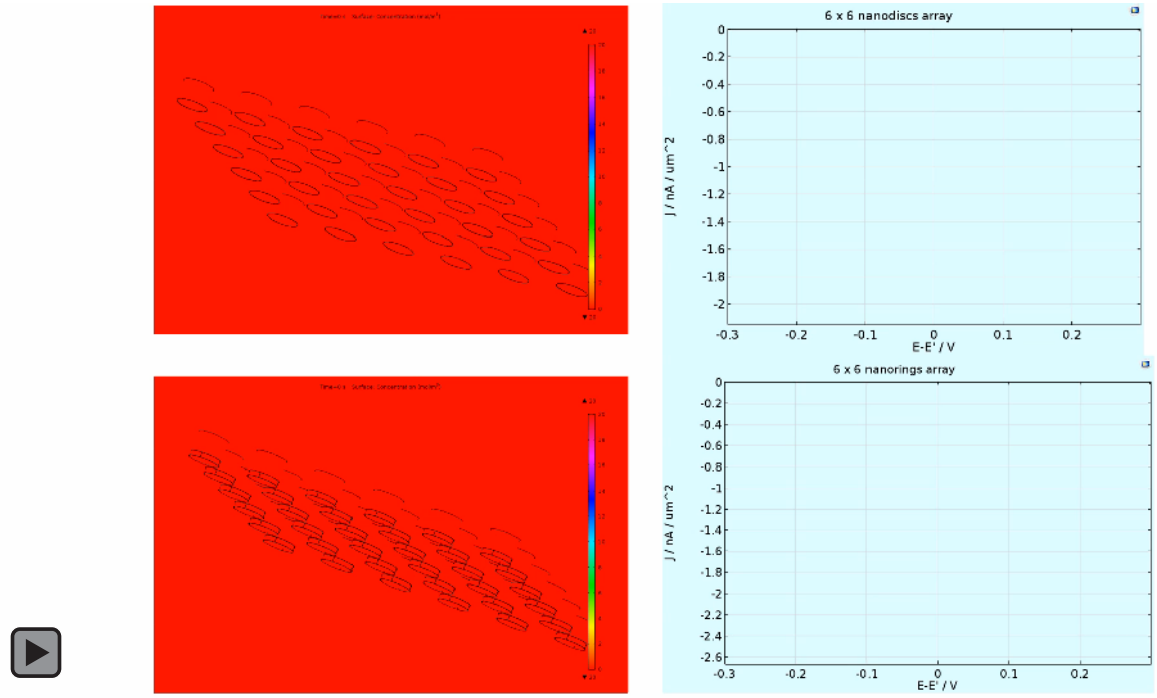

Animation 4-2. 3D concentration profile evolution of the entire nanodiscs and nanorings arrays with time

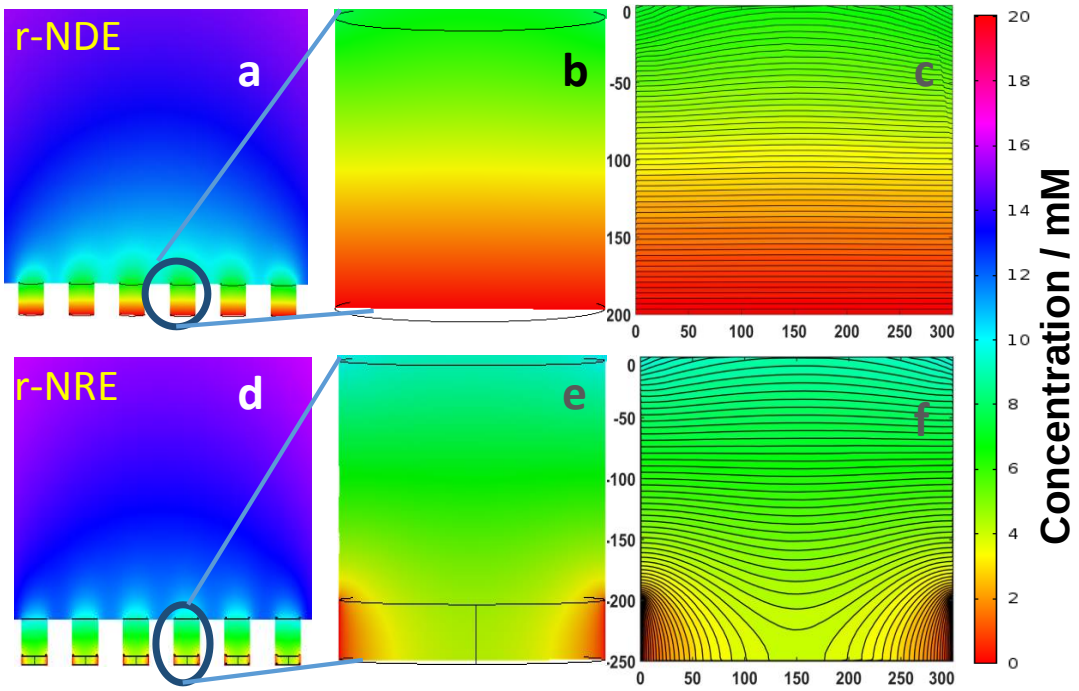

Figure 4-9. Comparison of the shape of the diffusion profiles within the nanoholes at the vicinity of the electroactive area of the r-NDE and r-NRE in the arrays. (a, d) 2D (y−z plane) slice concentration profiles at the center of the nanoholes; (b, e) close-up images of the concentration profiles for a r-NDE and a r-NRE; (c, f) concentration contour maps for a r-NDE and a r-NRE. All the parameters used in the simulations are the same as ones used in Figure 2. E = −0.2 V (steady-state condition).

Figure 4-9 illustrates differences in the transport characteristics between a r-NRE compared to a r-NDE. Figure 4-9Figure 3 shows that the mass transport properties within a single r-NRE and a single r-NDE can be broadly classified as “radial” and “planar diffusion,” respectively. This difference in transport characteristics should contribute to the increased current density obtained by the nanorings array in comparison with the nanodiscs array (Figure 4-5 and Figure 4-6). Figure 4-9e, f shows that the radial flux of molecules from the center-bottom of the hole toward the ring electroactive surface area enhances the mass transport of molecules from the bulk solution to the hole. Animation 4-3 shows the evolution of the concentration profiles within a single r-NRE and

r-NDE at the same conditions as Figure 4-9 and helps to illustrate the effect further. Figure 4-9a,d shows that the concentration profile (see the concentration scale bar in Figure 4-9), both within the holes and on the top opening of the holes, are dissimilar for each type of array. For instance, Figure 4-9d indicates that ~7 mM concentration of the oxidized species (ferricyanide) is expected to be inside the r-NRE hole, while for the r-NDE the same concentration is spread over the hole opening. This confirms that the radial flux of molecule to the r-NRE surface is more efficient in supplying fresh molecules from the bulk solution to the electroactive area in comparison with the flux of material to the r-NDE array (for the geometric parameters used in Figure 4-5).

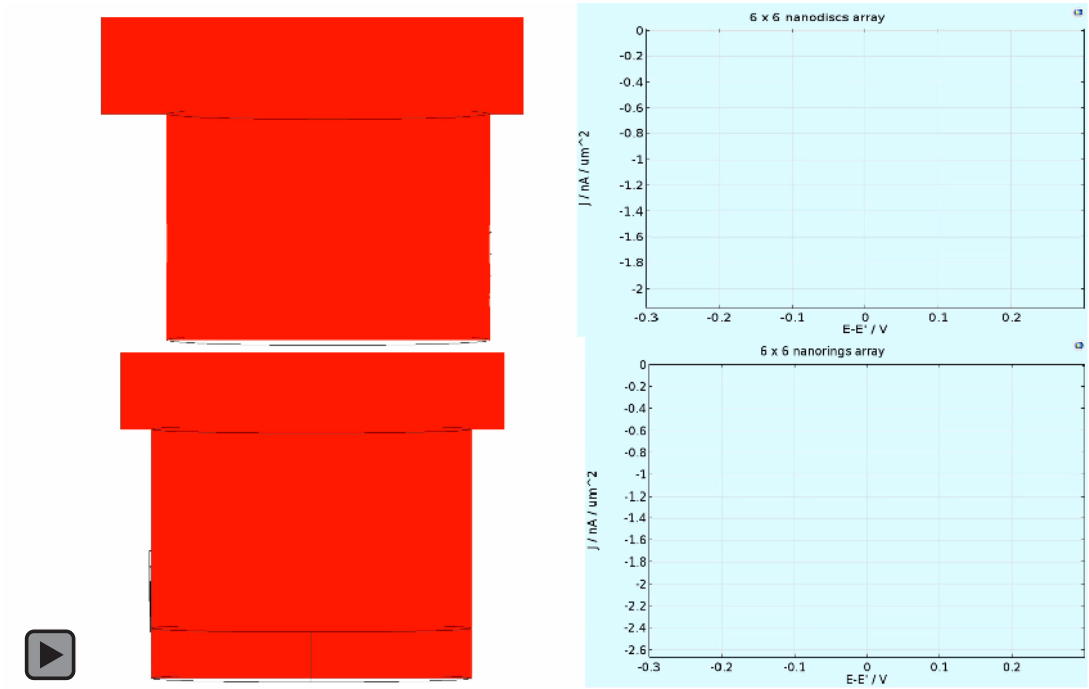

Animation 4-3. The evolution of the concentration profile within a single nanoring and nanodisc electrode as being discussed in Figure 4-9a, d.

4.3.2 Influence of the Hole Radius and the Nanoring Height on the Current Density Magnitude

The main conclusion from Figure 4-9 is that higher current densities for the r-NRE array compare to that of the r-NDE array can be achieved only when a radial diffusion contribution from the center toward the nanorings surface (within the nanoholes) dominate the transport. This implies that geometric parameters (*r* and *h*) that affect the nature of the diffusion layer geometry at the center of a r-NRE should have a strong influence on the magnitude of its current density. Figure 4-10 shows simulated voltammograms obtained at different *h*-values. The scan rate and the hole radius were kept constant. The other parameters used in the simulations were the same as those used in Figure 4-6.

Figure 4-10 shows that the highest steady-state current density magnitude is obtained from the r-NRE with h = 25 nm (the shortest ring height considered in Figure 4-10). The limiting current density for an array of r-NRE decreased as the ring height was increased. The values of the steady-state current densities from r-NRE arrays with h = 75 and 100 nm were less than that observed from an array of r-NDE with the same radius.

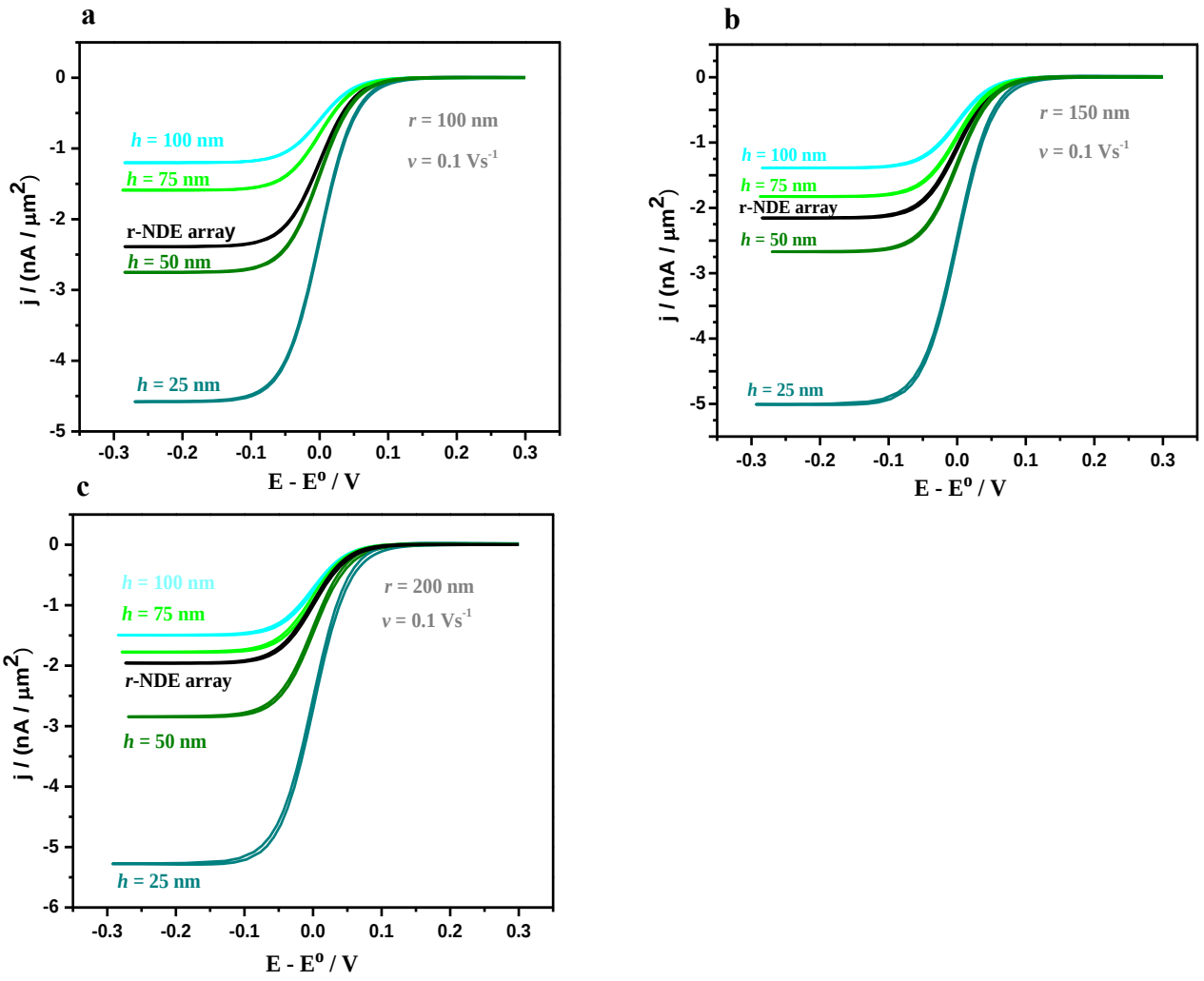

Figure 4-10**.** Comparison of simulation results for cyclic voltammograms represented base on the current density for 6 × 6 r-NDE and r-NRE microarrays with different heights, 25 nm (*r/h* = 6), 50 nm (*r/h* = 3), 75 nm (*r/h* = 2), and 100 nm (*r/h* = 1.5). The scan rate ($v = 0.1\ Vs^{-1}$) and hole radius a) *r* = 100 nm, b) *r* = 150 nm, and c) *r* = 200 nm were kept constant in Figure 4-10a, b, and c, respectively. The rest of parameters used in the simulations were the same as those in Figure 4-6.

The behavior from Figure 4-10 can be explained by analyzing the diffusion profiles provided in Figure 4-11. The concentration profiles in Figure 4-11 were taken at the limiting current potential. Specifically, the close-up concentration profiles were calculated from the third nanohole on the

first row of the array. Figure 4-11 confirms that the radial diffusion component dominates the transport in a nanoring element for small *h* values. The radial nature of the flux geometry at the hole center decreases with increasing the ring height for constant values of scan rate and hole radius. As the ring height increases, the degree of the depletion of material from the center of the hole increased. This leads to an overlap of the radial diffusion layer at the center, which reduces the current density.

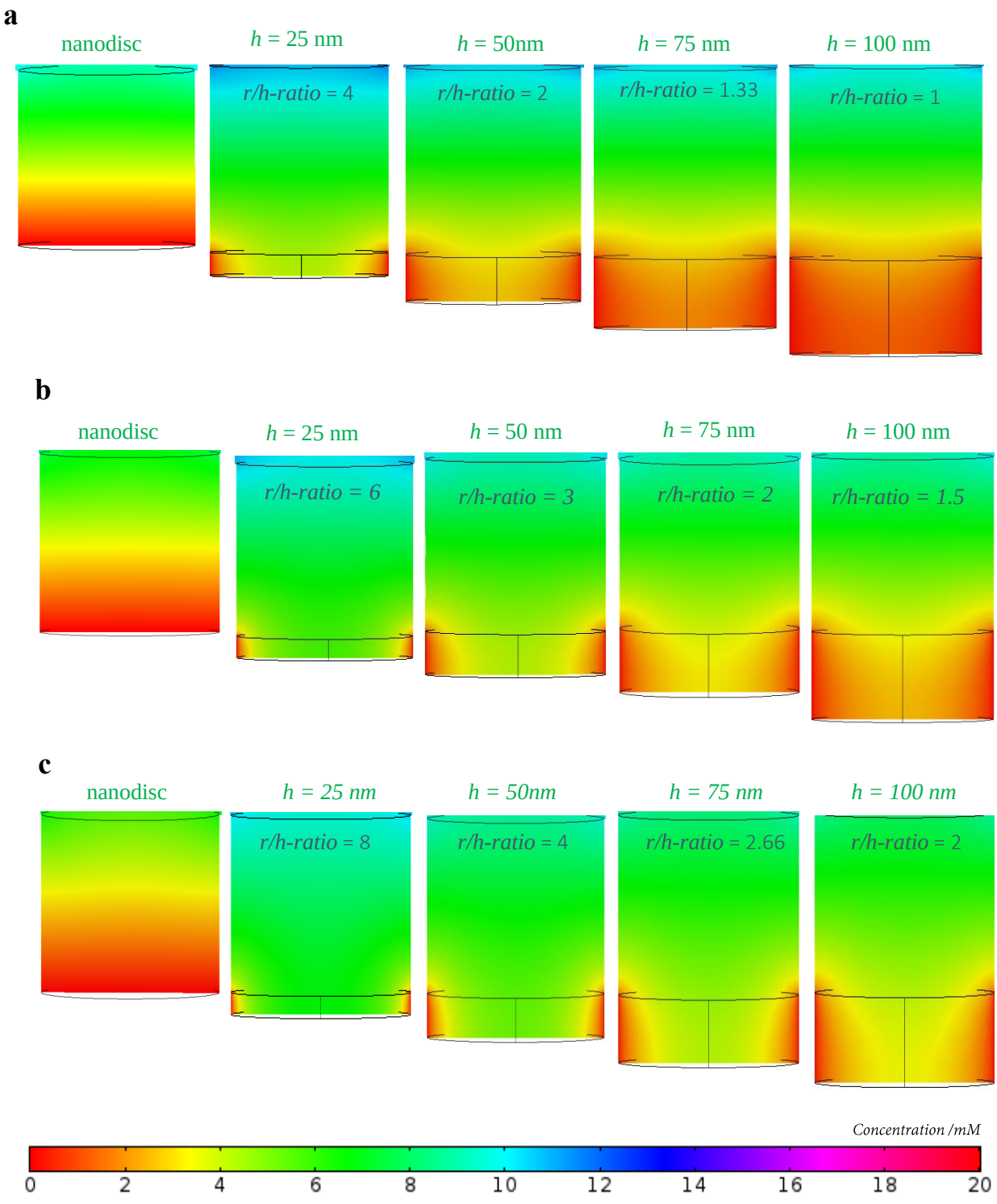

Figure 4-11**.** Concentration distributions for species O within the hole next to the electrode surface for the r-NRE microarray with different heights (25 nm, 50 nm, 75 nm, 100 nm) and for the r-NRE

microarray. The close-up concentration profile images are taken from the third nanohole on the first array's row. (The emphasis is on the center of the bottom section of the hole surrounded by ring). The hole radius a) ***r* = 100 nm**, b) ***r* = 150 nm,** and c) ***r* = 200 nm** and the scan rate (v = 0.1 Vs^{-1}) were the same for each set a, b, and c, respectively. Each concentration profile illustrates the variation of the diffusion layer in the center as a function of ring height. As the ring height increases the diffusion layer extends further in the center and the size of diffusion zone in the center which is completely depleted from the species increases (the red color representing this regime).

The concentration profiles in Figure 4-11 indicate some similarities between the general characteristics of the diffusion layer within the holes between the r-NRE with h = 75 nm and h = 100 nm and that of a r-NDE. However, the r-NRE array with h = 75 nm and h = 100 nm presented lower current density magnitudes when compared to that of the r-NDE array. This is due to the height associated to the nanorings. Therefore, in the conditions of diffusion layer overlap at the center of the hole, a nanoring would be comparable to a deeper recessed nanodisc of the same radius. The current density for a recessed nanodisc decrease with the recessed depth[46].

Similar transition between transport characteristics (as in Figure 4-11) was also observed when the height of the ring was kept constant, but the radius of the nanohole varied instead (Figure 4-12). In summary, the effect of increasing the ring height (for a given radius), Figure 4-10 and Figure 4-11, is the same as decreasing the radius for a constant ring height (Figure 4-12).

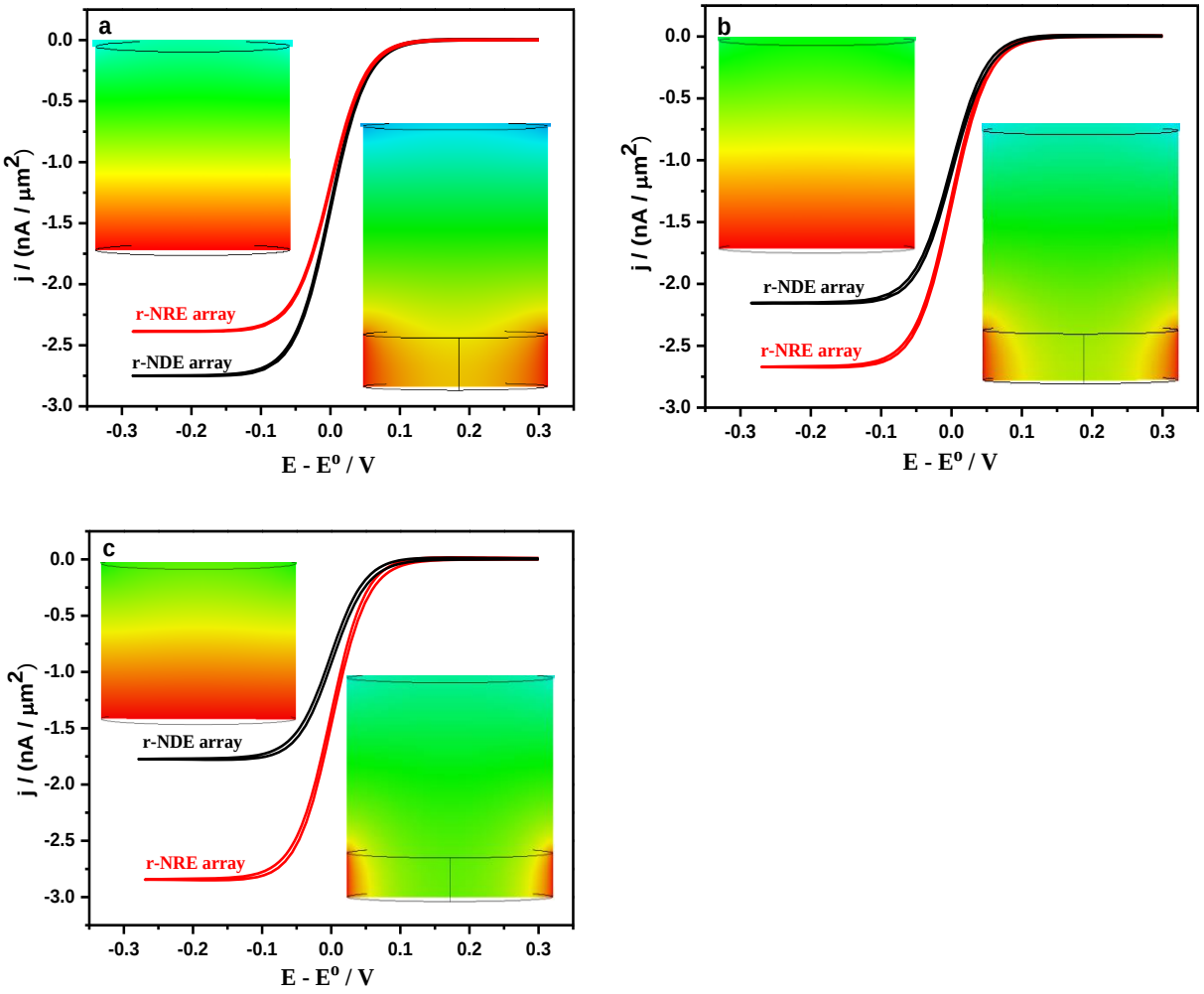

Figure 4-12**.** Comparison of simulated cyclic voltammograms represented for 6 × 6 r-NDE and r-NRE microarrays with different hole radii a) r = 100 nm b) r = 150 nm and c) r = 200 nm. The scan rate $v = 0.1\ Vs^{-1}$ and ring height h = 50 nm were kept constant. The rest of parameters used in the simulations were the same as those in Figure 4-6. In order to make a reasonable comparison, the inter-electrode distance between the nanoholes on each array was maintained as 4r. This means that the overall size of each set of microarray (kept with 6 × 6 elements) changed as the nanohole's radius varied. For arrays with r = 100 nm, the whole size of the microarray was 2.2 μm × 2.2 μm ; for r = 150 nm, the entire microarray size was 3.3 μm × 3.3 μm; and for r = 200 nm the microarray size was 4.4 μm × 4.4 μm.

The geometrical parameters, *r*, and *h*, have a strong influence on the shape of the diffusion profile within the r-NRE. The interplay between both parameters (also illustrated in Animation 4-4) suggests that optimization of the electrochemical performance of r-NRE microarrays requires analyses of the *r/h* ratio.

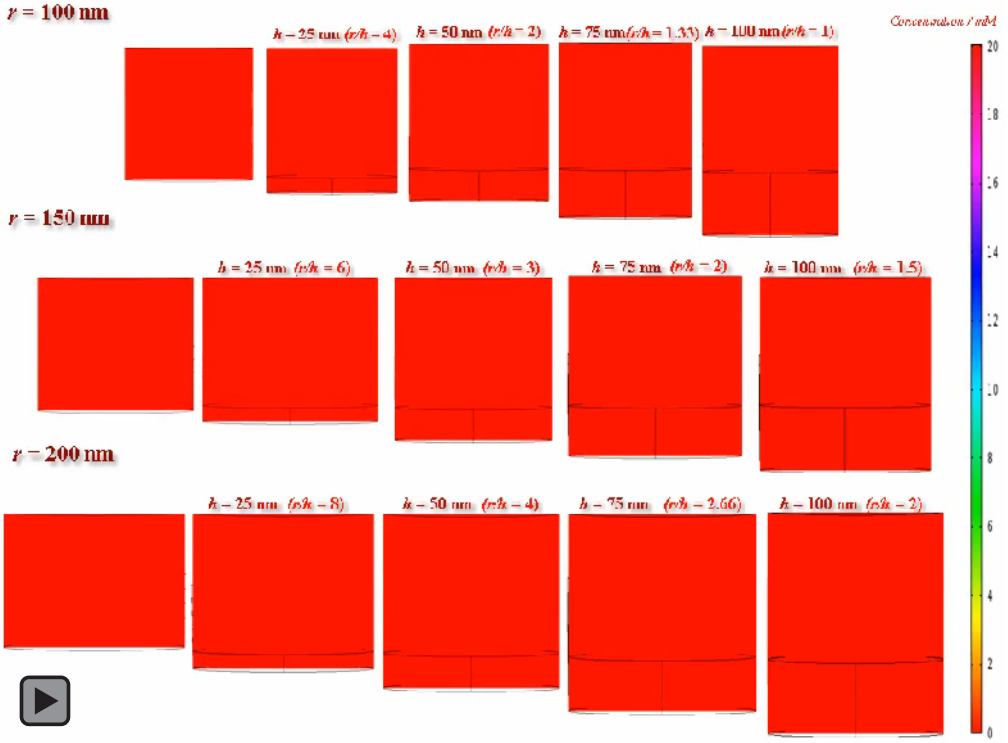

Animation 4-4. The evolution of the concentration profiles within the single nanoring an nanodisc electrode by varying the hole radius and ring height being discussed in Figure 4-11 and Figure 4-12.

Figure 4-13 shows a plot of the steady-state current density response, *j*, against *r/h* ratio for different nanohole diameters. The horizontal dashed lines correspond to the calculated *j* value for a r-NDE microarray with the indicated radius. The symbols in Figure 4-13 are experimental steady-state current (*j* values) obtained at the same electrochemical conditions as in Figure 4-5. The experimental values matched the calculated current densities (solid lines in Figure 4-13) within

5%. This matching with the experimental values for different geometrical parameters further validates the numerical approach.

Figure 4-13 reveals that, under steady-state conditions, the relative current density differences between the two microarrays, r-NRE, and r-NDE, largely depends on the *r/h* ratio. This occurs because the extent of the radial diffusion within the hole center is controlled by the relative interplay between *r* and *h*. As the *r/h* ratio increases, the shape of the diffusion layer within the holes near the ring surface becomes more pronounced (Figure 4-11 and Figure 4-12). The shaded region in Figure 4-13 shows that when the *r/h* ratio is about 2.4, the current density response of the r-NRE microarray will be the same as that of the r-NDE array with the same nanohole radius. The current density of the r-NRE will be higher/lower than of a r-NDE when the *r/h* value is more/less than 2.4, for a constant nanohole radius (Figure 4-13). Notice that the geometrical area of a r-NRE will be equal to a r-NDE when the *r/h* ratio is equal to 2.

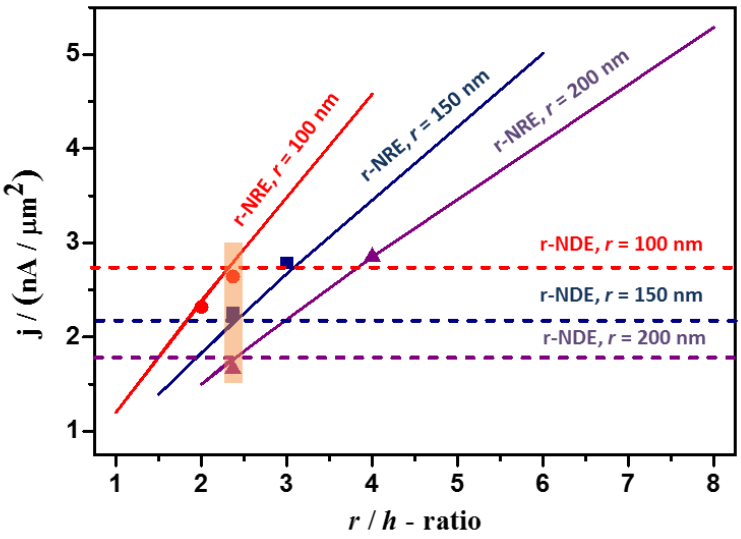

Figure 4-13. Steady-state current density plotted against the *r/h* ratio for arrays of r-NREs. The solid lines were calculated using COMSOL. The horizontal dashed lines correspond to the calculated steady−state current density value of r-NDE arrays. The symbols correspond to *j* values obtained experimentally using the same electrochemical conditions as in Figure 4-5. The radii of each of the nanoholes in the microarrays are indicated. The shaded region highlights the condition where the steady-state currents from both r-NRE and r-NDE arrays are the same for a particular nanohole radius. The symbols in the shaded region are experimental results for r-NDEs. The scan rate v = 0.1 V $s^{-1,}$ and interelectrode distance was 4r in all of the simulations.

4.3.3 Influence of the Scan Rate

The size of the diffusion layer also depends on the timescale of the experiment, which in voltammetry is dictated by the scan rate. Fast scan rates lead to smaller diffusion zones. At sufficiently high scan rates, the diffusion layer thickness becomes much smaller than the smallest dimension of the electrode. In this case, the planar diffusion to the microarray surface dominates the transport, and the current density turns proportional to the electrode surface area and becomes unaffected by the electrode geometry[41].

Figure 4-14 shows cyclic voltammograms for r-NRE and r-NDE microarrays at five different scan rates (from 0.1 to 1000 V s^{-1}). Insets in Figure 4-14 and Table 4-1 present the 2D (y−z plane) slice concentration profiles of species O for the first row of the microarray (remembering that all simulations were performed in the 3D domain). The concentration profiles were taken either at the steady-state potentials or at the peak potentials, depending on the shape of the voltammetric wave.

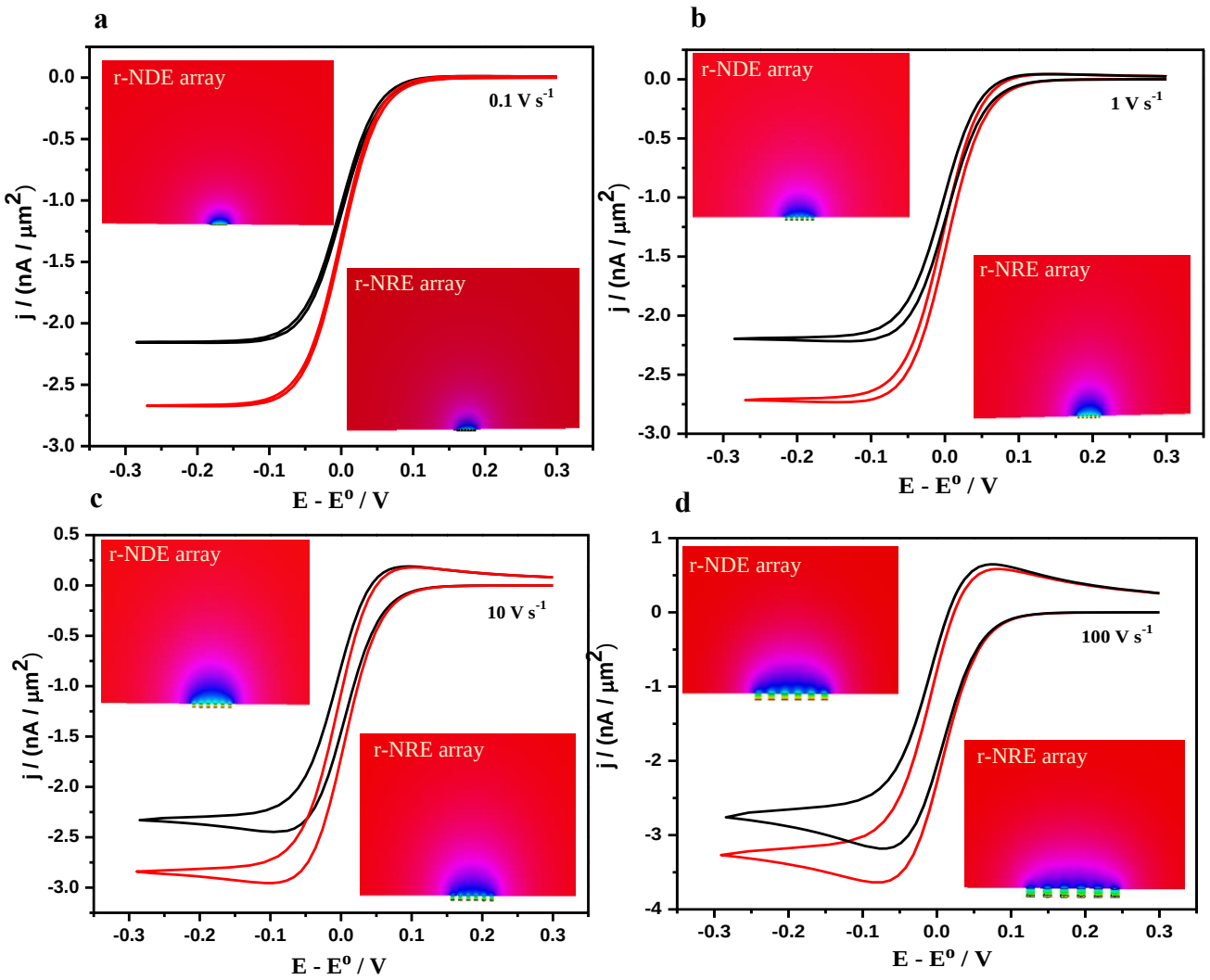

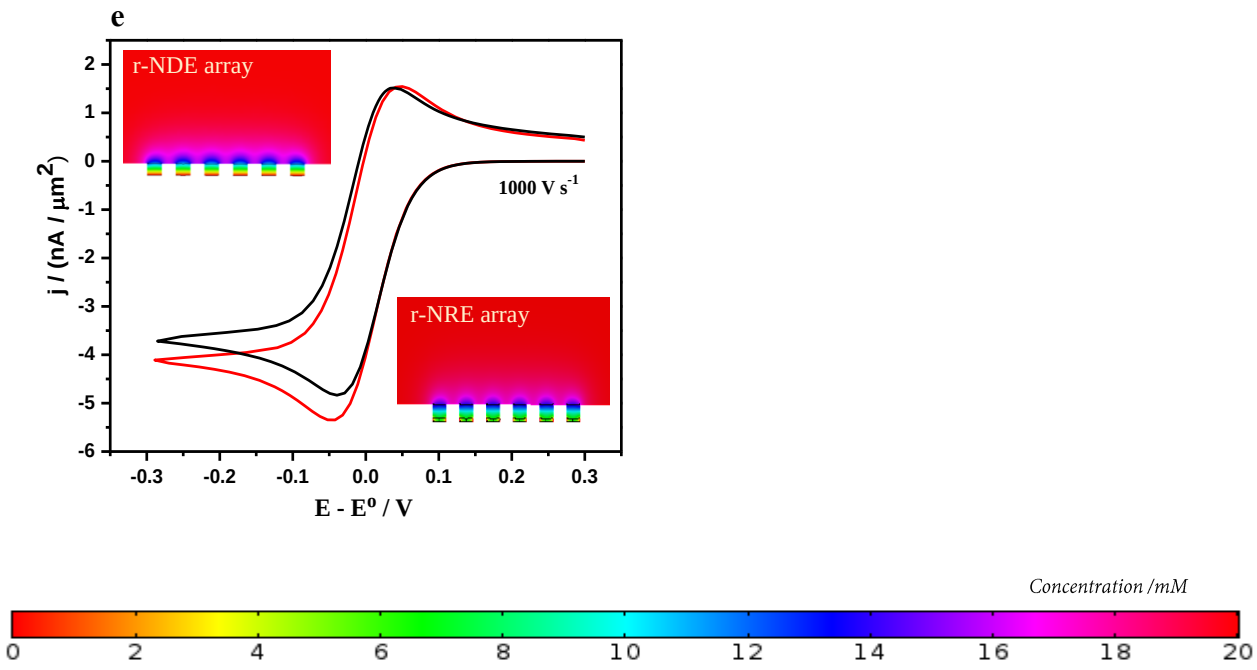

Figure 4-14. Simulated cyclic voltammetry for r-NRE and r-NDE microarrays at different scan rates: (a) v = 0.1 V s^{-1}, (b) v = 1 V s^{-1}, (c) v = 10 V s^{-1}, (d) v = 100 V s^{-1} and (e) v = 1000 V s^{-1}. The same parameters as in Figure 4-5 were used except for the scan rates which are indicated in the Figure. Insets are the 2D (y−z plane) slices concentration profiles of species O at the center of the nanoholes over the first row of the array. These are taken at the steady state potentials or at the peak potentials depending on the voltammetric wave shape.

An immediate observation from Figure 4-14 is that both the geometry of the concentration profile over the whole microarrays and the voltammogram wave shapes are similar for the r-NREs and r-NDEs. The shape of the diffusion layer over the whole microarrays always presents a radial component within the r-NRE, independently of the scan rates (*r/h* ratio = 3 in Figure 4-14). Figure 4-14 shows that the current density differences between the two nanohole geometries become less important as the scan rate increases. At slow and intermediate scan rates, a radial diffusion layer dominates over the whole array, increasing the efficiency of the mass transport. Accordingly, a greater difference in current density magnitudes between r-NRE and r-NDE is observed (Figure

4-14a , b). The 3D diffusion layer over the whole array amplifies the effect of the radial diffusion toward the nanorings surface within the nanoholes. The efficient transport at low scan rates leads to a voltammogram with a sigmoidal waveform in Figure 4-14a, b. The transport characteristics move toward a mixed hemispherical and planar geometry and finally to a planar geometry at large values of *v*. These changes in transport characteristics are reflected in the voltammogram waveforms. For instance, a peak-shaped voltammogram, indicating the dominance of planar diffusion, is shown in Figure 4-14e. The current density from r-NRE microarrays is still slightly higher than that of the r-NDE array even at a scan rate of 1000 V s^{-1}. The small difference between the peak currents values of the r-NRE and r-NDE arrays is consistent with the differences in their diffusion layer inside the holes. These can also be visualized in Animation 4-5, where 2D slices concentration profiles time evolution over the whole arrays and the corresponding voltammogram at various scan rate are shown.

The comparison of the electrochemical behavior of r-NREs and r-NDEs microarrays presented so far should provide guidance on possible implementation of devices based on those geometries. One of the advantages of the r-NRE is that the electrochemical characteristics for a given nanohole radius can be tuned by adjusting the *h* value. This can provide opportunities to improve the electrochemical response while maintaining the footprint of the microarray. For instance, Figure 4-15 shows arrays of r-NRE (*r/h* = 3) and r-NDE of the same radius, but with distinct electrochemical responses. In a multiarray device, according to Figure 4-15, the arrays of r-NRE could be placed ~2 μm closer together than arrays of r-NDE (Figure 4-15 and Table 4-2) and still provide independent electrochemical response. This property has obvious advantages on the design of addressable multiple electrochemical sensors in a miniaturized footprint.

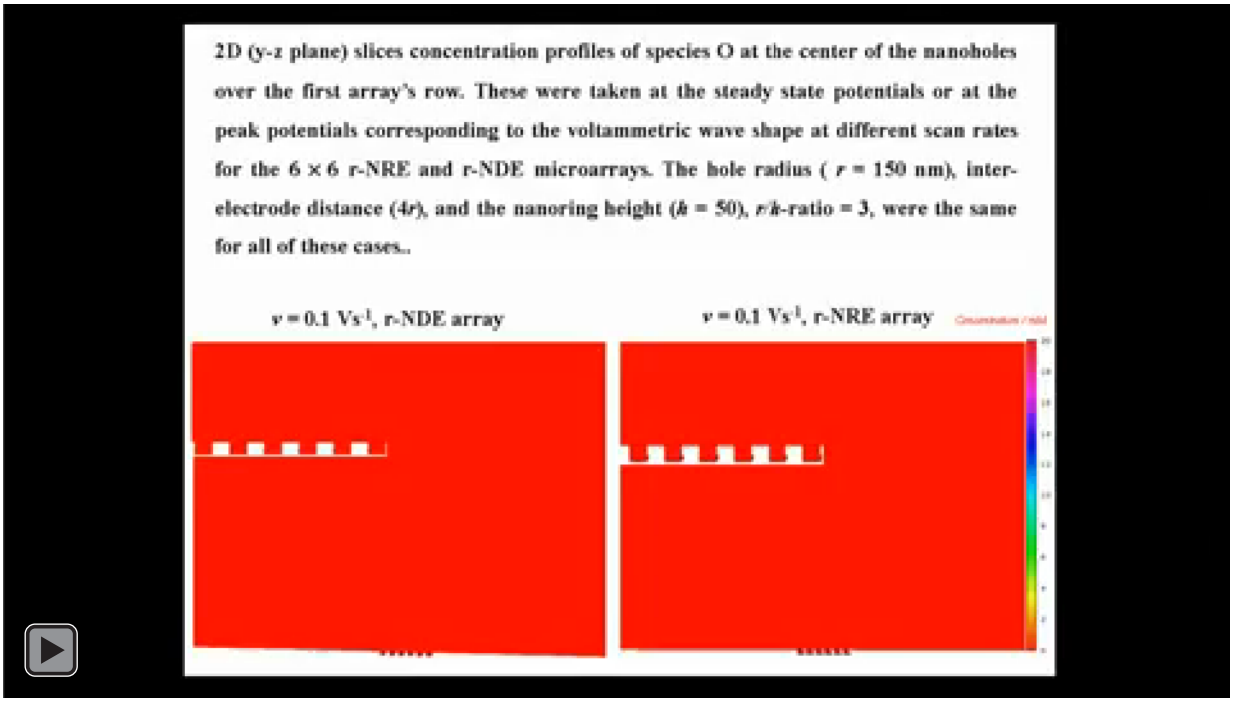

Animation 4-5. 2D slices concentration profiles evolution over the whole arrays of nanorings and nanodiscs with time and corresponding voltammogram response by varying the scan rate.

Scan rate	r-NDE array		r-NRE array	
	2D slice close-up concentration profile images at the center of the nanoholes in the first array row	Concentration contours images of the concentration profiles within a nanohole at the vicinity of the electrode	2D slice close-up concentration profile images at the center of the nanoholes in the first array row	Concentration contours images of the concentration profiles within a nanohole at the vicinity of the electrode
0.1 Vs^{-1}	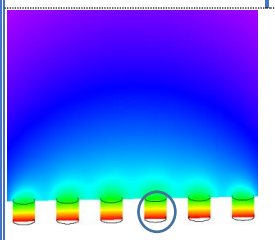	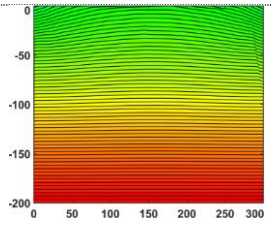	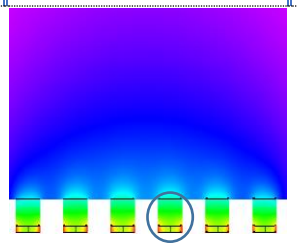	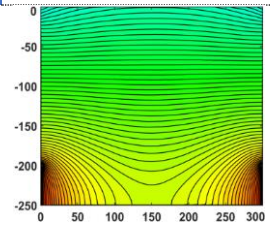
1 Vs^{-1}	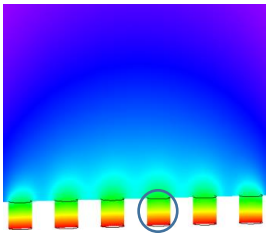	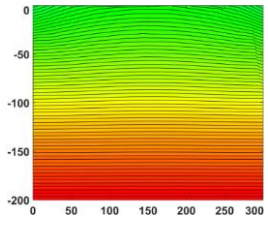	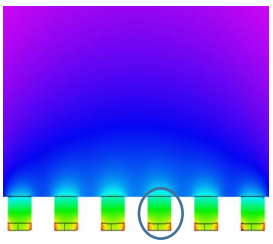	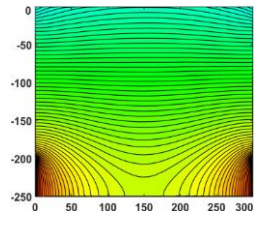
10 Vs^{-1}	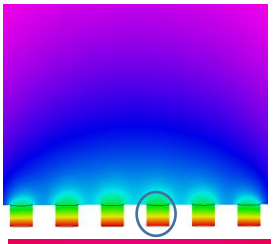	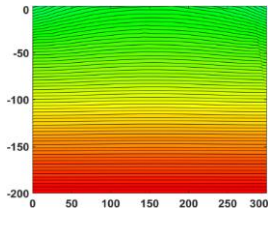	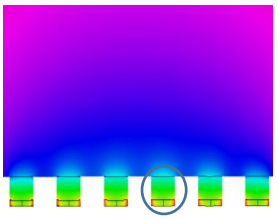	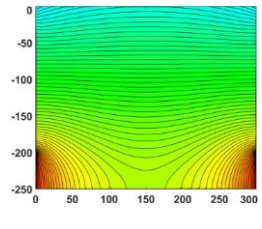
100 Vs^{-1}	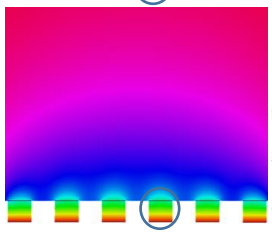	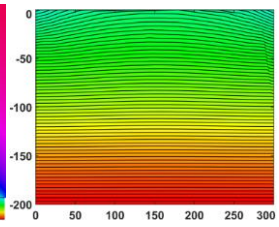	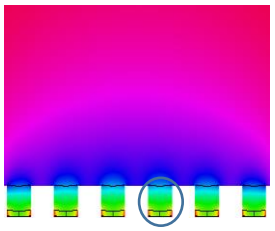	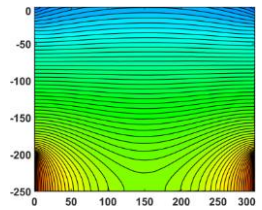
1000 Vs^{-1}	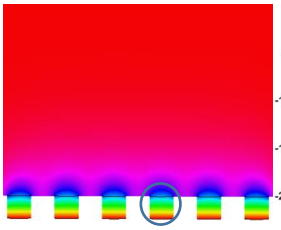	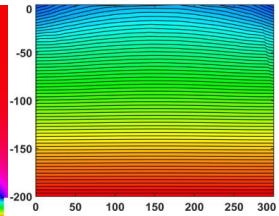	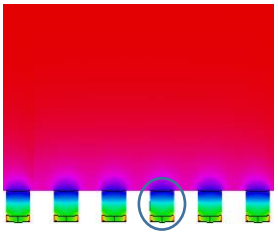	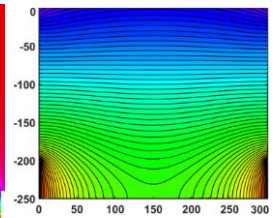

Table 4-1**.** 2D slice close-up concentration profile images at the center of the nanoholes in the first array row and the concentration contours images of the concentration profiles within a nanohole at the vicinity of the electrode for r-NRE and r-NDE array.

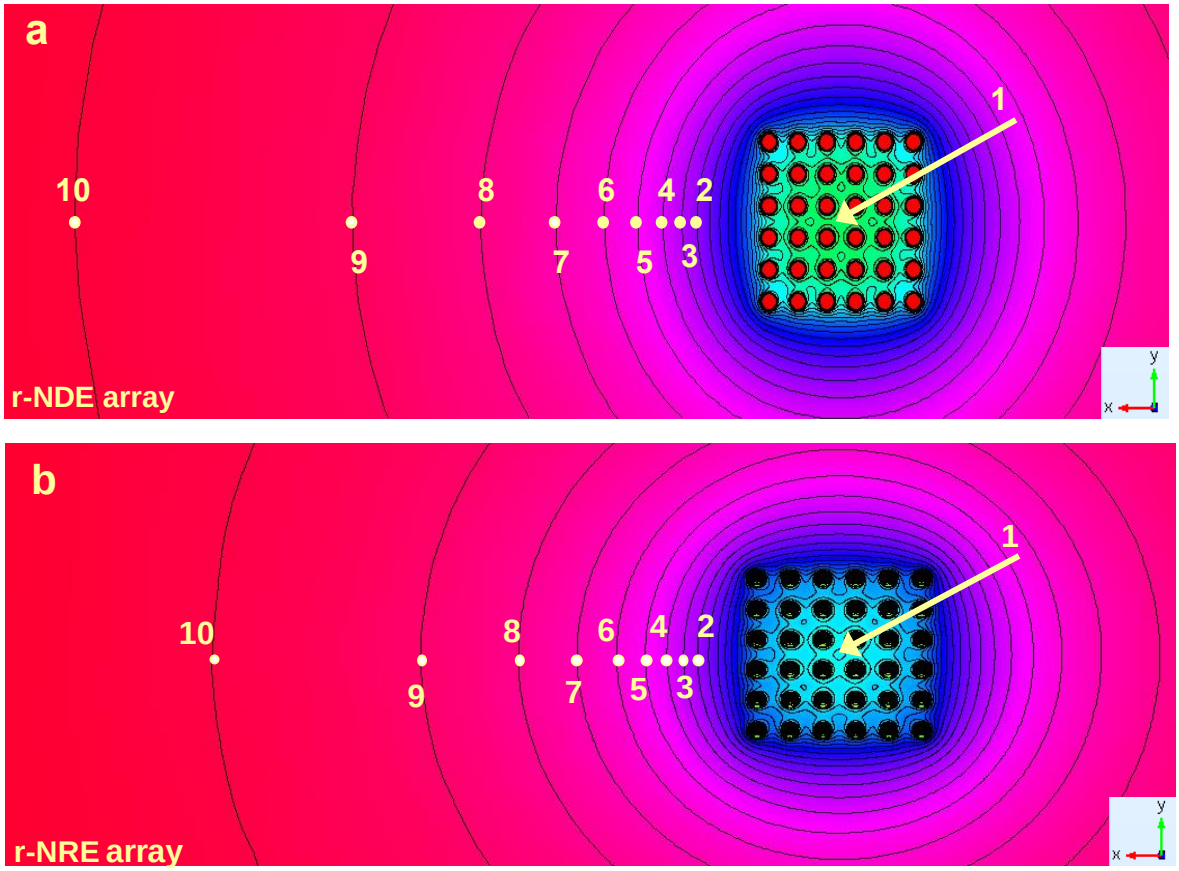

Figure 4-15**.** 3D Contour surface concentration profiles for 6 × 6 (a) r-NDE and (b) r-NRE arrays of the same hole radius (r = 150 nm), interelectrode distance (600 nm), and scan rate (v = 50 mVs^{-1}). The nanorings height (h) were 50 nm. $E^{0} = 0.25\ V$, D = $6.5 \times 10^{-10}\ m^2s^{-1}$.[31] Each counter plot (the solid black circles) corresponds to the lines of isoconcentration. The X position and the concentration value at each designated point on the counter lines are given in Table 4-2. The values of the concentrations at particular distances from the center of the arrays, indicated by "point 1" in Figure 4-15. The results from Figure 4-15 indicate that the diffusion layer thickness of the whole r-NRE array is smaller than that of the r-NDE array. This means that if one wants to design a chip with several array elements, where each element can be individually addressed electrochemically, then the separation distance between the r-NDE arrays must be larger than that for the r-NRE arrays (considering these particular geometric parameters). The requirement for each array to be electrochemically independent is that the diffusion layer of two adjacent arrays should not overlap. Arrays of r-NRE (r = 150 nm, h = 50 nm and inter-electrode distance = 600 nm) could be placed ~ 2 µm closer together than arrays of r-NDE.

	r-NDE array		r-NRE array	
Point #	X position / nm	Concentration / mM	X position / nm	Concentration / mM
1	0	8.0589	0	10.114
2	3019.8	15.298	2498.5	15.318
3	3321.7	15.754	2729.2	15.76
4	3710	16.238	3075.1	16.283
5	4227.7	16.76	3497.9	16.772
6	4939.4	17.249	4074.5	17.266
7	5931.7	17.729	4881.7	17.749
8	7506.2	18.26	6150.1	18.248
9	10180.9	18.76	8437.3	18.756
10	15961.9	19.257	13280.4	19.252

Table 4-2**.** The distance of concentration layers from 6 × 6 r-NDE array and r-NRE array of the same hole radius (r = 150 nm), inter-electrode distance (600 nm), and scan rate (v = 50 mVs^{-1}). The nanorings height (h) was 50 nm. The X positions and concentration values were obtained using COMSOL® point surface concentration probe.

4.4 CONCLUSIONS

A comparison of the electrochemical characteristics of microarrays of r-NDEs and r-NREs was carried out. The experimental results were confirmed by three-dimensional mathematical modeling. The effect of geometrical parameters, such as nanohole radius and ring height on the output current densities of the microarrays with different geometries, r-NRE, and r-NDE, was revealed. The fundamental differences between the electrochemical responses of the r-NRE and r-NDE arrays have been clarified by considering the mass transport properties within the nanoholes. In the case of the r-NRE, the characteristic mass transport inside an individual hole is controlled

by the *r/h* ratio. In principle, when the *r/h* ratio is higher than 2.4, the shape of the diffusion layer inside the nanohole is virtually radial, and a higher steady state current density is obtained for the r-NRE microarray in comparison to a r-NDE microarray (with the same microarray dimension and identical hole radius). Note that the radial diffusion geometry near the r-NRE surface (inside the nanoholes) increases with the *r/h* ratio. This leads to an increase in the percentage difference between the steady-state current density responses of the r-NRE and r-NDE microarrays. On the other hand, it has been shown that when the *r/h* ratio is lower than 2.4 the shape of the concentration field within the r-NRE is virtually planar, similar to that of a r-NDE array. However, the current density of the r-NRE array, in this case, is lower than that of the r-NDE array. This is due to the extra height associated with the r-NRE. The nanoring electrode, in this case, would be comparable to a deeper recessed nanodiscs electrode with the same radius. Numerical simulations on the effect of the scan rate on the output current densities responses of the nanoholes microarrays were performed and the shapes of the voltammograms at different experimental time scales were predicted. Finally, this work provided guidance toward the potential implementation of practical electrochemical devices and sensors based on r-NRE microarrays.

4.5 ACKNOWLEDGMENTS

We would like to thank Mr. Adam Schuetze for valuable discussions about the nanoarrays fabrication and for his assistance with the fabrications and Z-contrast imaging. We also thank Dr. Elaine Humphrey for her aid in collecting the Z-contrast images. We acknowledge CMC Microsystems (Kingston, ON, Canada) for providing access to the COMSOL Multiphysics. We would like to thank WestGrid and Compute Canada for providing computational resources. This work was supported by the NSERC Discovery Grant and the NSERC CREATE Programs

4.6 REFERENCES

1. Arrigan, D. W. M., Nanoelectrodes, Nanoelectrode Arrays and Their Applications. *Analyst (Cambridge, U. K.)* **2004**, *129*, 1157-1165.
2. Fernandez, J. L.; Wijesinghe, M.; Zoski, C. G., Theory and Experiments for Voltammetric and Secm Investigations and Application to Orr Electrocatalysis at Nanoelectrode Ensembles of Ultramicroelectrode Dimensions. *Anal. Chem.* **2015**, *87*, 1066-1074.
3. Henstridge, M. C.; Compton, R. G., Mass Transport to Micro- and Nanoelectrodes and Their Arrays: A Review. *Chemical Record* **2012**, *12*, 63-71.
4. Liu, Y.; Sairi, M.; Neusser, G.; Kranz, C.; Arrigan, D. W. M., Achievement of Diffusional Independence at Nanoscale Liquid Liquid Interfaces within Arrays. *Anal. Chem.* **2015**, *87*, 5486-5490.
5. Murray, R. W., Nanoelectrochemistry: Metal Nanoparticles, Nanoelectrodes, and Nanopores. *Chem. Rev.* **2008**, *108*, 2688-2720.
6. Bagal-Kestwal, D.; Karve, M. S.; Kakade, B.; Pillai, V. K., Invertase Inhibition Based Electrochemical Sensor for the Detection of Heavy Metal Ions in Aqueous System: Application of Ultra-Microlelectrode to Enhance Sucrose Biosensor's Sensitivity. *Biosensors & Bioelectronics* **2008**, *24*, 657-664.
7. Li, F.; Xue, M.; Ma, X.; Zhang, M.; Cao, T., Facile Patterning of Reduced Graphene Oxide Film into Microelectrode Array for Highly Sensitive Sensing. *Anal. Chem.* **2011**, *83*, 6426-6430.
8. Conyers, J. L.; White, H. S., Electrochemical Characterization of Electrodes with Submicrometer Dimensions. *Anal. Chem.* **2000**, *72*, 4441-4446.
9. Baker, W. S.; Crooks, R. M., Independent Geometrical and Electrochemical Characterization of Arrays of Nanometer-Scale Electrodes. *J. Phys. Chem. B* **1998**, *102*, 10041-10046.
10. Hirota, K.; Tajima, K.; Hashimoto, K., Facile Preparation of Nanoelectrode Ensembles Using Amphiphilic Block Copolymer Film. *Langmuir* **2005**, *21*, 11592-11595.
11. Krishnamoorthy, K.; Zoski, C. G., Fabrication of 3d Gold Nanoelectrode Ensembles by Chemical Etching. *Anal. Chem.* **2005**, *77*, 5068-5071.
12. Kang, S.; Nieuwenhuis, A.; Mathwig, K.; Mampallil, D.; Lemay, S. G., Electrochemical Single-Molecule Detection in Aqueous Solution Using Self-Aligned Nanogap Transducers. *Acs Nano* **2013**, *7*, 10931-10937.
13. Lemay, S. G.; Kang, S.; Mathwig, K.; Singh, P. S., Single-Molecule Electrochemistry: Present Status and Outlook. *Acc. Chem. Res.* **2013**, *46*, 369-377.
14. Lanyon, Y. H.; Arrigan, D. W. M., Recessed Nanoband Electrodes Fabricated by Focused Ion Beam Milling. *Sens. Actuators, B* **2007**, *121*, 341-347.
15. Godino, N.; Borrise, X.; Xavier Munoz, F.; Javier del Campo, F.; Compton, R. G., Mass Transport to Nanoelectrode Arrays and Limitations of the Diffusion Domain Approach: Theory and Experiment. *J. Phys. Chem. C* **2009**, *113*, 11119-11125.
16. Zaino, L. P.; Ma, C. X.; Bohn, P. W., Nanopore-Enabled Electrode Arrays and Ensembles. *Microchimica Acta* **2016**, *183*, 1019-1032.
17. Lanyon, Y. H.; De Marzi, G.; Watson, Y. E.; Quinn, A. J.; Gleeson, J. P.; Redmond, G.; Arrigan, D. W. M., Fabrication of Nanopore Array Electrodes by Focused Ion Beam Milling. *Anal. Chem.* **2007**, *79*, 3048-3055.

18. Brolo, A. G.; Gordon, R.; Leathem, B.; Kavanagh, K. L., Surface Plasmon Sensor Based on the Enhanced Light Transmission through Arrays of Nanoholes in Gold Films. *Langmuir* **2004**, *20*, 4813-4815.
19. Escobedo, C.; Brolo, A. G.; Gordon, R.; Sinton, D., Flow-through Vs Flow-Over: Analysis of Transport and Binding in Nanohole Array Plasmonic Biosensors. *Anal. Chem.* **2010**, *82*, 10015-10020.
20. Menezes, J. W.; Ferreira, J.; Santos, M. J. L.; Cescato, L.; Brolo, A. G., Large-Area Fabrication of Periodic Arrays of Nanoholes in Metal Films and Their Application in Biosensing and Plasmonic-Enhanced Photovoltaics. *Adv. Funct. Mater.* **2010**, *20*, 3918-3924.
21. Monteiro, J. P.; Carneiro, L. B.; Rahman, M. M.; Brolo, A. G.; Santos, M. J. L.; Ferreira, J.; Girotto, E. M., Effect of Periodicity on the Performance of Surface Plasmon Resonance Sensors Based on Subwavelength Nanohole Arrays. *Sens. Actuators, B* **2013**, *178*, 366-370.
22. Monteiro, J. P.; de Oliveira, J. H.; Radovanovic, E.; Brolo, A. G.; Girotto, E. M., Microfluidic Plasmonic Biosensor for Breast Cancer Antigen Detection. *Plasmonics* **2016**, *11*, 45-51.
23. Sinton, D.; Gordon, R.; Brolo, A. G., Nanohole Arrays in Metal Films as Optofluidic Elements: Progress and Potential. *Microfluidics and Nanofluidics* **2008**, *4*, 107-116.
24. Valsecchi, C.; Jones, T.; Wang, C.; Lochbihler, H.; Menezes, J. W.; Brolo, A. G., Low-Cost Leukemic Serum Marker Screening Using Large Area Nanohole Arrays on Plastic Substrates. *Acs Sensors* **2016**, *1*, 1103-1109.
25. Ebbesen, T. W.; Lezec, H. J.; Ghaemi, H. F.; Thio, T.; Wolff, P. A., Extraordinary Optical Transmission through Sub-Wavelength Hole Arrays. *Nature (London, U. K.)* **1998**, *391*, 667-669.
26. Valsecchi, C.; Brolo, A. G., Periodic Metallic Nanostructures as Plasmonic Chemical Sensors. *Langmuir* **2013**, *29*, 5638-5649.
27. Atighilorestani, M.; dos Santos, D. P.; Jaimes, R.; Rahman, M. M.; Temperini, M. L. A.; Brolo, A. G., Electrochemical Control of Light Transmission through Nanohole Electrode Arrays. *Acs Photonics* **2016**, *3*, 2375-2382.
28. Ferreira, J.; Santos, M. J. L.; Rahman, M. M.; Brolo, A. G.; Gordon, R.; Sinton, D.; Girotto, E. M., Attomolar Protein Detection Using in-Hole Surface Plasmon Resonance. *J. Am. Chem. Soc.* **2009**, *131*, 436-+.
29. Howell, J. O.; Kuhr, W. G.; Ensman, R. E.; Wightman, R. M., Background Subtraction for Rapid Scan Voltammetry. *J. Electroanal. Chem.* **1986**, *209*, 77-90.
30. http://www.comsol.com.
31. Godino, N.; Borrise, X.; Munoz, F. X.; del Campo, F. J.; Compton, R. G., Mass Transport to Nanoelectrode Arrays and Limitations of the Diffusion Domain Approach: Theory and Experiment. *J. Phys. Chem. C* **2009**, *113*, 11119-11125.
32. Dickinson, E. J. F.; Streeter, I.; Compton, R. G., Theory of Chronoamperometry at Cylindrical Microelectrodes and Their Arrays. *J. Phys. Chem. C* **2008**, *112*, 11637-11644.
33. Menshykau, D.; Compton, R. G., The Influence of Electrode Porosity on Diffusional Cyclic Voltammetry. *Electroanalysis* **2008**, *20*, 2387-2394.
34. Davies, T. J.; Compton, R. G., The Cyclic and Linear Sweep Voltammetry of Regular and Random Arrays of Microdisc Electrodes: Theory. *J. Electroanal. Chem.* **2005**, *585*, 63-82.
35. Guo, J.; Lindner, E., Cyclic Voltammograms at Coplanar and Shallow Recessed Microdisk Electrode Arrays: Guidelines for Design and Experiment. *Anal. Chem.* **2009**, *81*, 130-138.
36. Lavacchi, A.; Bardi, U.; Borri, C.; Caporali, S.; Fossati, A.; Perissi, I., Cyclic Voltammetry Simulation at Microelectrode Arrays with Comsol Multiphysics (R). *J. Appl. Electrochem.* **2009**, *39*, 2159-2163.

37. Streeter, I.; Fietkau, N.; del Campo, J.; Mas, R.; Munoz, F. X.; Compton, R. G., Voltammetry at Regular Microband Electrode Arrays: Theory and Experiment. *J. Phys. Chem. C* **2007**, *111*, 12058-12066.
38. Dickinson, E. J. F.; Streeter, I.; Compton, R. G., Chronoamperometry and Cyclic Voltammetry at Conical Electrodes, Microelectrodes, and Electrode Arrays: Theory. *J. Phys. Chem. B* **2008**, *112*, 4059-4066.
39. Beriet, C.; Ferrigno, R.; Girault, H. H., Simulation of the Chronoamperometric Response of a Regular Array of Micro-Disc Electrodes. *J. Electroanal. Chem.* **2000**, *486*, 56-64.
40. Lee, H. J.; Beriet, C.; Ferrigno, R.; Girault, H. H., Cyclic Voltammetry at a Regular Microdisc Electrode Array. *J. Electroanal. Chem.* **2001**, *502*, 138-145.
41. Amatore, C.; Fosset, B., Equivalence between Microelectrodes of Different Shapes: Between Myth and Reality. *Anal. Chem.* **1996**, *68*, 4377-4388.
42. Mahon, P. J.; Feldberg, S. H. W., Simulations of Cyclic Voltammetric and Chronoamperometric Electrode Responses at a Disk Electrode Using Combinations of Spherical and Cylindrical Electrode Geometries. *Langmuir* **2007**, *23*, 10380-10388.
43. Davies, T. J.; Ward-Jones, S.; Banks, C. E.; del Campo, J.; Mas, R.; Munoz, F. X.; Compton, R. G., The Cyclic and Linear Sweep Voltammetry of Regular Arrays of Microdisc Electrodes: Fitting of Experimental Data. *J. Electroanal. Chem.* **2005**, *585*, 51-62.
44. Henstridge, M. C.; Dickinson, E. J. F.; Compton, R. G., Mass Transport to and within Porous Electrodes. Linear Sweep Voltammetry and the Effects of Pore Size: The Prediction of Double Peaks for a Single Electrode Process. *Russ. J. Electrochem.* **2012**, *48*, 629-635.
45. Oldham, K. B., A Hole Can Serve as a Microelectrode. *Anal. Chem.* **1992**, *64*, 646-651.
46. Bartlett, P. N.; Taylor, S. L., An Accurate Microdisc Simulation Model for Recessed Microdisc Electrodes. *J. Electroanal. Chem.* **1998**, *453*, 49-60.

Chapter 5 : Recessed Gold Nanoring-Ring Microarray Electrodes

The following chapter is adapted from: M. Atighilorestani, and A. G. Brolo, Recessed Gold Nanoring-Ring Microarray Electrodes, Anal. Chem., http://pubs.acs.org/doi/abs/10.1021/acs.analchem.7b01943 The supporting information has been embedded within the text.

A 6 × 6 recessed Au nanoring-ring electrodes microarray was fabricated over a glass substrate using focused ion beam milling. The electrochemical responses of this device to a reversible redox pair were examined. In redox cycling mode, the lower ring acts as a generator and the upper ring as a collector. High collection efficiencies (close to 100 %) and amplification factors (~ 3.5) were achieved with this configuration. The redox-cycling behavior of this device was modeled using COMSOL Multiphysics®. The effects of scaling the geometric parameters of the electrodes (ring height and radius), potential sweep rates, and inter-electrode gap distance were evaluated through simulations. The computational models showed that the attainable limiting current depends strongly on the ring radius, while it is almost independent of the ring height variations (for a particular inter-electrode gap). The effects of the scan rate and inter-electrode gap distance on the electrochemical characteristics of the device are also discussed. This study provides insights on the influence of the geometry on the performance of these arrays, which should guide the development of future applications.

5.1 Introduction

Micro/nanoelectrode systems have been widely studied due to their potential for electroanalytical and biosensing applications[1-2]. They display smaller capacitive charging currents, smaller ohmic drop, enhanced mass transport, faster electrochemical response, higher current density, and higher signal-to-noise ratio than that of macroelectrode systems[3-5]. However, the low current response is the main disadvantage of using a single micro/nanoelectrode. This challenge can be overcome by employing arrays or ensembles of micro/nanoelectrodes operating in parallel.[3, 6-8] Moreover, redox cycling is an efficient approach to enhance the sensitivities, limits of detection and steady-state currents of micro/nanoelectrode systems.[4, 9] Redox cycling requires two working electrodes (or two arrays of working electrodes): a generator and a collector electrode. The electrodes should be located close to each other and individually polarized at different potentials. In dual mode operation, a redox species in solution undergo a reversible or quasi-reversible oxidation (or reduction) at the generator electrode. The oxidation (or reduction) product diffuses to the collector electrode, and it is converted back to the starting material. The regenerated species, formed on the collector electrode, then diffuses back to the generator where it is again electrolyzed. This cycle continues as long as the electrodes are properly polarized. Therefore, the same redox-active molecule, contributes multiple electrons to the measured current, leading to an enhancement of electrochemical response from both generator and collector electrodes.[4-5, 9-10]

The redox cycling approach has been used for a wide variety of applications. They include measurements of reaction kinetics[4, 11], diffusion studies[12], in vitro analysis of dopamine in the presence of ascorbic acid[13-14], development of DNA biosensor[15], detection of the reaction intermediates[16], development of electrochemical sensors[17], and application in bioassays[18]. The performance of redox cycling systems is commonly evaluated using two parameters[19]: the

collection efficiency (η) and amplification factor (A_f). η is defined as the ratio between the collector current, i_{CE}, and the generator current, $i_{GE_{cycl}}$, during redox cycling (dual mode)[4]:

$$\eta = -\frac{i_{CE}}{i_{GE_{cycl}}} \qquad \text{Eq. 5-1}$$

And the amplification factor, A_f, is given as the ratio between the generator current in dual mode, $i_{GE_{cycl}}$, and the generator current in single mode (in the absence of redox cycling), i_{GE}:

$$A_f = \frac{i_{GE_{cycl}}}{i_{GE}} \qquad \text{Eq. 5-2}$$

The collector electrode is left at the open circuit during single mode operation, while the potential of the generator electrode is biased in the same manner as in the dual mode. The performance of redox cycling systems depends on the geometry and design of the electrodes. Improved performance is obtained by decreasing the electrodes size as well as the inter-electrode spacing (interelectrode gap). In these conditions (smaller electrodes and gap), fewer redox-active molecules escape from the redox cycling trap into the bulk solution [9, 20-21]. A broad range of redox cycling systems, with different geometries, has been proposed and investigated over the years. These include dual cylinders[22], dual discs[23-24], dual bands[25-26], triple bands[27-28], and the interdigitated band electrodes (IBEs)[4-5, 29-31]. IBEs are a natural evolution from the dual band redox cycling systems that show greater sensitivities. The performance of IBEs is improved by decreasing the width of the bands, decreasing the interelectrode gap between the generator and the collector [5], and increasing the height of the bands[32]. Planar interdigitated ring electrodes (IREs)[33-35] are an important variation of the IBEs. Compton et al. demonstrated that IREs with small radii show larger current enhancements in comparison to IBEs, due to the higher radial diffusion and

more efficient mass transport [33]. Important alternatives to the planar interdigitated configurations are vertically separated electrodes. A dielectric (insulating) material defines the interelectrode gap between the generator and collector electrodes. The gap can be simply tuned by varying the thickness of the dielectric layer through thin film deposition [36]. Vertically separated electrodes provide several advantages over planar electrodes, including highly improved collection efficacy and signal amplification, due to the more efficient trapping of redox active species[36, 37] . In addition, their three-dimensional nature makes them ideal for lab-on-a-chip integration[37]. The recessed ring-disk electrodes array is one example of vertically aligned generator-collector electrode systems that has been extensively studied [37-40]. In this geometry, the disc electrodes, acting as generators, are completely surrounded by the ring electrodes (acting as collector electrodes), leading to a very high collection efficiencies.

Very recently, Bohn et al.[41] have proposed a novel redox cycling system structure: the recessed Au nanoring-ring electrodes array (Au-NRRA), shown schematically in Figure 5-1. They experimentally demonstrated that the collection efficacy of this new configuration is ~100 % [41]. The Au-NRRA is derived from the recessed nanoring-disc electrodes array configuration, but the identical electrode geometry in the Au-NRRA helps to improve further the collection efficiency. Herein, a more detailed understanding of the main characteristics of the Au-NRRA is provided through numerical simulations using COMSOL Multiphysics®. The model was first validated by comparing the results with experimental data. The results presented here provide valuable information for the future development of applications of Au-NRRA in several areas ranging from fundamental studies of electrochemical mechanisms to integrated lab-on-a-chip detection systems.

5.2 EXPERIMENTAL SECTION

5.2.1 Chemicals and Instrumentation

Potassium ferricyanide and potassium chloride were purchased from Caledon Laboratories. All solutions were prepared using ultrapure water (18.2 MΩ.cm) obtained from NANO pure Diamond TM deionization system (Barnstead). Prior to measurements, the solution was purged with Argon gas for 30 minutes. Electrochemical measurements were carried out with two Gamry Reference 600 potentiostats connected to each other. Data acquisition of the two potentiostats was synchronized using scripts made available by the manufacturer (Gamry Instruments, USA). A platinum wire was used as a pseudo-reference electrode. Another platinum wire served as a counter electrode. Notice that the experiments could have been performed using only one Pt wire. However, we chose to keep a four (or three)-electrode configuration to be consistent with the previous works in this area. All the experiments were performed after an equilibration time of 10 s and in a Faraday cage.

5.2.2 Recessed Nanoring-Ring Microarray's Geometry and Fabrication

Figure 5-1a shows a schematic cross-sectional diagram of 6×6 Au-NRRA arranged in a square lattice. Each nanohole contains two nanoring electrodes that are electrically isolated and arranged vertically relative to each other. Nanohole structures in the array are formed by milling through a first insulating layer, recess depth, l, (SiO_2 or SiN_x, 150 nm); and a first metal layer, upper ring electrode, h_c, (Au, 50 nm); down to a second insulating layer, insulating gap, g, (SiO_2 or SiN_x ,

150 nm); and a second metal layer, lower ring electrode, h_g, (Au , 50 nm), using FIB technique. The upper and lower ring heights (h_c and h_g) and the gap thickness (g) could all, in principle, be modified while maintaining the same array footprint. Here the heights of both lower and upper ring were the same, 50 nm. The details of the fabrication process are given in Figure 5-2 and Figure 5-3.

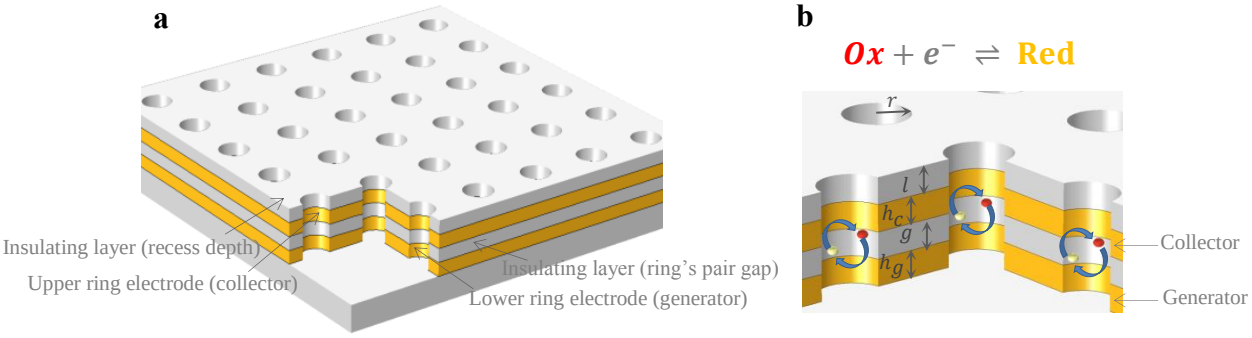

Figure 5-1. Schematic representations of (a) the 6×6 recessed generator-collector ring-ring microarray geometry, and b) the redox cycling process. Hole radius, r, recessed depth, l, collector height, h_c, nanoring's pair gap, g, and generator height, h_g, are indicated (b).

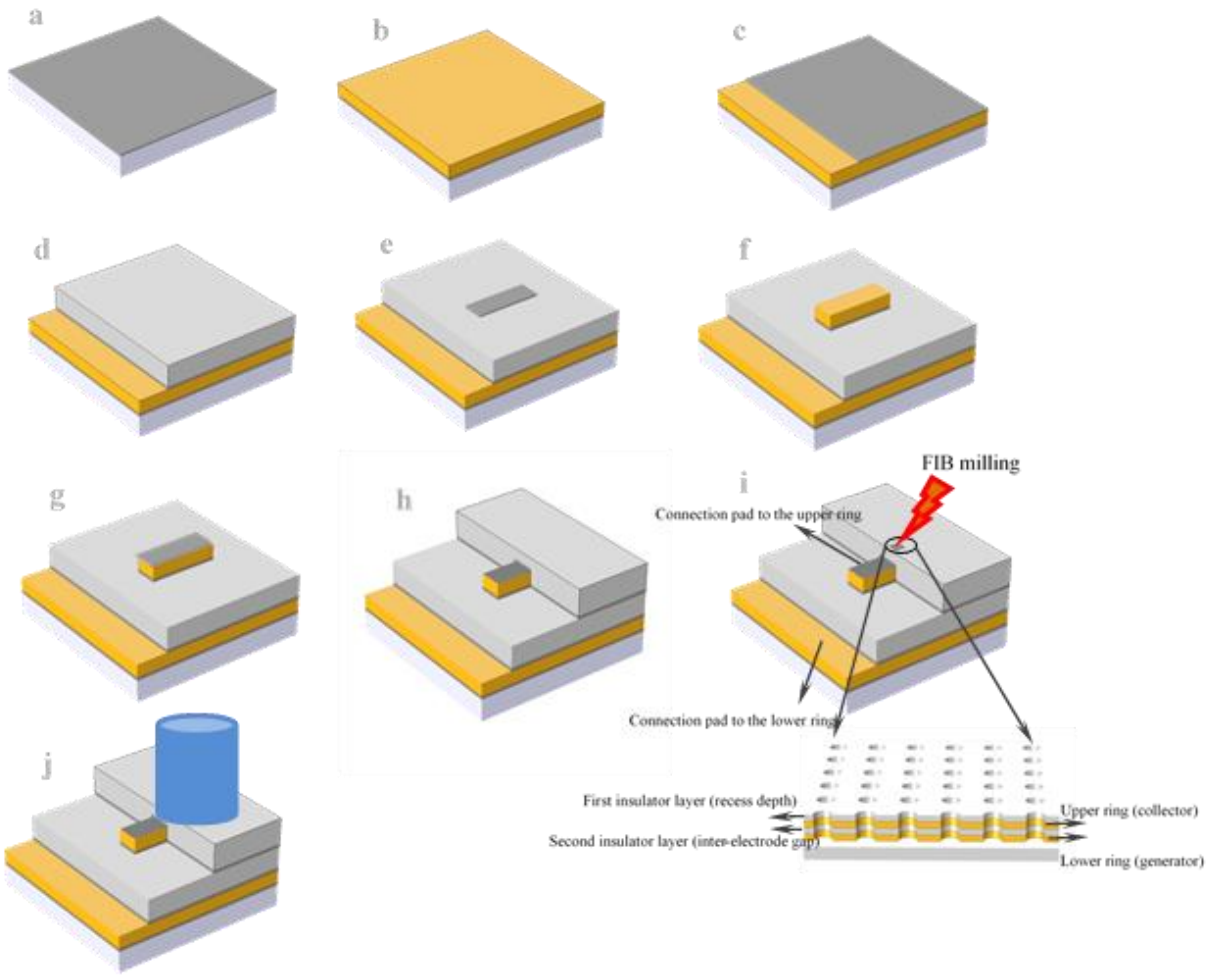

Figure 5-2**.** Schematic representations of the Au-NRRA fabrication process (a-j). All the layers in the Ti (7nm) / Au (50 nm) / Ti (7 nm) / SiO_2 or SiN_x (150 nm) / Ti (7 nm) / Au (50 nm) / Ti (7 nm) /SiO_2 or SiN_x (150 nm) stack were sputtered using Mantis® QUBE sputter deposition system, except for the SiN_x layer which was deposited using plasma-enhanced chemical vapor deposition method. Dimensions are not down to scale.

Note that, in contrast to the fabrication process described in ref [41] (which was a combination of standard photolithography, layer-by-layer deposition, and FIB milling), our fabrication process only included the layer-by-layer deposition steps and FIB milling. In the previous study[41], the areas

of the electrodes and connection pads were defined using standard photolithography technique. Instead, we have designated these features simply by defining those specified areas using Teflon tape masks during the depositions. In short, our fabrication process was simpler and included fewer fabrication steps in comparison with the previous study[41]. It is important to emphasize that standard photolithography involves several steps, including photoresist spin coating, baking the samples to cure the photoresist, illuminate the photoresist through a photomask to pattern the sample and the lift-off step. By eliminating the photolithography, we then significantly simplified the fabrication. Moreover, our process resulted in very clean samples, since we did not have to be concerned with photoresist residues.

a) A 7 nm Ti was sputtered over the whole cleaned (~ 9 mm × 9 mm) glass slides. The Ti layer was used to improve the adhesion of subsequent gold layer onto the glass substrates.
b) A 50 nm thick gold film was then sputtered over the Ti adhesion layer on the entire glass slides.
c) Once the gold was deposited, one edge of the glass substrates was wrapped with Teflon tape to protect the metal film on that area. This protected region was later used as the electrical contact pad on the first gold layer (lower nanoring electrodes). Next, a 7 nm Ti adhesion film was sputtered.
d) Subsequently, a 150 nm thick SiO_2 (or SiN_x) layer was sputtered in the presence of oxygen (Ar: O2 - 4: 1 and Flow Rate 8 sccm (standard cubic centimeter per minute)), to improve its quality. This SiO_2 provided electrical isolation and also separation (gap, g) between the lower and upper nanoring electrodes in the final configuration.
e) After the deposition of the first passivation layer, all the edges of the glass substrates were wrapped with Teflon tape and only a small rectangular area (~5 mm × 1 mm) in the middle

was left unprotected. A 7 nm thick Ti adhesion layer was then sputtered over the defined area by the Teflon tape.

f) Subsequently, the second Au layer (50 nm thick) was sputtered over the Ti layer on the designated region by the Teflon tape.

g) Followed by sputtering of 7 nm adhesion Ti layer over the gold film.

h) After this step, half side of the substrates was wrapped with the Teflon tape before the sputtering of the final 150 nm thick SiO_2 passivation layer. In this case, the Teflon tape protected the metal film regions on the substrates' edge, and the middle part served later as the electrical contact pads to the first and second gold layers, respectively. The final SiO_2 layer was then sputtered in the presence of the oxygen (Ar: O2 - 4: 1 and Flow Rate 8 sccm (standard cubic centimeter per minute)), to improve its isolation quality. This layer was provided the electrical isolation to the second gold layer (upper nanoring electrodes) and also defined the upper ring electrodes recessed depth on the final device.

i) Finally, the recessed nanoring-ring electrodes array (3.3 μm × 3.3μm) with r = 150 nm and the interelectrode distance of 600 nm were fabricated using FIB on the Ti (7nm) / Au (50 nm) / Ti (7 nm) / SiO_2 (150 nm) / Ti (7 nm) / Au (50 nm) / Ti (7 nm) /SiO_2 (150 nm) stack in the middle of the substrate.

j) An NMR tube (which was cut to less than 8 mm length) was fixed over the Ti/Au /Ti/SiO_2/Ti /Au/Ti /SiO_2 stack containing the recessed nanoring-ring array with a dielectric epoxy and served as the electrochemical cell.

5.2.3 Optimization of the FIB fabrication parameters using Z-contrast images

We followed the same procedure for the fabrication of the 6×6 Au-NRRA as those we explained in our previous work[42]. Briefly, the FIB cut were defined with the following parameters: dwell time in microseconds (i.e. the amount of time the beam stays at a particular pixel point as it raster across the pattern) and N (the number of raster passes). Only the numbers of N were increased from array to array and the dwell time was kept constant. Next, the Z-contrast imaging (also called backscattering imaging) was used to find out which FIB conditions were the proper ones for the fabrication of Au-NRRA. Z-contrast imaging gives the elemental information in contrast to the SEM image which provides only the topographical information. In Z-contrast imaging the secondary electrons are filtered out, and the image shows the presence of different elements.

In contrast to our previous work[42], in which we had to be very careful to find the proper parameters for the fabrication of the disc electrodes. (We had to stop cutting right after the appearance of the Au-disc). Here, the primary concern was to mill deep enough, all the way through all the four layers of insulator/metal/insulator/metal and to reach the glass substrate. (Here, reaching the glass substrate was a proper indication that we have cut deep enough, though all four layers). Z-contrast imaging allowed us to achieve this goal with confidence. Since the Z-contrast imaging shows the different materials used in the fabrication (SiNx as the first (l) and second (g) insulator layers, Au as the first and second metal layers, and the glass substrate) in different colors.

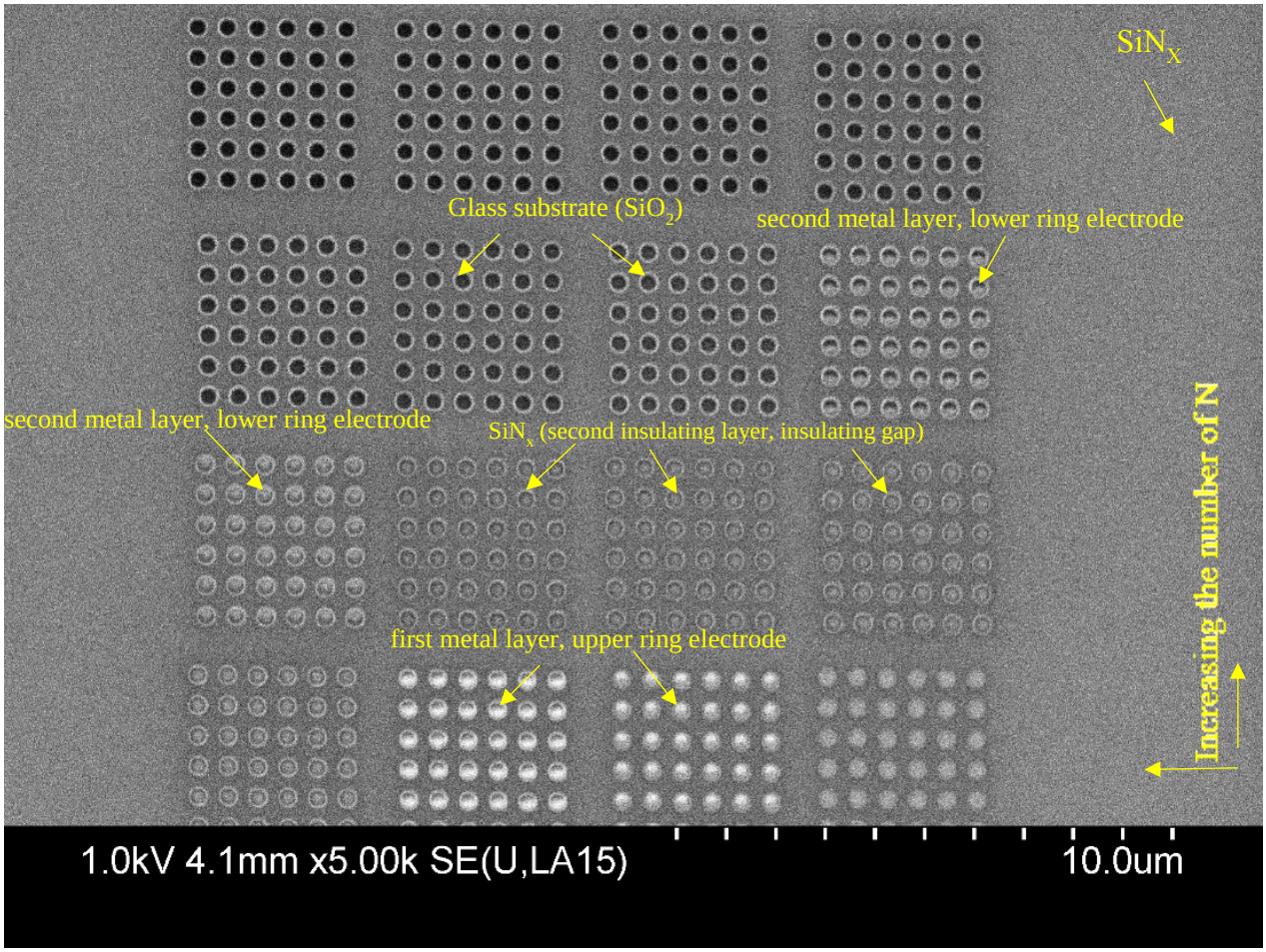

Figure 5-3**.** Optimization of the FIB fabrication parameters using Z-contrast images.

5.2.4 Simulations Details

We have performed both 3D and 2D simulations on the 6×6 Au-NRRA operating in either single or dual mode, respectively. Simulations were carried out using a commercial finite-element software package (COMSOL Multiphysics® ver. 5.2). The 2D simulations were run on our PC workstation with 32.0 GB RAM (Lenovo Thinkstation), and the 3D simulations were run on WestGrid and Compute Canada clusters. In all the simulation studies, the recess depth (the first insulator layer's thickness), *l*, and the nanoring's pair gap (the second insulating layer), *g*, were

kept constant, 150 nm. The height of both upper, h_c, and lower, h_g, ring electrodes was varied from 25 nm to 100 nm, and the nanoholes' radius, *r*, was varied from 100 nm to 200 nm to study the effect of these parameters on the array performance. The active area of the upper and lower nanorings was kept identical to each other in all the simulation studies. In the redox cycling studies, depicted in Figure 5-1b, the lower nanoring electrodes act as generator electrode at which the potential was swept between 0.3 and -0.3 V, at a sweep rate of 0.05 to 1000 Vs^{-1}, while, the potential of the upper nanoring electrodes, acting as the collector electrodes, was held at a constant oxidizing potential, 0.3 V. For the case without redox cycling, single mode, the upper ring was assumed to be an insulator layer. Therefore the cyclic voltammetry simulations were conducted on an array of nanoholes containing only the recessed lower ring electrodes, Figure 5-4. The recess depth of the nanoring electrodes in single mode corresponds to the depth of the lower ring in dual mode, which is the summation of the thicknesses of the top insulating layer, upper ring height and the gap between the rings pair in the case of dual mode, Figure 5-4, to accurately investigate the extent of redox cycling effect on the current respond of the lower ring in single and dual modes (the current amplification factor). For the single mode, the simulations have been performed in 3D domains; detailed information on the simulation is given in our previous work[42].

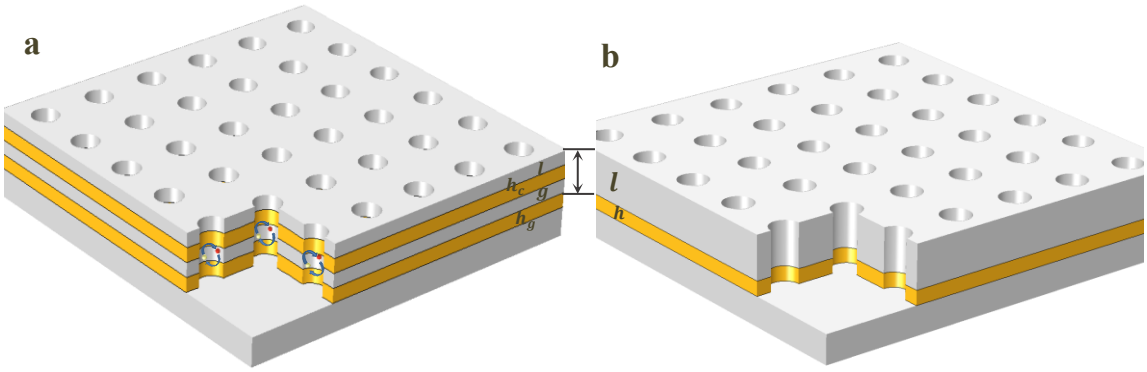

Figure 5-4**.** Schematic representations of a) 6×6 recessed generator-collector nanoring-ring microarray b) 6×6 recessed nanorings microarray (recessed nanoring-ring microarray operating in single mode). Recessed depth, l, collector height, h_c, nanoring's pair gap, g, generator height, h_g, and ring height, h, are indicated in Figures. Magnitude of the recessed depth, l, in 6×6 recessed nanorings microarray (recessed nanoring-ring microarray operating in single mode) corresponds to the summations of the values of l and h_c and g in Figure 5-4a.

Briefly, Figure 5-5a shows the 2D slice concentration profile of species O on the first row of a 6×6 recessed nanorings electrode array. Figure 5-5a illustrates that recessed nanorings array at single mode operation experiences a radial diffusion over the whole array due to the small size of the entire array when the diffusion zones among the adjacent nanoholes extremely overlap. As a result, the whole array behaves like a single microelectrode with the same size of the array with a steady state response. Considering the overall radial shape of the diffusion layer over the whole array the contribution of the each nanohole electrode to the overall response of the array is different from each other, and it very depends on where the nanohole is located in the array. Therefore, the 2D simulation base on the diffusion domain approximation[43] cannot provide satisfactory results and a 3D simulation is required to be performed in order to study the voltammetric response of the micrometer-sized array6 accurately. Detailed information on the simulation is given in our previous report.[42]

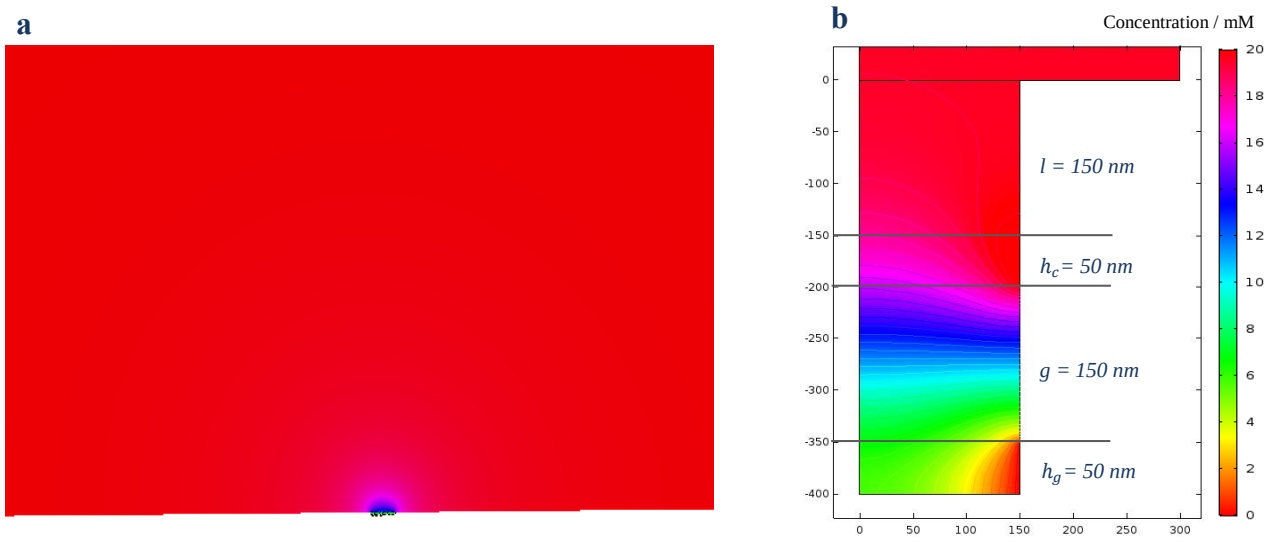

Figure 5-5**.** a) 2D slice concentration profile for a 6 × 6 recessed ring array, no redox cycling. (the 6×6 Au-NRRA configuration operating in single mode). b) Simulated concentration profile for a 6×6 Au-NRRA operating in redox cycling mode. The hole radius (r = 150 nm), ring height (h = 50 nm), scan rate (v = 0.05 Vs^{-1}), interelectrode distance (600 nm), were the same for both array. The recessed depth of ring electrodes in a) was 350 nm, which coincide with the recessed depth of lower ring in ring-ring geometry, Figure 5-4. The recessed depth was (l = 150 nm), and ring gap was (g = 150 nm) in the ring-ring array geometry. The concentration profiles were obtained for the species O at the potential in which the steady-state current was established, on the forward scan.

In dual mode (redox cycling mode), the potential of the lower ring (generator) was scanned between 0.3 and -0.3 V, and the upper ring (collector) was held at a fix oxidizing potential, 0.3 V, such that redox species generated at the lower electrode was reoxidized to starting material at the upper electrode. The cycling of the redox species between the recessed ring and ring electrodes totally eliminated the overlap of the diffusional fields of adjacent nanoholes (containing ring-ring pair) Figure 5-5b. Since the nanoholes (containing ring-ring generator-collector pair) electrodes are diffusionally independent, based on the diffusion domain approximation[43] the response of only one ring-ring pair needs to be simulated, Figure 5-6. Furthermore, the cylindrical symmetry of the electrodes allowed the simulation of half of the nanorings pair electrodes. Hence, the redox cycling

simulations at the ring-ring generator-collector pair electrodes were carried out over two-dimensional domains.

The cyclic voltammetry was performed at the lower ring electrode (generator), and the simulation of a simple reversible redox reaction was considered at this electrode accordingly:

$$A + \bar{e} \rightleftharpoons B \qquad \text{Eq. 5-3}$$

while the upper ring electrode (collector) was subjected to a fixed potential to oxidized the species B back to its starting form:

$$B - \bar{e} \rightarrow A \qquad \text{Eq. 5-4}$$

Where A and B are both soluble species, which are $Fe(CN)_6^{3-}$ and $Fe(CN)_6^{4-}$ respectively in this current study, but only species A is supposed to be present in the solution with an initial bulk concentration of 20 mM.

The rate of electron transfer is given by the Bulter-Volmer kinetics:

$$D_A \frac{\partial c_A}{\partial r}\Big|_{-el} = (k_f c_A - k_b c_B)\Big|_{el} \qquad \text{Eq. 5-5}$$

Where $D_A \frac{\partial c_A}{\partial r}\Big|_{el}$ is the diffusional flux of species A to the electrode surface, and k_f and k_b, the forward and reverse reaction rate constants, respectively, and they are described as:

$$k_f = k^0 \exp\left(-\frac{\alpha F}{RT}\left(E - E^{\acute{0}}\right)\right) \qquad \text{Eq. 5-6}$$

$$k_b = k^0 \exp\left(\frac{(1-\alpha)F}{RT}\left(E - E^{\acute{0}}\right)\right) \qquad \text{Eq. 5-7}$$

k^0 is the heterogeneous rate constant for the redox couple, taken as $10^{-2}\ ms^{-1}$, and $E^{\acute{0}}$ is the formal electrode potential, set at $0.25\ V$.[6] E is the potential applied to the electrode. α is the effective transfer coefficient, assumed to be 0.5. The temperature, T, fixed at $298\ K$. R and F are the universal gas constant the Faraday's constant, respectively

The diffusion of the redox species is characterized by the following equation:

$$\frac{\partial c}{\partial t} = \nabla.(D\nabla c) \qquad \text{Eq. 5-8}$$

Where c is the concentration and D is the diffusion coefficient (assumed equal for both species), set as $6.5 \times 10^{-10} m^2 s^{-1}$.[6] This equation assumes that the transport of O and R is solely controlled by diffusion, a valid approximation, considering an excess of supporting electrolyte is present so that migration is negligible. The bulk solution condition is assigned at the outer boundary of the model, at a distance $6\sqrt{t_{tot}D}$, from the electrode surface where $t_{tot}$the total simulation time is. Beyond this, the influence of the domain size on the simulation result is not important

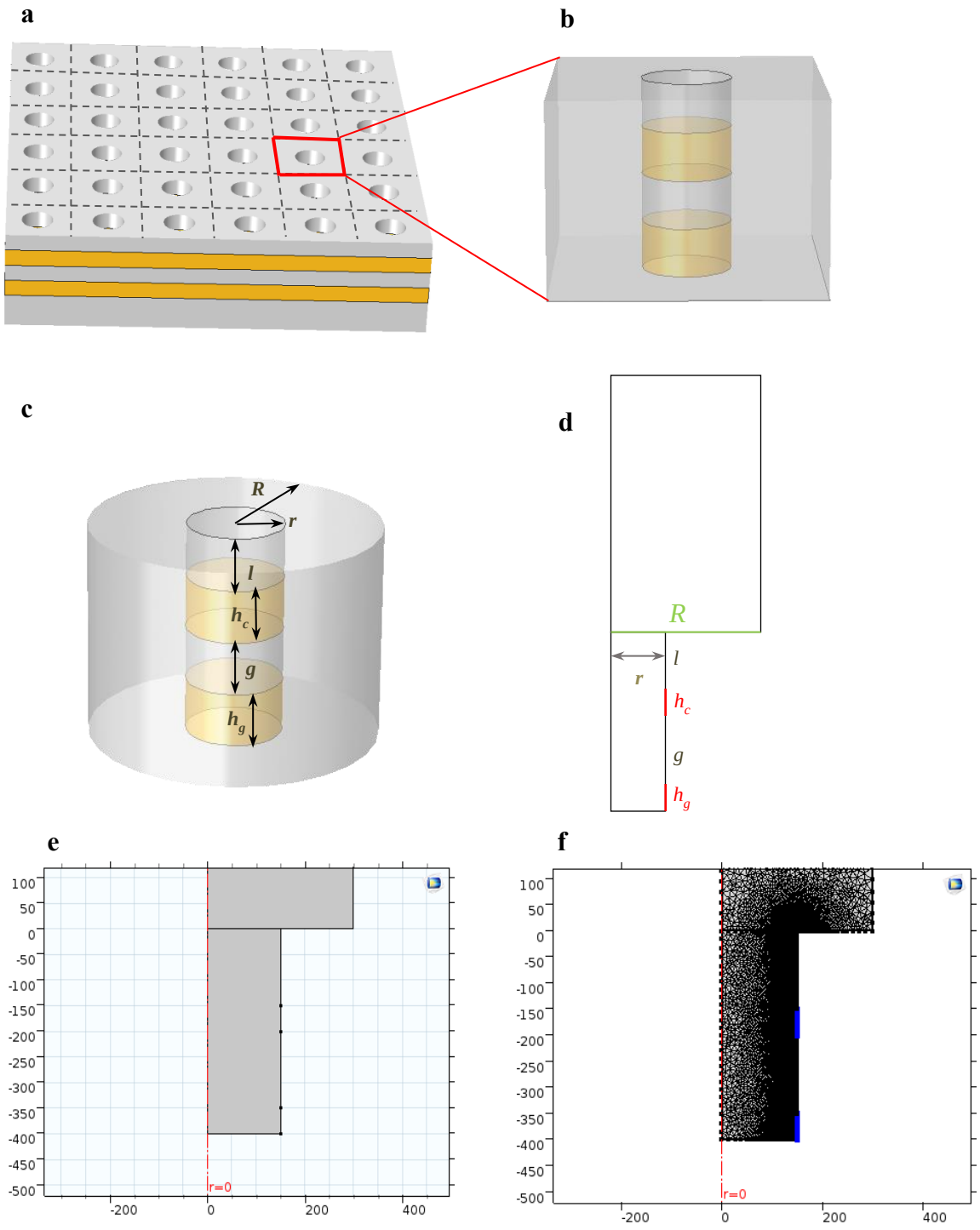

Figure 5-6. a) Schematic representation of the unit cell for a 6×6 Au-NRRA; b) individual unit cell in Cartesian coordinates; c) tantamount diffusion domain approximation in cylindrical coordinates; and d) sketch of the 2D simulation space used for the simulation of recessed nanoring-

ring array performance operating in redox cycling mode. [39, 43] (2 × R = interelectrode distance); and e) close-up 2D model of the simulation space and f) its meshing.

5.3 RESULTS AND DISCUSSION

5.3.1 Electrochemical investigation at recessed nanoring-rings microarray

The experimental and simulated cyclic voltammetric curves for a 6×6 Au-NRRA ($r = 150\,nm, g = l = 150\,nm$) for both single and dual mode operation are shown in Figure 5-7a and Figure 5-7b, respectively. The surface areas of both lower and upper ring electrodes were the same ($h_c = h_g$ = 50 nm). In single mode, the lower rings were swept at 0.05 Vs^{-1} and the upper ring electrodes were considered as an insulator layer. This means that, in single mode operation, the cyclic voltammetry simulation was performed on a 6×6 nanorings array with 350 nm recess depth (See Figure 5-4). In dual mode, the lower ring (generator) was swept at 0.05 Vs^{-1} while the potential of the upper ring (collector) was held at a constant oxidizing potential. As shown in Figure 5-7, the lower rings current responses reach steady state for both single and dual mode operation. However, the lower rings response in dual mode was several times higher than without redox cycling (single mode).

The presence of the second ring electrode constrains the depletion layer within the nanoholes and confines the mass transport. The interaction (overlap of their diffusion layers) between the lower and upper ring electrodes induces the redox cycling and enhances the current responses of both rings. These results reveal the impact of the upper ring electrodes on the performance of the lower ring electrodes. When the upper ring electrodes (collector) operates in single mode (open circuit

potential), the diffusion layers among adjacent nanoholes in the array extremely overlaps (see Figure 5-5). The whole array then presents a steady state response due to the hemispherical diffusion zone above the entire micro-size array.

The performance of Au-NRRA as a redox cycling system was evaluated by determining the collection efficiency (η) and the amplification factor (A_f), defined in Eq. 5-1 and Eq. 5-2. The simulation (Figure 5-7b) shows that the steady-state current response at the generator electrodes was amplified by 3.5 and η was 99.85. These values agreed very well with the experiment (Figure 5-7a), where 99.7 and 3.4 were measured for η and, A_f, respectively. However, there is a small difference on the magnitude of the limiting current between the experimental and the simulated results. This is probably due to the fact that we have considered a cylindrical geometry for the nanohole. However, the actual geometry of the electrodes cut by FIB is conical, as it was shown by Bohn et al.[41] In any case, the good matching between the experimental and the computational results in Figure 5-7 validates our approach. Notice that, at first glance, the amplification factor of the Au-NRRA configuration might seem a bit low for a redox cycling system with such a high collection efficiency. This is because A_f depends on the electrode geometry and scales with the electrode size[44]. A clarification of these effects is in the section "Notes on the amplification factor".

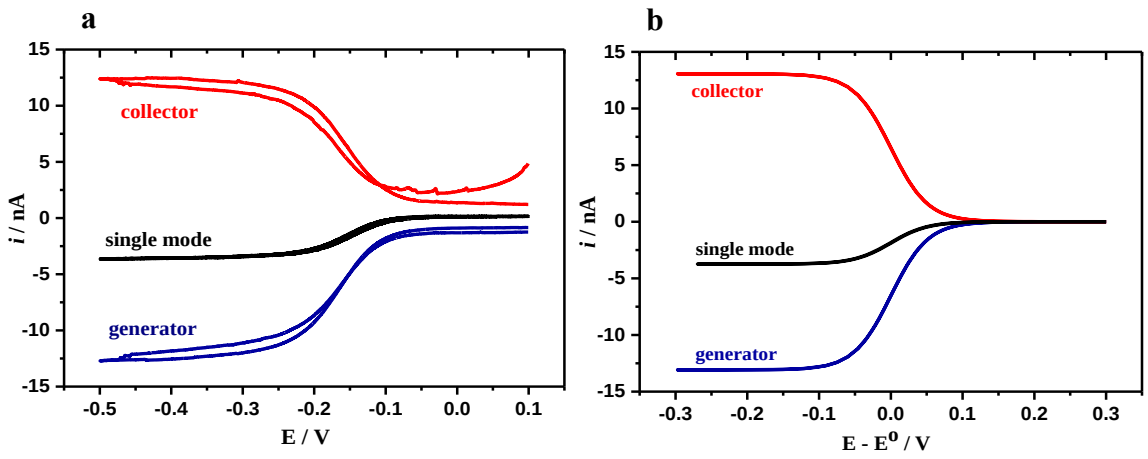

Figure 5-7**.** Comparison of cyclic voltammograms for 20 mM potassium ferricyanide and 0.5 M KCl in a 6 × 6 Au-NRRA (3.3 µm × 3.3 µm) operating in single mode (black curves) and redox cycling mode (red curve – collector and blue curve - generator. a) Experimental results; b) Simulated results. For single mode, the lower ring electrodes were swept at 0.05 Vs^{-1} while the upper ring electrodes remained at open circuit. For redox cycling mode, the lower ring electrodes (the generator) were cycled at 0.05 Vs^{-1} while the potential of the upper ring electrodes was kept at 0.1 V (vs. pseudo-Pt reference) in the experiment and at 0.3 V in the simulation.

5.3.2 Effect of scaling of electrode's dimensions on the recessed nanoring-ring electrodes microarray performance

The results from Figure 5-7 indicates that a computational investigation on the effect of geometric parameters in the performance of Au-NRRA should provide a description of the system that matches well with the experiments, while also allowing some insights into the transport mechanism. The geometry of the ring electrodes in Au-NRRAs is controlled via two parameters: height, *h*, and radius, *r*. The goal in this section is to use the numerical methods validated in Figure 5-7 to understand the effect of *h* and *r* on the performance of Au-NRRA. Simulations were performed for either constant height or constant radius conditions. The recessed depth, *l* = 150 nm,

the insulating gap, g = 150 nm, interelectrode distance, 4r, and the scan rate, v = 0.1 Vs^{-1}, were kept constant in all the simulations. In addition, the height of the lower and upper ring electrodes were considered to be equal, $h_c = h_g$. Three different radiuses, 100 nm, 150 nm, and 200 nm, were considered. The current responses of the rings with different heights ($h = h_c = h_g$) of 25 nm, 50 nm, 75 nm, and 100 nm in dual mode were investigated for each radius. The influence of the scaling of the electrode dimensions on redox cycling response of Au-NRRA is summarized in Figure 5-8. The results in Figure 5-8 are shown in terms of both the limiting current (i) and current density (j).

Figure 5-8a and b display simulated limiting current ($i_{GE_{cycl}}$ (nA)) and limiting current density values ($j_{GE_{cycl}}$ ($\frac{nA}{\mu m^2}$)), from Au-NRRA in dual mode. The cyclic voltammograms and a summary of i and j values for different geometrical parameters are further shown in Figure 5-9 and Table 5-1. As it can be seen in Figure 5-8a, upon increasing h, at a fixed ring radius, the limiting current does not vary remarkably. For example, for r = 150 nm, an increase in the ring height from 25 nm to 50 nm results in an increase of ~10.4 % in the limiting current. Moreover, scaling from h = 50 nm to h = 75 nm results in an increase of ~ 3.9 %, and varying from h = 75 nm to h = 100 nm results in a further increase of only ~ 1.5 %. In contrast to Figure 5-8a, Figure 5-8b shows a significant change in the limiting current density responses for Au-NRRA of constant ring radius upon varying the h-values. For example, for r = 150 nm, varying the ring height from 25 nm to 50 nm, 50 nm to 75 nm and 75 to 100 nm results in decrease of the limiting current magnitude of ~ 44.8 %, ~ 30.7 %, and ~ 26.7%, respectively (variations for other values of r, are also shown in Table 5-1). The current density on the generator decreased significantly with h because the height does not have any sensible effect on the limiting current magnitudes.

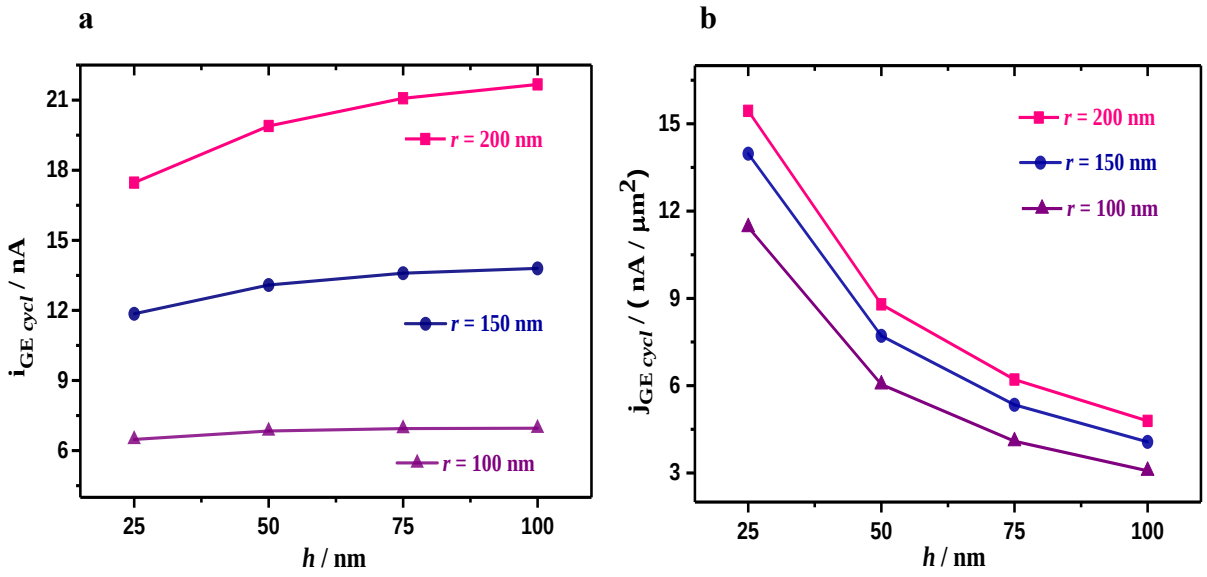

Figure 5-8. The performance of the current characteristics of Au-NRRAs calculated using COMSOL. a) dependence of the limiting current on the ring height (h) for holes of different radii. b) dependence of the limiting current density on the ring height (h) for holes of different radii. The recessed depth, l = 150 nm, the insulating gap, g = 150 nm, interelectrode distance, 4r, and the scan rate, v = 0.1 Vs^{-1}, were kept constant, in all the simulations. The height of the lower and upper ring electrodes were considered to be equal, $h_c = h_g$, for all these cases. The rest of parameters used are given in the text.

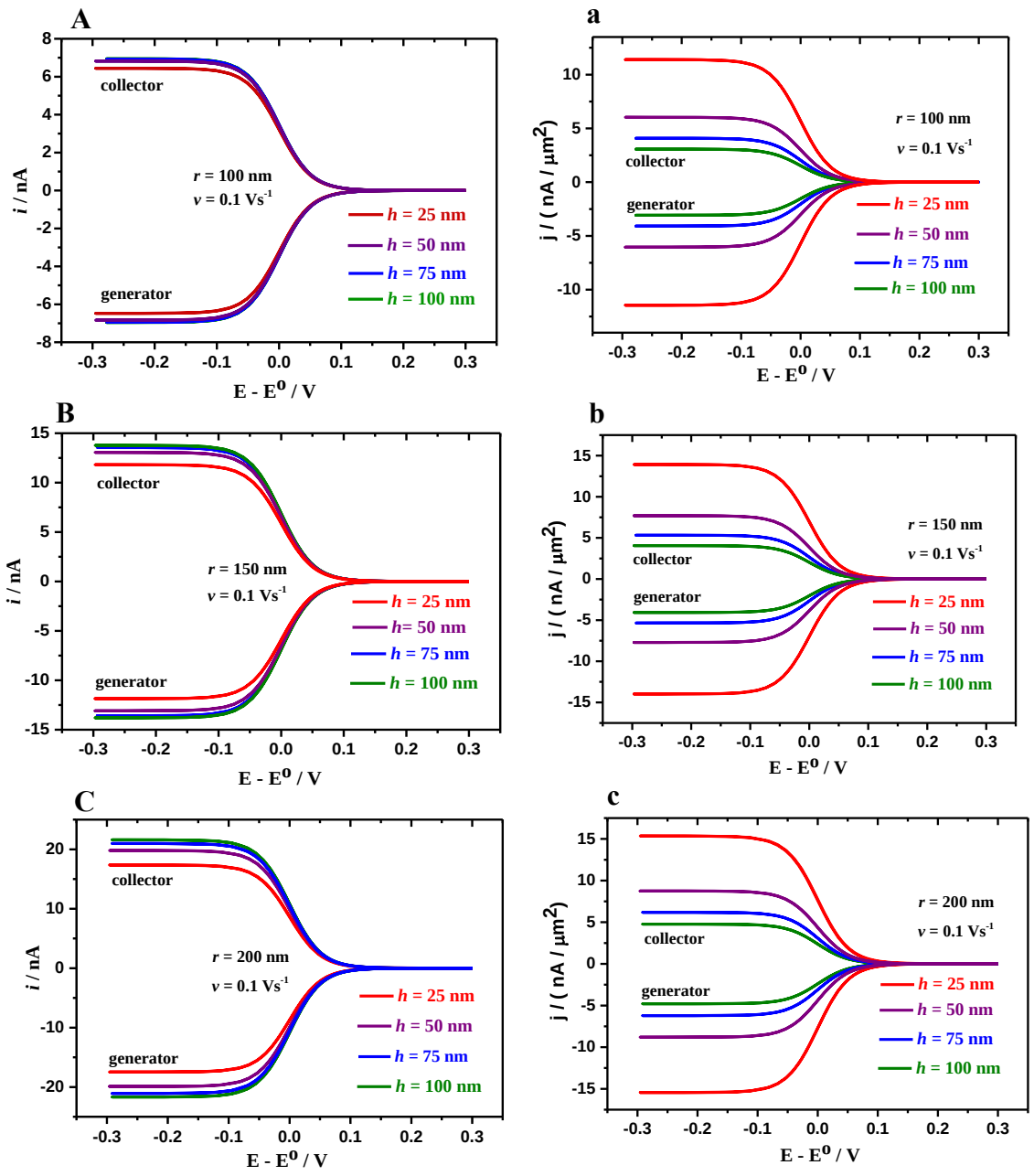

Figure 5-9**.** Comparison of simulation results for cyclic voltammograms represented base on the limiting current and current density for the 6×6 Au-NRRAs with different rings heights, 25 nm, 50 nm, 75 nm, and 100 nm, operating in redox cycling mode. The height of lower ring (generator) and upper ring (collector) was kept the same in all of the simulations. The scan rate ($v = 0.1\ Vs^{-1}$) and hole radius A) and a) r = 100 nm; B) and b) r = 150 nm; C) and c) r = 200 nm were kept constant in Figure 5-9A, a; B, b; and C, c; respectively. The rest of parameters used are given in the text.

Table 5-1. Influence of the varying ring height on the 6×6 Au-NRRA performance, Table 5-1a) r = 100, Table 5-1b) r = 150 nm, and Table 5-1c) r = 200 nm. The simulation parameters are the same as those in Figure 5-9.

a

h (nm) r = 100	i_{GE} /nA	$i_{GE_{cycl}}$/ nA	$j_{GE_{cycl}}$/ (nA/um^2)	i_{CE}/nA	j_{CE}/ (nA/um^2)	Ƞ / %	A_f
25	-2.069	-6.47	-11.44	6.44	11.40	99.54	3.1
50	-2.068	-6.83	-6.04	6.82	6.03	99.85	3.3
75	-	-6.94	-4.09	6.93	4.08	99.85	-
100	-1.953	-6.95	-3.07	6.95	3.07	100	3.6

Limiting current: increasing the ring height from h = 25 nm to h = 50 nm results in an increase of 5.6 %, from h = 50 nm to h = 75 nm results in an increase of about 1.61 %., and from h = 75 nm to h = 100 nm results in an increase of about 0.14 %, in the limiting current value.

Current density: increasing the ring height from h = 25 nm to h = 50 nm results in a decrease of about 47.2 %, from h = 50 nm to h = 75 nm results in a decrease of about 32.3 %, and from h = 75 nm to h = 100 nm results in a decrease of about 24.9 %, in the current density value.

b

h(nm) r = 150	i_{GE} / nA	$i_{GE_{cycl}}$/ nA	$j_{GE_{cycl}}$/ (nA/um^2)	i_{CE} / nA	j_{CE} / (nA/um^2)	η / %	A_f
25	-3.649	-11.85	-13.97	11.81	13.93	99.67	3.2
50	-3.743	-13.08	-7.71	13.06	7.69	99.85	3.5
75	-3.708	-13.59	-5.34	13.56	5.32	99.78	3.7
100	-3.637	-13.79	-4.06	13.77	4.05	99.85	3.8

Limiting current: increasing the ring height from h = 25 nm to h = 50 nm results in an increase of 10.4 %, from h = 50 nm to h = 75 nm results in an increase of about 3.9 %, and from h = 75 nm to h = 100 nm results in an increase of about 1.5 %, in the limiting current value.

Current density: increasing the ring height from h = 25 nm to h = 50 nm results in a decrease of about 44.8 %, from h = 50 nm to h = 75 nm results in a decrease of about 30.7 %, and from h = 75 nm to h = 100 nm results in a decrease of about 26.7 %, in the current density value.

c

h (nm) r = 200	i_{GE} / nA	$i_{GE_{cycl}}$/ nA	$j_{GE_{cycl}}$/ (nA/um^2)	i_{CE}/ nA	j_{CE} / (nA/um^2)	η / %	A_f
25	-5.288	-17.46	-15.44	17.36	15.35	99.42	3.3
50	-5.523	-19.89	-8.79	19.82	8.75	99.64	3.6
75	-5.536	-21.05	-6.20	20.99	6.19	99.71	3.8
100	-5.481	-21.67	-4.79	21.61	4.77	99.72	3.9

Limiting current: increasing the ring height from h = 25 nm to h = 50 nm results in an increase of 13.9 %, from h = 50 nm to h = 75 nm results in an increase of about 5.8 %, and from h = 75 nm to h = 100 nm results in an increase of about 2.9 %, in the limiting current value.

Current density: increasing the ring height from h = 25 nm to h = 50 nm results in a decrease of about 43 %, from h = 50 nm to h = 75 nm results in a decrease of about 29.5 %, and from h = 75 nm to h = 100 nm results in a decrease of about 22.9 %, in the current density value.

Particular attention to the concentration profiles next of the rings is required for the understanding of the behavior revealed in Figure 5-8. Figure 5-10a, b, c and Figure 5-11a, b, c show the effect of the varying the ring height (25nm-100nm) on the evolution of the concentration profile next to the generator electrode, at a constant ring radius, a) r =100 nm, b) r =150 nm, and c) r =200 nm, respectively. As it can be seen in Figure 5-10 and Figure 5-11, the radial diffusion pattern next to the generator electrode weakens as the electrode height increases. As a result, a ring with a short height of 25 nm shows a relatively high limiting current compared to, for instance, a 100 nm ring, due to the pronounced effect of the radial diffusion next to the generator electrode. The height increase still leads to an overall increase in limiting current due to the effect of increasing the surface area of the electrodes.

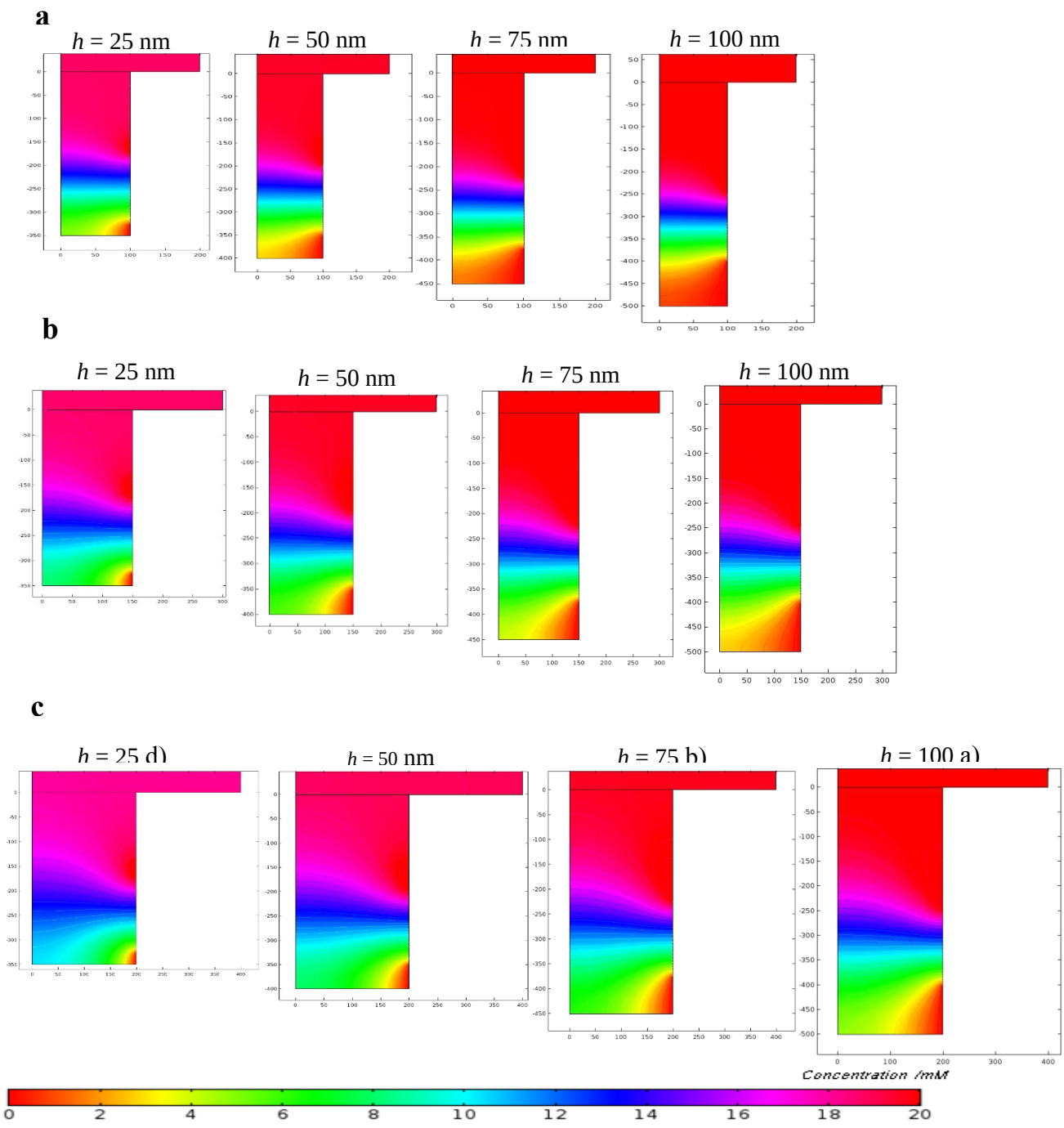

Figure 5-10**.** Surface concentration profiles for species O within the hole next to the electrode surface for the Au-NRRA with different heights (25 nm, 50 nm, 75 nm, 100 nm). The concentration profile images are taken at the steady state potentials. The hole radius a) r = 100 nm, b) r = 150 nm c) r = 200 nm, and the scan rate (v = 0.1 Vs^{-1}) were the same for each set a, b, and c, respectively.

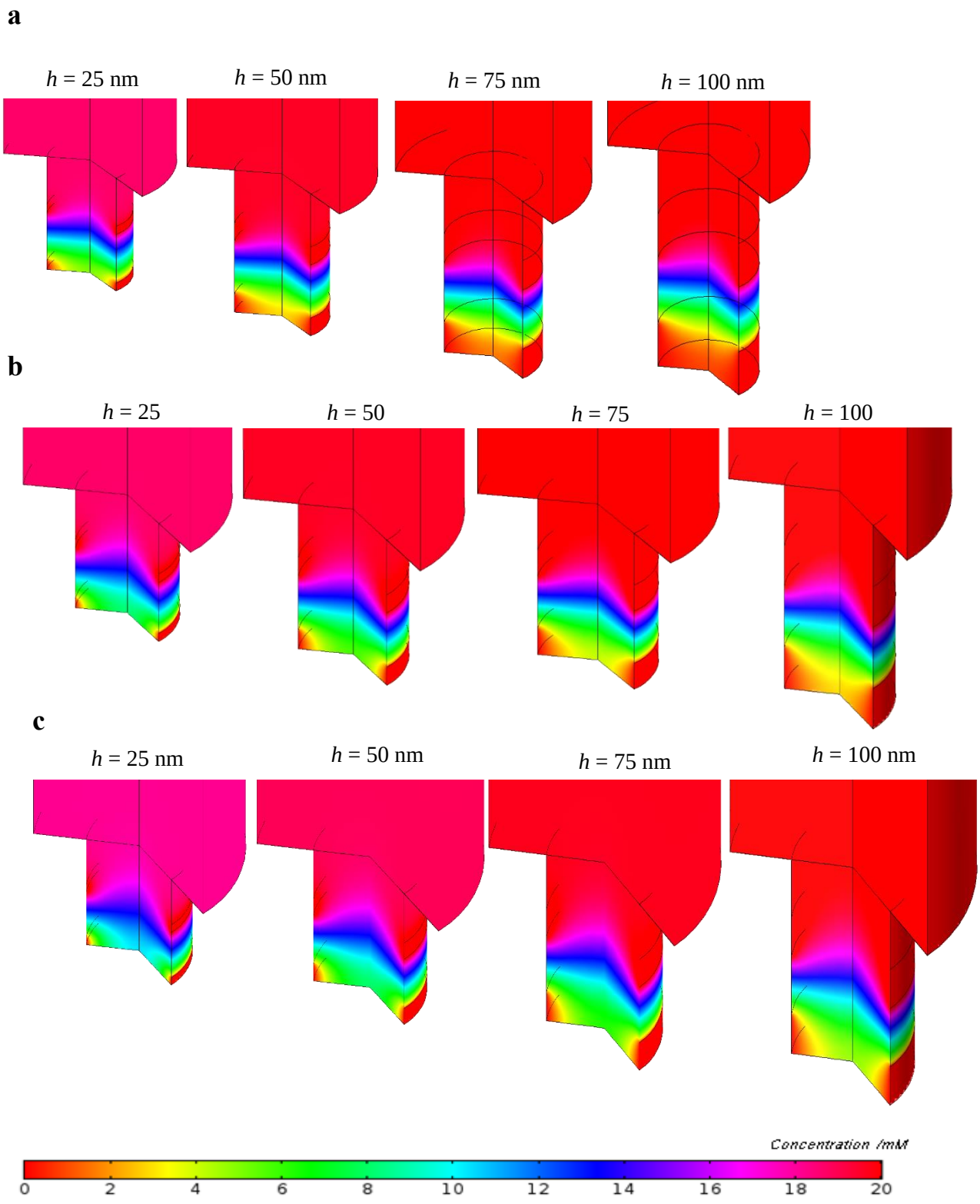
a
h = 25 nm
h = 50 nm
h = 75 nm
h = 100 nm
b
h = 25
h = 50
h = 75
h = 100
c
h = 25 nm
h = 50 nm
h = 75 nm
h = 100 nm
Concentration /mM
0
2
4
6
8
10
12
14
16
18
20

Figure 5-11**.** Volume concentration profiles (revolution 2D) for species O within the hole next to the electrode surface for the Au-NRRA with different heights (25 nm, 50 nm, 75 nm, 100 nm). The concentration profile images are taken at the steady state potentials. The hole radius a) r = 100 nm, b) r = 150 nm c) r = 200 nm, and the scan rate (v = 0.1 Vs^{-1}) were the same for each set a, b, and c, respectively.

The results presented in Figure 5-8a and b as well as in Figure 5-12 also indicate that at a constant value of h the magnitude of both i and the j magnitude with the hole radius. Figure 5-13 shows the variations in the shape of concentration profile at the vicinity of the generator electrode at the base of the hole for different r values (100 nm, 150 nm, and 200 nm), at a fixed height, 50 nm. The concentration profile for other h values is given in Figure 5-10. Obviously, the electroactive surface area available for the redox cycling increases with r. However, more importantly, the wider hole radius also amplifies the radial diffusion flux effect next to the generator electrode. Therefore, the increase in the limiting current due to ring enlargement has contributions from a combination of effects involving both an increase in surface area and the predominant radial diffusion near the generator electrode. The role of the radial diffusion contribution is seen in the increasement in the limiting current density with the electrode radius in Figure 5-8b and Figure 5-12. In summary, the dependence of the current density on h and r is consistent with the shape of the diffusion profile within the ring-hole geometry. The efficient transport within the hole should introduce a degree of limitation on the amount of material potentially available to the generator during redox cycling. These results suggest that the width of the holes plays an important role in enhancing the redox cycling performance of Au-NRRAs.

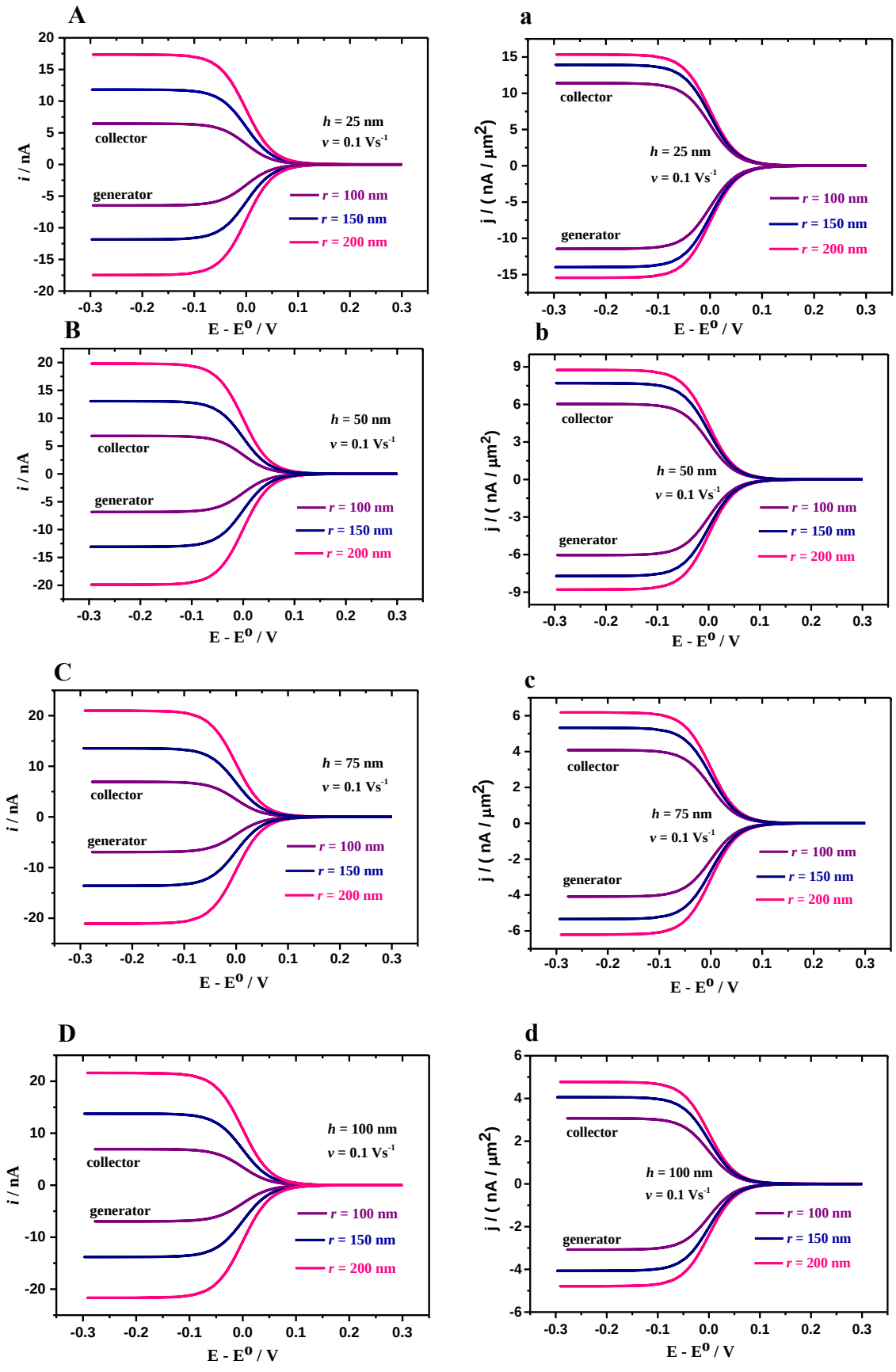
A
i / nA
collector
generator
h = 25 nm
v = 0.1 Vs-1
r = 100 nm
r = 150 nm
r = 200 nm
E - E0 / V
a
j / (nA / μm2)
collector
generator
h = 25 nm
v = 0.1 Vs-1
r = 100 nm
r = 150 nm
r = 200 nm
E - E0 / V
B
i / nA
collector
generator
h = 50 nm
v = 0.1 Vs-1
r = 100 nm
r = 150 nm
r = 200 nm
E - E0 / V
b
j / (nA / μm2)
collector
generator
h = 50 nm
v = 0.1 Vs-1
r = 100 nm
r = 150 nm
r = 200 nm
E - E0 / V
C
i / nA
collector
generator
h = 75 nm
v = 0.1 Vs-1
r = 100 nm
r = 150 nm
r = 200 nm
E - E0 / V
c
j / (nA / μm2)
collector
generator
h = 75 nm
v = 0.1 Vs-1
r = 100 nm
r = 150 nm
r = 200 nm
E - E0 / V
D
i / nA
collector
generator
h = 100 nm
v = 0.1 Vs-1
r = 100 nm
r = 150 nm
r = 200 nm
E - E0 / V
d
j / (nA / μm2)
collector
generator
h = 100 nm
v = 0.1 Vs-1
r = 100 nm
r = 150 nm
r = 200 nm
E - E0 / V

Figure 5-12**.** Comparison of simulation results for cyclic voltammograms represented base on the limiting current and current density for the 6×6 Au-NRRA with different hole radiuses, 100 nm, 150 nm, and 200 nm, operating in redox cycling mode. The scan rate ($v = 0.1\,Vs^{-1}$) and ring heights A) and a) *h* = 25 nm; B) and b) *h* = 50 nm; C) and c) *h* = 75 nm; D and d) *h* = 100 nm were kept constant in A, a; B, b; C, c; and D, d; respectively. The height of lower ring, generator, and upper ring, collector, were kept the same in all of the simulations. The rest of the simulation parameters are the same as those in Figure 5-9.

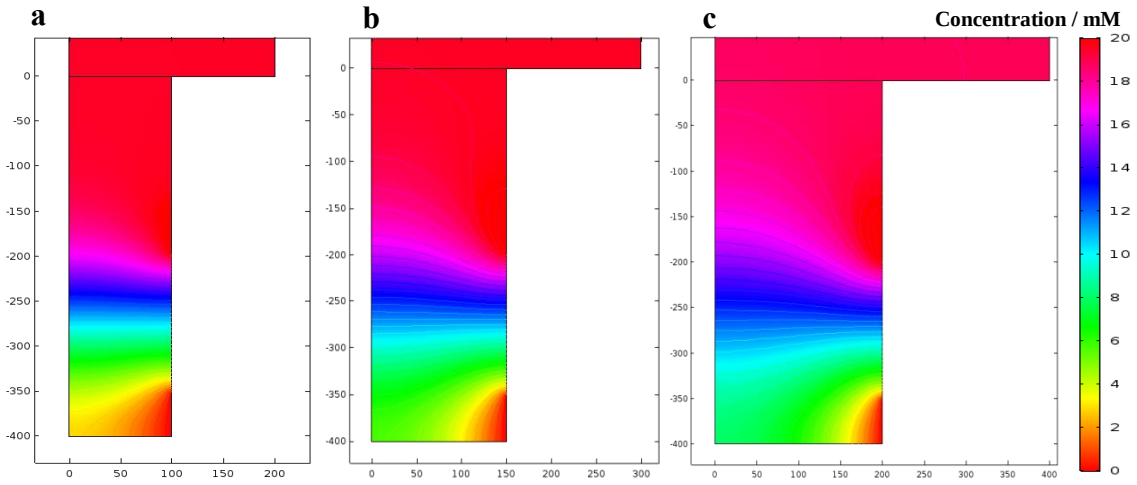

Figure 5-13**.** Concentration profiles for species O within the hole next to the electrode surface for Au-NRRAs with different radiuses: (a) 100 nm, (b) 150 nm, and (c) 200 nm. The *h* = 50 nm and *v* = 0.1 Vs^{-1} were the same for all these cases. The concentration profiles are taken at the steady state potentials.

5.3.3 Effect of scan rate on recessed nanoring-ring electrodes microarray performance

It should be noted that an important characteristic of the redox cycling systems (dual mode operation) is that the collector electrode, which is kept at a constant potential, show a much smaller

charging current in comparison to the generator electrode. This feature of redox cycling systems allows fast scan cyclic voltammetry (CV) measurements to be used for monitoring electrogenerated intermediates with very short lifetime and to study electrochemical reaction mechanisms [5, 20, 45] . Therefore, one of the valuable futures of redox cycling devices is their performance at high scan rates. For this main reason, we have studied the effect of the scan rate on the performance of the Au-NRRA.

Figure 5-14compares simulated cyclic voltammogram curves for 6×6 Au-NRRA (a) r = 100, b) r = 150 nm, and c) r = 200 nm) in single and dual mode operation at various scan rates, ranging from 0.05 Vs^{-1} up to 1000 Vs^{-1}. Here again, for single mode simulations, the potential of the lower rings was swept between 0.3 and -0.3 V at different scan rates and the upper ring electrodes were considered as insulator layers. In dual mode, the lower ring (generator) potential was swept in the same way as in the single mode, while the upper ring potential (collector) was kept constant at 0.3 V. As it can be seen from Figure 5-14B, the cyclic voltammogram curves for both the generator and collector electrodes show a sigmoidal shape for all the scan rates investigated (between 0.05 and 1000 Vs^{-1}), which confirms that valuable characteristic of the Au-NRRA. It should be noted that the current on the collector electrodes was nearly a mirror image of the generator response up to scan rates of 1 Vs^{-1}. Consequently, the η-values were closer to the unity in that range of scan rates (up to 1 Vs^{-1}). A small decrease in the collector current was observed as the scan rate increased up to 100 Vs^{-1}, whereas the generator current magnitude remained practically constant. As a result, η decreased to 97.1 %. A scan rate of 1000 Vs^{-1} induced a quasi-steady state wave at both generator and collector electrodes. Although the generator current magnitude remained similar to the values of lower scan rates, the magnitude of the current at the collector decreased even further (η reached 90.86 % in this case (1000 Vs^{-1})). The dependence of lower ring generator

current on the scan rate was significantly different for single mode operation, as shown in Figure 5-14b. The current response of the array in single mode gradually shifted from steady-state waves (at scan rates up to 1 Vs^{-1}) to quasi-steady state waves (at the scan rates between 10 and 100 Vs^{-1}) and to, finally, a peak-shaped wave at highest scan rate (1000 Vs^{-1}). The current magnitude of the generator electrode at single mode is almost constant up to scan rate of 0.1 Vs^{-1} and then it gradually increases at higher scan rates. The diffusion layer from adjacent nanoelectrodes completely overlap in single mode operation over the range scan rates investigated due to the relative small separation between the nanoholes on the array. Consequently, the whole array behaves like a single 3.3 μm × 3.3 μm microelectrode. The current response of the array at higher scan rates (>10 Vs^{-1}) deviated from steady-state because the shape of the diffusion layer over the whole array shifted from hemispherical to a mixed hemispherical and planar diffusion.[42] At fastest scan rate (1000 Vs^{-1}), the planar diffusion towards the whole array completely dominates[42].

The values for η and A_f for different scan rates are summarized in Table 5-2. (Again, an important discussion on the seemingly low amplification factor of the Au-NRRA system is given in the section "Notes on the amplification factor". As indicated in Table 5-2, the magnitude of A_f decreases with the scan rate. This is because the magnitude of the generator current is practically independent of the scan rate in dual mode operation, whereas the current magnitude gradually increases with the scan rate at single mode.

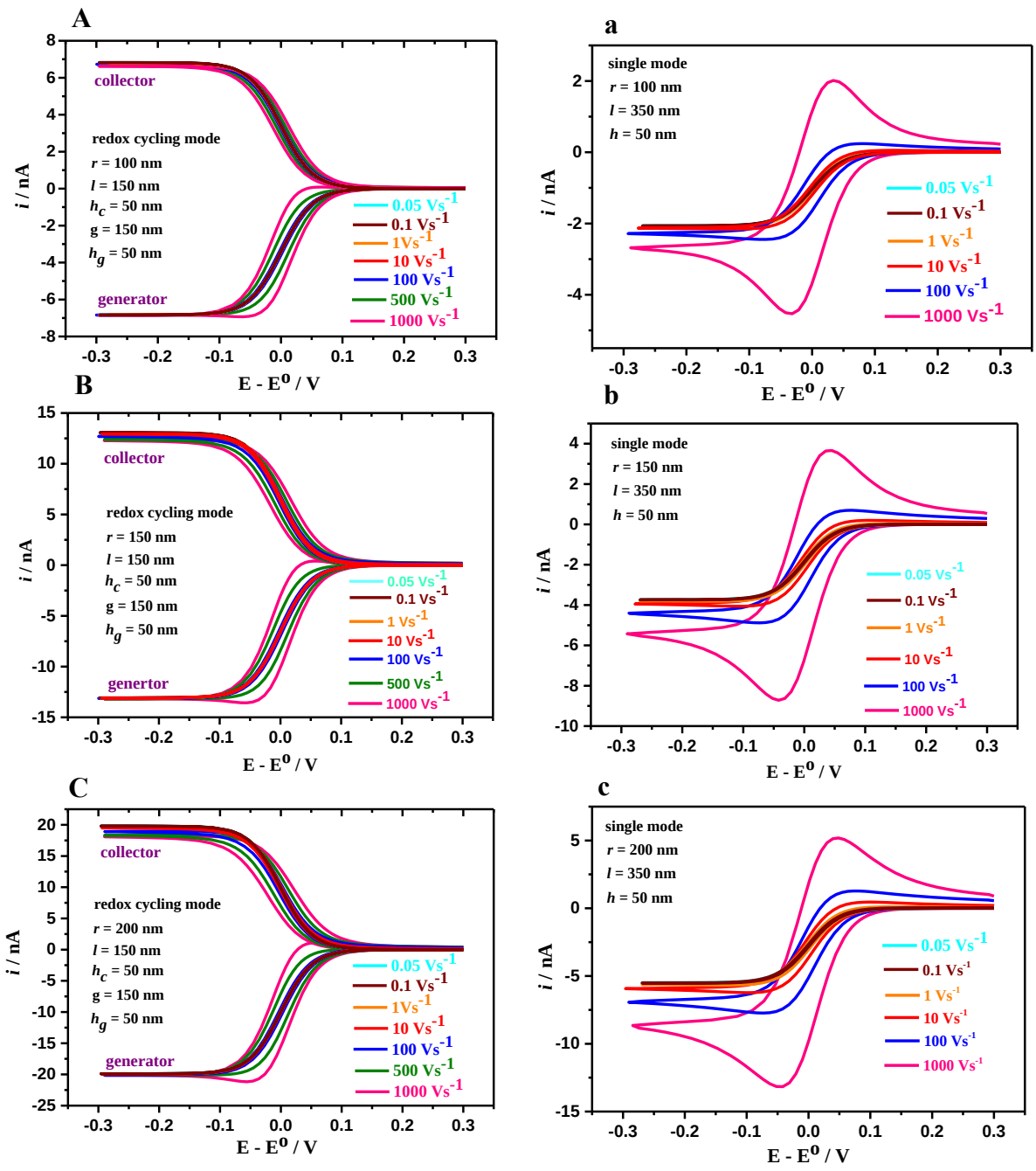

Figure 5-14. Simulated cyclic voltammograms under various scan rates for a 6×6 Au-NRRA operating in A, B, and C) redox cycling mode, and a, b and c) single mode. The ring height (h = 50 nm), and the interelectrode distance were set (4r) in all the simulations. The recessed depth (l = 150 nm) and ring gap (g = 150 nm) were the same for all the simulations in A), B) and C). The recessed depth was (l = 350 nm) in a), b) and c), which coincide with the recessed depth of lower ring in ring-ring geometry, Figure 5-4. The hole radius was r = 100 nm in A and a) and it was r =

150 nm in B and b), and r = 200 nm in C) and c). In single mode simulations, the potential of lower rings were swept between 0.3 and -0.3 V at different scan rates ranging from 0.05 Vs^{-1} up to 1000 Vs^{-1} and the upper ring electrodes were considered as insulator layers. In dual mode, the lower ring (generator) potential was swept in the same way as in the single mode, at a sweep rate of 0.05-1000 Vs^{-1} while the upper ring potential (collector) was kept constant at 0.3 V. The rest of simulation conditions are given in the text.

a

Scan rate /Vs^{-1}	i_{GE} / nA)	$i_{GE_{cycl}}$ / nA	i_{CE} / nA	η / %	A_f
0.05	-2.065	-6.834	6.822	99.82	3.31
0.1	-2.067	-6.834	6.821	99.81	3.31
1	-2.087	-6.837	6.811	99.62	3.28
10	-2.159	-6.838	6.792	99.33	3.17
100	-2.447	-6.841	6.736	98.46	2.79
1000	-4.533	-6.933	6.635	95.70	1.53

b

Scan rate / Vs^{-1}	i_{GE} / nA	$i_{GE_{cycl}}$ / nA	i_{CE} / nA	η / %	A_f
0.05	-3.74	-13.08	13.06	99.85	3.5
0.1	-3.74	-13.08	13.06	99.85	3.5
1	-3.81	-13.09	13.04	99.62	3.4
10	-4.06	-13.09	12.94	98.85	3.2
100	-4.88	-13.11	12.73	97.1	2.7
1000	-8.72	-13.57	12.33	90.86	1.5

Scan rate / Vs^{-1}	i_{GE} / nA	$i_{GE_{cycl}}$ / nA	i_{CE} / nA	η / %	A_f
0.05	-5.504	-19.890	19.809	99.59	3.6
0.1	-5.522	-19.892	19.799	99.53	3.6
1	-5.669	-19.906	19.734	99.14	3.5
10	-6.227	-19.947	19.531	97.91	3.2
100	-7.732	-20.052	19.018	94.84	2.6
1000	-13.16	-21.119	18.196	86.16	1.6

Table 5-2**.** Influence of the scan rate on the 6×6 recessed ring-ring array performance. The array characteristics were: ring height (*h* = 50 nm) in all cases. a) hole radius (*r* = 100), b) hole radius (*r* = 150), c) hole radius (*r* = 200).

5.3.4 Effect of inter-electrode gap on recessed nanoring-ring electrodes microarray performance

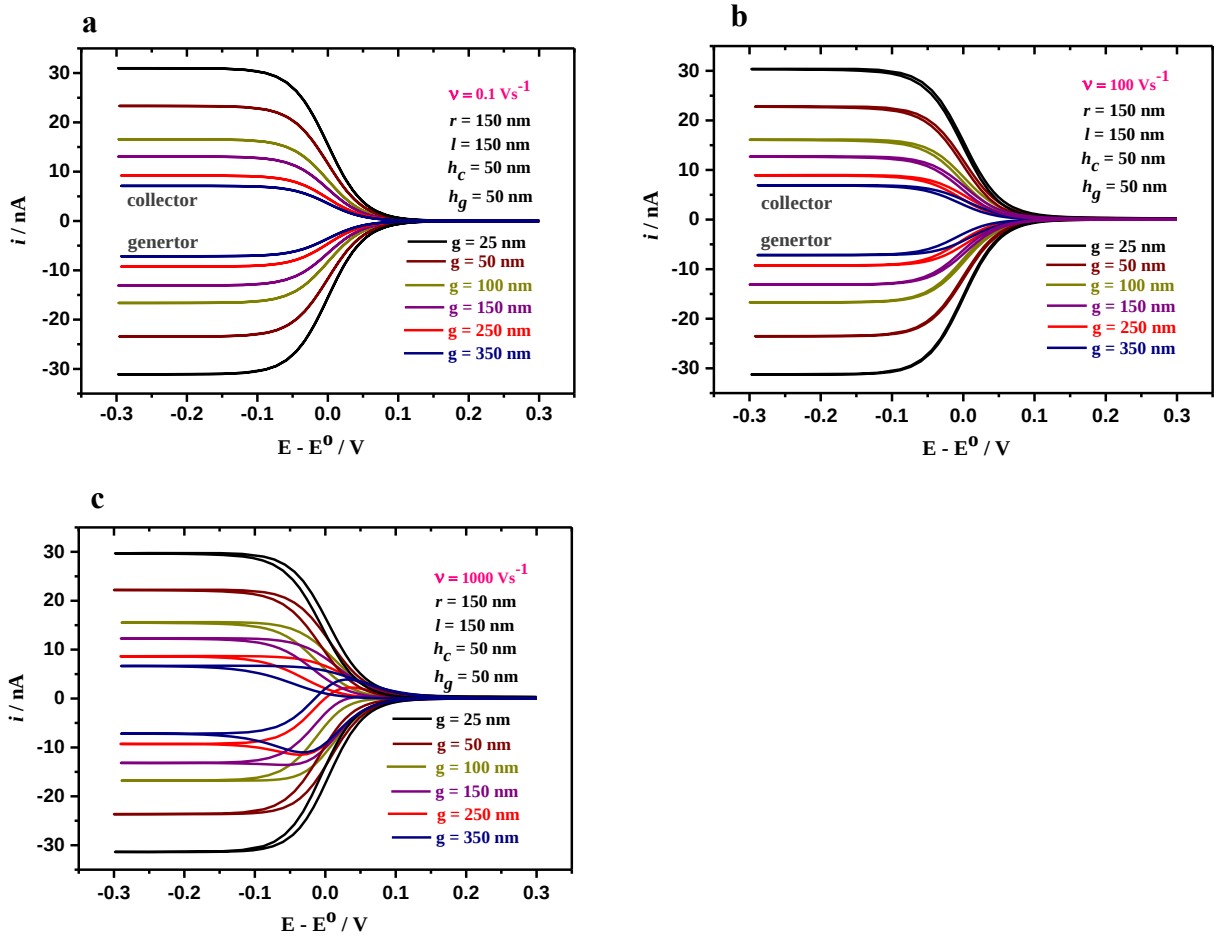

Figure 5-15**.** Comparison of simulated cyclic voltammograms for the 6×6 Au-NRRAs (operating in redox cycling mode) with different inter-electrode gaps, 25 nm, 50 nm, 100 nm, 150 nm, 250 nm, 350 nm, at different scan rates: a) v = 0.1 V s^{-1} b) v = 100 V s^{-1} and c) v = 1000 V s^{-1}. The hole radius (r =150 nm), recessed depth (l = 150 nm), ring height (h_c = h_g = 50 nm), and the interelectrode distance (4r) were the same in all the simulations.

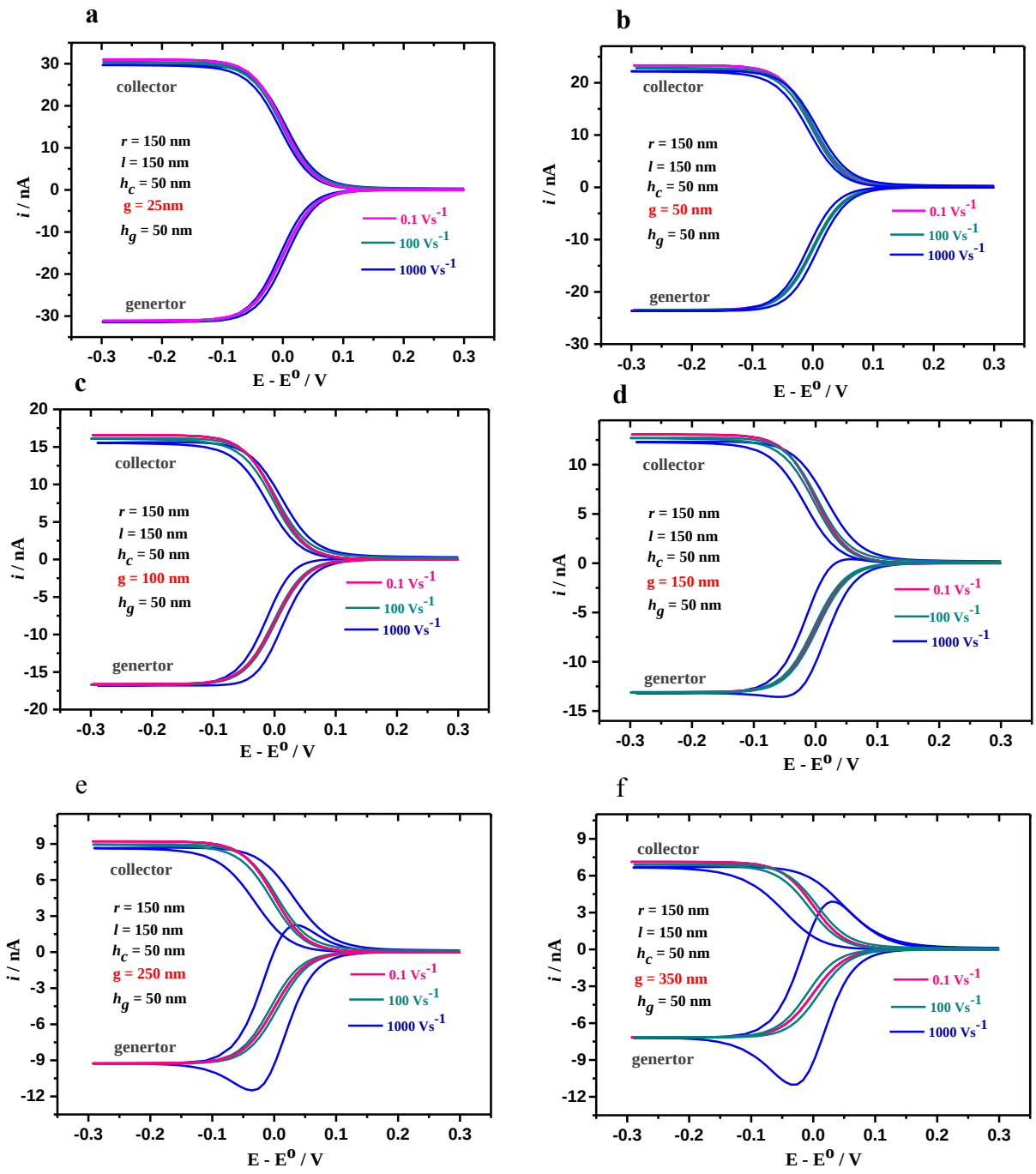

Figure 5-16. Simulated cyclic voltammograms under various scan rates for a 6×6 Au-NRRA operating in redox cycling mode. The hole radius (r =150 nm), recessed depth (l = 150 nm), ring height ($h_c = h_g$ = 50 nm), and the inter-electrode distance ($4r$) were the same in all the simulations. The interelectrode gap was a) 25 nm, b) 50 nm, c) 100 nm, d) 150 nm, e) 250 nm, f) 350 nm.

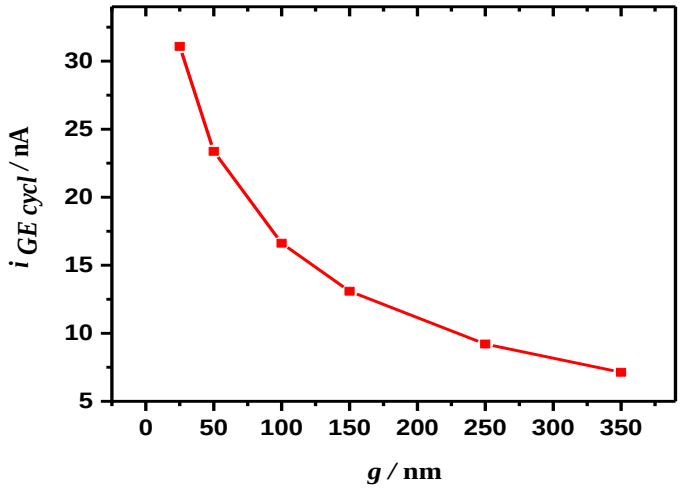

Figure 5-17**.** Dependence of the limiting current on the interelectrode gap (the gap between generator and collector electrodes). Scan rate $v = 0.1$ Vs^{-1}. The simulation parameters' are the same as Figure 5-15 and Figure 5-16. (Note the electrodes' surface areas are the same in all these simulated arrays of different inter-electrode gap). As can be seen from this graph, the current response of the 6×6 Au-NRRA configuration operating in dual mode increases as the inter-electrode gap decreases, as it was expected.

Interelectrode gap/ nm	Scan rate /Vs^{-1}	$i_{GE_{cycl}}$/nA	i_{CE} /nA	η /%
25	0.1	-31.09	30.99	99.67
25	100	-31.25	30.39	97.25
25	1000	-31.39	29.75	94.78
50	0.1	-23.44	23.37	99.70
50	100	-23.53	22.89	97.28
50	1000	-23.65	22.24	94.04
100	0.1	-16.62	16.56	99.64
100	100	-16.68	16.19	97.06
100	1000	-16.79	15.62	93.03
150	0.1	-13.08	13.06	99.85
150	100	-13.11	12.73	97.10
150	1000	-13.57	12.33	90.86
250	0.1	-9.25	9.21	99.56
250	100	-9.27	8.97	96.76
250	1000	-11.50	8.69	75.56
350	0.1	-7.15	7.13	99.72
350	100	-7.17	6.93	96.65
350	1000	-11.01	6.70	60.85

Table 5-3**.** Influence of the interelectrode gap on the 6×6 Au-NRRA performance. The simulation conditions are the same as Figure 5-15 and Figure 5-16.

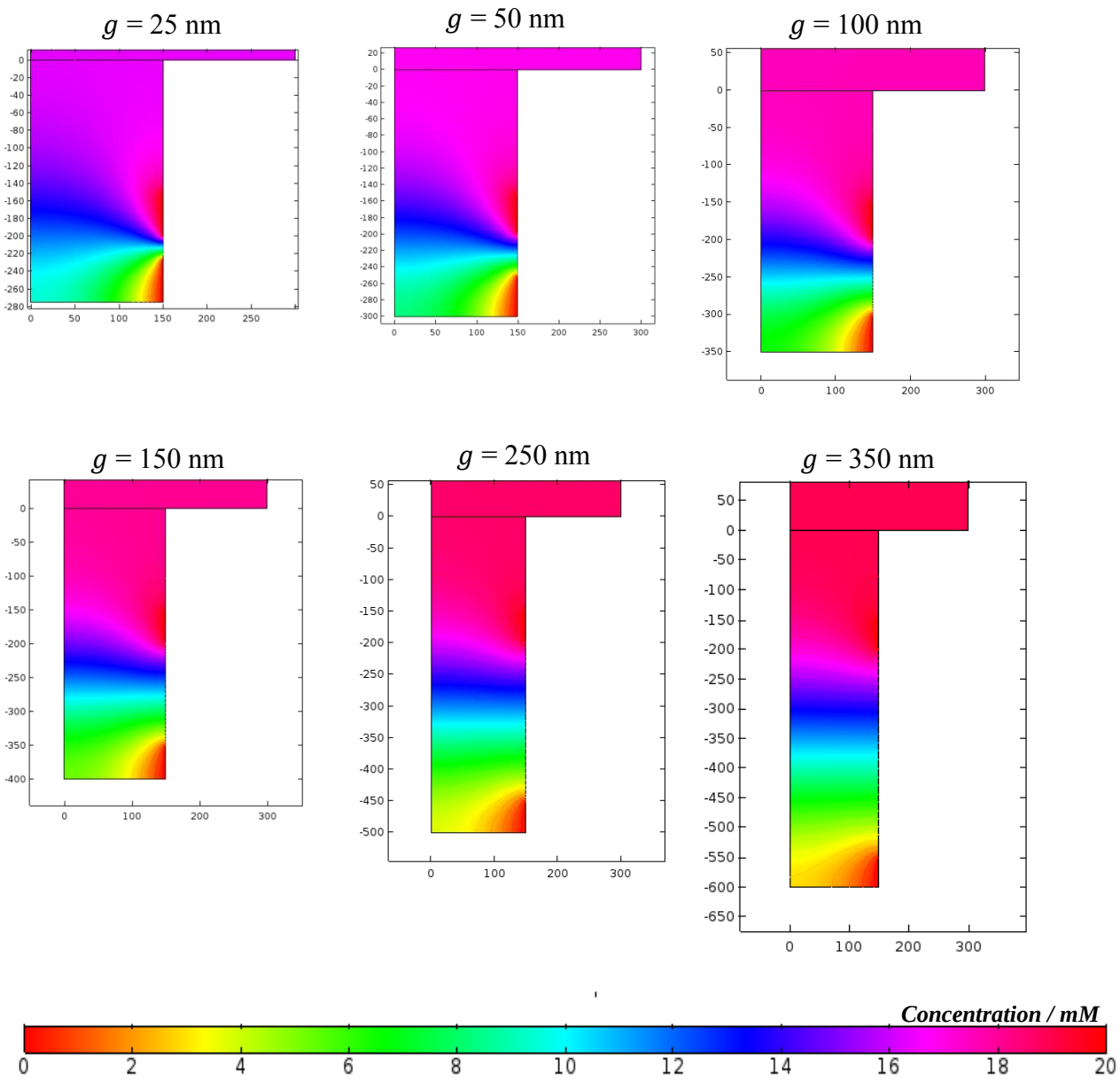

Figure 5-18**.** Surface concentration profiles for species O within the hole next to the electrode surface for the Au-NRRA with different interelectrode gaps (25 nm, 50 nm, 100 nm, 150 nm, 250 nm, 350 nm). The concentration profile images were taken at the steady state potentials. The hole radius (r = 150 nm), recessed depth (l = 150 nm), ring height ($h_c = h_g$ = 50 nm), the scan rate (v = 0.1 Vs^{-1}), and the interelectrode distance ($4r$) were the same in all the simulations.

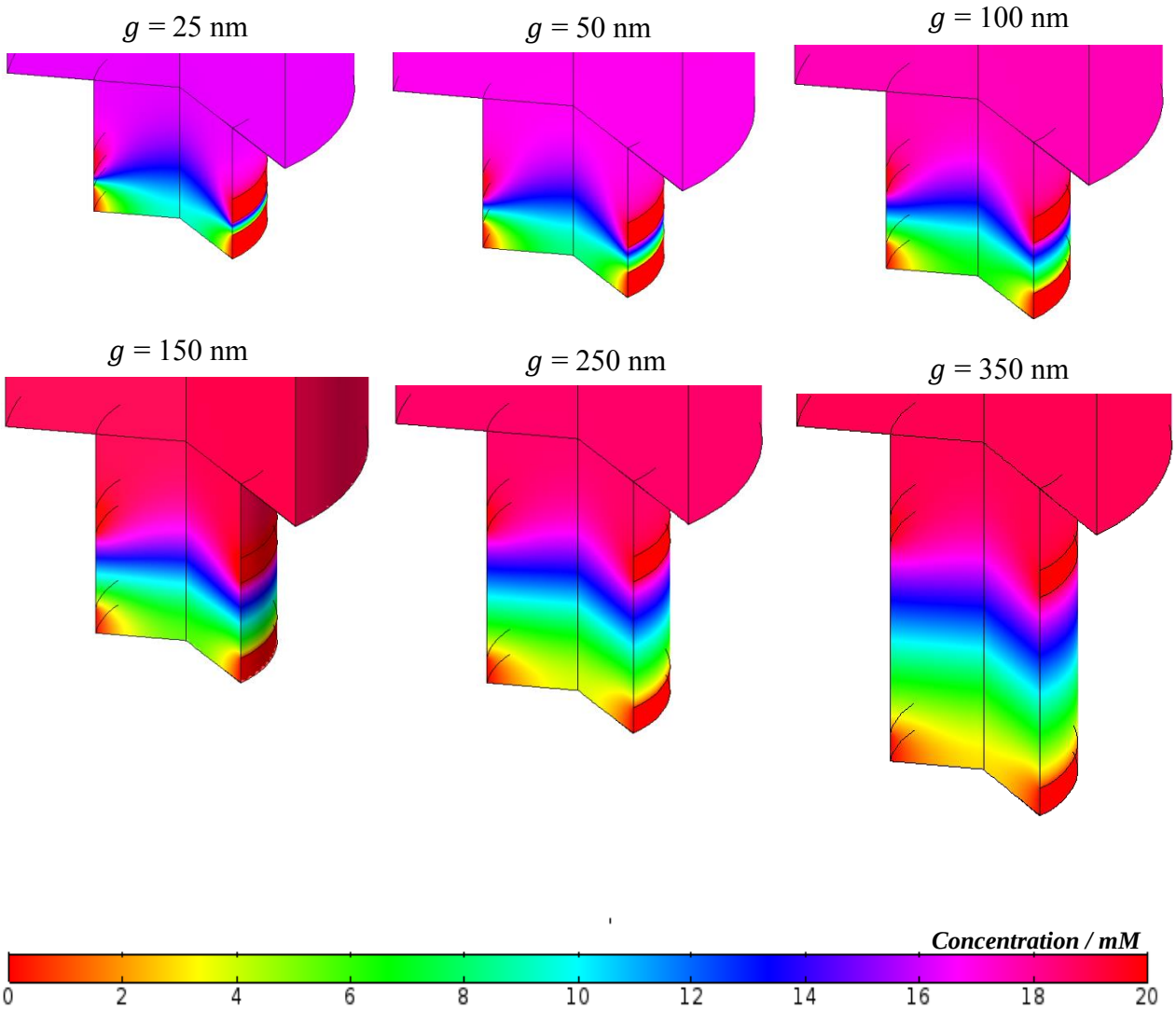

Figure 5-19**.** Volume concentration profiles (revolution 2D) for species O within the hole next to the electrode surface for the Au-NRRA with different interelectrode gaps (25 nm, 50 nm, 100 nm, 150 nm, 250 nm, 350 nm). The concentration profile images were taken at the steady state potentials. The hole radius (r = 150 nm), recessed depth (l = 150 nm), ring height ($h_c = h_g$ = 50 nm), the scan rate (v = 0.1 Vs^{-1}), and the interelectrode distance ($4r$) were the same in all the simulations.

5.3.5 Notes on the amplification factor

The amplification factor (A_f), as defined in Eq. 5-2, is one of the parameters widely used to evaluate the performance of a redox cycling system. However, this factor is not often a proper parameter for a direct comparison between the performances of different redox cycling structures. The inefficacy of this factor for directly comparing the performance of different configurations arises from its definition. A_f basically compares the behavior of a specific system under investigation (a set of electrodes or arrays of electrodes) operating in redox cycling mode to the same type of system operating in single mode. Since nanoelectrodes operate very efficiently in single mode, they might yield low A_f, even when the redox cycling significantly improves the performance. In another example, Wolfrum et al.[44] have previously pointed out that this simple factor cannot be used to evaluate the performance of a small confined redox cycling system that generates a finite limiting current while operating in dual mode. Because in single mode due to the confined environment, the system can be completely depleted from the electroactive molecule of interest after all the molecules being oxidized or reduced and the current will approach zero. Since Eq. 5-2 compares the behavior of a particular system operating in dual mode with itself when it is running under the single mode, the denominator here goes to zero and the amplification factor would tend to infinity.

In addition to being very dependable on the configuration of the system, A_f is also very dependent on the whole size of the array.

It is well known that the shape of the diffusion layer has a huge influence on the performance of an electrode. 3D diffusion enhances the mass transport at a small electrode (when the overall electrode size is smaller than the diffusion layer). The mass transport keeps improving as the

electrode becomes smaller. In the case of a very small array of electrodes that can operate in redox cycling mode, like the ones studied in this manuscript, the current increases significantly in redox cycling mode. However, the current amplification will be calculated using the single mode operation from a small array that also benefits from enhanced mass transport, due to 3D diffusion layer.

We have investigated very small arrays of recessed nanoring-ring electrodes (6 × 6). The work was limited to small arrays to allow rigorous comparison to calculated results (large arrays would be computationally expensive and very time-consuming). As we have shown, there is no significant diffusion layers overlap among the adjacent nanoholes on the array in redox cycling mode. The presence of the top ring confines the diffusion layer within each nanohole. Then using a larger array will improve the response of this device greatly, because the current response of each nanohole (containing the nanoring-ring electrodes) will simply add up.

On the other hand, as the whole size of the array increases the mass transport at the array operating in single mode decreases. As a result, as the array becomes larger, the A_f value for this device (Au-NRRA) will increase. This demonstrates that the amplification factor is very dependent on the properties of the array.

Next, using a very simple example, we will further illustrate the dependency of the A_f value on the whole size of the array. In Table 5-4 we have estimated the A_f for arrays of four different sizes.

We have estimated the current of the array opening in single mode using Eq. 5-9[6]. (The analytical solution for the recessed disc electrode).

$$I = \frac{4nFcDr_o}{\left(\frac{4L}{\pi r_o}+1\right)} \qquad \text{Eq. 5-9}$$

Where *n* is the number of the transfer electrons, r_o is the electrode radius and L is the recess depth value. (Here, we considered the whole square array operating in single mode as a single disc electrode of identical surface area and estimated its current using Eq. 5-9[6]). Table S-4 clearly shows that the estimated A_f values increase with the number of elements (size) of the array.

Another interesting aspect to be pointed out is the relationship between the amplification factor (A_f) and the number of redox cycles (N_{RC}), defined below:

$$N_{RC} = \frac{1}{1-\eta^2} \qquad \text{Eq. 5-10}$$

Where the collection efficiency of the collector electrode (CE) was considered the same as the collection efficiency at the generator electrode (GE), i.e., $\eta_{CE} = \eta_{GE} = \eta$

Niwa et al[5] have shown that the value of N_{RC} approaches A_f for large values of average diffusion lengths (a few μm). In our case, the average diffusion length is very small. Therefore, the values of A_f and N_{RC} obtained experimentally from Figure 5-7 are very different.

Array size(μm)	Array size (# of electrodes)	Total # of electrodes	$i_{GE_{cycl}}$ / nA (Simulated results)	i_{GE} / nA (Simulated value)	Estimated i_{GE} / nA from eq S-7	A_f (Simulated value)	A_f (Estimated value)
$3.3\ \mu m \times 3.3\ \mu m$	6×6	36	13.08	3.74	6.52	3.5	2.01
$25.5\ \mu m \times 25.5\ \mu m$	43×43	1849	671.92	N/A	61.81	N/A	10.87
$50.1\ \mu m \times 50.1\ \mu m$	84×84	7056	2564.15	N/A	123.48	N/A	20.76
$100.5\ \mu m \times 100.5\ \mu m$	168×168	28224	10256.60	N/A	249.9	N/A	41.04

Table 5-4**.** Demonstration of dependency of the amplification factor on numbers of the electrode available in redox cycling (the array size). The hole radius (r =150 nm) and the inter-electrode distance ($4r$).

5.4 Conclusions

The electrochemical response of gold nanoring-ring array (Au-NRRA) electrodes was simulated using COMSOL®. The simulations were first validated by comparing the computational results with experiments at both single and dual modes. The experiments were carried out using a 6 × 6 Au-NRRA (3.3 µm ×3.3 µm) fabricated on a metal/insulator/metal/insulator stack over a glass substrate. The nanopattern was created by FIB milling. In redox cycling mode, the upper ring electrodes which were polarized at a constant potential acted as the collector electrodes and the lower ring electrode at which the potential was swept acted as generator electrodes. With redox cycling the recessed nanoring-ring electrodes array showed a much higher limiting current compared to that of a recessed nanoring-ring electrodes array (without redox cycling). The Au-NRRA configuration showed a collection efficiency close to 100 % at moderate scan rates. The high collection efficiency of this configuration is because of the upper ring electrodes, the collector,

constrain the depletion layer within the nanoholes and confine the mass transport inside the nanoholes. The generator electrode is completely surrounded by the collector electrode with the same geometry. In addition, both generator and collector are located in a nanohole with a very small gap in between. Information on the influence of the scan rates and scaling of electrode dimensions on the redox cycling behaviors of the Au-NRRAs was obtained through numerical simulations. Simulations on the effect of the scan rate on the performance of these devices showed a quasi-steady-state response in the redox cycling mode even at 1000 Vs^{-1}. This confirms that capability of Au-NRRA to monitor electrogenerated intermediates with very short lifetime and to study electrochemical reaction mechanisms. The effect of the electrode dimensions on the performance of Au-NRRA in redox cycling mode revealed that the magnitude of the attainable limiting current depends strongly on the ring radius, while it is almost independent of the ring height variations. The information reported here should be useful for the design of recessed nanoring-ring arrays with improved redox cycling performance for future applications.

5.5 Acknowledgments

We gratefully thank Prof. David Harrington for lab access and helpful discussions. We acknowledge CMC Microsystems (Kingston, ON, Canada) for providing the COMSOL Multiphysics®. We would like to thank WestGrid and Compute Canada for providing computational resources. This work was supported by the NSERC Discovery Grant and the NSERC CREATE Programs.

5.6 References

1. Ahmadalinezhad, A.; Chen, A. C., *Nanomaterial-Based Electrochemical Biosensors*, 2014, p 339-355.
2. Wang, J., Carbon-Nanotube Based Electrochemical Biosensors: A Review. *Electroanalysis* **2005**, *17*, 7-14.
3. Arrigan, D. W. M., Nanoelectrodes, Nanoelectrode Arrays and Their Applications. *Analyst (Cambridge, U. K.)* **2004**, *129*, 1157-1165.
4. Bard, A. J.; Crayston, J. A.; Kittlesen, G. P.; Shea, T. V.; Wrighton, M. S., Digital-Simulation of the Measured Electrochemical Response of Reversible Redox Couples at Microelectrode Arrays - Consequences Arising from Closely Spaced Ultramicroelectrodes. *Anal. Chem.* **1986**, *58*, 2321-2331.
5. Niwa, O.; Morita, M.; Tabei, H., Electrochemical-Behavior of Reversible Redox Species at Interdigitated Array Electrodes with Different Geometries - Consideration of Redox Cycling and Collection Efficiency. *Anal. Chem.* **1990**, *62*, 447-452.
6. Godino, N.; Borrise, X.; Munoz, F. X.; del Campo, F. J.; Compton, R. G., Mass Transport to Nanoelectrode Arrays and Limitations of the Diffusion Domain Approach: Theory and Experiment. *J. Phys. Chem. C* **2009**, *113*, 11119-11125.
7. Hees, J.; Hoffmann, R.; Kriele, A.; Smirnov, W.; Obloh, H.; Glorer, K.; Raynor, B.; Driad, R.; Yang, N. J.; Williams, O. A.; Nebel, C. E., Nanocrystalline Diamond Nanoelectrode Arrays and Ensembles. *Acs Nano* **2011**, *5*, 3339-3346.
8. Lanyon, Y. H.; Arrigan, D. W. M., Recessed Nanoband Electrodes Fabricated by Focused Ion Beam Milling. *Sens. Actuators, B* **2007**, *121*, 341-347.
9. Cohen, A. E.; Kunz, R. R., Large-Area Interdigitated Array Microelectrodes for Electrochemical Sensing. *Sens. Actuators, B* **2000**, *62*, 23-29.
10. Barnes, E. O.; Lewis, G. E. M.; Dale, S. E. C.; Marken, F.; Compton, R. G., Generator-Collector Double Electrode Systems: A Review. *Analyst (Cambridge, U. K.)* **2012**, *137*, 1068-1081.
11. Wollenberger, U.; Paeschke, M.; Hintsche, R., Interdigitated Array Microelectrodes for the Determination of Enzyme-Activities. *Analyst (Cambridge, U. K.)* **1994**, *119*, 1245-1249.
12. Chen, C. H.; Postlethwaite, T. A.; Hutchison, J. E.; Samulski, E. T.; Murray, R. W., Electrochemical Measurements of Anisotropic Diffusion in Thin Lyotropic Liquid-Crystal Films Using Interdigitated Array Electrodes. *J. Phys. Chem.* **1995**, *99*, 8804-8811.
13. Niwa, O.; Morita, M.; Tabei, H., Highly Sensitive and Selective Voltammetric Detection of Dopamine with Vertically Separated Interdigitated Array Electrodes. *Electroanalysis* **1991**, *3*, 163-168.
14. Oleinick, A.; Zhu, F.; Yan, J. W.; Mao, B. W.; Svir, I.; Amatore, C., Theoretical Investigation of Generator-Collector Microwell Arrays for Improving Electroanalytical Selectivity: Application to Selective Dopamine Detection in the Presence of Ascorbic Acid. *Chemphyschem* **2013**, *14*, 1887-1898.
15. Finot, E.; Bourillot, E.; Meunier-Prest, R.; Lacroute, Y.; Legay, G.; Cherkaoui-Malki, M.; Latruffe, N.; Siri, O.; Braunstein, P.; Dereux, A., Performance of Interdigitated Nanoelectrodes for Electrochemical DNA Biosensor. *Ultramicroscopy* **2003**, *97*, 441-449.
16. Lee, C. G.; Ojima, H.; Umeda, M., Electrooxidation of C-1 to C-3 Alcohols with Pt and Pt-Ru Sputter Deposited Interdigitated Array Electrodes. *Electrochim. Acta* **2008**, *53*, 3029-3035.

17. Morita, M.; Niwa, O.; Horiuchi, T., Interdigitated Array Microelectrodes as Electrochemical Sensors. *Electrochim. Acta* **1997**, *42*, 3177-3183.
18. Ino, K.; Saito, W.; Koide, M.; Umemura, T.; Shiku, H.; Matsue, T., Addressable Electrode Array Device with Ida Electrodes for High-Throughput Detection. *Lab on a Chip* **2011**, *11*, 385-388.
19. Vandaveer, W. R.; Woodward, D. J.; Fritsch, I., Redox Cycling Measurements of a Model Compound and Dopamine in Ultrasmall Volumes with a Self-Contained Microcavity Device. *Electrochim. Acta* **2003**, *48*, 3341-3348.
20. Ma, C.; Contento, N. M.; Gibson, L. R., II; Bohn, P. W., Redox Cycling in Nanoscale-Recessed Ring-Disk Electrode Arrays for Enhanced Electrochemical Sensitivity. *Acs Nano* **2013**, *7*, 5483-5490.
21. Paeschke, M.; Wollenberger, U.; Kohler, C.; Lisec, T.; Schnakenberg, U.; Hintsche, R., Properties of Interdigital Electrode Arrays with Different Geometries. *Anal. Chim. Acta* **1995**, *305*, 126-136.
22. Seddon, B. J.; Wang, C. F.; Peng, W. F.; Zhang, X. J., Preparation and Amperometric Response of Carbon and Platinum Dual-Cylinder Microelectrodes. *Electrochim. Acta* **1995**, *40*, 455-465.
23. Baur, J. E.; Motsegood, P. N., Diffusional Interactions at Dual Disk Microelectrodes: Comparison of Experiment with Three-Dimensional Random Walk Simulations. *J. Electroanal. Chem.* **2004**, *572*, 29-40.
24. Cutress, I. J.; Wang, Y.; Limon-Petersen, J. G.; Dale, S. E. C.; Rassaei, L.; Marken, F.; Compton, R. G., Dual-Microdisk Electrodes in and Theory Transient Generator-Collector Mode: Experiment. *J. Electroanal. Chem.* **2011**, *655*, 147-153.
25. Barnes, E. O.; Lewis, G. E. M.; Dale, S. E. C.; Marken, F.; Compton, R. G., Dual Band Electrodes in Generator-Collector Mode: Simultaneous Measurement of Two Species. *J. Electroanal. Chem.* **2013**, *703*, 38-44.
26. Rajantie, H.; Strutwolf, J.; Williams, D. E., Theory and Practice of Electrochemical Titrations with Dual Microband Electrodes. *J. Electroanal. Chem.* **2001**, *500*, 108-120.
27. Bartelt, J. E.; Deakin, M. R.; Amatore, C.; Wightman, R. M., Construction and Use of Paired and Triple Band Microelectrodes in Solutions of Low Ionic-Strength. *Anal. Chem.* **1988**, *60*, 2167-2169.
28. Fosset, B.; Amatore, C.; Bartelt, J.; Wightman, R. M., Theory and Experiment for the Collector-Generator Triple-Band Electrode. *Anal. Chem.* **1991**, *63*, 1403-1408.
29. Belmont, C.; Girault, H. H., Coplanar Interdigitated Band Electrodes for Electrosynthesis .3. Epoxidation of Propylene. *Electrochim. Acta* **1995**, *40*, 2505-2510.
30. Tomcik, P.; Krajcikova, M.; Bustin, D., Determination of Pharmaceutical Dosage Forms Via Diffusion Layer Titration at an Interdigitated Microelectrode Array. *Talanta* **2001**, *55*, 1065-1070.
31. Tomcik, P.; Mesaros, S.; Bustin, D., Titrations with Electrogenerated Hypobromite in the Diffusion Layer of Interdigitated Microelectrode Array. *Anal. Chim. Acta* **1998**, *374*, 283-289.
32. Honda, N.; Inaba, M.; Katagiri, T.; Shoji, S.; Sato, H.; Homma, T.; Osaka, T.; Saito, M.; Mizuno, J.; Wada, Y., High Efficiency Electrochemical Immuno Sensors Using 3d Comb Electrodes. *Biosensors & Bioelectronics* **2005**, *20*, 2306-2309.
33. Barnes, E. O.; Fernandez-la-Villa, A.; Pozo-Ayuso, D. F.; Castano-Alvarez, M.; Lewis, G. E. M.; Dale, S. E. C.; Marken, F.; Compton, R. G., Interdigitated Ring Electrodes: Theory and Experiment. *J. Electroanal. Chem.* **2013**, *709*, 57-64.

34. Liu, Z. M.; Niwa, O.; Kurita, R.; Horiuchi, T., Carbon Film-Based Interdigitated Array Microelectrode Used in Capillary Electrophoresis with Electrochemical Detection. *Anal. Chem.* **2000**, *72*, 1315-1321.
35. Niwa, O.; Morita, M., Carbon Film-Based Interdigitated Ring Array Electrodes as Detectors in Radial Flow Cells. *Anal. Chem.* **1996**, *68*, 355-359.
36. Niwa, O.; Morita, M.; Tabei, H., Fabrication and Characteristics of Vertically Separated Interdigitated Array Electrodes. *J. Electroanal. Chem.* **1989**, *267*, 291-297.
37. Ma, C. X.; Contento, N. M.; Gibson, L. R.; Bohn, P. W., Redox Cycling in Nanoscale-Recessed Ring-Disk Electrode Arrays for Enhanced Electrochemical Sensitivity. *Acs Nano* **2013**, *7*, 5483-5490.
38. Fu, K. Y.; Han, D.; Ma, C. X.; Bohn, P. W., Electrochemistry at Single Molecule Occupancy in Nanopore-Confined Recessed Ring-Disk Electrode Arrays. *Faraday Discuss.* **2016**, *193*, 51-64.
39. Menshykau, D.; del Campo, F. J.; Munoz, F. X.; Compton, R. G., Current Collection Efficiency of Micro- and Nano-Ring-Recessed Disk Electrodes and of Arrays of These Electrodes. *Sens. Actuators, B* **2009**, *138*, 362-367.
40. Menshykau, D.; O'Mahony, A. M.; del Campo, F. J.; Munoz, F. X.; Compton, R. G., Microarrays of Ring-Recessed Disk Electrodes in Transient Generator-Collector Mode: Theory and Experiment. *Anal. Chem.* **2009**, *81*, 9372-9382.
41. Han, D.; Zaino, L. P.; Fu, K. Y.; Bohn, P. W., Redox Cycling in Nanopore-Confined Recessed Dual-Ring Electrode Arrays. *J. Phys. Chem. C* **2016**, *120*, 20634-20641.
42. Atighilorestani, M. B., A. G., Comparing the Electrochemical Response of Nanostructured Electrode Arrays. *Anal. Chem., Article ASAP, DOI: 10.1021/acs.analchem.7b00932* **2017**.
43. Davies, T. J.; Compton, R. G., The Cyclic and Linear Sweep Voltammetry of Regular and Random Arrays of Microdisc Electrodes: Theory. *J. Electroanal. Chem.* **2005**, *585*, 63-82.
44. Katelhon, E.; Wolfrum, B., On-Chip Redox Cycling Techniques for Electrochemical Detection. *Rev. Anal. Chem* **2012**, *31*, 7-14.
45. Liu, F.; Kolesov, G.; Parkinson, B. A., Preparation, Applications, and Digital Simulation of Carbon Interdigitated Array Electrodes. *Anal. Chem.* **2014**, *86*, 7391-7398.

Chapter 6 : Electrochemical Control of Light Transmission through Nanohole Electrode Arrays

This chapter is adapted from: M. Atighilorestani, D. P. dos Santos, R. FVV Jaimes, M. M Rahman, M. LA Temperini, and A. G. Brolo, Electrochemical Control of Light Transmission through Nanohole Electrode Arrays, ACS Photonics 2016, 3, 2375-2382. Copyright: Reproduced with permission. The supporting information has been embedded within the text.

Control of the surface plasmon resonance (SPR) enhanced light transmission through an array of nanoholes on gold films was achieved by modifying the metal surface with a thin layer of electroconductive polymer film. The electrochromic properties of the polymer were then triggered by tuning the electrochemical potential. Conducting polymer-modified nanohole array electrodes were prepared by electrodeposition of polypyrrole (PPy) using cyclic voltammetry. Only the gold surfaces inside the holes were accessible for film formation. The doping level of the PPy film was tuned by the electrochemical potential allowing fine control for the amount of light transmitted through the arrays. The concept demonstrated here paves the way for the fabrication of a new type of controllable nanometric optoelectronic devices based on polymeric materials.

6.1 Introduction

The increasing need for smaller and faster optoelectronic devices is unquestionable. However, the minimum size of conventional photonics devices is limited by the diffraction of light. Moreover, traditional electronics systems suffer from significant signal and thermal delay problems[1]. Surface plasmon resonance (SPR) emerges as a key nanotechnology to bridge between photonics and electronics on the nanoscales, based on its capability to couple light to coherent electronic excitations near a metallic nanostructured surface[2-4]. The ability to active control and tune the SPR responses in real time by external parameters (active plasmonic systems[1]) have important potential applications in nanophotonic integrated circuits, optical communication, and high-performance displays[5-6]. One convenient, easy, and low-cost approach for reversible modulation of SPR properties is the use of an electroconductive polymer immobilized on metallic nanostructured surfaces[7-13]. Conductive polymers, such as polypyrrole (PPy), can be electrochemically synthesized simply by oxidative polymerization of the monomers[14]. In these kinds of active plasmonic devices, the metallic nanostructures serve as both the SPR modulating medium and the working electrode[15]. Combined SPR and electrochemical measurements, electrochemical SPR (EC-SPR), is also a powerful approach for in-situ observation and characterization at electrode/electrolyte interfaces [15-18]. The electropolymerization proceeds only at the electrode surface and results in uniform thin polymer films. In addition, the thicknesses of the electrodeposited polymer film can be easily controlled by monitoring the electric charge[19-21]. Electroconductive polymers can be reversibly switched from a doped form (conductive state) to a dedoped form (insulating state) using an externally applied potential. The structures of PPy in the reduced (dedoped) and oxidized (doped) states are presented in Scheme 1. The optical properties of a polymer are related to its doping levels; therefore, the applied potential can easily modulate

the SPR response. This type of control over the SPR properties by tuning the doping level of electroconductive polymers have been mainly performed on nanoparticles[8-13, 22-23] . More recently other plasmonic nanostructures have been used as active plasmonic systems, including nanoslits[24] and nanogratings[7]. The advantage of using thin metallic nanostructured films, such as slits and grating patterns (e.g., nanohole arrays), as the active plasmonic system is that they support enhanced light transmission enabled by SPR[25-28].

Control over extraordinary transmission of gold nanohole arrays has been previously demonstrated using electro-optical effect[29-30] (control of light by voltage), all-optical effect[31-32] (control of light by light), and thermo-optical effect[33] (control of light by temperature). For the all-optical effect, the light transmission control was carried out by spin-coating a thin layer of nonlinear polymer[32] or by spin coating of poly(methyl methacrylate) (PMMA) doped with a dye molecule[31] on the surface of the nanohole arrays. A thermoresponsive polymer was integrated with nanohole array in the case of control of the light transmission using thermo-optical effects[33]. Light transmission control using electro-optical effect has been conducted by the integration of liquid crystals with nanohole arrays[29-30]. However, we are not aware of any previous report on the electro-optical control in nanohole arrays using electroconductive polymers.

In this work, 100 nm gold films on glass slides were coated with an insulating layer. Nanoholes were milled in the multilayer structure, generating nanoelectrodes. The arrays of nanoholes were then modified with electrically conducting polypyrrole (PPy), see Scheme 1. The in situ electrodeposition of PPy by cyclic voltammetry was monitored by SPR-enhanced transmission. The SPR enhanced transmission spectra showed a dramatic red-shift and intensity changes during the electropolymerization process. This correlated well with the changes in the dielectric properties of the film as it grows and switches between redox states. The SPR transmitted intensity through

the modified nanoholes array was controlled and tuned externally by the doping−dedoping process (represented in Scheme 1). The potential-dependent changes in transmission intensity due to the PPy doping/dedoping process were reversible, as expected for a conductive polymer film.

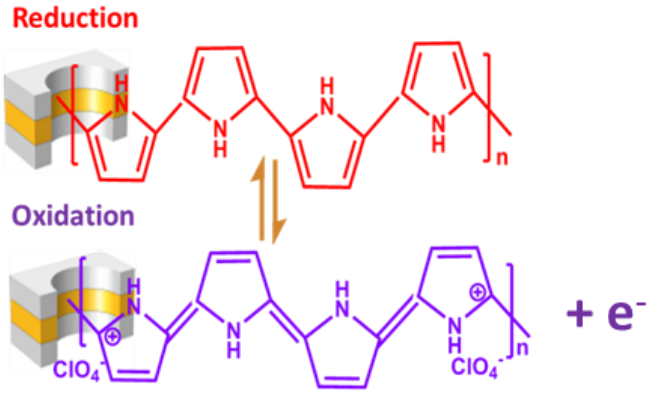

Scheme 1. Structures of PPy in the Reduced (Dedoped) and Oxidized (Doped) States. All experiments were performed using ClO_4^- as the dopant anion (0.1 M $KClO_4$ solutions).

6.2 EXPERIMENTAL SECTION

6.2.1 Materials

Sodium perchlorate ($NaClO_4$; ACP) was used as received. Pyrrole (Py; Aldrich) was purified by distillation and stored in the dark at a low temperature before use. Commercial glass gold slides were purchased from EMF, Ithaca, NY. The glass slides were coated with 100 nm thick Au and 5 nm thick Cr adhesion layers. Then about 100 nm, thick Si_3N_4 insulating layer was deposited on top of the gold films by plasma enhanced chemical vapor deposition (PECVD). Films of Au and SiO_2 (100 nm) with 5 nm Ti adhesion (Ti (5 nm)/Au (100 nm)/Ti (5 nm)/SiO_2 (100 nm)) were deposited on glass substrates using sputtering deposition system (MANTIS, QUBE series). All

solutions were prepared using ultrapure water (18.2 MΩ cm) obtained from NANO pure Diamond TM deionization system (Barnstead).

6.2.2 Nanohole Arrays Fabrication

Arrays of nanoholes were fabricated by focused-ion-beam (FIB) milling into the gold glass slides coated with an insulating layer (either SiO_2 or Si_3N_4)[34]. The 30 × 30 nanoholes (∼13.3 μm × 13.3 μm) arrays were prepared in each sample with a nanohole periodicity of 450 nm. The diameter of the holes was 200 nm. The fabricated arrays were imaged by scanning electron microscopy (SEM), as shown in Figure 6-1. Additional SEM images and differential pulse voltammetry measurements are presented in Figure 6-2 and Figure 6-3, respectively to confirm that only the inside of the nanoholes was accessible electrochemically.

SEM images were obtained in order to demonstrate that the polymer growth only occurred inside the nanoholes. Figure 6-2a shows the top view SEM of an array before the electropolymerization, while Figure 6-2b shows a tilted image of the same array after the polymerization. No significant accumulation of material was observed on the top surface (outside the hole area) in Figure 6-2b (after electropolymerization). In fact, the morphology of the top surface has not significantly changed between Figure 6-2a and Figure 6-2b. The absence of materials accumulation on the top surface of the array showed in Figure 6-2b, is a good indication that only the inside area of the holes was electrochemically accessible.

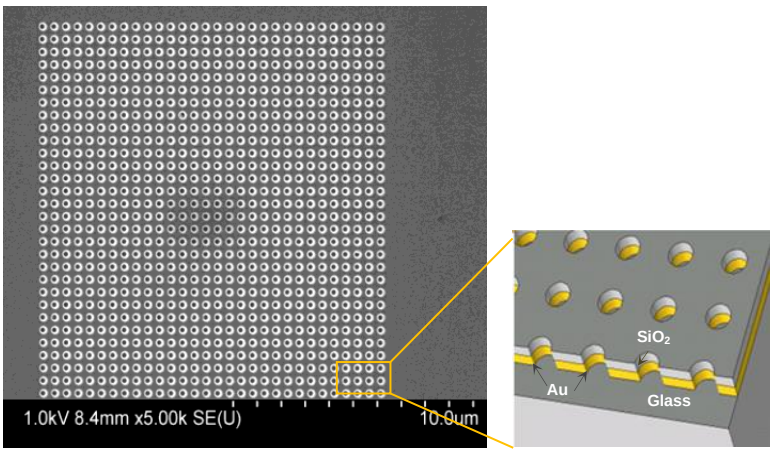

Figure 6-1. SEM image of the nanohole electrode array (30 × 30) fabricated by focused ion beam milling through a SiO_2 film (100 nm thick) on top of a gold film (100 nm thick). Equivalent arrays with Si_3N_4 coatings were also fabricated. The hole diameter was 200 nm, and the periodicity was 450 nm, as indicated in the cross-section schematic diagram.

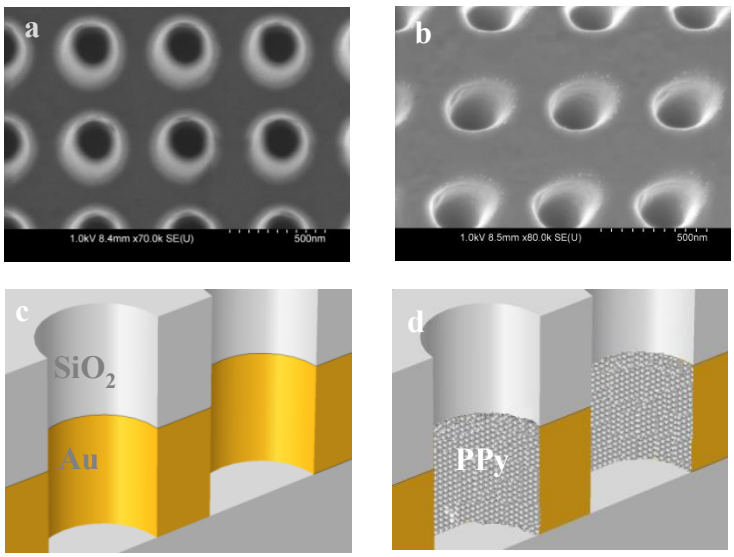

Figure 6-2**.** SEM images of the nanohole electrodes array a) top-view, before PPy electropolymerization; b) tilted view, after the PPy polymerization process. The growth of PPy on the top surface was prevented by the SiO_2; c) and d) cross-section schematic diagrams of the nanohole electrodes before and after electropolymerization, respectively.

Other techniques were attempted to further confirm the blocking of the top surface towards electrochemical processes. EDX characterization of the film inside the nanoholes was attempted, but the N and C signals were too weak relative to Au and Si, and the results were not conclusive. Cross-section FIB-cut of the samples were also obtained and imaged by SEM, but the thin organic film seemed to detach from the Au surface yielding, again, inconclusive results. Finally, it was possible to demonstrate further that only the inside area was electrochemically active by performing differential pulse voltammetry (DPV) [35-36].

DPV is similar to CV, in the sense that the current is recorded during a potential scan. However, in DPV the linear potential scan of CV is substituted by a staircase potential ramp. The current is then measured in each step after a certain time, and the current difference between the steps is plotted against the potential. This procedure eliminates capacitive contributions to the total current, allowing the current component to faradaic processes to be identified. This is useful for nanoelectrodes since the small area yields low absolute current values that can be buried in noise due to capacitive events. Figure 6-3 shows a DPV curve obtained using 1 mM of a reversible redox pair ($[Fe(CN)_6]^{4-}/([Fe(CN)_6]^{3-}]$) in 0.1 M Na_2SO_4 for an array of nanohole electrodes. The magnitude of the anodic current presented in Figure 6-3 is ~ 1.5nA. This current value is compatible to the expected for a reversible electrochemical process occurring in an electroactive area just inside the apertures.

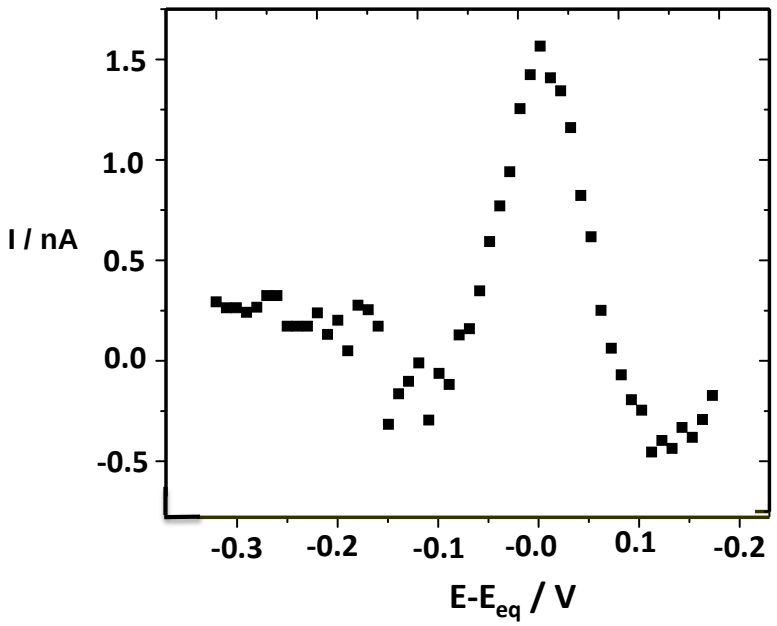

Figure 6-3. DPV experiment using an array of nanoholes. Hole diameter was 200 nm, and the periodicity was 450 nm. The top surface was insulated using Si_3N_4. 1 mM $[Fe(CN)_6]^{4-}$ in 0.1 M Na_2SO_4. The scan rate was 100 mV/s and 5 mV step amplitude at 100 Hz.

6.2.3 In Situ EC-SPR Measurements Setup

Figure 6-4 schematically shows the setup for the electrochemical−SPR combined experiments. A slide containing an array of nanoholes was fastened in a Teflon cell with an O-ring creating a liquid-tight seal. The Teflon cell volume was about 2.5 mL. The EC-SPR cell was then mounted on the stage of an upright metallurgical microscope (Olympus BHSM). Surface plasmons excitations at the metal-dielectric interface were carried out in a collinear transmission mode using a 63× water immersion objective lens (Leica), with NA (numerical aperture) = 0.9. The EC-SPR cell had an opening of about 26 mm diameter; the 63× water immersion objective lens was

immersed in the electrochemical test solution inside the cell and was focused only on one single array of nanoholes. The 100 W halogen lamp from the Olympus BHSM microscope was the white light source for the SPR transmission measurements. The transmitted light through the illuminated array was then collected by an optical fiber (NA = 0.22 and 25.4° full collection angle), connected to a computer-controlled UV−vis spectrometer (USB 4000-UV−vis Ocean Optics). Electrochemical measurements were carried out simultaneously using a three electrode system. The cylindrical Au confined within each of the FIB fabricated nanoholes was used as both the surface plasmon medium and the working electrode. A platinum wire was used as the counter electrode, and an $Ag|AgCl|KCl_{(satd)}$ electrode served as the reference electrode. A computer-controlled Autolab potentiostat-galvanostat (PGSTAT 30) was used for the electrochemical measurements. The PPy films were synthesized on the cylindrical Au within each of nanohole in the array by performing continuous potential cycling between −0.8 and 0.7 V at a scan rate of 20 mV/s from an aqueous solution containing 0.05 M Py monomer and 0.1 M $NaClO_4$ as the supporting electrolyte. Five cycles were performed for the film preparation. The PPy film growth process was concurrently monitored by SPR. After the film growth, the PPy-modified nanohole arrays were thoroughly rinsed with a monomer free 0.1 M $NaClO_4$ solution. Then EC-SPR cell was filled only with supporting electrolyte (0.1 M $NaClO_4$), and the electrochromic properties of the PPy-modified nanohole electrodes arrays were studied by combined transmission-SPR with cyclic voltammetry as well as potential steps.

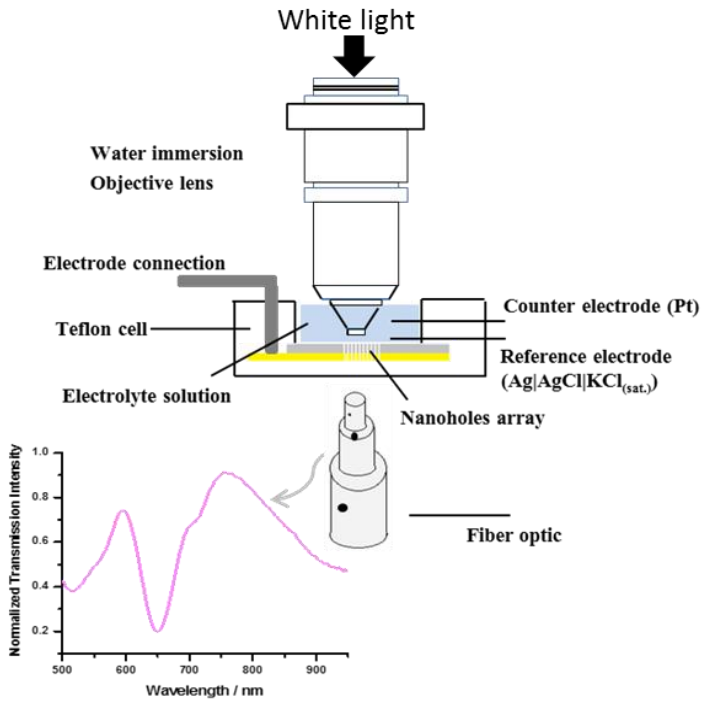

Figure 6-4. Schematic of electrochemical SPR experimental setup.

6.3 RESULTS AND DISCUSSION

6.3.1 In Situ Monitoring of PPy Electropolymerization by Light Transmission through an Array of Nanohole Electrodes

The electrochemical formation of the PPy film on the gold electrode surface confined inside the array of nanoholes was monitored by measuring the transmission-SPR spectra. Figure 6-5 shows the evolution of the normalized transmission-SPR spectra for an array of nanoholes during five potential scans. The color scale bar in Figure 6-5 corresponds to the intensity values of the transmitted light: the red color (top of the scale bar) is for the highest transmission intensity and the blue color (bottom of the scale bar) the lowest transmission intensity value.

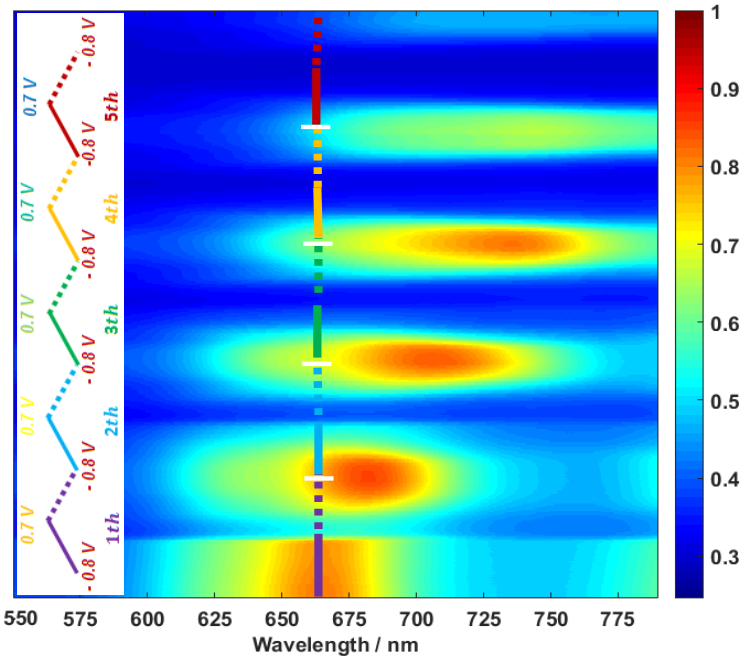

Figure 6-5. Normalized transmission-SPR spectra temporal evolution of an array of nanoholes during the PPy electropolymerization. Five potential scans between −0.8 V and +0.7 V at a scan rate of 20 mV/s are shown. The electropolymerization was carried out in 0.05 M pyrrole (Py) and a 0.1 M $NaClO_4$ solution. The color scale bar indicates the normalized transmission intensity values. The colored triangle wave on the left side of the Figure shows the five potential ramps. The colors of the triangular waves match the vertical line in the Figure (solid line-dotted line). The solid and dotted segments, in both the triangular waves and in the vertical solid, dotted line, represent the anodic and the cathodic part of the scan, respectively.

Periodic arrays of nanoholes on thin gold films support an optical phenomenon called extraordinary optical transmission (EOT). In EOT, the intensity of the light transmitted through the nanoholes at certain wavelengths is significantly enhanced due to excitation of surface plasmon resonances by grating coupling[37]. For a square array of nanoholes, the resonance wavelengths can be estimated using Eq. 6-1 (for normal incidence ($\theta=0^0$))[38].

$$\lambda_{max}(i,j) = \frac{a_0}{\sqrt{i^2 + j^2}} \sqrt{\frac{\varepsilon_m \varepsilon_d}{\varepsilon_m + \varepsilon_d}} \qquad \text{Eq. 6-1}$$

where a_0 is the spacing between the holes (periodicity), and ε_m and ε_d are dielectric properties of the metal and of the dielectric in contact with the metal, respectively. The parameters i and j correspond to the scattering order of the grating. The periodicity of the array in Figure 6-5 was 450 nm, and the gold surface was coated with a thin layer of SiO_2 (see details of the sample fabrication in the Experimental Section). Considering the refractive index of SiO_2 equals to 1.5 and using the optical properties of gold from Johnson and Christy, [39] the transmission peak in Figure 6-5, initially centered at ~660 nm, can be assigned to the (1, 0) resonance mode of the array. The peak position was slightly different when Si_3N_4 was used as the insulator coating, but the resonance of all arrays before polymerization was within 640−660 nm, which is consistent with the (1, 0) mode for arrays of nanoholes with 450 nm periodicity.

The solid-dashed vertical line in Figure 6-5, situated at ~660 nm, indicates the maximum transmission before electropolymerization. This vertical line serves as a guide to demonstrate the SPR shift during the experiment. The potential sweep of each cyclic voltammogram is shown as colored triangle waves on the left side of Figure 6-5. Different colors represent different sweeps; the solid portion is the anodic scan while the dotted portion is the cathodic scan, respectively. The (1, 0) peak in the transmission-SPR systematically redshifts in Figure 6-5 due to changes in the dielectric constant at the gold surface caused by two effects: the polymer film growth and the doping−dedoping processes (Scheme 1) of the resulting PPy film.

The electropolymerization led to a continuous growth of the PPy film. This process contributes to a SPR red-shift since the dielectric constant of the film is higher than that of the solution containing

the Py monomers.[40-41] Although this observation is in agreement with Eq. 6-1, that equation merely considers a surface wave propagating on top of the array. In the experiment described here, the top surface is blocked, and the film growth occurs only inside the holes (see Figure 6-2 and Figure 6-3). Therefore, other contributions must be taken into account to explain the strong red-shift observed in Figure 6-5. The sensitivity to refractive index changes inside the nanoholes has been investigated mainly in the context of biosensing[42-44]. The effect of the in-hole environment on the SPR of grating structures is significant because the EOT mechanism also involves a contribution from the localized surface plasmon mode inside the holes[45-48]. These contributions are essential to explain, for instance, the hole-shape dependence on the resonance conditions[49-50]. The overall EOT mechanism is complex and involves the coupling of the mode inside the holes with the diffraction characteristics of the top surface. On the other hand, the effect of dielectric changes inside the hole on the resonance position can be explained, in a first approximation, by just considering the optical mode inside the hole. The Helmholtz equation provides a solution for the longitudinal field of the lowest order mode[34]. The large longitudinal field component at the surface is responsible for the strong in-hole sensitivity. A similar effect has been observed for metallic mesh structures in the middle infrared range. The introduction of a dielectric material (a polystyrene bead, in that case) inside the hole led to a strong red-shift of the grating resonance and an enhancement in the optical transmission[51].

PPy is a known electrochromic material; that is, its optical properties (color) vary with the degree of oxidation (doping level). In order to verify this effect, we have electrochemically deposited, using the same parameters as in Figure 6-5, a PPy film on a smooth gold surface, and then measured the spectral changes provoked by an applied potential in reflectivity mode. The data, presented in Figure 6-6, indicated a broad absorption band in the visible range throughout the near-

infrared (~800 nm) for the oxidized form (potentials more positive than −0.2 V). The reduced form dominated at applied potentials more negative than −0.2 V and showed strong reflectivity centered at around 700 nm. As observed from Figure 6-5, in addition to the SPR red-shift, the transmission intensity also changed within each potential cycle. The transmission-SPR intensity is low when the PPy is deposited during the anodic scan (at potentials more positive than −0.2 V), but it increases during the cathodic scan (at potentials more negative than −0.2 V). The increase in transmission-SPR intensity upon reduction (for potential more negative than −0.2 V) is due to changes in the optical properties of the PPy film (shown in Figure 6-6) and not because of change in the PPy film thickness. During anodic and cathodic scans the PPy film is submitted to a redox (doping− dedoping) process (Scheme 1), which changes its optical properties and conductivity (the value of the imaginary part of the complex dielectric constant depends on both the optical and the conductive properties of the polymer)[40, 52]. The anodic scan (potentials more positive than −0.2 V) was related to the formation of a light absorbing PPy film in the wavelength range between ~500 to ~800 nm. The reduced form of PPy film does not absorb light strongly in that wavelength range[53-56]. The PPy film absorbs light at wavelengths shorter than ~500 nm in its reduced form[53, 55-56]. The two main observations, red shift, and intensity changes, can be further visualized in Figure 6-7. The observations from Figure 6-5 are in excellent agreement with the spectral characteristics of the PPy redox species indicated in Figure 6-6.

The optical properties of the PPy film at different applied potential were obtained by reflectance spectroscopy. Figure 6-6 shows the in-situ UV–vis reflectance spectra of the PPy film in 0.1 M $KClO_4$ recorded in a potential range between -0.8 to +0.8 V.

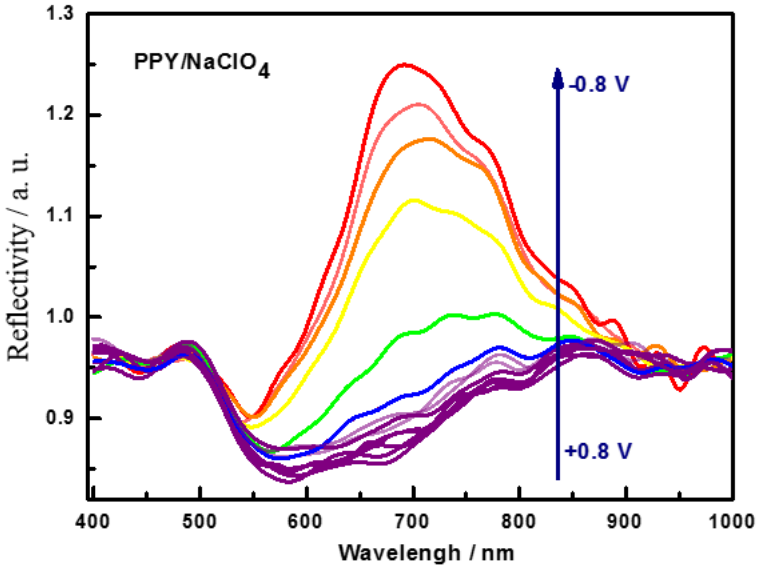

Figure 6-6. In-situ UV–vis reflectance spectra for a PPy modified gold slide in a monomer-free 0.1 M $NaClO_4$ solution carried out in the potential range between−0.8 and 0.8V (spectra obtained in 100 mV intervals).

Figure 6-7 summarizes the two effects (red shift and intensity changes) observed in the CVs in the presence of the Py monomer.

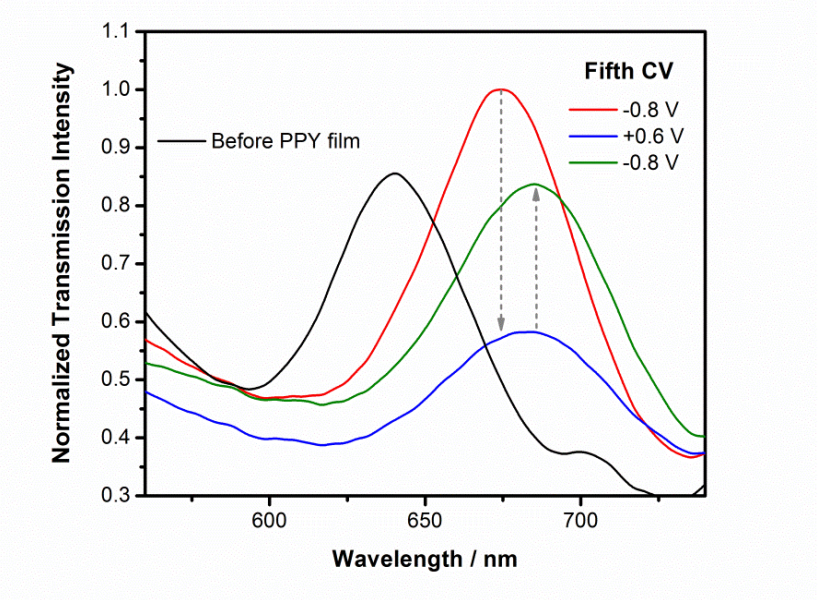

Figure 6-7**.** Selected transmission spectra from an array of nanoholes in 0.1 M $NaClO_4$ and 0.05 M pyrrole (Py) obtained in a CV experiment similar to Figure 6-5 in the main text. Arrays fabricated using a 100 nm gold film coated with 100 nm Si_3N_4.

The black curve in Figure 6-7 was obtained at -0.8 V before the electropolymerization. After full four CVs, the red curve was recorded at -0.8 V, at the start of the fifth scan. Therefore, the peak shift from the original black curve was mainly due to the film growth. The potential was then swept to +0.6 V (the anodic scan). At that potential, the film oxidizes, and the intensity of the transmitted light decreased dramatically (blue curve) because the oxidized form of the film absorbs light strongly in the visible range. After +0.6 V the direction of the potential sweep was switched to the initial potential, -0.8 V, the cathodic scan (green spectrum). Notice that the green curve is red-shifted and less intense than the one obtained before at the same potential (red curve). This is because the excursion to anodic (positive) potentials during the fifth scan has led to the further accumulation of PPy film inside the nanoholes.

6.3.2 Tuning of Transmission Intensity of an Array of Nanoholes Modified with PPy by Cyclic Voltammetry

After the electropolymerization, the PPy-modified array of nanoholes was thoroughly rinsed with a monomer-free 0.1 M $NaClO_4$ solution. Then, the electrochromic properties of the PPy-modified array of nanoholes electrodes were further explored by combining transmission-SPR and cyclic voltammetry. Figure 6-8 presents a comparison of the electrochemical behavior (cyclic voltammograms in a monomer-free 0.1 M $NaClO_4$ solution) of a flat gold slide modified with PPy (a macroelectrode with the surface area of about 3.14 cm^2, Figure 6-8a) and a SiO_2-coated gold

slide containing one PPy-modified array of nanoholes (Figure 6-8b). The cyclic voltammograms from Figure 6-8a, b were recorded in the same EC-SPR cell. Two characteristic voltammogram curves were obtained; a peak-shaped voltammogram (Figure 6-8a) and a quasi-sigmoidal shaped curve (Figure 6-8b) for the PPy-modified macroelectrode and for the PPy-modified nanoholes array, respectively. The peak-shaped voltammogram can be related to the linear diffusion to the macroelectrode while the quasi-sigmoidal voltammogram can be correlated to the mixed spherical and linear diffusion toward the array of nanoholes (nanoelectrodes). The transport characteristics of an array of nanoelectrodes depend on several factors, such as the time scale of the experiment, the diffusion coefficient of the electroactive species, the radius and spacing between nanoelectrodes in the array, and on the dimensions of the whole array [57]. When the diffusion layers of the nanoelectrode elements on the array strongly overlap, then the array behaves like a single microelectrode with an area corresponding to the whole geometric area of the array[57]. The nanoholes were separated by 450 nm in the experiment reported in Figure 6-8b. The short distance between the nanoholes results in an extreme overlap of the diffusion layers of each individual element in the time scale of the CV experiments. Therefore, the whole nanohole array behaved as a single 13.25 μm × 13.25 μm (size of the array) microelectrode [57].

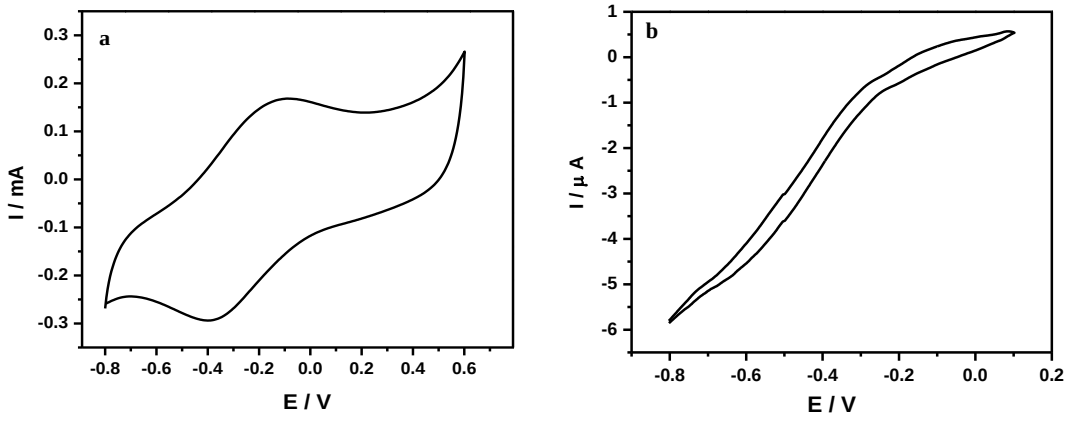

Figure 6-8. Cyclic voltammograms obtained in a monomer-free 0.1 M $NaClO_4$ solution. The scan rate was 20 mV/s. (a) Glass/Cr/Au PPy-modified electrode−flat electrode with the surface area of about A = 3.14 cm^2; (b) Glass/Ti/Au/Ti/SiO_2 slide with an array of nanoholes (450 nm periodicity and 200 nm hole diameter). The inside surface of the holes was coated with PPy, as described in the text.

Transmission-SPR spectra were recorded during the acquisitions of the CV in Figure 6-8b, and they are presented in Figure 6-9a (only the anodic scan (from −0.8 to 0.1 V) is shown for simplicity). Figure 6-9b plots the changes in the transmission-SPR intensity as a function of applied potential for a PPy-modified array of nanoholes array at the wavelength of 755 nm (dashed blue vertical line in Figure 6-9a). The transmission-SPR intensity gradually decreased during the anodic scan reaching a minimum at ∼−0.2 V (redox process indicated in Scheme 1). The minimum value did not change at more positive potentials, corresponding to the steady state current in the CV (Figure 6-8b). In contrast, during the cathodic scan, the transmission-SPR intensity started to gradually increase from potentials more negative than −0.2 V and reached a maximum transmission intensity at the cathodic limit, −0.8 V. As it can be seen by comparing Figure 6-8b and Figure 6-9b, the transmission-SPR intensity changes follow the same trend as the current in the voltammogram. The behavior in Figure 6-8b and Figure 6-9 corroborate the link between the

electrochemically controlled doping level (and conducting state) and the optical properties of the PPy film (Figure 6-6) [58-59]. As it was mentioned before, through the process known as doping dedoping[60], represented in Scheme 1, PPy can reversibility switch between its oxidized conductive and reduced-insulating states by applying appropriate electrical potentials[14]. The amount of light that PPy absorbs at a particular wavelength range is associated with its oxidation states[14, 56, 61] . Therefore, each applied potential in the cyclic voltammetry scan can modulate the optical properties of the polymer films and consequently results in a change in the transmission-SPR intensity of the modified nanoholes array. The transmission-SPR intensity is proportional to the applied potentials (Figure 6-8b and Figure 6-9b), indicating that the extent of the transmitted light intensity through the PPy-modified nanoholes array can be fine-tuned and adjusted by electrochemical potential. The changes in the optical properties during the potential scans are reversible for the PPy films. Accordingly, the ability to fine control the transmitted intensity through the modified nanoholes array by the applied potentials can lead to new applications for SPRbased optical sensors[62].

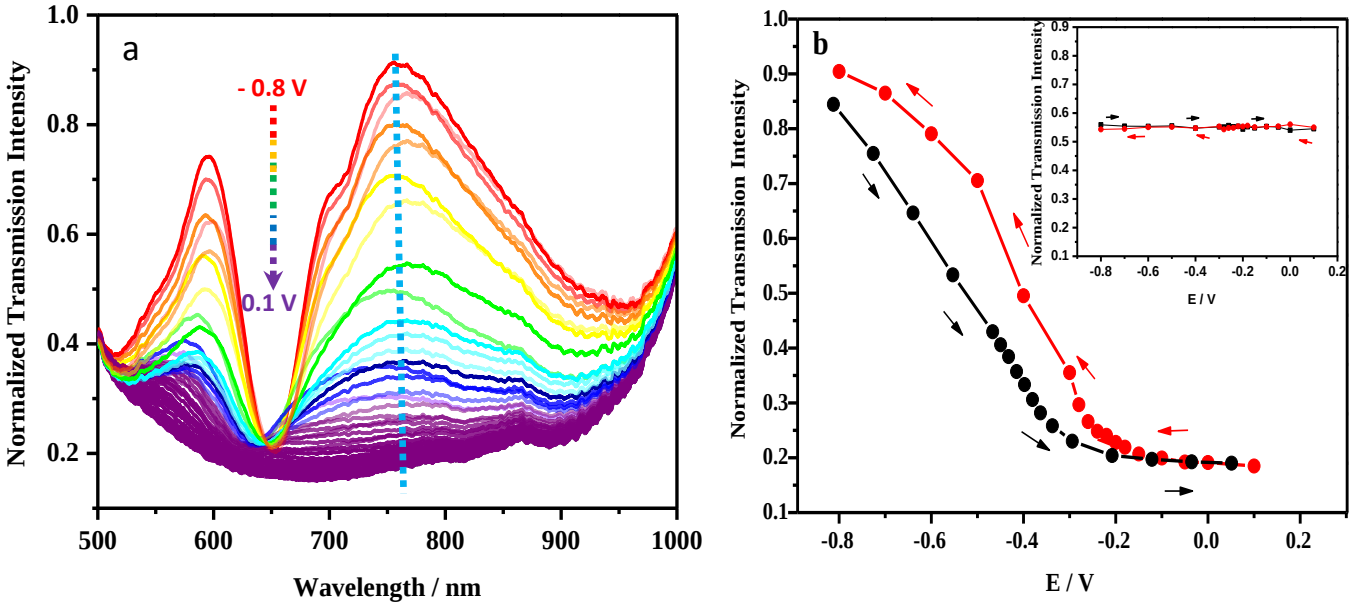

Figure 6-9. (a) In situ transmission-SPR curves obtained during the CV anodic scan (from −0.8 to 0.1 V) for a PPy-modified nanohole electrode array in a monomer-free 0.1 M $NaClO_4$ solution; (b) Transmission-SPR intensity as a function of applied potential for the PPy-modified nanoholes array at a fixed wavelength of 755 nm (dashed blue vertical line in (a)). The black line shows the transmission-SPR intensity changes during the anodic scan (from −0.8 to 0.1 V). The red line indicates the transmission-SPR intensity changes during the cathodic scan (from 0.1 to −0.8 V). The inset represents the transmission-SPR intensity at 755 nm as a function of applied potential for bare nanoholes array (before PPy electropolymerization) in a monomer-free 0.1 M $NaClO_4$ solution. The scan rate was 20 mV/s.

6.3.3 Electro-Optical Switching Using PPy-Modified Nanoholes Array

The electrochromic properties of the PPymodified arrays of nanohole electrodes were further demonstrated in potential step experiments presented in Figure 6-10. The transmission-SPR intensity was monitored at a fixed wavelength (λ = 755 nm), while the polymer film was electrochemically switched between its neutral and oxidized states in a monomer free 0.1 M $NaClO_4$ solution. The electrode potential was repeatedly stepped between −0.8 V (where the PPy film was in its fully neutral state) and +0.1 V (where the PPy film was in its fully oxidized state). Each potential was applied for 10 s. Figure 6-10 shows the transmission-SPR intensity changes (λ = 755 nm) as a function of time. It is clear from Figure 6-10 that the transmission-SPR intensity could be electrically switched on and off by changing the polymer film between its fully doped and dedoped states. Dramatic transmission-SPR intensity changes at anodic and cathodic applied potentials were attributed to the high optical contrast between doped and dedoped states of the PPy film. The transmission-SPR intensity changes in Figure 6-10 are consistent with the observed transmitted intensity changes during the CV measurements in Figure 6-8b. The transmission-SPR intensity experienced a slight delay before achieving steady state after each applied potential due to the transport of the perchlorate counterion. However, the intensity response of the PPy to the applied potential showed a good stability for over more than 120 repetitive potential steps.

The work presented here demonstrated the capabilities of nanohole arrays in combination to conductive polymers for optoelectronic applications. The field of conductive polymeric materials is very active, and there are several reported examples of materials that present faster response time than PPy. For instance, two electrochromic polymers, polyaniline (PANI) and poly(2,2-

dimethyl-3,4 propylenedioxythiophene) (PolyPro-DOT-Me2) electrodeposited on the Au nanoslit and Al nanoslit (used active plasmonic systems), respectively, showed a good stability and fast electrochromic switching [24]. Another potential new direction for this platform is to explore the controlled transmission through a single nanohole. In this limiting case, a practical subwavelength optical switching device can be implemented.

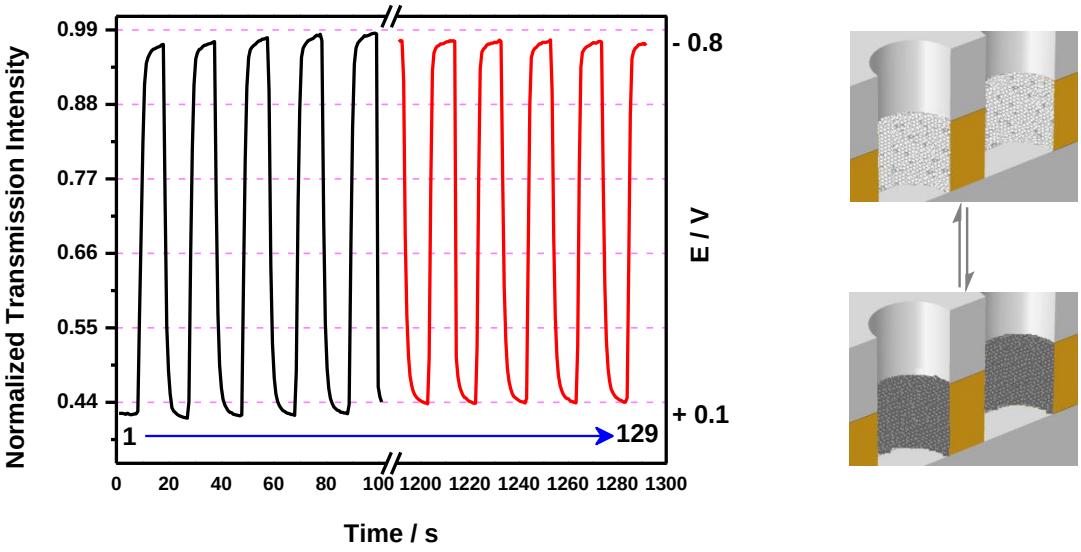

Figure 6-10. Electrochemical switching of 755 nm light transmitted through a PPy-modified nanohole electrodes array (glass/Ti/Au/Ti/SiO_2 slide with an array of nanoholes; 450 nm periodicity and 200 nm hole diameter) in a monomer-free 0.1 M $NaClO_4$ solution. Potential steps were between −0.8 and 0.1 V, with a residence time of 10 s. A cross-section schematic diagram of the PPy-modified nanohole electrodes arrays at anodic (absorbing) and cathodic (transparent) limits is also shown. The step numbers (1 → 129) are indicated in the figure.

6.4 CONCLUSIONS

Nanoholes electrode arrays were fabricated on a gold slide coated with a thin layer of a dielectric material using focused ion beam milling. The electroactive area of the nanoelectrodes was

confined to the gold surface inside the holes. The plasmonic properties of the nanoholes electrode arrays (extraordinary light transmission through the array of nanoholes) allowed simultaneous transmission-SPR and electrochemical measurements. The surface of the nanohole electrodes was modified by the electrically conducting PPy polymer. The electrodeposition of PPy by cyclic voltammetry was simultaneously monitored by SPR enhanced transmission. The maximum transmission-SPR showed a dramatic red-shift and intensity changes during the electropolymerization process. The observed changes in the transmission-SPR curves were associated with changes in the dielectric constant due to film growth and also due to the modulation of the doping level of the PPy as the polymer switched between its redox states. The electrochromic properties of the PPy-modified nanohole electrode arrays were evaluated by in situ transmission-SPR coupled to cyclic voltammetry. The transmitted light intensity through the modified nanohole arrays was switched on and off by potential steps, demonstrating the potential of this platform to be incorporated into optoelectronic devices.

6.5 ACKNOWLEDGMENTS

We would like to thank Dr. M. J. L. Santos for the help with the measurement of the UV−vis reflectance spectra of the PPy film. This work was supported by a Discovery Grant provided by NSERC. The authors thank the Center for Advanced Materials and Related Technologies (CAMTEC) for access to the fabrication and characterization facilities.

6.6 REFERENCES

1. Sun, Y.; Jiang, L.; Zhong, L.; Jiang, Y.; Chen, X., Towards Active Plasmonic Response Devices. *Nano Res.* **2015**, *8*, 406-417.
2. Dionne, J. A.; Diest, K.; Sweatlock, L. A.; Atwater, H. A., Plasmostor: A Metal-Oxide-Si Field Effect Plasmonic Modulator. *Nano Lett.* **2009**, *9*, 897-902.
3. Muhlschlegel, P.; Eisler, H. J.; Martin, O. J. F.; Hecht, B.; Pohl, D. W., Resonant Optical Antennas. *Science (Washington, DC, U. S.)* **2005**, *308*, 1607-1609.
4. Ohtsu, M.; Kobayashi, K.; Kawazoe, T.; Sangu, S.; Yatsui, T., Nanophotonics: Design, Fabrication, and Operation of Nanometric Devices Using Optical near Fields. *IEEE J. Sel. Top. Quantum Electron.* **2002**, *8*, 839-862.
5. Jiang, M.-M.; Chen, H.-Y.; Shan, C.-X.; Shen, D.-Z., Tunability of Hybridized Plasmonic Waveguide Mediated by Surface Plasmon Polaritons. *Phys. Chem. Chem. Phys.* **2014**, *16*, 16233-16240.
6. Lee, H. W.; Papadakis, G.; Burgos, S. P.; Chander, K.; Kriesch, A.; Pala, R.; Peschel, U.; Atwater, H. A., Nanoscale Conducting Oxide Plasmostor. *Nano Lett.* **2014**, *14*, 6463-6468.
7. Baba, A.; Tada, K.; Janmanee, R.; Sriwichai, S.; Shinbo, K.; Kato, K.; Kaneko, F.; Phanichphant, S., Controlling Surface Plasmon Optical Transmission with an Electrochemical Switch Using Conducting Polymer Thin Films. *Adv. Funct. Mater.* **2012**, *22*, 4383-4388.
8. Leroux, Y.; Eang, E.; Fave, C.; Trippe, G.; Lacroix, J. C., Conducting Polymer/Gold Nanoparticle Hybrid Materials: A Step toward Electroactive Plasmonic Devices. *Electrochem. Commun.* **2007**, *9*, 1258-1262.
9. Leroux, Y.; Lacroix, J. C.; Fave, C.; Stockhausen, V.; Felidj, N.; Grand, J.; Hohenau, A.; Krenn, J. R., Active Plasmonic Devices with Anisotropic Optical Response: A Step toward Active Polarizer. *Nano Lett.* **2009**, *9*, 2144-2148.
10. Leroux, Y.; Lacroix, J. C.; Fave, C.; Trippe, G.; Felidj, N.; Aubard, J.; Hohenau, A.; Krenn, J. R., Tunable Electrochemical Switch of the Optical Properties of Metallic Nanoparticles. *Acs Nano* **2008**, *2*, 728-732.
11. Leroux, Y. R.; Lacroix, J. C.; Chane-Ching, K. I.; Fave, C.; Felidj, N.; Levi, G.; Aubard, J.; Krenn, J. R.; Hohenau, A., Conducting Polymer Electrochemical Switching as an Easy Means for Designing Active Plasmonic Devices. *J. Am. Chem. Soc.* **2005**, *127*, 16022-16023.
12. Schaming, D.; Van-Quynh, N.; Martin, P.; Lacroix, J.-C., Tunable Plasmon Resonance of Gold Nanoparticles Functionalized by Electroactive Bisthienylbenzene Oligomers or Polythiophene. *J. Phys. Chem. C* **2014**, *118*, 25158-25166.
13. Stockhausen, V.; Martin, P.; Ghilane, J.; Leroux, Y.; Randriamahazaka, H.; Grand, J.; Felidj, N.; Lacroix, J. C., Giant Plasmon Resonance Shift Using Poly(3,4-Ethylenedioxythiophene) Electrochemical Switching. *J. Am. Chem. Soc.* **2010**, *132*, 10224-10226.
14. Genies, E. M.; Pernaut, J. M., Characterization of the Radical Cation and the Dication Species of Polypyrrole by Spectroelectrochemistry - Kinetics, Redox Properties, and Structural-Changes Upon Electrochemical Cycling. *J. Electroanal. Chem.* **1985**, *191*, 111-126.
15. Baba, A.; Tian, S. J.; Stefani, F.; Xia, C. J.; Wang, Z. H.; Advincula, R. C.; Johannsmann, D.; Knoll, W., Electropolymerization and Doping/Dedoping Properties of Polyaniline Thin Films as Studied by Electrochemical-Surface Plasmon Spectroscopy and by the Quartz Crystal Microbalance. *J. Electroanal. Chem.* **2004**, *562*, 95-103.

16. Atighilorestani, M.; Menezes, J. W.; Brolo, A. G., Large Area Plasmonic Gold Nanopillar 3-D Electrodes. *Electrochim. Acta* **2016**, *188*, 91-97.
17. Badia, A.; Arnold, S.; Scheumann, V.; Zizlsperger, M.; Mack, J.; Jung, G.; Knoll, W., Probing the Electrochemical Deposition and/or Desorption of Self-Assembled and Electropolymerizable Organic Thin Films by Surface Plasmon Spectroscopy and Atomic Force Microscopy. *Sens. Actuators, B* **1999**, *54*, 145-165.
18. Iwasaki, Y.; Horiuchi, T.; Morita, M.; Niwa, O., Time Differential Surface Plasmon Resonance Measurements Applied for Electrochemical Analysis. *Electroanalysis* **1997**, *9*, 1239-1241.
19. Constantin, V.-A.; Bongard, D.; Walder, L., Triply Branched Viologen Stars: Synthesis and Polymerization by Peripheral Benzyl Coupling. *Eur. J. Org. Chem.* **2012**, 913-921.
20. Gadgil, B.; Dmitrieva, E.; Damlin, P.; Aaritalo, T.; Kvarnstrom, C., Redox Reactions in a Linear Polyviologen Derivative Studied by in Situ Esr/Uv-Vis-Nir Spectroelectrochemistry. *J. Solid State Electrochem.* **2015**, *19*, 77-83.
21. Inzelt, G.; Pineri, M.; Schultze, J. W.; Vorotyntsev, M. A., Electron and Proton Conducting Polymers: Recent Developments and Prospects. *Electrochim. Acta* **2000**, *45*, 2403-2421.
22. Jiang, N.; Ruan, Q.; Qin, F.; Wang, J.; Lin, H.-Q., Switching Plasmon Coupling through the Formation of Dimers from Polyaniline-Coated Gold Nanospheres. *Nanoscale* **2015**, *7*, 12516-12526.
23. Jiang, N.; Shao, L.; Wang, J., (Gold Nanorod Core)/(Polyaniline Shell) Plasmonic Switches with Large Plasmon Shifts and Modulation Depths. *Adv. Mater. (Weinheim, Ger.)* **2014**, *26*, 3282-+.
24. Xu, T.; Walter, E. C.; Agrawal, A.; Bohn, C.; Velmurugan, J.; Zhu, W.; Lezec, H. J.; Talin, A. A., High-Contrast and Fast Electrochromic Switching Enabled by Plasmonics. *Nat. Commun.* **2016**, *7*.
25. Brolo, A. G., Plasmonics for Future Biosensors. *Nature Photonics* **2012**, *6*, 709-713.
26. Ebbesen, T. W.; Lezec, H. J.; Ghaemi, H. F.; Thio, T.; Wolff, P. A., Extraordinary Optical Transmission through Sub-Wavelength Hole Arrays. *Nature (London, U. K.)* **1998**, *391*, 667-669.
27. Porto, J. A.; Garcia-Vidal, F. J.; Pendry, J. B., Transmission Resonances on Metallic Gratings with Very Narrow Slits. *Phys. Rev. Lett.* **1999**, *83*, 2845-2848.
28. Valsecchi, C.; Brolo, A. G., Periodic Metallic Nanostructures as Plasmonic Chemical Sensors. *Langmuir* **2013**, *29*, 5638-5649.
29. Dickson, W.; Wurtz, G. A.; Evans, P. R.; Pollard, R. J.; Zayats, A. V., Electronically Controlled Surface Plasmon Dispersion and Optical Transmission through Metallic Hole Arrays Using Liquid Crystal. *Nano Lett.* **2008**, *8*, 281-286.
30. Kim, T. J.; Thio, T.; Ebbesen, T. W.; Grupp, D. E.; Lezec, H. J., Control of Optical Transmission through Metals Perforated with Subwavelength Hole Arrays. *Opt. Lett.* **1999**, *24*, 256-258.
31. Dintinger, J.; Klein, S.; Ebbesen, T. W., Molecule-Surface Plasmon Interactions in Hole Arrays: Enhanced Absorption, Refractive Index Changes, and All-Optical Switching. *Adv. Mater. (Weinheim, Ger.)* **2006**, *18*, 1267-1270.
32. Wurtz, G. A.; Pollard, R.; Zayats, A. V., Optical Bistability in Nonlinear Surface-Plasmon Polaritonic Crystals. *Phys. Rev. Lett.* **2006**, *97*.
33. Sharma, N.; Keshmiri, H.; Zhou, X.; Wong, T. I.; Petri, C.; Jonas, U.; Liedberg, B.; Dostalek, J., Tunable Plasmonic Nanohole Arrays Actuated by a Thermoresponsive Hydrogel Cushion. *J. Phys. Chem. C* **2016**, *120*, 561-568.

34. Ferreira, J.; Santos, M. J. L.; Rahman, M. M.; Brolo, A. G.; Gordon, R.; Sinton, D.; Girotto, E. M., Attomolar Protein Detection Using in-Hole Surface Plasmon Resonance. *J. Am. Chem. Soc.* **2009**, *131*, 436-+.
35. Huang, W. H.; Pang, D. W.; Tong, H.; Wang, Z. L.; Cheng, J. K., A Method for the Fabrication of Low-Noise Carbon Fiber Nanoelectrodes. *Anal. Chem.* **2001**, *73*, 1048-1052.
36. Shen, J.; Wang, W.; Chen, Q.; Wang, M. S.; Xu, S. Y.; Zhou, Y. L.; Zhang, X. X., The Fabrication of Nanoelectrodes Based on a Single Carbon Nanotube. *Nanotechnology* **2009**, *20*.
37. Gordon, R.; Brolo, A. G.; Sinton, D.; Kavanagh, K. L., Resonant Optical Transmission through Hole-Arrays in Metal Films: Physics and Applications. *Laser Photonics Rev.* **2010**, *4*, 311-335.
38. Ghaemi, H. F.; Thio, T.; Grupp, D. E.; Ebbesen, T. W.; Lezec, H. J., Surface Plasmons Enhance Optical Transmission through Subwavelength Holes. *Phys. Rev. B* **1998**, *58*, 6779-6782.
39. Johnson, P. B.; Christy, R. W., Optical Constants of Noble Metals. *Phys. Rev. B* **1972**, *6*, 4370-4379.
40. Damos, F. S.; Luz, R. C. S.; Kubota, L. T., Investigations of Ultrathin Polypyrrole Films: Formation and Effects of Doping/Dedoping Processes on Its Optical Properties by Electrochemical Surface Plasmon Resonance (Espr). *Electrochim. Acta* **2006**, *51*, 1304-1312.
41. Kang, X. F.; Jin, Y. D.; Chen, G. J.; Dong, S. J., Surface Plasmon Resonance Studies on the Electrochemical Doping/Dedoping Processes of Anions on Polyaniline-Modified Electrode. *Langmuir* **2002**, *18*, 10305-10310.
42. Dahlin, A.; Zach, M.; Rindzevicius, T.; Kall, M.; Sutherland, D. S.; Hook, F., Localized Surface Plasmon Resonance Sensing of Lipid-Membrane-Mediated Biorecognition Events. *J. Am. Chem. Soc.* **2005**, *127*, 5043-5048.
43. Sannomiya, T.; Scholder, O.; Jefimovs, K.; Hafner, C.; Dahlin, A. B., Investigation of Plasmon Resonances in Metal Films with Nanohole Arrays for Biosensing Applications. *Small* **2011**, *7*, 1653-1663.
44. Xiong, K. L.; Emilsson, G.; Dahlin, A. B., Biosensing Using Plasmonic Nanohole Arrays with Small, Homogenous and Tunable Aperture Diameters. *Analyst (Cambridge, U. K.)* **2016**, *141*, 3803-3810.
45. Ding, Y.; Yoon, J.; Javed, M. H.; Song, S. H.; Magnusson, R., Mapping Surface-Plasmon Polaritons and Cavity Modes in Extraordinary Optical Transmission. *IEEE Photonics J.* **2011**, *3*, 365-374.
46. Martin-Moreno, L.; Garcia-Vidal, F. J.; Lezec, H. J.; Pellerin, K. M.; Thio, T.; Pendry, J. B.; Ebbesen, T. W., Theory of Extraordinary Optical Transmission through Subwavelength Hole Arrays. *Phys. Rev. Lett.* **2001**, *86*, 1114-1117.
47. Zhou, R. L.; Li, H. J.; Wang, X. W.; Liu, X. J.; Zhou, B. J.; Gao, Y. Y.; Wu, L. X.; Chen, X. S.; Lu, W., Two Resonances Effect for Light Transmission Assisted with Surface Plasmon through Perforated Metal Film. *Phys. B (Amsterdam, Neth.)* **2009**, *404*, 278-284.
48. Zhu, J., Refractive Index Dependent Local Electric Field Enhancement in Cylindrical Gold Nanohole. *J. Nanopart. Res.* **2011**, *13*, 87-95.
49. Koerkamp, K. J. K.; Enoch, S.; Segerink, F. B.; van Hulst, N. F.; Kuipers, L., Strong Influence of Hole Shape on Extraordinary Transmission through Periodic Arrays of Subwavelength Holes. *Phys. Rev. Lett.* **2004**, *92*.
50. van der Molen, K. L.; Klein Koerkamp, K. J.; Enoch, S.; Segerink, F. B.; van Hulst, N. F.; Kuipers, L., Role of Shape and Localized Resonances in Extraordinary Transmission through Periodic Arrays of Subwavelength Holes: Experiment and Theory. *Phys. Rev. B* **2005**, *72*.

51. Heer, J.; Corwin, L.; Cilwa, K.; Malone, M. A.; Coe, J. V., Infrared Sensitivity of Plasmonic Metal Films with Hole Arrays to Microspheres in and out of the Holes. *J. Phys. Chem. C* **2010**, *114*, 520-525.
52. Pirvu, C.; Manole, C. C., Electrochemical Surface Plasmon Resonance for in Situ Investigation of Antifouling Effect of Ultra Thin Hybrid Polypyrrole/Pss Films. *Electrochim. Acta* **2013**, *89*, 63-71.
53. Li, Y. F.; Qian, R. Y., Effect of Anion and Solution Ph on the Electrochemical-Behavior of Polypyrrole in Aqueous-Solution. *Synth. Met.* **1989**, *28*, C127-C132.
54. Santos, M. J. L.; Brolo, A. G.; Girotto, E. M., Study of Polaron and Bipolaron States in Polypyrrole by in Situ Raman Spectroelectrochemistry. *Electrochim. Acta* **2007**, *52*, 6141-6145.
55. Scott, J. C.; Bredas, J. L.; Yakushi, K.; Pfluger, P.; Street, G. B., The Evidence for Bipolarons in Pyrrole Polymers. *Synth. Met.* **1984**, *9*, 165-172.
56. Wong, J. Y.; Langer, R.; Ingber, D. E., Electrically Conducting Polymers Can Noninvasively Control the Shape and Growth of Mammalian-Cells. *Proc. Natl. Acad. Sci. U. S. A.* **1994**, *91*, 3201-3204.
57. Godino, N.; Borrise, X.; Xavier Munoz, F.; Javier del Campo, F.; Compton, R. G., Mass Transport to Nanoelectrode Arrays and Limitations of the Diffusion Domain Approach: Theory and Experiment. *J. Phys. Chem. C* **2009**, *113*, 11119-11125.
58. Lee, C.; Kwak, J. Y.; Bard, A. J., Polymer-Films on Electrodes .24. Ellipsometric Study of the Electrochemical Redox Processes of a Polypyrrole Film on a Platinum-Electrode. *J. Electrochem. Soc.* **1989**, *136*, 3720-3724.
59. Xia, C. J.; Advincula, R. C.; Baba, A.; Knoll, W., In Situ Investigations of the Electrodeposition and Electrochromic Properties of Poly (3,4-Ethylenedioxythiophene) Ultrathin Films by Electrochemical-Surface Plasmon Spectroscopy. *Langmuir* **2002**, *18*, 3555-3560.
60. John, R.; Wallace, G. G., Doping Dedoping of Polypyrrole - a Study Using Current-Measuring and Resistance-Measuring Techniques. *J. Electroanal. Chem.* **1993**, *354*, 145-160.
61. Santos, M. J. L.; Girotto, E. M.; Brolo, A. G., Controlling the Photoluminescence from a Laser Dye through the Oxidation Level of Polypyrrole. *Macromol. Rapid Commun.* **2010**, *31*, 289-294.
62. Najiminaini, M.; Vasefi, F.; Kaminska, B.; Carson, J. J. L., Nanohole-Array-Based Device for 2d Snapshot Multispectral Imaging. *Sci. Rep.* **2013**, *3*.

Chapter 7 : Large Area Plasmonic Gold Nanopillar 3-D Electrodes

This Chapter is published as: M. Atighilorestani, J. W. Menezes, and A. G. Brolo, Large Area Plasmonic Gold Nanopillar 3-D Electrodes, Electrochimica Acta 2016, 188, 91-97.

All the fabrications, measurements, and simulations have been performed by M. Atighilorestani. The laser interference lithography setup used for samples fabriation in this work has been developed by J. W. Menezes.

Three-dimensional (3-D) periodic nanopillar electrodes have a significantly increased electroactive surface area compared to a conventional flat surface. The fabrication of organized nanostructured surfaces generally requires advanced nanofabrication methods. Those can be both time-consuming and expensive. Moreover, the use of nanostructured electrodes combined with optical methods in studies of electrochemical processes provides a distinct advantage for the investigation of mechanistic details, since it adds another dimension to the classical electrochemical approaches. In this work, we have implemented a method, based on interference lithography technique, for the fabrication of 3-D nanopillar electrodes. The electrical current measured from those high-density 3-D nanopillars was ~17% higher than from a smooth gold surface, which was confirmed by numerical simulations using COMSOL®. Finally, gold-coated nanopillar electrodes support the phenomenon of surface plasmon resonance (SPR). Therefore, the optical characteristic of the surface (SPR) was measured simultaneously to the classical electrochemical data. A simple reversible redox system (ferrocyanide/ferricyanide) was used in a proof-of-concept experiment to demonstrate this application of the nanostructured surface.

7.1 Introduction

Nanopillar electrodes are three-dimensional (3-D) nanostructures that provide larger electrochemically active surface areas than conventional planar electrodes resulting in higher currents [1-4]. Nanopillar structures have been used in various fields; for instance, in bioanalytical chemistry, as non-enzymatic glucose sensors[1]; in energy applications, including fuel cells[5-6] and solar cells[7]; in environmental remediation for the treatment of wastewater[8]; and in electrophysiology[9] . Numerous methods have been implemented for the fabrication of the nanostructures. Most of these fabrication techniques produce random assemblies of nanopillars [, 1, 7-8, 10-13]. However, certain applications (for example solar cells) benefit from organized periodic nanopillar arrays [2, 14]. Advanced nanofabrication tools, such as electron beam lithography (EBL), have been used to fabricate those periodic nanostructures [3, 15-18]. Although EBL leads to well-organized and reproducible pattern with high geometrical precision, the fabrication process is suitable neither for large-area patterning nor for mass production.

In this work, we employed the interference lithography (IL) approach, followed by a thin metal film deposition, to fabricate large areas (2 cm x 2 cm) 3-D gold nanopillar electrode (Au-NPE) arrays. Interference lithography is a rapid, high-throughput, and cost-effective technique for patterning uniform periodic micro/ nanostructures. Two-dimensional nanogrid patterns were fabricated by double exposure of the photoresist to an interference pattern of fringes. 3-D nanopillar structures were obtained after developing the photoresist grids[19]. Electron beam deposition of a thin gold film on the array template at an oblique angle resulted in fully conductive 3-D Au-NPEs[20].

The use of gold as the electrode material enabled another advantage: Nanostructured gold is known to support an optical phenomenon in the visible range of the electromagnetic spectrum called surface plasmon resonance (SPR) [21-22]. Consequently, the electrochemical information obtained from 3-D Au-NPEs can be combined with an optical method (SPR). This combination of electrochemistry and spectroscopy (spectroelectrochemistry) is a powerful approach to study reaction mechanisms, kinetic parameters, and reaction intermediates of organic, inorganic and biological redox species [23-25]. In the particular case of SPR, the optical response can provide information on changes in the refractive index of the environment close to the metal surface[21-22], including the ones related to molecular adsorption and film formation. Electrochemical surface plasmon resonance (EC-SPR) is routinely carried out using a planar metal film, as both the SPR sensor and the working electrode[26]. The application of EC-SPR with a planar electrode, Kretschmann configuration, is well established and has been used in a diversity of investigations, including electrochemical current imaging[27], electrochemical polymerization[28-29], bioelectrochemistry[30-31], and surface bound redox species[32]. However, the Kretschmann configuration used in these EC-SPR experiments requires precise optical alignment and provides less opportunity for setup simplification and miniaturization[21]. Nanoparticles have also been employed in EC-SPR studies where the optical collinear setup simplifies their optical alignment. However, the limitation of utilizing nanoparticles in EC-SPR is their stabilities; as they might show irreversible behavior under applied potentials[33].

Here, we demonstrated the feasibility of utilizing stable 3-D Au- NPEs as working electrode in combination with EC-SPR detection. Utilizing 3-D Au-NPEs in EC-SPR studies offer many benefits owing to their larger electrochemically-active sensing area; besides the other advantages resulting from their simple optical collinear arrangement. The potential dependent concentration

changes of the reversible redox species, ferri/ferrocyanide ($Fe(CN)_6^{3-/4-}$), near the working electrode surface were followed. The current responses of the 3-D Au-NPEs were further modeled numerically using the finite element (FEM) software COMSOL Multiphysics®.

7.2 EXPERIMENTAL PART

7.2.1 Chemicals

Microposit SC 1827 Positive Photoresist, Microposit Thinner Type P, SU-8 3010, SU-8 2000 Thinner and Microposit 351 Developer were purchased from Rohm and Haas Electronic Materials LLC. Potassium nitrate was obtained from Sigma-Aldrich. Potassium ferricyanide and potassium ferrocyanide were purchased from ACP Chemicals Inc. All solutions were prepared using ultrapure water (18.2 MV cm) obtained from NANO pure Diamond TM deionization system (Barnstead).

7.2.2 Fabrication process

Figure 7-1(a-e) schematically illustrates the fabrication steps for the 3-D Au-NPEs. First, the glass substrates were ultrasonically cleaned in acetone, ethanol, methanol, and isopropanol for 10 min each, respectively. The substrates were then rinsed with deionized water and dried in an oven at 120 °C for 20 min. A positive photoresist (SC 1827, Rohm and Haas) was used to record the interference patterns. To improve the adhesion property between the SC 1827 layer and the glass substrate, a negative photoresist (SU-8 3010, Rohm and Haas) layer was introduced[34]. SU-8 was applied to the substrates by spin-coating at 4500 rpm for 40 s, and soft baked at 90 °C for 15 min.

After soft baking, the substrates were exposed to UV light and followed by a post exposure bake at 90 °C for 15 min, then, the substrates were allowed to cool to room temperature. Next, SC 1827 was spin coated on the SU-8 cured substrates, at 4500 rpm and baked at 80 °C for 20 min (Figure 7-1a). The resulting photoresist thickness was about 530 nm (determined by scanning electron micrograph - SEM). The samples were next exposed to an interference pattern produced by a Lloyd's mirror apparatus[35] in conjunction with a Coherent Argon ion laser Ar-ion laser operating at a wavelength of 457.9 nm (Figure 7-1b). A double exposure of the samples to the same interference pattern (with a dose of 300 mJ cm^2), by rotating the samples 90° between the exposures, was used to fabricate the 2D periodic nanogrid structures with a square lattice[19] (Figure 7-1c). After the second exposure, the photoresist film was developed in Microposit 351 Developer (Rohm and Haas, 1:3 diluted in water) for 40 seconds, and a periodic array of 3-D photoresist template was achieved (Figure 7-1d). The 3-D nanostructured arrays, with a periodicity of around 590 nm, were fabricated on the substrates coated with SC 1827[19]. Finally, a 2 nm Ti film was deposited by electron beam evaporation onto the 3-D photoresist templates, as an adhesion layer, following by the deposition of a 100 nm Au film and fully conductive 3-D Au- NPEs were obtained (Figure 7-1e). The final height and diameter of the Au-coated nanopillars were about 630 nm and 330 nm, respectively. The position of the substrate relative to the metal beam is important to obtain a uniform deposited film since the evaporation process is highly directional. Additionally, substrate rotation provides a better dispersion and ensures the uniformity of the deposited film [20, 36-37] . Therefore, to improve the uniformity of the metal film deposition on the patterned structures, the substrates were mounted on the rotating substrate holder at an oblique with respect to the metal source.

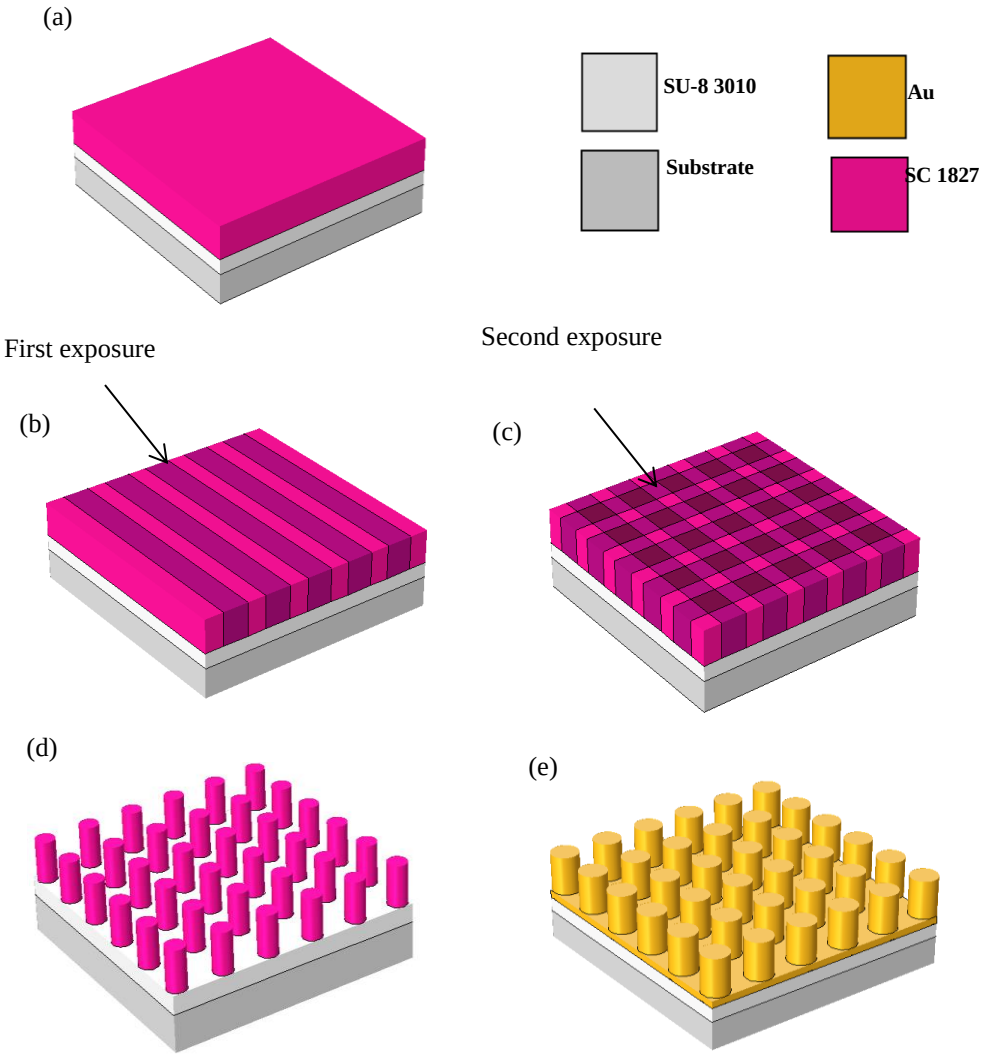

Figure 7-1. Fabrication steps of the large area Au-NPEs using interference lithography (a-e). (a) SU-8 cured glass substrate coated with SC 1827 positive photoresist. (b) First exposure of SC 1827 photoresist to the interference pattern. (c) Second exposure of the SC 1827 photoresist to the interference pattern after a 90° sample rotation. (d) Develop the exposed SC 1827 photoresist to obtain 3-D photoresist template. (e) Metal deposition using electron beam evaporation onto the 3-D photoresist template to obtain 3-D Au- NPEs.

7.2.3 Bulk Refractive Index and in Situ EC-SPR Measurements

The 3-D Au-NPEs were mounted in a Teflon® cell with an O-ring providing a liquid-tight seal. The Teflon® cell volume was about 0.8 ml. The cell opening was capped with a VWR® micro cover glass window after filling the cell with a proper test solution during all the measurements. The cell was designed specially to allow simultaneous measurement of both electrochemical and SPR signals (EC-SPR cell). The EC-SPR cell was fixed on the stage of an upright metallurgical microscope (Olympus BHSM). Surface plasmons were excited at the metal-dielectric interface using collimated white light illumination from a halogen lamp. The transmitted light through the illuminated electrode was then collected by a fiber-coupled spectrometer (USB 4000-UV-VIS Ocean Optics) connected to a computer. The exposed geometrical surface area to the solution was a circle of radius about 6 mm. The bulk refractive index sensitivities of the 3-D Au-NPEs were obtained from the changes in the transmission spectra recorded in the presence of glucose solutions with different refractive indexes. The intensity (S_I) and wavelength shift (S_λ) sensitivities to refractive indexes changes were obtained from the experimental plots[38]:

$$s_I = \left(\frac{\partial I}{\partial n}\right)/I_0 \times 100\% \qquad \text{Eq. 7-1}$$

$$s_\lambda = \frac{\partial \lambda}{\partial n} \qquad \text{Eq. 7-2}$$

All electrochemical measurements were performed simultaneously to in situ SPR using a three electrodes system. In these EC-SPR experiments, the 3-D Au-NPEs was the working electrode, a Pt foil was used as counter electrode, and an Ag|AgCl|$KCl_{(sat.)}$ electrode served as a reference

electrode. A computer-controlled Autolab potentiostat-galvanostat (PGSTAT 30) was used for performing the voltammetric experiments.

7.2.4 Characterization of the 3-D Au-NPE

The surface profiles of the nanopillars were characterized by a field-emission scanning electron microscope (FE-SEM) (Hitachi S4800, Hitachi, Japan). Figure 7-2a shows a tilted SEM image of the photoresist template (before the metal deposition). The Z-contrast cross section image, depicted in Figure 7-2b, was used to determine the gold layer thickness on the side walls of the nanopillars. Quartz PCI image acquisition software (Version 8.1) was used to calculate the height, spacing, and gold film thicknesses. The image in Figure 7-2b shows that the vertical side walls of the nanopillars were uniformly coated with the metal film.

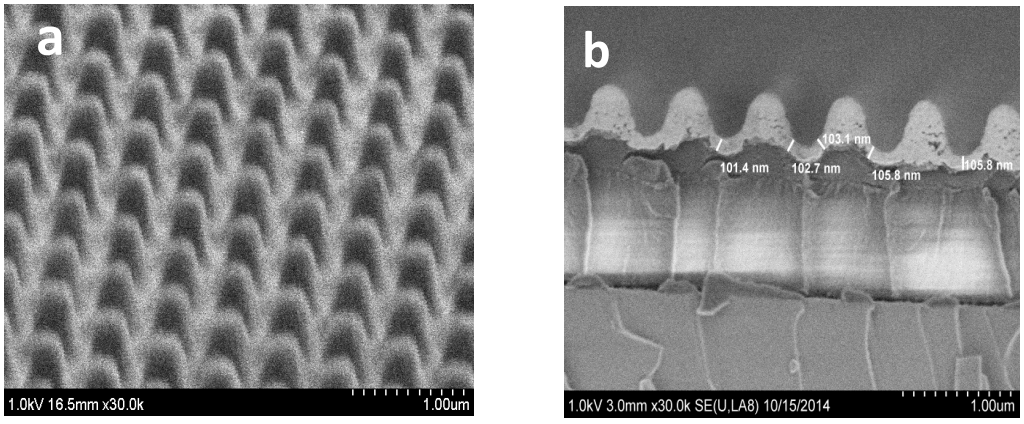

Figure 7-2. (a) Tilted SEM image of the photoresist template and (b) Z-contrast cross-section image of the metal-coated nanopillars.

7.3 Results and Discussion

7.3.1 Electrochemical Performance of the 3-D Au-NPEs

Figure 7-3 (dotted line curves a and b) shows a comparison of the experimental CVs obtained from a 3-D Au-NPEs and a flat electrode with an equivalent geometric area in 1 mM ferricyanide/0.5 M KNO_3 at 100 mV s^{-1}. The electrochemical responses of the Au-NPEs were also simulated using finite element (FEM) software (COMSOL Multiphysics® version 4.3a), and the simulated results are presented as solid lines in Figure 7-3. The peak current intensity from the 3-D Au-NPEs in Figure 7-3a is about seventeen percent higher than that of an equivalent flat electrode, in Figure 7-3b. The enhanced peak current was observed because the surface area of the Au-NPE is larger than in the case of the flat electrode. The increased surface area depends on the pillars radius, height, and density. In the particular case here, for a 590 nm periodicity array, the anodic electrochemical charge was 25% higher for the 3-D Au-NPEs compared to the flat electrode.

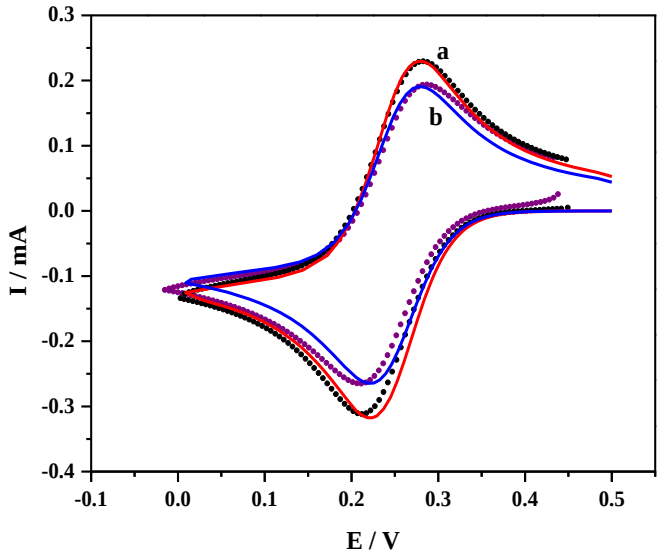

Figure 7-3. Experimental (dotted line) and simulated (solid line) CV responses of (a) a 3- D Au-NPE and (b) an equivalent flat electrode with the surface area A = 1.131 cm^2 in 1 mM ferricyanide/0.5 M of KNO_3 at the scan rate of 100 mV s^{-1}. Dimensions of the pillars used in the simulations: diameter: 330 nm, height: 620 nm, periodicity: 590 nm.

The simulation of cyclic voltammograms (CVs) for both the 3-D Au-NPEs and an equivalent flat electrode in the two-dimensional domain and one-dimensional domain have been considered respectively. The simulations of the CVs (solid lines in Figure 7-3) at nanopillars employed the diffusion domain approximation, as discussed in ref[4] (and also in Chapter 2). For micro/nanoelectrodes arrays, the optimum response is obtained under the predominance of radial (three-dimensional) diffusion to each of the pillars in the array. To achieve steady state voltammograms (i.e. sigmoidal shape) at micro/ nanoelectrodes arrays, there should be sufficient spacing between adjacent features in the array, so that each nanopillar in the array experiences its own independent diffusion regime. When the nanopillars in the array are placed very close to each other, the diffusion regimes of neighboring features are completely overlapped, and the whole

array behaves as a flat electrode with an equivalent area [39-40]. In our work, since the nanopillars arrays were densely packed on a large area and the whole surface was electroactive, the 3-D Au-NPEs behaved as a macroelectrode with a transient response (linear diffusion). Figure 7-4 illustrates the plots of peak current vs. the square root of scan rates for a 3-D Au-NPE, determined experimentally (black circles) and by simulations (red line), and for an equivalent flat electrode as predicted by the Randles–Ševcik equation (pink line) [41] . Figure 7-4 shows that the peak current for 3-D Au-NPEs is always larger than the expected from the Randles–Ševcik equation for a flat electrode, over the whole range of scan rate considered. The difference between the current response of 3-D Au-NPEs and the flat electrode increased as the scan rate increased (Figure 7-4). This is not surprising since the slope of the I_p vs. $v^{1/2}$ plot is expected to increase with the surface area. Furthermore, Figure 7-4 emphasizes the good agreement between the simulated and experimental results obtained for the 3-D Au-NPEs.

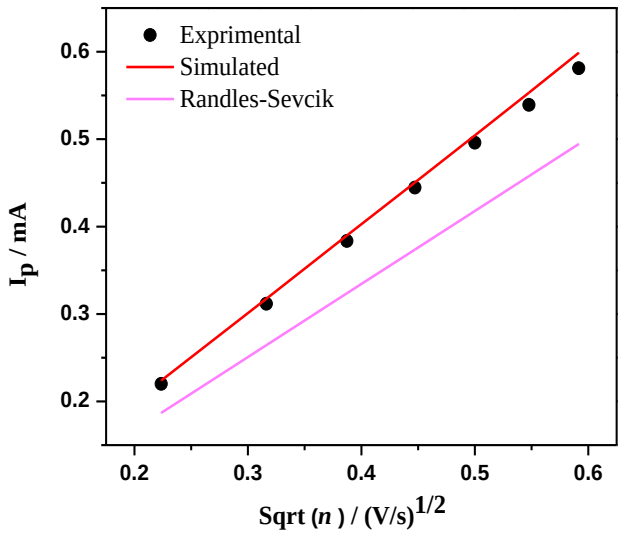

Figure 7-4. Relationship between the peak current and square root of scan rate for experimental and numerical simulated (COMSOL) cyclic voltammograms at 3-D Au NPEs and for an equivalent flat electrode determined by the Randles-Ševcik equation.

7.3.2 SPR Bulk Refractive Index Sensitivities of 3-D Au-NPEs

There are several contributing factors to the SPR refractive index sensitivity of 3-D Au-NPEs, including their geometry, diameter, periodicity, gold film thickness, and nanopillar aspect ratio. We concentrated in array electrodes with the periodicity of around 590 nm coated with a gold film thickness of 100 nm (the height and diameter of the nanopillars, determined from the SEM images, were ~630 nm and 330 nm, respectively). This periodicity was easily achieved in our simple Lloyd's mirror apparatus with an Ar^+ laser (457.9 nm), and the gold thickness was the maximum that allowed the experiments to be performed in transmission geometry (the reflection geometry was avoided to simplify the optical setup). The results for white light transmission measurements through the 3-D Au-NPE exposed to aqueous solutions of glucose of different concentrations (the corresponding refractive index ranged between 1.3332 and 1.3555) are shown in Figure 7-5A. Figure 7-5A illustrates that, as the refractive index increased, an increase on the relative amplitudes of the transmitted spectra was observed together with a shift of the SPR peak to longer wavelengths. Normally in the plasmonic field, the sensitivity of the sensor is determined by either monitoring the dependence of the peak wavelength with the refractive index or the change in overall intensity for a fixed wavelength. Figure 7-5B(a) illustrates the transmission intensity changes vs. the refractive index of glucose solutions at the wavelength of 660 nm (indicated as dashed line in Figure 7-5A). The intensity sensitivity calculated using Eq. 7-1 was 566 %/RIU. Figure 7-5B(b) shows the calibration plot of SPR wavelength shift vs. the refractive index of glucose solutions. The sensitivity calculated from Eq. 7-2 was 687 nm/RIU. The observed SPR

sensitivity to refractive index changes values, obtained from Figure 7-5B, are comparable to literature values from different plasmonic structures [19, 38, 42].

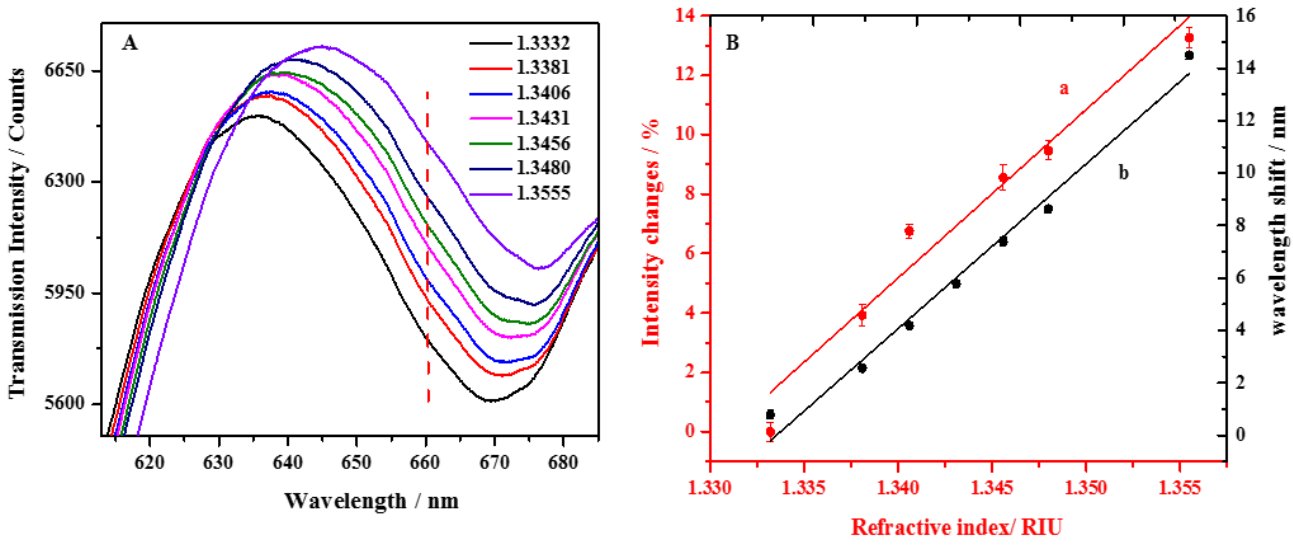

Figure 7-5. (A) Optical transmission spectra of a 3-D Au-NPE exposed to solutions with different refractive index values, ranging from 1.3332 to 1.3555. (B) Calibration plots: (a) SPR intensity changes as a function of the refractive index of glucose solutions at the wavelength of 660 nm (dashed vertical line in Figure 7-5A); (b) SPR wavelength shift vs. the refractive index of glucose solutions. The error bars indicate the standard deviation from the average of 10 spectra obtained under the same conditions. The acquisition time was 40 ms, and 10 accumulations were recorded for each spectrum.

7.3.3 EC-SPR using 3-D Au-NPEs

A combination of electrochemical and SPR measurements was used to examine the capability of the 3-D Au-NPEs to monitor a redox couple, $Fe(CN)_6^{3-/4-}$, at the metal-solution interface. In an EC-SPR measurement, the working electrode simultaneously served as the SPR sensing element. Initially, a CV at a scan rate of 100 mV/s, displayed in Figure 7-6A, was carried out in a solution of mM $K_3[Fe(CN)_6]$ and 0.5 M KNO_3 to determine the potential range of the redox couple. Accordingly, a selected range of step potentials was programmed, between 0.40 and 0.05 V, in

successive increments of -0.05 V. A series of potential step measurements was also performed in the supporting electrolyte (0.5 M KNO_3), in the absence of the redox pair, as a control experiment. The SPR transmission spectra were acquired 2 s after each potential step, and the system was held at each potential for a total of 15 s. The data points in Figure 7-6B(a) are the experimental SPR transmission intensity at 660 nm versus applied potentials for the supporting electrolyte (0.5 M KNO_3), in the absence of the Fe $(CN)_6^{3-/4-}$ redox couple. The wavelength of 660 nm was chosen because the highest SPR intensity changes for mixtures containing $Fe(CN)_6^{3-/4-}$ were observed at that wavelength. This is also a common wavelength for inexpensive diode lasers and light-emitting diodes. Therefore, 660 nm is an appropriate parameter for future development of integrated plasmonic devices based on these nanostructures. The SPR transmission intensity at different applied potentials shows little variation when only the supporting electrolyte is present (Figure 7-6B(a)). We emphasize that in the case of the supporting electrolyte (0.5 M KNO_3), no significant variations were observed in the SPR intensity changes at any other wavelengths. The data points in Figure 7-6B(b) correspond to the SPR transmission intensity changes at 660 nm for each applied potential in the presence of 1 mM $K_3[Fe(CN)_6]$. As it can be seen in Figure 7-6B(b), the transmission intensity is almost constant at applied potentials between 0.40 V and 0.30 V. The SPR transmission intensity at 660 nm then increased after 0.30 V (cathodic sweep) and halted again after 0.15 V. Depending on the applied potential, either $[Fe(CN)_6]^{3-}$, $[Fe(CN)_6]^{4-}$ or a concentration ratio of both forms exists near the working electrode surface. The CV in Figure 7-6A illustrates that at the starting step potential of 0.40 V (Figure 7-6B), only the oxidized form $[Fe(CN)_6]^{3-}$ was present at the interface. The cathodic currents in the CV (Figure 7-6A), developed at lower potentials values than 0.30 V, corresponded to the $[Fe\ (CN)_6]^{3-}$ reduction to $[Fe(CN)_6]^{4-}$. The reduction form $[Fe(CN)_6]^{4-}$ was predominant after 0.15 V (in a negative sweep, as shown in

Figure 7-6A). The clear change in SPR intensity responses in Figure 7-6B can then be directly correlated to the relative concentrations of [Fe $(CN)_6]^{4-}$ and $[Fe(CN)_6]^{3-}$ adjacent to the electrode surface[39-40]. This is further confirmed by Figure 7-6C that presents the SPR intensity changes of a 3-D Au-NPE exposed to freshly prepared solutions of $[Fe(CN)_6]^{3-}$ and $[Fe(CN)_6]^{4-}$ with different concentration ratios, ranging between 0 and 1 mM, recorded at open circuit potential. The magnitude of the observed SPR intensity changes in Figure 7-6C is indeed comparable with the data points observed in Figure 7-6B(b). The refractive index of 100 mM $Fe(CN)_6^{4-}$ solution was reported to be 0.003 higher than of $Fe(CN)_6^{3-}$ [43] . The refractive indexes of mixtures of this redox couple rise linearly with increasing their molar concentration ratios, in agreement with Figure 7-6C[44]. Finally, the solid line through the data points in Figure 7-6B(b) correspond to the concentration ratios between the redox species $Fe(CN)_6^{3-/4-}$ estimated at the electrode surface by the Nernst equation. A very good agreement was observed between the experimental SPR results and the Nernst equation calculation, as demonstrated in Figure 7-6B. The E° for the $Fe(CN)_6^{3-/4-}$ redox pair was determined from the Nernstian fit to the SPR data, and its value (+0.25 V vs. Ag/AgCl/ $KCl_{(sat)}$) agreed well with electrochemical measurements (Figure 7-6A and Figure 7-6B, dashed line).

Iwasaki et al. have used a Kretschmann-type instrument to detect the SPR angle shifts induced by the changes in the local refractive index in the bulk solution near the metal film during the $Fe(CN)_6^{3-/4-}$ electrochemical redox reaction. In their experiments, higher SPR angle shifts were recorded by increasing the concentration of the $[Fe(CN)_6]^{3-}$ in solution. 30.4 mM was the lowest concentration of $[Fe(CN)_6]^{3-}$ at which a detectable SPR angle shift was measured and reported[44]. In this work, the detectable SPR intensity changes were acquired at much lower concentrations for the couple $Fe(CN)_6^{3-/4-}$ using a simpler optical arrangement (transmission measurements). These

results seem to indicate that the 3D Au-NPEs introduced here is an efficient platform for EC-SPR and could be used to substitute the Kretschmann substrate in those types of applications.

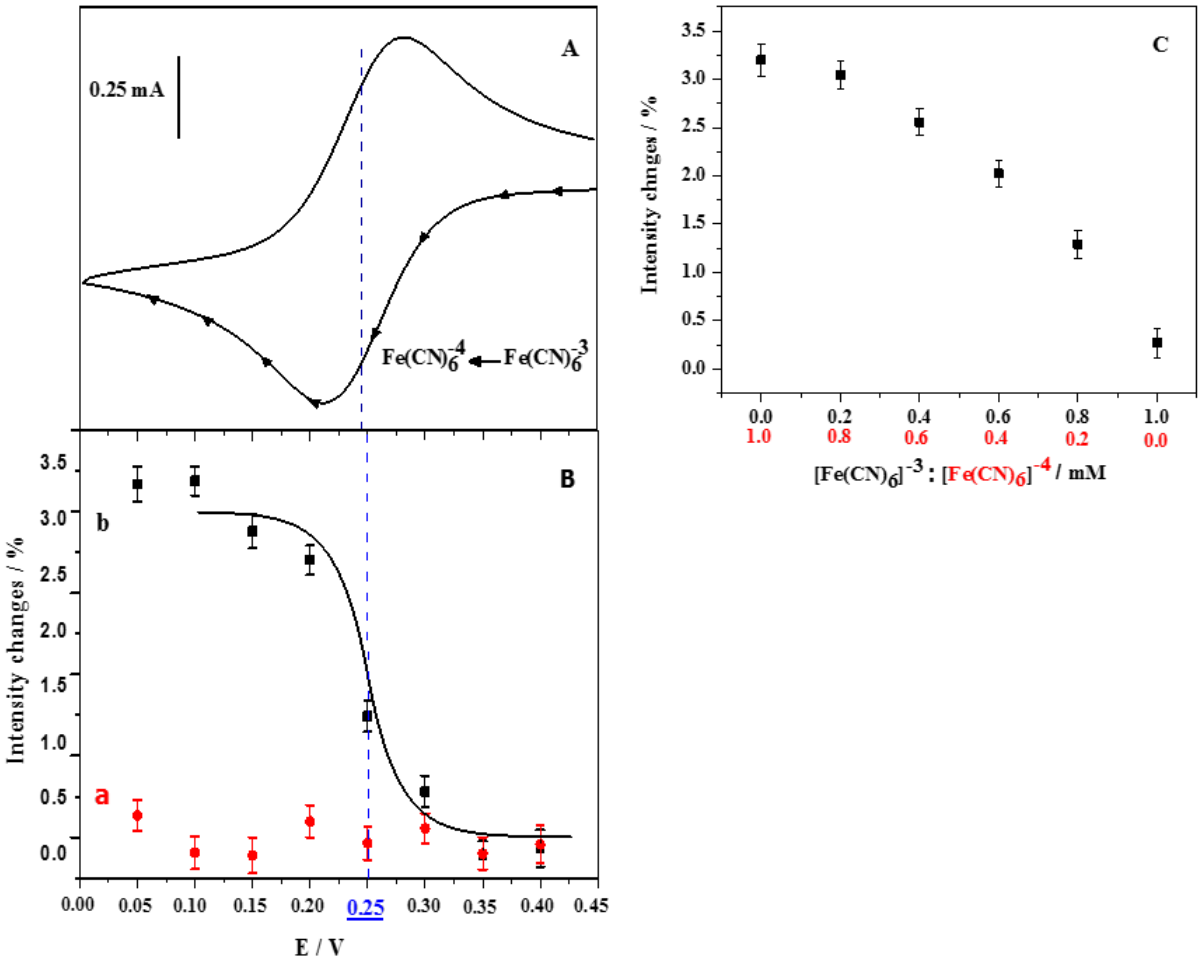

Figure 7-6. (A) CV from an Au-NPE in 1 mM ferricyanide/0.5 M of KNO_3 at 0.1 Vs^{-1} scan rate; (B) SPR intensity changes (%) at each applied potential for (a) the supporting electrolyte (0.5 M KNO_3) in the absence of the $Fe(CN)_6^{3-/4-}$ redox couple and (b) the 1 mM ferricyanide in 0.5, at Au-NPEs. The solid line in B) correspond to the ratio $[Fe\ (CN)_6]^{4-}/[Fe(CN)_6]^{3-}$ at the interface at each applied potential calculated using the Nernst equation. The duration of each potential step was 15 s. The acquisition time was 40 ms, and 10 average accumulations were recorded for each spectrum. The EC-SPR experiment was repeated six times with different samples. (C) SPR transmission intensity changes (%) from an Au-NPE exposed to freshly prepared solutions of different $[Fe(CN)_6]^{4-}/[Fe(CN)_6]^{3-}$ ratios. $[Fe(CN)_6]^{3-}$: $[Fe(CN)_6]^{4-}$, 0 mM: 1 mM, 0.2 mM: 0.8 mM, 0.4 mM:

0.6 mM, 0.6 mM: 0.4 mM, 0.8 mM: 0.2 mM, 1 mM: 0 mM. The transmission measurements were recorded at open circuit potential.

7.4 Conclusions

3-D Au-NPEs on the large area were fabricated using the IL technique. Uniform, clean and stable 3-D Au-NPEs were obtained by directly coating IL 3-D photoresist templates with a metal (gold) film deposited at an oblique angle. The presence of the nanopillars on the surface significantly increased the electroactive surface area of the electrode. The Au-NPEs, with 590 nm periodicity, 100 nm-thick gold film, showed about 17% higher voltammetric current values than that of a flat gold electrode. The increased electrical current was confirmed by numerical simulations using COMSOL Multiphysics®. The Au-NPEs were also implemented in EC-SPR measurements of the $Fe(CN)_6^{4-,3-}$ redox couple, serving simultaneously as both working electrode and SPR sensing area. The Au- NPEs showed detectable SPR intensity changes in the presence of electrogenerated $Fe(CN)_6^{3-/4-}$ redox species at relatively low concentrations (total concentration of 1 mM).

7.5 Acknowledgment

M. A. would like to thank Mr. Ahmed A. Al Balushi, Ph.D. candidate from Department of Electrical and Computer Engineering of the University of Victoria for all his help with the IL set up alignments. This work was funded by the NSERC Discovery Grant Program.

7.6 References

1. Cherevko, S.; Chung, C.-H., Gold Nanowire Array Electrode for Non-Enzymatic Voltammetric and Amperometric Glucose Detection. *Sensors and Actuators B: Chemical* **2009**, *142*, 216-223.
2. Fan, Z.; Ruebusch, D. J.; Rathore, A. A.; Kapadia, R.; Ergen, O.; Leu, P. W.; Javey, A., Challenges and Prospects of Nanopillar-Based Solar Cells. *Nano Res.* **2009**, *2*, 829-843.
3. Kandziolka, M.; Charlton, J. J.; Kravchenko, II; Bradshaw, J. A.; Merkulov, I. A.; Sepaniak, M. J.; Lavrik, N. V., Silicon Nanopillars as a Platform for Enhanced Fluorescence Analysis. *Anal. Chem.* **2013**, *85*, 9031-9038.
4. Prehn, R.; Abad, L.; Sánchez-Molas, D.; Duch, M.; Sabaté, N.; del Campo, F. J.; Muñoz, F. X.; Compton, R. G., Microfabrication and Characterization of Cylinder Micropillar Array Electrodes. *J. Electroanal. Chem.* **2011**, *662*, 361-370.
5. Fan, Z.; Razavi, H.; Do, J. W.; Moriwaki, A.; Ergen, O.; Chueh, Y. L.; Leu, P. W.; Ho, J. C.; Takahashi, T.; Reichertz, L. A.; Neale, S.; Yu, K.; Wu, M.; Ager, J. W.; Javey, A., Three-Dimensional Nanopillar-Array Photovoltaics on Low-Cost and Flexible Substrates. *Nat Mater* **2009**, *8*, 648-653.
6. Tang, Y.-H.; Huang, M.-J.; Shiao, M.-H.; Yang, C.-R., Fabrication of Silicon Nanopillar Arrays and Application on Direct Methanol Fuel Cell. *Microelectron. Eng.* **2011**, *88*, 2580-2583.
7. Rider, D. A.; Tucker, R. T.; Worfolk, B. J.; Krause, K. M.; Lalany, A.; Brett, M. J.; Buriak, J. M.; Harris, K. D., Indium Tin Oxide Nanopillar Electrodes in Polymer/Fullerene Solar Cells. *Nanotechnology* **2011**, *22*, 085706.
8. Gao, M.-J.; Wang, X.-D.; Guo, M.; Zhang, M., Contrast on Cod Photo-Degradation in Coking Wastewater Catalyzed by Tio2 and Tio2–Tio2 Nanorod Arrays. *Catal. Today* **2011**, *174*, 79-87.
9. Patolsky, F.; Timko, B. P.; Yu, G.; Fang, Y.; Greytak, A. B.; Zheng, G.; Lieber, C. M., Detection, Stimulation, and Inhibition of Neuronal Signals with High-Density Nanowire Transistor Arrays. *Science (Washington, DC, U. S.)* **2006**, *313*, 1100-1104.
10. Anandan, V.; Gangadharan, R.; Zhang, G., Role of Sam Chain Length in Enhancing the Sensitivity of Nanopillar Modified Electrodes for Glucose Detection. *Sensors (Basel)* **2009**, *9*, 1295-1305.
11. Evans, P.; Hendren, W. R.; Atkinson, R.; Wurtz, G. A.; Dickson, W.; Zayats, A. V.; Pollard, R. J., Growth and Properties of Gold and Nickel Nanorods in Thin Film Alumina. *Nanotechnology* **2006**, *17*, 5746-5753.
12. Hulteen, J. C.; Martin, C. R., A General Template-Based Method for the Preparation of Nanomaterials. *J. Mater. Chem.* **1997**, *7*, 1075-1087.
13. Sanetra, N.; Feig, V.; Wolfrum, B.; Offenhäusser, A.; Mayer, D., Low Impedance Surface Coatings Via Nanopillars and Conductive Polymers. *physica status solidi (a)* **2011**, *208*, 1284-1289.
14. Ji, S.; Song, K.; Nguyen, T. B.; Kim, N.; Lim, H., Optimal Moth Eye Nanostructure Array on Transparent Glass Towards Broadband Antireflection. *ACS Appl Mater Interfaces* **2013**, *5*, 10731-10737.
15. Dhawan, A.; Gerhold, M.; Madison, A.; Fowlkes, J.; Russell, P. E.; Vo-Dinh, T.; Leonard, D. N., Fabrication of Nanodot Plasmonic Waveguide Structures Using Fib Milling and Electron Beam-Induced Deposition. *Scanning* **2009**, *31*, 139-146.

16. Golobokova, L. S.; Nastaushev, Y. V.; Dultsev, F. N.; Gulyaev, D. V.; Talochkin, A. B.; Latyshev, A. V., Fabrication and Optical Properties of Silicon Nanopillars. *Journal of Physics: Conference Series* **2014**, *541*, 012074.
17. Himcinschi, C.; Singh, R.; Radu, I.; Milenin, A. P.; Erfurth, W.; Reiche, M.; Gösele, U.; Christiansen, S. H.; Muster, F.; Petzold, M., Strain Relaxation in Nanopatterned Strained Silicon Round Pillars. *Appl. Phys. Lett.* **2007**, *90*, 021902.
18. Zin, M. T.; Leong, K.; Wong, N.-Y.; Ma, H.; Sarikaya, M.; Jen, A. K. Y., Surface-Plasmon-Enhanced Fluorescence from Periodic Quantum Dot Arrays through Distance Control Using Biomolecular Linkers. *Nanotechnology* **2009**, *20*, 015305.
19. Menezes, J. W.; Ferreira, J.; Santos, M. J. L.; Cescato, L.; Brolo, A. G., Large-Area Fabrication of Periodic Arrays of Nanoholes in Metal Films and Their Application in Biosensing and Plasmonic-Enhanced Photovoltaics. *Adv. Funct. Mater.* **2010**, *20*, 3918-3924.
20. Gartia, M. R.; Xu, Z.; Behymer, E.; Nguyen, H.; Britten, J. A.; Larson, C.; Miles, R.; Bora, M.; Chang, A. S. P.; Bond, T. C.; Liu, G. L., Rigorous Surface Enhanced Raman Spectral Characterization of Large-Area High-Uniformity Silver-Coated Tapered Silica Nanopillar Arrays. *Nanotechnology* **2010**, *21*.
21. Brolo, A. G., Plasmonics for Future Biosensors. *Nature Photonics* **2012**, *6*, 709-713.
22. Valsecchi, C.; Brolo, A. G., Periodic Metallic Nanostructures as Plasmonic Chemical Sensors. *Langmuir* **2013**, *29*, 5638-5649.
23. Kato, Y.; Sugiura, M.; Oda, A.; Watanabe, T., Spectroelectrochemical Determination of the Redox Potential of Pheophytin a, the Primary Electron Acceptor in Photosystem Ii. *Proc Natl Acad Sci U S A* **2009**, *106*, 17365-17370.
24. Klod, S.; Dunsch, L., A Combination of in Situ Esr and in Situ Nmr Spectroelectrochemistry for Mechanistic Studies of Electrode Reactions: The Case of P-Benzoquinone. *Magn. Reson. Chem.* **2011**, *49*, 725-729.
25. Murgida, D. H.; Hildebrandt, P., Disentangling Interfacial Redox Processes of Proteins by Serr Spectroscopy. *Chem. Soc. Rev.* **2008**, *37*, 937-945.
26. Baba, A.; Knoll, W.; Advincula, R., Simultaneous in Situ Electrochemical, Surface Plasmon Optical, and Atomic Force Microscopy Measurements: Investigation of Conjugated Polymer Electropolymerization. *Rev. Sci. Instrum.* **2006**, *77*, 064101.
27. Shan, X.; Patel, U.; Wang, S.; Iglesias, R.; Tao, N., Imaging Local Electrochemical Current Via Surface Plasmon Resonance. *Science (Washington, DC, U. S.)* **2010**, *327*, 1363-1366.
28. Baba, A.; Advincula, R. C.; Knoll, W., In Situ Investigations on the Electrochemical Polymerization and Properties of Polyaniline Thin Films by Surface Plasmon Optical Techniques. *J. Phys. Chem. B* **2002**, *106*, 1581-1587.
29. Xia, C. J.; Advincula, R. C.; Baba, A.; Knoll, W., In Situ Investigations of the Electrodeposition and Electrochromic Properties of Poly (3,4-Ethylenedioxythiophene) Ultrathin Films by Electrochemical-Surface Plasmon Spectroscopy. *Langmuir* **2002**, *18*, 3555-3560.
30. Baba, A.; Taranekar, P.; Ponnapati, R. R.; Knoll, W.; Advincula, R. C., Electrochemical Surface Plasmon Resonance and Waveguide-Enhanced Glucose Biosensing with N-Alkylaminated Polypyrrole/Glucose Oxidase Multilayers. *ACS Appl Mater Interfaces* **2010**, *2*, 2347-2354.
31. Iwasaki, Y.; Horiuchi, T.; Niwa, O., Detection of Electrochemical Enzymatic Reactions by Surface Plasmon Resonance Measurement. *Anal. Chem.* **2001**, *73*, 1595-1598.

32. Boussaad, S.; Pean, J.; Tao, N. J., High-Resolution Multiwavelength Surface Plasmon Resonance Spectroscopy for Probing Conformational and Electronic Changes in Redox Proteins. *Anal. Chem.* **2000**, *72*, 222-226.
33. Sannomiya, T.; Dermutz, H.; Hafner, C.; Voeroes, J.; Dahlin, A. B., Electrochemistry on a Localized Surface Plasmon Resonance Sensor. *Langmuir* **2010**, *26*, 7619-7626.
34. Menezes, J. W.; Barea, L. A. M.; Chillcce, E. F.; Frateschi, N.; Cescato, L., Comparison of Plasmonic Arrays of Holes Recorded by Interference Lithography and Focused Ion Beam. *IEEE Photonics J.* **2012**, *4*, 544-551.
35. Xie, Q.; Hong, M. H.; Tan, H. L.; Chen, G. X.; Shi, L. P.; Chong, T. C., Fabrication of Nanostructures with Laser Interference Lithography. *J. Alloys Compd.* **2008**, *449*, 261-264.
36. Cao, Z., Thin Film Growth Physics, Materials Science and Applications. In *Woodhead Publishing in materials* [Online] Woodhead Pub.,: Cambridge, UK ; Philadelphia, PA, 2011; p. 1 online resource (1 v. http://proxy.lib.sfu.ca/login?url=http://proquest.safaribooksonline.com/?uiCode=simonfraser&xmlId=9781845697365 Full text - Safari Books Online limited to 8 simultaneous users.
37. Franssila, S., *Introduction to Microfabrication*; J. Wiley: Chichester, West Sussex, England ; Hoboken, NJ, 2004, p xvii, 401 p.
38. Lin, E.-H.; Tsai, W.-S.; Lee, K.-L.; Lee, M.-C. M.; Wei, P.-K., Enhancing Detection Sensitivity of Metallic Nanostructures by Resonant Coupling Mode and Spectral Integration Analysis. *Opt. Express* **2014**, *22*.
39. Godino, N.; Borrise, X.; Xavier Munoz, F.; Javier del Campo, F.; Compton, R. G., Mass Transport to Nanoelectrode Arrays and Limitations of the Diffusion Domain Approach: Theory and Experiment. *J. Phys. Chem. C* **2009**, *113*, 11119-11125.
40. Henstridge, M. C.; Compton, R. G., Mass Transport to Micro- and Nanoelectrodes and Their Arrays: A Review. *Chem Rec* **2012**, *12*, 63-71.
41. Bard, A. J.; Faulkner, L. R., *Electrochemical Methods : Fundamentals and Applications*, 2nd ed.; Wiley: New York, 2001, p xxi, 833 p.
42. Gordon, R.; Sinton, D.; Kavanagh, K. L.; Brolo, A. G., A New Generation of Sensors Based on Extraordinary Optical Transmission. *Acc. Chem. Res.* **2008**, *41*, 1049-1057.
43. Kragt, H. J.; Smith, C. P.; White, H. S., Refractive-Index Mapping of Concentration Profiles. *J. Electroanal. Chem.* **1990**, *278*, 403-407.
44. Iwasaki, Y.; Horiuchi, T.; Morita, M.; Niwa, O., Electrochemical Reaction of Fe (Cn)(6)(3-)/(4-) on Gold Electrodes Analyzed by Surface Plasmon Resonance. *Surf. Sci.* **1999**, *427-28*, 195-198.

Chapter 8 : Summary and Future Work

8.1 Summary

The electrochemical characteristics of an electrode are strongly influenced by its size and geometry. In Chapter 4, the electrochemical behaviors of 6 × 6 recessed nanoring electrode (r-NRE) arrays were compared to the 6 × 6 recessed nanodisc electrode (r-NDE) arrays. The 6 × 6 r-NDE and r-NRE arrays were fabricated on Si_4N_3/Ti/Au/Ti/glass slides by focused ion beam (FIB) milling. Their FIB fabrication parameters were optimized using Z-contrast imaging. Comprehensive three-dimensional (3D) simulations using COMSOL Multiphysics ® were carried out to explain the possible differences in the mass transport mechanism between these two geometries. Analysis of the diffusing layer shape within the nanohole electrodes revealed that differences between the electrochemical performance of the r-NDE and r-NDE arrays come from the differences in diffusion regime at the vicinity of the electrodes (within the nanoholes). We have shown that the shape of the diffusion layer within nanoring electrodes is very dependent on the geometrical parameters *r* and *h*. We have further defined a minimum *r*/*h*-ratio value that is needed for a recessed nanorings microarray to show a higher current density in comparison to that of a recessed nanodiscs microarray. The relationship between *r* and *h*, investigated in Chapter 4, allows an easy way to choose the proper geometrical parameters for a r-NRE microarray to present higher current density, compared to that of a r-NDE array occupying the same geometric area, without a need for complicated simulations. The results presented in chapter 4 are the first combination of experimental and numerical studies that elucidate the transport on nanoring electrode arrays. The comparison of the electrochemical performance between microsized arrays of nanostructures using full 3D simulations is also novel.

In Chapter 5, we have presented a comprehensive numerical study on the redox cycling performance properties of a 6 × 6 recessed nanorings-ring electrode array, Au-NRRA. In this configuration, each nanohole contains two nanoring electrodes that are electrically isolated and arranged vertically relative to each other. In redox cycling mode, the upper ring electrodes acted as the collector electrodes, and the lower ring electrodes acted as generator electrodes. The 6 ×6 Au-NRRA, (3.3 µm × 3.3 µm), (r =150 nm, $g = l$ = 150 nm, and hc= hg = 50 nm) was fabricated on metal/ insulator/metal/ insulator stack over a glass slide using FIB. This Au-NRRA presented a collection efficiency about 100 % and an amplification factor of about 3.5, which both were in good agreements with the simulation results. After validating the model against the experiment, a comprehensive computational investigation on the effects of the scan rates and scaling of the geometric parameters of the electrodes (ring height and radius) on the performance of this system have been performed. The simulation results revealed the performance capability of the Au-NRRA at very high scan rates. The numerical studies on the effect of electrode dimensions on the Au-NRRA's performance shows that the value of the attainable limiting current depends strongly on the ring radius, while it is almost independent of the ring height variations. In summary, this work provided useful information for the design of NRRA with improved redox cycling performance.

In Chapter 6, we have illustrated a novel active plasmonic device based on a new switching mechanism for the nanohole electrodes array. First, a nanoholes array was fabricated on a Si_3N_4/Ti/Au/Ti/glass slide using FIB. Since the top gold surface was coated with the Si_3N_4, the electroactive area was confined only to the Au surface inside the nanoholes. The Au surface within the nanoholes was then coated with a thin layer of an electroconductive polymer, polypyrrole (PPy). The electrodeposition of the PPy within the nanoholes by cycling the potentials was simultaneously monitored by SPR-enhanced transmission. The SPR-enhanced transmission

spectra of the nanoholes array exhibited a significant red-shift and intensity changes during the electropolymerization process. These observed changes in the transmission spectra properties of the nanoholes were associated well with the variations in the dielectric properties of the polymer film as it was growing and switching between its redox states. Further, it was shown that SPR-intensity through the PPy- modified nanohole electrodes can be easily tuned by applying external potentials. The capability of this device to be incorporated in optoelectronic devices was also demonstrated by switch on and off the transmitted light intensity through the modified nanohole arrays via potential steps.

In Chapter 7, we have fabricated the 3-D gold nanopillar electrodes (3-D Au-NPEs) array on a large area (2 cm× 2 cm) using laser interference lithography (IL). IL is a fast, high-throughput, and inexpensive method for fabricating uniform periodic micro/ nanostructures on large areas. The 3-D nanoelectrodes provide a remarkably larger electroactive surface area in comparison to a flat electrode with an equivalent geometric surface area. The electrochemical characteristics of these 3-D Au-NPEs were computationally and experimentally examined and compared to a conventional flat gold electrode. The 3-D Au-NPEs provided a higher current response (~ 17%) than that of a flat gold electrode. The 3-D Au-NPEs array was further used for *in-situ* electrochemical and surface plasmon resonance (EC-SPR) measurements. In EC-SPR measurements, the 3-D Au-NPEs array served as both the working electrode and the SPR sensor. The potential dependent concentration changes of a reversible redox species, $Fe(CN)_6^{4-,3-}$, near the 3-D Au-NPEs surface (at the metal-solution interface) were successfully monitored. There is a small difference between the refractive indexes of the ferri/ferrocyanide redox pair [1]. The refractive index of 100 mM $Fe(CN)_6^{4-}$, solution was reported to be 0.003 higher than that of $Fe(CN)_6^{3-}$.[2] In a previous attempt, the more common Kretschmann geometry was used to detect the SPR angle shifts

produced by the changes in the local refractive index in the bulk solution near the metal film during the $Fe(CN)_6^{4-,3-}$ electrochemical redox reaction. The 30.4 mM was the lowest $Fe(CN)_6^{4-,3-}$concentration at which the SPR angle shift was able to detect in that work. The transmission-based SPR measurements reported here measured a much lower $Fe(CN)_6^{4-,3-}$concentration (1 mM).

8.2 Future work

The nanoelectrodes studied in this dissertation can be implemented in a wide variety of different electroanalytical and biosensing measurements. Some future directions that this work can be taken are being discussed here.

The recessed nanoring arrays (Chapter 4) were fabricated using FIB. We could also use the IL technique for fabricating them, Figure 8-1, which will be a more cost-efficient approach.

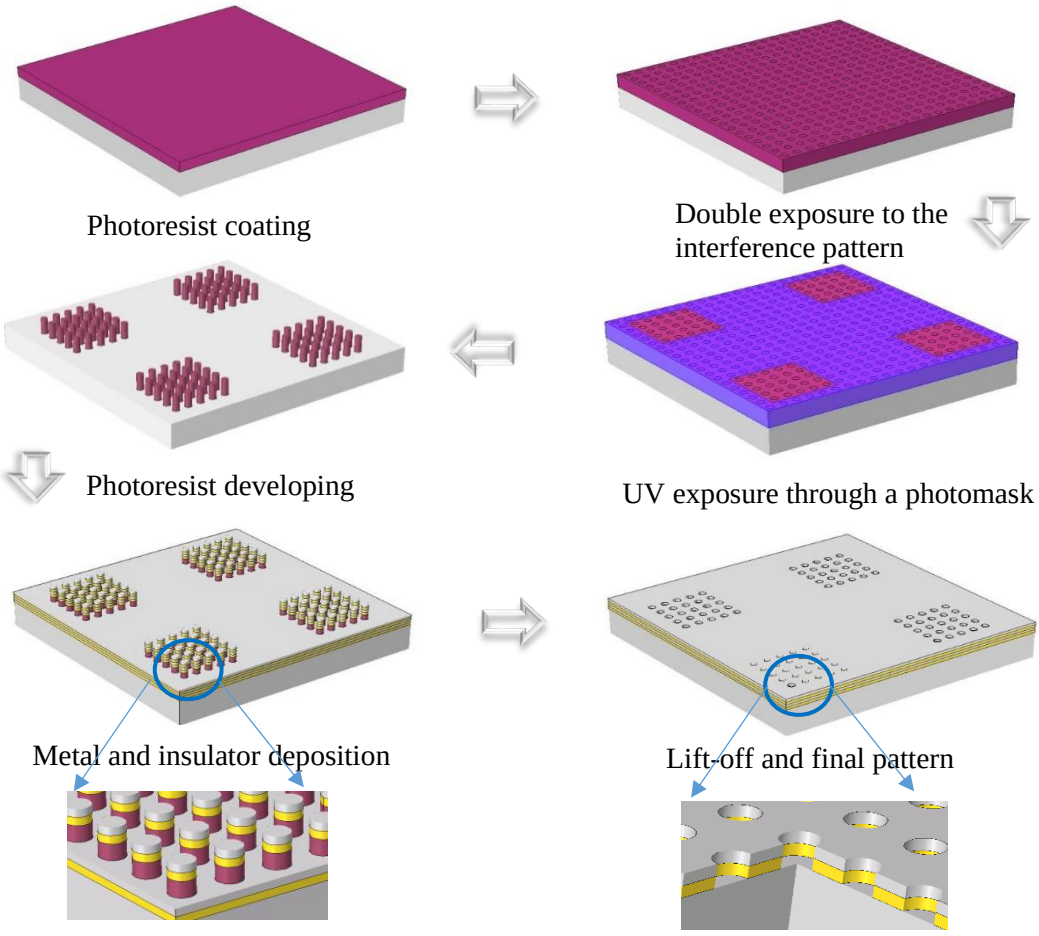

Figure 8-1. Schematic illustration of the fabrication steps of recessed nanoring addressable arrays using interference lithography.

Through computational studies, we have demonstrated the high-performance capability of Au-NRRA configuration at very high scan rates. One interesting future project would be the practical application of this system for detecting the electrogenerated intermediates with very short lifetime and also to study the electrochemical reaction mechanisms.

For the sake of the simulation studies, we have investigated the very small arrays of recessed nanoring-rings electrodes (6 × 6). Because for calculating the amplification factor for this configuration, we had to run 3D simulations on the recessed nanoring arrays (Au-NRRA operating

in single mode). These 3D simulations were very computationally expensive and time-consuming and limited us to study a larger array (but still microsize). In the future applications larger array of Au-NRRA should be used. As we have shown in chapter 5, there are not any diffusion layers overlap between the adjacent nanoholes on the array in redox cycling mode. The presence of the top ring confines the diffusion layer within each nanohole. Then using larger array will improve the response of this device greatly, because the current response of each nanohole (containing the nanoring-ring electrodes) will simply add up.

Since there is no cross taking between the nanoholes in the Au-NRRA configuration (operating in redox cycling mode) this configuration would be a very attractive tool in single molecule analysis of the reversible or quasi-reversible electroactive species.

And as each nanohole in the Au-NRRA configuration works individually without any significant interaction with its neighboring nanohole, therefore, in this case, it is true to talk about the nanoliter volume for each nanohole. Hence, in the analysis where the sample volume is very limited, the recessed nanoring-rings configuration can be a possible solution. There are situations like in health care measurement and analysis where the volume of the sample in very limited e.g. sweat samples.

And in terms of the numerical studies, that would also be interesting to compare the performance of Au-NRRA configuration with other vertical redox cycling systems, for example with that of the well studied recessed nanoring-disc configuration.

The large-area plasmonic nanopillars, fabricated and investigated in Chapter 7, also opens up many possibilities for biosensing and the other applications where a large organized area of nanostructures is desirable.

The nanopillars array could be used in dye wastewater treatments (e.g. for studying the photodegradation of Rhodamine B) and/or to remove the heavy metals from wastewater. This can be done by depositing the proper materials over the nanopillars (for example TiO_2). They can also be used as a sensor to detect for example glucose, by coat them with a thin layer of carbon.

Highly uniform plasmonic substrates are also desirable in surface-enhanced Raman spectroscopy (SERS) measurements. This makes the fully conductive large area Au nanopillars an attractive candidate for future SERS and sensing applications.

Besides these possible applications, the influence of the nanopillar aspect ratio, the periodicity, and the metal thickness on their SPR sensitivity need further investigations.

8.3 References

1. Iwasaki, Y.; Horiuchi, T.; Morita, M.; Niwa, O., Electrochemical Reaction of Fe (Cn)(6)(3-)/(4-) on Gold Electrodes Analyzed by Surface Plasmon Resonance. Surf. Sci. **1999**, 427-28, 195-198.
2. Kragt, H. J.; Smith, C. P.; White, H. S., Refractive-Index Mapping of Concentration Profiles. J. Electroanal. Chem. **1990**, 278, 403-407.